



HAL
open science

Source rock evaluation in the Eastern Mediterranean Sea: An integrated approach of organic geochemistry, stratigraphic forward modeling and petroleum system modeling

Sebastian Grohmann

► **To cite this version:**

Sebastian Grohmann. Source rock evaluation in the Eastern Mediterranean Sea: An integrated approach of organic geochemistry, stratigraphic forward modeling and petroleum system modeling. Applied geology. Sorbonne Université; Rheinisch-westfälische technische Hochschule (Aix-la-Chapelle, Allemagne), 2019. English. NNT : 2019SORUS690 . tel-04643258

HAL Id: tel-04643258

<https://theses.hal.science/tel-04643258>

Submitted on 10 Jul 2024

HAL is a multi-disciplinary open access archive for the deposit and dissemination of scientific research documents, whether they are published or not. The documents may come from teaching and research institutions in France or abroad, or from public or private research centers.

L'archive ouverte pluridisciplinaire **HAL**, est destinée au dépôt et à la diffusion de documents scientifiques de niveau recherche, publiés ou non, émanant des établissements d'enseignement et de recherche français ou étrangers, des laboratoires publics ou privés.

Sorbonne Université

Ecole doctorale 398 Géosciences, Ressources Naturelles et Environnement

Institut des Sciences de la Terre de Paris – Paléoenvironnements, Paléoclimats, Bassins

et

Rheinisch-Westfälische Technische Hochschule

Aachen

Fakultät für Georessourcen und Materialtechnik

*Energy and Mineral Resources Group – Institute of Geology and Geochemistry of
Petroleum and Coal*

Source rock evaluation in the Eastern Mediterranean Sea: An integrated approach of organic geochemistry, stratigraphic forward modeling and petroleum system modeling

Par Sebastian Grohmann

Thèse de doctorat de géosciences du pétrole

Dirigée par Prof. Dr. François Baudin et Prof. Dr. Ralf Littke

Présentée et soutenue publiquement le 30 Septembre 2019

Devant un jury composé de :

Prof. Dr. François Baudin, directeur de thèse

Prof. Dr. Ralf Littke, directeur de thèse

Prof. Dr. Fadi Henri Nader, co-directeur de thèse

Dr. Maria Fernanda Romero-Sarmiento, promoteur de thèse

Prof. Dr. Christian Gorini, examinateur

Prof. Dr. Jan Schwarzbauer, examinateur

Dr. Zahie Anka, rapporteur

Dr. Mohammed Boussafir, rapporteur



Eidesstattliche Erklärung

Hiermit versichere ich eidesstattlich, dass ich die Dissertation selbstständig verfasst und alle in Anspruch genommenen Hilfen in der Dissertation angegeben habe.

Sebastian Grohmann

Aachen, den _____

Ort, Datum

Déclaration sur l'honneur

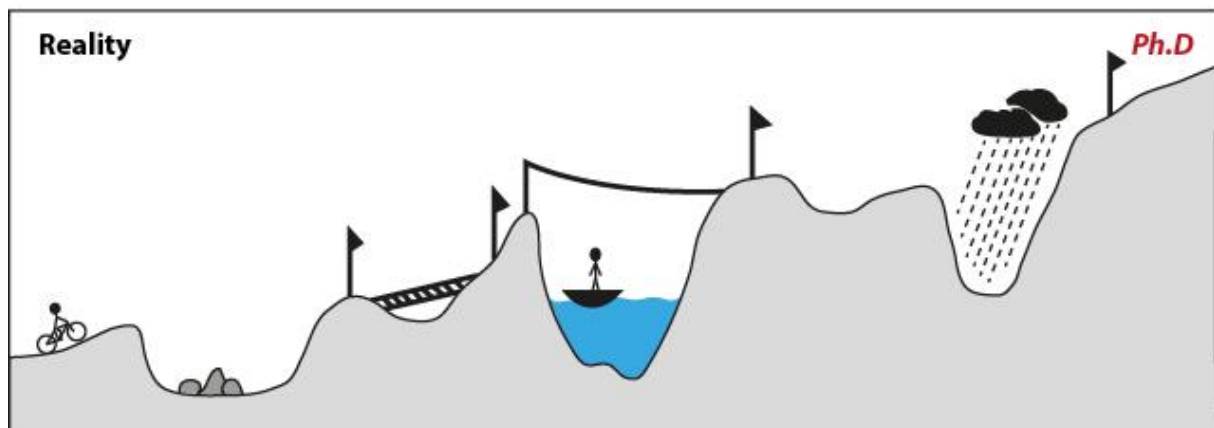
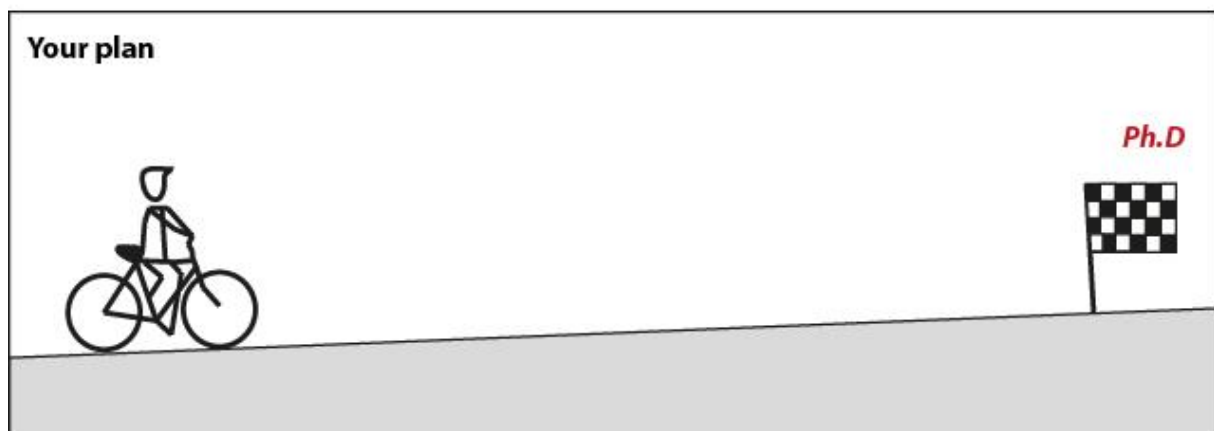
J'affirme par la présente que j'ai rédigé moi-même la thèse et indiqué toutes les aides utilisées dans la thèse.

Sebastian Grohmann

Aix-la-Chapelle, le _____

lieu, date

The great experience of doing a Ph.D



Acknowledgements

Looking back at the last three years of my life as a PhD student, I realize that neither my success in my scientific work, my publications and contributions to scientific conferences, nor all the fun I had during that time, would have been possible without the support of many great people.

First of all, I want to thank my thesis directors Prof. Ralf Littke and Prof. François Baudin for their continuous support and believe in my qualification as a researcher. It was an honor to learn from their long professional experience, and I am grateful for the many excellent discussion we had. Further, I want to thank my two IFPEN promoters Dr. Fadi Nader and Dr. Maria Romero-Sarmiento, who made my time at the IFPEN in France a great experience. Next to the many interesting scientific discusses we had, I am especially thankful for the general organization and management skills I could learn from them. All in all, I can say that I had the best team of supervisors a PhD student can wish for. Thank you very much for the great moments we spent together. Especially our time together on Cyprus will always stay in my mind.

Further, I thank *Beicip Franlab* for providing the licenses for *DionisosFlow*® and *TemisFlow*® and I thank Dr. Benoit Chauveau and Dr. Renaud Traby, who gave great supported with the technical aspects of using the respective software packages. Another thank you goes to Dr. Nicolas Hawie for good discussions about modeling the Eastern Mediterranean.

Next to my thesis supervisors and good colleagues, it is of course all the other people, colleagues and friends who are important to survive the ups and downs of a PhD life. There is the great team of the LEK, which are more friends and family rather than just colleagues. I love to think back on all the moments we spent together, from thesis related geological discussions to additional, more fun related lazer experiments.

Also in Paris, I met a lot of great people who helped me to survive my time in France and made my stay there one of the best experiences of my life so far.

A very special thank you goes out to all the friends, who were there during the harder times of my PhD and listened to my several little and bigger problems. Without you guys, this PhD would not have been possible. Thank you very much, Steffen, Garri, Felix, Laura, Jannik, Ingo, Asja, Elli, Chris, Iman, Kanchana, Martina, and Damaris.

Of course I also want to thank my family, for their constant believe in me taking the right decisions and supporting me in each kind of way.

Table of content

Structure of this thesis	i
Abstract	ii
Résumé	iv
Zusammenfassung	vi
Abbreviations	viii
1 Introduction	1
1.1 The Eastern Mediterranean Sea – a new frontier area for hydrocarbon exploration	2
1.2 Previous work	3
1.3 Aim of this thesis	5
2 Geological setting of the Eastern Mediterranean	7
2.1 Tectonic history of the Eastern Mediterranean	7
2.2 Crustal characteristics of the Eastern Mediterranean	9
2.3 Geology of the greater Cyprus area	10
2.3.1 Circum Troodos Sedimentary Succession.....	11
2.3.2 Mamonia Complex	14
2.3.3 Eratosthenes Seamount	15
3 Field campaigns and sample collection	19
3.1 First field campaign	19
3.1.1 Summary.....	19
3.1.2 Outcrop and sample description	20
3.2 Second field campaign.....	27
3.2.1 Summary.....	27
3.2.2 Outcrop and sample description	28
3.3 Sampling ODP Leg 160 cores at Marum, Bremen, Germany.....	36
3.3.1 ODP Leg 160 campaign.....	36
3.3.2 Sample description	37
4 Source rock characterization of Mesozoic to Cenozoic organic matter-rich marls and shales of the Eratosthenes Seamount, Eastern Mediterranean Sea	39
4.1 Introduction.....	40
4.2 Geological background	42
4.3 Material and methods	44
4.3.1 Samples	44

4.3.2	Elemental analysis and Rock-Eval pyrolysis.....	44
4.3.3	Organic petrographic analysis	47
4.3.4	Molecular geochemistry.....	48
4.4	Results	49
4.4.1	Elemental analysis and Rock-Eval pyrolysis.....	49
4.4.2	Petrographic analysis.....	54
4.4.3	Molecular geochemistry.....	56
4.5	Discussion	58
4.5.1	Depositional environment.....	58
4.5.2	Source rock potential and thermal maturity.....	62
4.5.3	Implications for petroleum systems.....	63
4.6	Conclusion	65
5	Geochemical and petrographic investigation of Triassic and Late Miocene organic-rich intervals from onshore Cyprus, Eastern Mediterranean.....	67
5.1	Introduction.....	68
5.2	Geological setting.....	70
5.3	Petroleum source rocks in the Eastern Mediterranean	72
5.4	Samples and methods	74
5.4.1	Sampling representative outcrop rocks: Onshore Cyprus.....	74
5.4.2	Sample preparation.....	75
5.4.3	Elemental analysis	78
5.4.4	Rock-Eval pyrolysis	79
5.4.5	Biomarker analysis.....	79
5.4.6	Organic petrography and palynofacies analysis.....	80
5.5	Results and interpretation.....	81
5.5.1	Organic matter-richness and carbonate content.....	81
5.5.2	Source rock quality and thermal maturity	81
5.5.3	Origin of organic matter and paleo-redox conditions.....	88
5.6	General discussion and hypothesis on the offshore area	94
5.6.1	Mechanisms of source rock deposition (Pakhna Fm.).....	95
5.6.2	Implications on petroleum systems in the Eastern Mediterranean Sea.....	98
5.7	Conclusion	99
6	Characterization of Late Cretaceous to Miocene source rocks in the Eastern Mediterranean Sea: An integrated numerical approach of stratigraphic forward modeling and petroleum system modeling.....	101
6.1	Introduction.....	102

6.2	Geological setting	105
6.3	Workflow	106
6.3.1	Stratigraphic forward modeling	107
6.3.2	Petroleum system modeling.....	112
6.4	Results and discussion.....	115
6.4.1	Stratigraphic forward modeling	115
6.4.2	Petroleum system model	124
6.5	Conclusion	132
7	Conclusion.....	135
7.1	Summary.....	135
7.1.1	Source rock characterization	135
7.1.2	Simulation of source rock deposition.....	139
7.1.3	Simulation of source rock maturation.....	140
7.2	Perspective	141
	Bibliography	143
	List of figures	156
	List of tables	164
	Appendix	166

Structure of this thesis

The present thesis follows the approach of three individual publications and one final conclusion rather than presenting one monography. However, the thesis is divided into 7 chapters:

1. The first chapter gives an introduction into the Eastern Mediterranean Sea as a new frontier hydrocarbon exploration area. There, the previous work about the area and the main scientific aims of this project are defined.
2. The second part provides an overview of the geological history of the Eastern Mediterranean in general with a special focus on the greater area of Cyprus.
3. In the third chapter, a detailed description of the performed sampling campaigns onshore Cyprus and at the Marum, University of Bremen, is provided.
4. The fourth chapter deals with the geochemical and petrographic characterization of organic-rich rocks offshore Cyprus. This chapter is published as “Grohmann, S., Fietz, S.W., Littke, R., Bou Daher, S., Romero-Sarmiento, M.F., Nader, F.H., Baudin, F. (2018). *Source rock characterization of Mesozoic to Cenozoic organic matter-rich marls and shales of the Eratosthenes Seamount, Eastern Mediterranean Sea. Oil and Gas Science and Technology – Rev. IFP Energies nouvelles* 73, 49.”
5. The fifth chapter deals with the geochemical and petrographic characterization of organic-rich rocks from onshore Cyprus. This chapter is published as “Grohmann, S., Romero-Sarmiento, M.F., Nader, F.H., Baudin, F., Littke, R. (2019). *Geochemical and petrographic investigation of Triassic and Late Miocene organic-rich intervals from onshore Cyprus, Eastern Mediterranean. International Journal of Coal Geology* 209, 94-116.”
6. The sixth chapter deals with the numerical simulation of source rocks in the Eastern Mediterranean. This chapter is going to be submitted to a peer-reviewed journal in the last three months of this thesis, after the thesis submission.
7. The seventh chapter gives a summary of the previous three main chapters, puts the different studies in a context to each other and provides an outlook on possible future projects.

Abstract

The Eastern Mediterranean Sea represents one of the world's most important hydrocarbon exploration areas. As one crucial element for the understanding and evaluation of petroleum systems, the focus of this thesis is the characterization of potential petroleum source rocks in the area. This includes three main tasks: the first one corresponds to the geochemical and petrographic analysis of previously unknown organic matter (OM)-rich rocks from onshore Cyprus and the ODP Leg 160 wells along the Eratosthenes Seamount (ESM) offshore southern Cyprus. The second part is dedicated to the numerical simulation of these and other source rocks in the greater area via stratigraphic forward modeling. And the last one corresponds to the thermal maturation of these source rocks, which was simulated via petroleum system modeling.

At the ESM, OM occurs in dark mudstones in the Upper Cretaceous and Eocene. Upper Cretaceous samples show good source rock properties with average total organic carbon (TOC) contents of about 0.9wt.% and average hydrogen index (HI) values of 319 mg HC/g TOC. A cumulative thickness of around 11 m is observed in the investigated cores. Eocene samples show a fair quality over a cumulative thickness of about 30 m reaching very good quality in a 3 m thick interval in the Upper Eocene with average TOC contents of 4.8wt.% and HI values of about 469 mg HC/g TOC. Rock-Eval results, biomarker ratios, and microscopic investigations indicate mainly type II kerogen for all offshore samples. A positive correlation between the TOC and the total sulfur (TS) content, as well as pristane (Pr) over phytane (Ph) ratios < 2 suggest a deposition under upwelling related increased primary productivity and the formation of an extended oxygen minimum zone. Hence, the lateral extent of these source rocks is restricted to the closer surrounding of the ESM. Vitrinite reflectance (VR_r) values $\leq 0.3\%$ indicate thermal immaturity. Burial depth has never been much deeper than at present day.

Onshore Cyprus, OM occurs within two geological formations (Fm.). In the Triassic Vlambouros Fm., thin clay layers are interbedded with meter thick sandstone units. OM is concentrated in the clay intervals with TOC contents of 1wt.% on average, but occurs also finely dispersed in the sandstones. HI values average 48 mg HC/g TOC. Microscopic analysis shows a dominance of higher land plants. Low TS/TOC and several biomarker ratios indicate oxygenated, fresh water conditions. VR_r values $\leq 0.6\%$ also indicate thermal immaturity.

In the Miocene Pakhna Fm., OM occurs in the upper part of the Fm. in outcrops located east of the Troodos Mountain. OM is present in fine-grained, argillaceous mudstone layers of about 20 cm thickness intercalated with similar thick, coarser grained limestones. Average TOC contents and HI values are 4wt.% and 238 mg HC/g TOC, respectively and OM is thermally immature ($VR_r \leq 0.5\%$). Based on Rock-Eval and biomarker results as well as microscopic investigation, the OM is interpreted as mainly marine type II kerogen with minor contributions of terrestrial type III material. TS/TOC

ratios ≥ 2.8 and biomarker ratios indicate dys- to even anoxic marine conditions. A positive correlation between the amount of OM and the silicate content indicates that such conditions were reached during enhanced primary productivity controlled by clastic derived nutrient input.

Stratigraphic forward modeling provides a best-fit model for Late Cretaceous, Eocene, and Oligo-Miocene source rocks in the Eastern Mediterranean. The model was calibrated by comparing simulated vs. actual thickness, simulated gross depositional environments (GDE) vs. published GDE maps, as well as simulated geochemical parameters vs. data obtained from rock samples of the ESM and the Levant Margin.

The model supports the idea of Late Cretaceous and Eocene upwelling systems as main controlling factor for source rock deposition along the ESM and the Levant margin. Deposited and preserved OM is restricted to the extended oxygen minimum zone resulting in a narrow, continuous source rock band parallel to the Levant shelf and a more patchy distribution on top of the ESM. During the Oligocene and Miocene, a small contribution of terrestrial OM via sediment input sources from the Nile area and the Levant Margin lead to a relative homogenous lateral and vertical distribution of OM, but low TOC contents ($\ll 1\%$) throughout the entire basin, which is in accordance with geochemical information on the Oligocene in the northern Nile Delta.

Petroleum system modeling results shows that the high quality parts of Late Cretaceous and Eocene source rocks are not affected by thermal maturation. Only at two locations, low TOC ($< 1\%$) source rocks fall within the zone of hydrocarbon generation. Offshore northern Lebanon, Late Cretaceous source rocks entered the oil window during the middle to late Eocene and reached the dry gas window at present-day burial. Southeast of the ESM, Late Cretaceous source rocks reached the end of the wet gas window during the deposition of the Messinian salt. The same holds true for Eocene source rocks, which reach at both locations into the zone of oil and wet gas generation at present day burial. Oligocene source rocks, which can be found throughout the basin, lie within the oil window in the southern basin and reach into the onset of the wet gas window in the northern part of the basin. Miocene source rocks, instead, are mainly immature throughout the entire basin.

Résumé

La Méditerranée orientale est l'une des plus importantes zones d'exploration d'hydrocarbures au monde. En tant qu'éléments cruciaux pour la compréhension et l'évaluation des systèmes pétroliers, les roches mères potentielles de la région et leur caractérisation sont le sujet central de cette thèse. Méthodologiquement, cette étude est articulée en trois étapes. La première correspond à l'analyse géochimique et pétrographique de roches riches en matières organiques (MO) provenant d'affleurements « onshore » échantillonnés à Chypre, et des puits de la campagne ODP 160 localisés tout au long du mont sous-marin dénommé « Eratosthenes Seamount (ESM) », situé au sud de Chypre. La deuxième partie est dédiée à la modélisation stratigraphique par simulation numérique de ces roches mères et d'autres roches mères potentielles de la région. Dans la troisième étape, la maturation thermique de ces roches mères a été simulée via les outils de modélisation de bassin.

Au niveau de l'ESM, la MO se trouve dans les argiles noires du Crétacé supérieur et de l'Éocène. Les échantillons du Crétacé supérieur présentent de bonnes propriétés de roche mère avec une teneur moyenne en carbone organique total (COT) d'environ 0,9% en poids et des valeurs d'indice d'hydrogène moyen (IH) de 319 mg HC / g de COT. Une épaisseur cumulée d'environ 11 m est observée dans les carottes étudiées. Les échantillons de l'Éocène montrent une qualité moyenne sur une épaisseur cumulée d'environ 30 m et une très bonne qualité dans un intervalle de 3 m d'épaisseur dans l'Éocène supérieur avec des teneurs moyennes en COT de 4,8% en poids et des valeurs d'IH d'environ 469 mg de HC / g de COT. Les résultats Rock-Eval, les rapports de biomarqueurs et les études microscopiques indiquent principalement des kérogènes de type II pour tous les échantillons « offshore ». Une corrélation positive entre le COT et la teneur en soufre total (TS), ainsi que des rapports de pristane (Pr) sur phytane (Ph) <2, suggèrent un dépôt en conditions d'upwelling impliquant une augmentation de la productivité primaire et en conséquence la formation d'une zone à minimum d'oxygène. Ainsi, l'étendue latérale de ces roches mères est limitée à l'environnement le plus proche de l'ESM. Des valeurs de réflectance de la vitrinite (VRr) $\leq 0,3\%$ indiquent une immaturité thermique et que la profondeur d'enfouissement ne peut pas avoir été beaucoup plus profonde qu'aujourd'hui.

Sur la côte chypriote, la MO est présente dans deux formations géologiques. Dans la « Triassic Vlambouros » Fm., de fines couches d'argile sont intercalées avec des unités de grès d'un mètre d'épaisseur. La MO est concentrée dans les argiles avec une teneur moyenne en COT de 1% en poids, mais se trouve également dispersée dans les grès. Les valeurs d'IH sont en moyenne de 48 mg de HC / g de COT. Les valeurs d'indice d'oxygène élevé (OI), ainsi que l'analyse microscopique permettent d'identifier une MO issue de plantes terrestres supérieures. Un rapport TS / COT bas et plusieurs ratios de biomarqueurs indiquent des conditions d'eau fraîche oxygénée. Les valeurs de VRr $\leq 0,6\%$ indiquent une immaturité thermique.

Dans la Fm. Pakhna, d'âge Miocène, la MO se situe dans la partie supérieure de la formation dans les affleurements à l'est de la montagne Troodos. La MO est présente dans des couches de mudstone argileux à grain fin d'environ 20 cm d'épaisseur intercalées avec des calcaires d'épaisseur similaire et à gros grain. Les teneurs en COT et les valeurs d'IH sont de 4% en poids et 238 mg de HC / g de COT en moyenne, respectivement ; la MO est thermiquement immature ($VRr \leq 0,5\%$). Sur la base des résultats Rock-Eval et des biomarqueurs, ainsi que de observations au microscope, la MO est interprétée comme étant principalement un kérogène de type II marin avec des contributions mineures de matériel de type III terrestre. Les ratios $TS / COT \geq 2,8$ et les rapports de biomarqueurs indiquent des environnements de dépôt dysoxiques voire anoxiques. Une corrélation positive entre la quantité de MO et la teneur en silicate indique que de telles conditions ont été atteintes pendant une productivité primaire accrue contrôlée par un apport en nutriments dérivés de l'apport clastique.

La modélisation stratigraphique directe fournit le meilleur modèle pour les roches mères du Crétacé supérieur, de l'Eocène et de l'Oligo-Miocène en Méditerranée orientale. Le modèle a été calibré en comparant l'épaisseur simulée par rapport à l'épaisseur réelle, les environnements de dépôt brut simulés par rapport aux cartes publiées, et les paramètres géochimiques simulés par rapport aux données réelles de l'ESM et de la marge du Levant.

Le modèle a pris en compte l'idée des systèmes d'upwelling du Crétacé supérieur et de l'Eocène en tant que principal facteur de contrôle du dépôt de la roche mère tout au long du ESM et de la marge du Levant. La MO déposée et préservée est limitée à la zone minimale d'oxygène, ce qui donne une bande de roche mère très fine et continue parallèle au plateau du Levant et une répartition plus inégale au-dessus du ESM. Pour l'Oligocène et le Miocène, une faible contribution de la MO terrestre via des sources d'apport de sédiments de la région du Nil et de la marge du Levant a conduit à une distribution latérale et verticale relativement homogène des faibles teneurs en COT ($\ll 1\%$) dans tout le bassin, conformément aux informations géochimiques de l'Oligocène dans le nord du delta du Nil.

La modélisation des systèmes pétroliers montre que les zones de haute qualité des roches mères du Crétacé supérieur et de l'Eocène ne sont pas affectées par la maturation thermique. Seuls deux sites, présentant des roches mères à faible COT ($<1\%$), ont atteint la zone de genèse des hydrocarbures. Au large des côtes septentrionales du Liban, les roches mères du Crétacé supérieur ont atteint la fenêtre à huile entre l'Eocène moyen et tardif, puis la fenêtre à gaz sec au niveau d'enfouissement actuel. Au sud-est de l'ESM, des roches mères du Crétacé supérieur ont atteint la fenêtre à gaz humide lors du dépôt du sel de Messinien. Il en va de même pour les roches mères de l'Eocène qui atteignent, en deux endroits, la zone de production d'huile et de gaz humide à l'enfouissement actuel. Aujourd'hui, les roches mères oligocènes, qui peuvent être trouvées dans tout le bassin, ont atteint l'enfouissement correspondant à la fenêtre à huile au sud et atteignent le début de la fenêtre à gaz humide dans la partie nord du bassin. Quant aux roches mères du Miocène, elles sont principalement immatures dans tout le bassin.

Zusammenfassung

Das östliche Mittelmeer ist eines der weltweit wichtigsten Explorationsgebiete für Kohlenwasserstoffe. Der Schwerpunkt dieser Arbeit liegt auf der Charakterisierung potenzieller Muttergesteine als entscheidendes Element für das Verständnis und die Bewertung von Kohlenwasserstoffsystemen. Dies umfasst drei Hauptziele: Das erste umfasst die geochemische und petrographische Analyse von bisher unbekanntem Organik (OM)-reichen Gesteinen auf Zypern und aus den ODP Leg 160 Bohrungen entlang des Eratosthenes Seamount (ESM) südlich vor Zypern. Das zweite Ziel behandelt die numerische Simulation dieser und anderer Muttergesteine im östlichen Mittelmeer durch stratigraphische Vorwärtsmodellierung. Das dritte Ziel beschäftigt sich mit der Simulation der thermischen Reifung dieser Muttergesteine mittels Beckenmodellierung.

Am ESM kommt OM in dunklen Mergeln der Oberkreide und des Eozäns vor. Proben aus der oberen Kreide zeigen gute Muttergesteinseigenschaften mit einem durchschnittlichen organischen Kohlenstoffgehalt (TOC) von 0,9 Gew.-% und einem durchschnittlichen Wasserstoffindex (HI) von 319 mg HC/g TOC. In den Kernen wird eine kumulative Mächtigkeit von ca. 11 m beobachtet. Eozänproben zeigen eine mittlere Qualität über eine kumulative Mächtigkeit von etwa 30 m und erreichen im oberen Eozän in einem 3 m mächtigen Intervall eine sehr gute Qualität mit durchschnittlichen TOC-Gehalten von 4,8 Gew.-% und HI-Werten von 469 mg HC/g TOC. Rock-Eval-Ergebnisse, Biomarker-Verhältnisse und mikroskopische Untersuchungen indizieren Typ II Kerogen in allen Offshore-Proben. Eine positive Korrelation zwischen dem TOC und dem Gesamtschwefel (TS) -Gehalt sowie Pristan (Pr) zu Phytan (Ph) Verhältnisse < 2 deuten auf eine Ablagerung unter upwelling-bedingter erhöhter Primärproduktivität im Bereich einer ausgedehnten Sauerstoffminimumzone hin. Die laterale Ausdehnung dieser Muttergesteine ist daher auf die nähere Umgebung des ESM beschränkt. Die Vitrinit Reflexion (VR_r) $\leq 0,3\%$ deutet auf thermische Unreife hin. Die Versenkungstiefe war nicht viel größer als zur heutigen Zeit.

Auf Zypern kommt OM in zwei geologischen Formationen (Fm.) vor. In der triassischen Vlambouros Fm. sind dünne Tonschichten zwischen meterdicken Sandsteinlagen eingelagert. OM ist in den Tonsteinen mit einem TOC-Gehalt von durchschnittlich 1 Gew.-% konzentriert, kommt aber auch fein verteilt in den Sandsteinen vor. HI-Werte betragen durchschnittlich 48 mg HC/g TOC. Die mikroskopische Analyse belegt, dass das OM im Wesentlichen von höherer Landpflanzen stammt. Niedrige TS/TOC-Werte und verschiedene Biomarkerverhältnisse weisen auf sauerstoffreiche Süßwasserbedingungen zur Zeit der Ablagerung hin. Die thermische Reife ist niedrig ($VR_r \leq 0,6\%$).

In der miozänen Pakhna Fm. kommt OM im oberen Teil der Fm. in Aufschlüssen östlich des Troodos-Gebirges vor. OM ist in feinkörnigen Mergeln von etwa 20 cm Dicke vorhanden, die mit ähnlich dicken, gröberkörnigen Kalksteinen wechsellagern. TOC-Gehalte und HI-Werte betragen im

Schnitt 4 Gew -% bzw. 238 mg HC/g TOC und das OM ist unreif ($VRr \leq 0,5\%$). Rock-Eval-, Biomarker-Ergebnisse und mikroskopische Untersuchungen zeigen, dass das OM hauptsächlich marines Kerogen vom Typ II mit geringen Anteilen von Typ III umfasst. TS/TOC-Verhältnisse $\geq 2,8$ und Biomarker-Verhältnisse zeigen dys- bis anoxische, marine Bedingungen an. Eine positive Korrelation zwischen der Menge an OM und dem Silikatgehalt zeigt, dass solche Bedingungen während Zeiten gesteigerter Primärproduktivität erreicht wurden, die durch den verstärkten Eintrag von klastischem Material und Nährstoffen gesteuert wurde.

Mit der stratigraphischen Vorwärtsmodellierung konnte ein Best-Fit-Modell für die Muttergesteine der Spätkreide, des Eozäns und des Oligo-Miozäns im östlichen Mittelmeerraum erstellt werden. Das Modell wurde kalibriert, indem simulierte und tatsächliche Mächtigkeit, simulierte Faziesverteilung (Gross depositional environments, GDE) und veröffentlichte GDE-Karten sowie simulierte geochemische Parameter mit Daten aus dem ESM und dem Levant Festland verglichen wurden. Das Modell unterstützt die Idee eines Upwellingsystems in der späten Kreide und im Eozän als Hauptkontrollfaktor für die Ablagerung von OM entlang des ESM und des Levant Kontinentlhanges. OM ist auf die ausgedehnte Sauerstoffminimumzone beschränkt, was zu einem schmalen, kontinuierlichen Band parallel zum Levant-Schelf und einer lückenhaften Verteilung auf dem ESM führt. Für das Oligozän und das Miozän führt ein geringer Anteil an terrestrischem OM über Sedimenteintragsquellen aus dem Nilgebiet und dem Levant Festland zu einer relativ homogenen, lateralen und vertikalen OM Verteilung bei niedrigem TOC-Gehalt ($\ll 1\%$) im gesamten Becken. Dies stimmt mit geochemischen Informationen zum Oligozän im Nildelta überein.

Die Beckenmodellierung zeigt, dass die OM-reichsten Gesteine aus der späten Kreide und dem Eozän unreif sind. Nur an zwei Stellen fallen Muttergesteine mit niedrigem TOC ($<1\%$) in die Zone der Kohlenwasserstoffbildung. Vor der Küste des Nordlibanons traten die spät kreidezeitlichen Muttergesteine während des mittleren Eozäns in das Ölfenster ein und reichen heute bis in das Trockengasfenster. Südöstlich des ESM liegen die spät kreidezeitlichen Muttergesteine in Bereich der Nassgasbildung seit der Ablagerung des messinischen Salzes. Gleiches gilt für eozäne Muttergesteine, die an beiden Stellen bis in die Zone der Nassgasbildung reichen. Bei heutiger Versenkungstiefe liegen die oligozänen Muttergesteine im südlichen Becken im Ölfenster und reichen bis in das Nassgasfenster im nördlichen Becken. Die miozänen Muttergesteine hingegen sind überwiegend unreif.

Abbreviations

Bcfg	=	Billion cubic feet of gas
CPI	=	Carbon preference index
DCM	=	Dichlormethane
DZ	=	Zone of upwelling related enhance primary bio productivity
Easy Ro	=	Simulated/calculated equivalent to vitrinite reflectance
ESM	=	Eratosthenes Seamount
ECB	=	Eratosthenes Continental Block
Fm.	=	Formation
GC	=	Gas chromatography
GC-FID	=	Gas chromatography coupled with a flame ionization detector
GC-MS	=	Gas chromatography coupled with mass spectrometry
HC	=	Hydrocarbon
HI	=	Hydrogen index (obtained from Rock-Eval)
Ma	=	Million years
Mbsf	=	Meter below sea floor
m/z	=	Mass / charge ratio in an ion in mass spectrometry
OEP	=	Odd even predominance
OI	=	Oxygen index (obtained from Rock-Eval)
OM	=	Organic matter
Ph	=	Phytane
Pr	=	Pristane
PP	=	Primary (bio) productivity
S1	=	First peak during Rock-Eval pyrolysis (free hydrocarbons)
S2	=	Second peak during Rock-Eval pyrolysis (generated hydrocarbons)
S3	=	Peak representing released CO ₂ during Rock-Eval pyrolysis
Tcfg	=	Trillion cubic feet of gas

T_{\max}	=	Temperature of highest HC during Rock-Eval pyrolysis
T_{peak}	=	Highest experienced temperature during burial
TOM	=	Total organic matter
TOC	=	Total organic carbon
TIC	=	Total inorganic carbon
TS	=	Total sulfur
T_{wh}	=	Terawatt hour
VR_r	=	Random vitrinite reflectance
Z_{up}	=	Bathymetry of highest upwelling PP

1 Introduction

We are living in a world with a rapidly growing population and an even faster progressing technology. Since 1950, the earth's population has increased by almost a factor of three from 2.53 to 7.33 billion, in 2016, with Asia and Africa counting for the highest contribution to that growth (Fig. 1.1; Klein Goldwei, 2016). Together with completely new ways of mobility and continuously developing industries, this has led to a significant increase in the demand of energy. From 1950 on, the world energy consumption increased from 30,000 to more than 140,000 TWh per year in 2010 (Fig. 1.2), which represents a growth by a factor of almost five (Smil, 2017). Future estimations predict a further increase in the energy demand at least for the next 20 years (Wolfram et al., 2012).

Even if renewable energies are becoming increasingly important, their capacities will not be able to cover the rising energy demand (BMW, 2017). Hence, fossil energies will remain an important contributor to the total energy mix in the future. While the usage of coal will most likely decrease, especially natural gas will gain importance as a main source to satisfy the need for energy (Fig. 1.3; BMW, 2017; theenergycollective.com, 2018). In this context, the exploration of new hydrocarbon areas is of great importance in order to find new conventional as well as unconventional reservoirs of oil and gas.

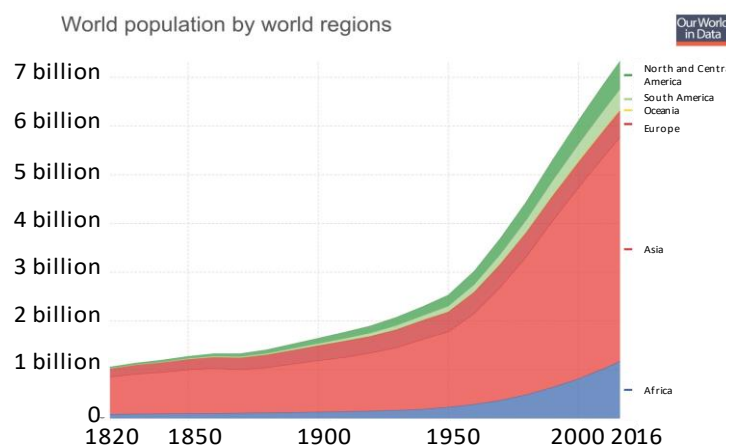


Fig. 1.1 Evolution of the world population between 1820 and 2016 with respect to the single evolution on each continent (figure from OurWorldinData.org; data from Klein Goldewi, 2016)

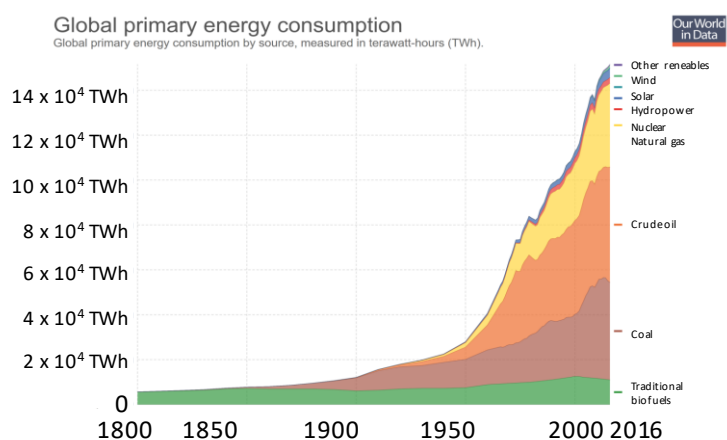


Fig. 1.2 Evolution of the global primary energy consumption between 1800 and 2016, separated by different energy sources. (figure from ourworldindata.org; data from Vaclav Smil, 2017).

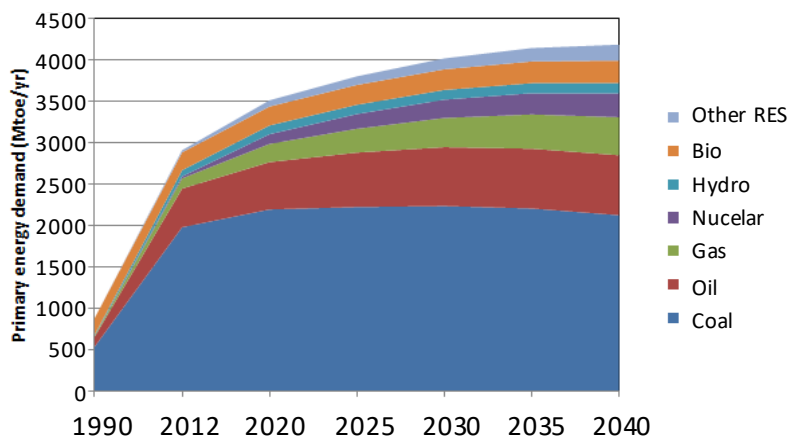


Fig. 1.3 Prediction of the primary energy demand till 2040. While the usage of coal will decrease Renewables but also gas as source of energy will increase. (*theenergycollective.com, 2018*)

The eastern Mediterranean Sea became recently one of the top candidates for such new frontier hydrocarbon exploration areas. This was previously suggested in a report by the US geological survey (Schenk et al., 2010), which claimed an estimated mean amount of 1689 million barrels of oil (MMBO) and a mean volume of 122,378 billion cubic feet of gas (Bcfg), waiting to be discovered in the area.

1.1 The Eastern Mediterranean Sea – a new frontier area for hydrocarbon exploration

Several large biogenic gas discoveries (Fig. 1.4) have set the eastern Mediterranean Sea to one of the world's most important frontier areas for hydrocarbon exploration. Apart from the Nile Delta, the eastern Mediterranean hosts the Levant and the Herodotus Basin, where the recently reported discoveries are located. The first two discoveries were made in 2009 with the Tamar and Leviathan Field (10 and 18 Tcf) offshore Israel. Two years later, the Aphrodite Field (7 Tcf) was found in the southern offshore exclusive economic zone (OEEZ) of Cyprus (Ratner, 2016). These fields are located within structural traps in Oligo-Miocene turbidite sequences, which are present throughout the whole Levant Basin (Gardosh et al., 2009).

However, the most important discovery, which draw the attention to the eastern Mediterranean Sea, was made in 2015 in the northern OEEZ of Egypt with the discovery of the giant gas field Zohr, which comprises a volume of 30 Tcf (Ratner, 2016). In contrast to the earlier discoveries, Zohr is located in late Mesozoic to Cenozoic shallow water carbonates at the southern flank of the Eratosthenes Seamount, south of Cyprus (Fig. 1.4). Its discovery brought up several new play targets for the area, which turned out to be very promising after more discoveries were made during the last two years. In 2018, gas was encountered in Cyprus offshore block 6 (ENI, 2018) and just recently, another gas field of approximately 5 Tcf was enounced to be located in Cyprus offshore block 10 (ExxonMobil, 2019).

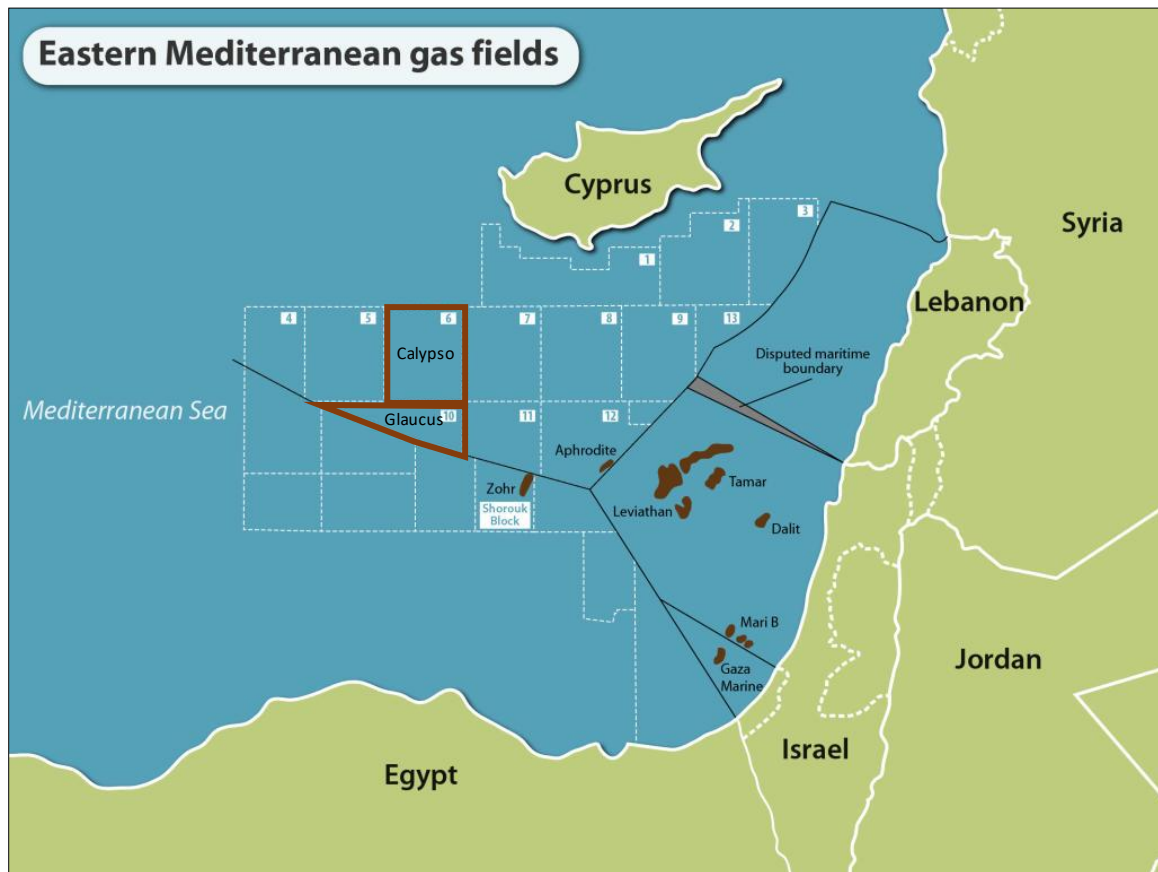


Fig. 1.4 Location of gas fields in the Eastern Mediterranean Sea (modified after: Crystolenergy.com).

All of these fields, either located in the Miocene turbidites or in the Mesozoic to Cenozoic shallow water carbonates, have in common that they are mainly charged by natural gas of biogenic origin. Nevertheless, thermogenic petroleum systems are suspected to occur in the area as well.

1.2 Previous work

In order to understand petroleum systems and allow predictions about potential hydrocarbon production, several parameters play an important role. The big challenge in frontier exploration areas, such as the eastern Mediterranean Sea, is that only very little well data is available for the offshore area. While there is a dense net of seismic lines available nowadays for the eastern Mediterranean Sea, a lack of available well data (the few existing wells are all confidential) makes it hard to precisely identify facies distribution or check depth conversion of seismic horizons.

Despite this limited availability of offshore well data, there have been many studies in the recent past, which brought new insights into the area. Different integrated approaches of numerous geological disciplines combining onshore field observations with seismic interpretation and different numerical modeling technics aimed to better characterize the on- and offshore areas of the Eastern Mediterranean

in order to improve the general understanding of the area, and hence, trying to reduce risks for hydrocarbon exploration.

Based on the interpretation of numerous seismic lines for the northern Levant Basin and extensive field work onshore Lebanon, Hawie et al. (2013b, 2017) could identify 8 major seismic packages and create 3D depth maps providing a good idea of the general architecture of the Levant Basin and its margin since the Mid Jurassic. Further, the identification of 15 seismic facies provides estimations of the sedimentary infill of the Levant Basin. It is shown that until the Oligocene the Levant Margin comprises mainly shallow marine carbonate platforms, while the basin consists of deep marine pelagic carbonates. From the Oligocene on, facies changed towards clastic dominated environments with huge amounts of clay, silt and sand in the basin. Numerical modeling of sediment transport could show that the Nile Cone Delta was, next to the Levant Margin, the main source for clastic material that filled the basin (Hawie et al. 2017).

In addition to this general litho-stratigraphic 3D model of the Levant Margin and Basin, Ghalayini et al. (2014) performed a detailed study on fold and fault systems, which can be observed onshore Lebanon as well as on the seismic sections of the offshore area. Four major groups of structural features within the Cenozoic were identified, which are inherited from older faults related to the Mesozoic rifting and were partly reactivated during the late Miocene compression and the sinistral movement along the Levant Fracture System.

By the interpretation of additional seismic lines covering the more western part of the area, Papadimitriou (2017) extended the previous 3D model of the eastern Levant area towards the western region including the Eratosthenes Seamount (ESM). Together with the combination of field observations onshore Cyprus (Papadimitriou et al., 2018; Symeou et al. 2018), structural features of the ESM, as well as other tectonic structures offshore southern Cyprus, such as the Cyprus arc or the Latakia ridge, could be correlated to the general tectonic history of the area, and mainly the compressional setting along the Cyprus arc during the Oligocene-Miocene period.

Inati et al. (2016, 2018) carried out another project aiming to enhance the knowledge about the heat flow in the area. By a combination of seismic interpretation and numerical modeling, new insights about the crustal style of the Levant region could be provided, which in turn can help to calculate the evolution of heat input and transfer originating from the upper mantle and affecting the overlying sediments. One major new insight from these studies is that the Levant Basin is floored with stretched continental crust and not, as previously assumed, by oceanic crust.

Bou Daher et al. (2014, 2015) focused on the identification of potential petroleum source rocks along the Levant Margin, in northern and southern Lebanon. They characterized marine, high quality source rocks within the Upper Cretaceous, which they could correlate to a Late Cretaceous upwelling system affecting the whole Levant Margin. Further, Bou Daher et al. (2016) created a first 3D petroleum system model for the eastern Levant Basin and Margin, simulated the thermal history of the area and

proposed assumptions about potential thermogenic petroleum systems in the area. Barabsch et al. (2018) enhanced this model by facies input maps generated by stratigraphic forward modeling and investigated potential petroleum migration pathways. However, both models are based on hypothetical assumptions on source rock distribution within the deeper parts of the basin.

1.3 Aim of this thesis

The above-mentioned studies clearly increase the geological knowledge about the Eastern Mediterranean and, thus, help a lot to better characterize and evaluate petroleum systems in the area. Nevertheless, the region remains still highly underexplored. In terms of potential source rocks for example, almost nothing is known about the northwestern margin of the Levant Basin. Also, the basin-ward extent of the previously mentioned Upper Cretaceous source rocks along the Levant Margin, as well as of other known source rocks at the southeastern margin of the Levant Basin remains highly speculative. In this respect, the work of this thesis focuses on three main aspects:

Two field campaigns onshore Cyprus, as well as core sampling of the ODP Leg 160 wells offshore southern Cyprus have been carried out with the aim to search for any organic matter (OM)-rich rocks, which might act as potential source rocks in the area. The obtained samples are characterized by means of organic geochemical and petrographic analysis, in order to obtain information on quality, quantity and thermal maturity of OM, as well as information which can help to reconstruct depositional conditions. This information can be used to propose different depositional models, which can help to predict the lateral, and especially basin-ward extent of these source rocks.

As a second objective, numerical simulation of sedimentary processes and the production, deposition and preservation of OM via stratigraphic forward modeling has been performed in order to create a 3D model of these and other petroleum source rocks in the area. Such models can provide a process-based, quantitative estimation of the lateral distribution of OM quantity and quality throughout the basin.

These source rock models are incorporated into a classic 3D petroleum system model, in order to investigate whether they were affected by thermal maturation through their burial history.

Overall, this thesis and its integrated workflow presents a way to characterize petroleum source rocks in underexplored sedimentary basins, even without the availability of deep offshore well data.

2 Geological setting of the Eastern Mediterranean

The area of interest belongs to the Eastern Mediterranean Sea and is located close to the triple junction point of the Eurasian, the African and the Arabian plates (Fig. 2.1). In the following chapter, the geological setting of the area is described in detail. However, a short summary of the geological setting is given as well in the beginning of the following main chapters.

2.1 Tectonic history of the Eastern Mediterranean

The Eastern Mediterranean Sea is characterized by a complex history of large scale tectonic events and has been intensively discussed by many authors (e.g. Gardosh et al., 2010; Le Pichon and Krämer, 2010; Robertson et al., 2012; Montadert et al., 2014). Its evolution started in Late Paleozoic time with the disintegration of Gondwana in the course of the Pangaea breakup (Robertson et al., 2012). The disintegration of Gondwana began with the separation and northward drift of the Cimmerian Terrains,

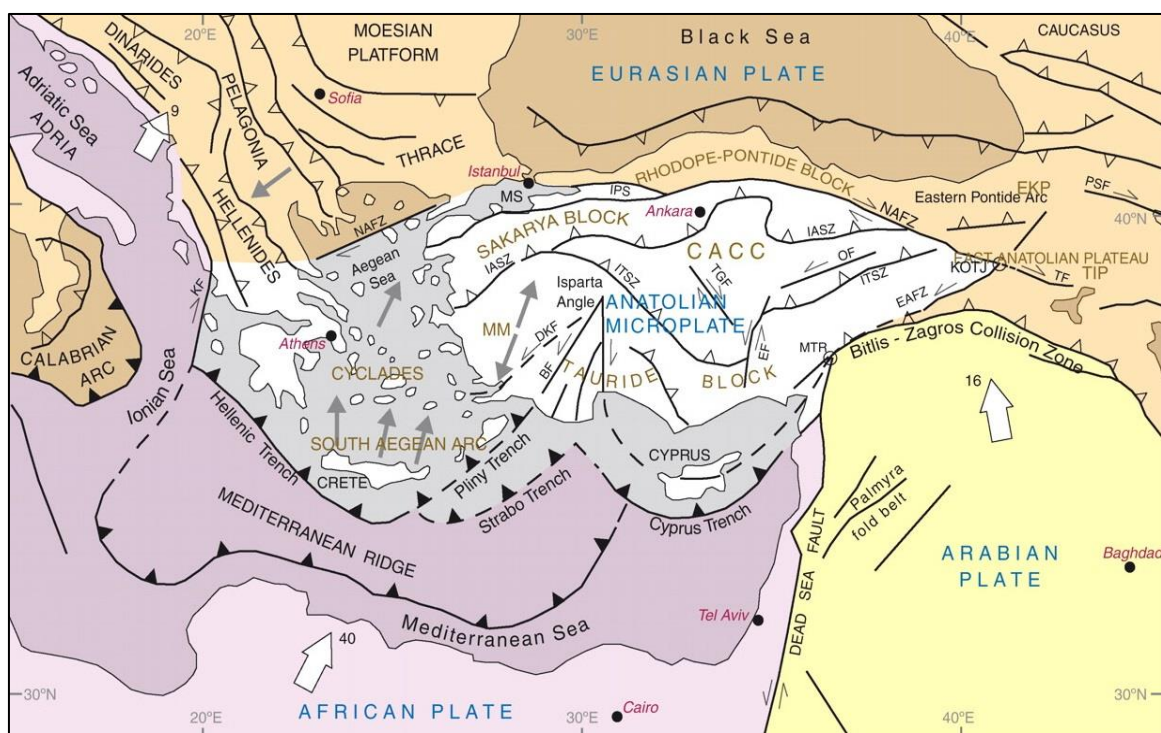


Fig. 2.1 Plate tectonic setting of the Eastern Mediterranean region (from Dilek & Sandvol, 2009)

which induced the opening of the Neotethys Ocean in the North of the Afro-Arabian plate (Fig. 2.2 A). Adjacent, the continental Palmyra trough evolved in the area of the present days Syria. It probably extended into the Levant rift and initiated the separation of the Taurid plate from the Afro-Arabian plate (Segev and Rybakov, 2010). The initial rifting phase is believed to have occurred in the Triassic and a main rift-drift event took place during the Early Jurassic (Segev and Rybakov, 2010; Hawie et al., 2013a; Hawie et al., 2013b; Ghalayini et al., 2014). This extension formed a southern arm of the Neotethys, the Mesotethys, which would later become the Mediterranean Sea. During the ongoing extension, in Late Jurassic to Early Cretaceous time, some authors (Robertson, 1998a; Gardosh and Druckman, 2006; Netzeband et al., 2006; Segev and Rybakov, 2010, Ghalayini, 2014; Montadert et al., 2014) consider that a continental fragment, the Eratosthenes Continental Block (ECB), was ripped off from the Afro-Arabian margin. It is believed that rifting propagated westwards along NNE-SSW oriented transform faults during the Triassic to Early Jurassic. Between the ECB and the continental margin, a southern arm of the Neotethys evolved which later formed the Levant basin (Gardosh and Druckman, 2006). However, this theory is contentious since clear evidences for an oceanic crust below the Levant basin are missing. Rifting with only thinning of continental crust without reaching break up is the recent interpretation (Inati et al., 2016, 2018).

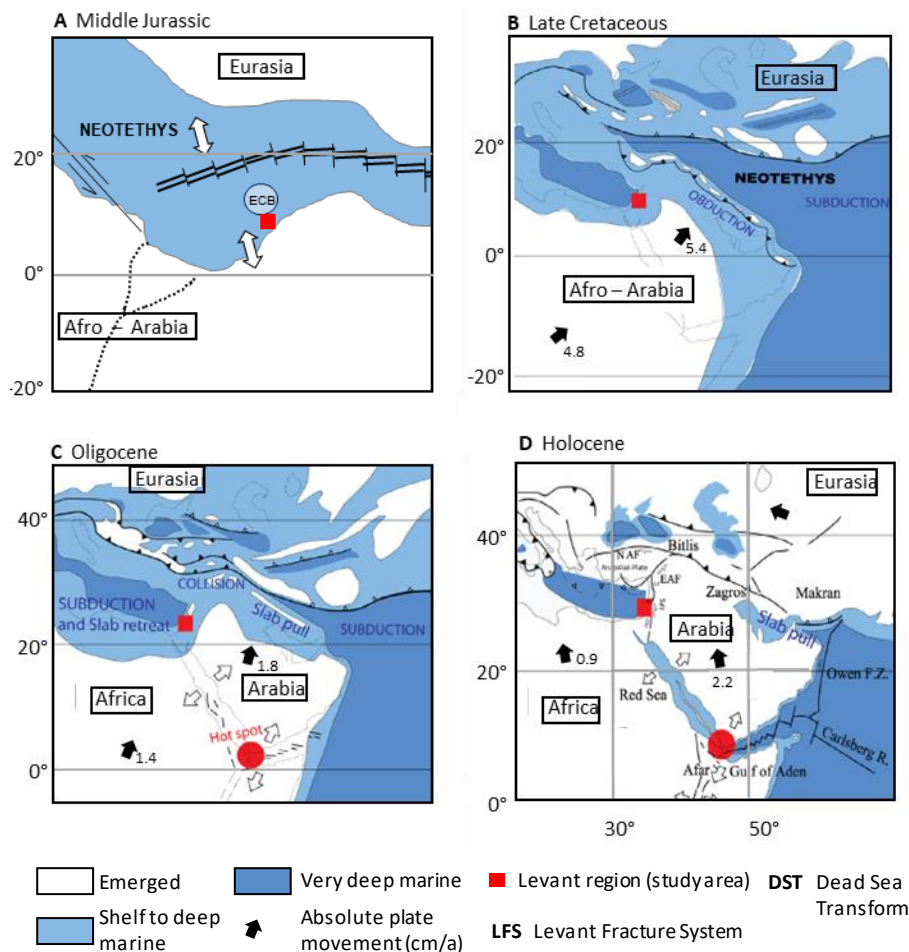


Fig. 2.2 Geological and tectonic evolution of the greater realm of the Eastern Mediterranean since the Middle Jurassic. (modified after Hawie et al., 2017 and Symeou et al., 2018).

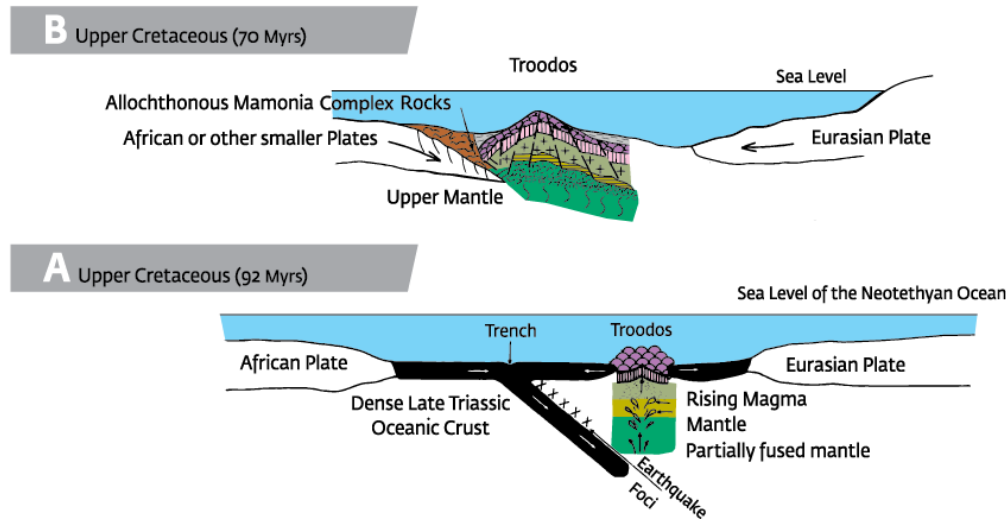


Fig. 2.3 Schematic sketch of the formation (A) and obduction (B) of the Troodos Ophiolite during the Late Cretaceous. (Geological Survey Departement Cyprus.)

Extension prevailed until the Late Cretaceous, when the tectonic regime changed and convergence of the Eurasian and Afro-Arabian plates set in (Fig. 2.2 B), which resulted in a northward oriented subduction and the creation of the Cyprus Arc (Hawie et al., 2013a; Montadert et al., 2014). Ongoing subduction led to the formation of multiple complex fault systems throughout the whole eastern Mediterranean Sea (Morris et al., 1998; Gardosh et al., 2010; Robertson et al., 2012). At several locations along the subduction zones parts of oceanic crust were obducted onto the Eurasian continental margin (Fig. 2.3), forming large ophiolite complexes of which one is the Troodos Ophiolite (Pearce and Robinson, 2010), today representing the core of the Island of Cyprus. In the Oligocene, the breakup of Afro-Arabia (Fig. 2.2 C), with an accelerated northward drift of the Arabian plate initiated the isolation of the Mediterranean Sea. Further, the breakup caused a strong uplift of the Levant Margin and a high input of clastic material into the Levant Basin (Gardosh et al., 2008; Nader, 2014).

Since the Miocene, the tectonic constellation is comparable to the present day state (Fig. 2.2 D). As another consequence of the ongoing subduction, the ECB is in a state of collision with the Troodos Ophiolite since the Pliocene causing a rapid uplift of the area and the rise of Cyprus above sea level (Robertson, 1998a; Galindo-Zaldivar et al., 2001).

2.2 Crustal characteristics of the Eastern Mediterranean

The greater area of Cyprus can be mainly subdivided into four important features (Fig. 2.4): (1) The island of Cyprus itself, comprising the Troodos Ophiolite. It is covered by Upper Cretaceous to Cenozoic sediments, representing the evolution from a deep to shallow marine environment. To the southwest and southeast Cyprus is bounded by the (2) Herodotus and (3) the Levant basins, respectively, which both formed during the Late Paleozoic – Mesozoic rifting along the northern margin of Gondwana

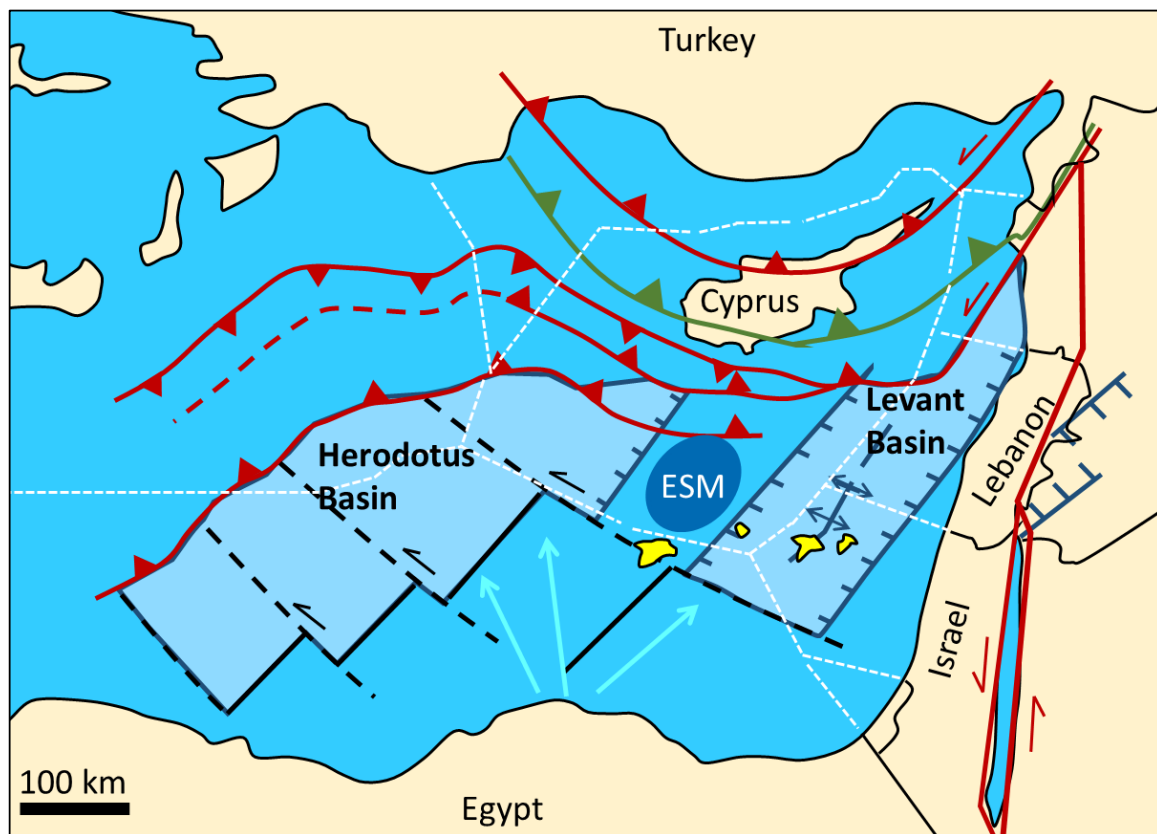


Fig. 2.4 Main geological features of the Eastern Mediterranean Sea (modified after Montadert et al., 2014).

(Gardosh et al., 2010, Robertson et al., 2012, Nader, 2014, Symeou et al., 2018). These two basins are separated by the ECB. Located on top of the ECB, the (4) Eratosthenes Seamount (ESM) represents a large carbonate platform, which evolved on this permanent bathymetric high throughout the basins history (Robertson, 1998b).

2.3 Geology of the greater Cyprus area

The island of Cyprus is divided into four geological terranes (Fig. 2.5): (1) The Kyrenia terrane, a fold and thrust belt in the north, (2) the Troodos Ophiolite in the center of the island, (3) the Circum Troodos Sedimentary Succession, and (4) the Mamonia Complex in the southwest. With respect to the aim of this thesis, the Circum Troodos Sedimentary Succession as well as the Mamonia Complex are of interest and, therefore, described in the following chapter: A simplified geological map and a stratigraphic column of the Circum Troodos Sedimentary succession are shown in Figures 2.5 and 2.6.

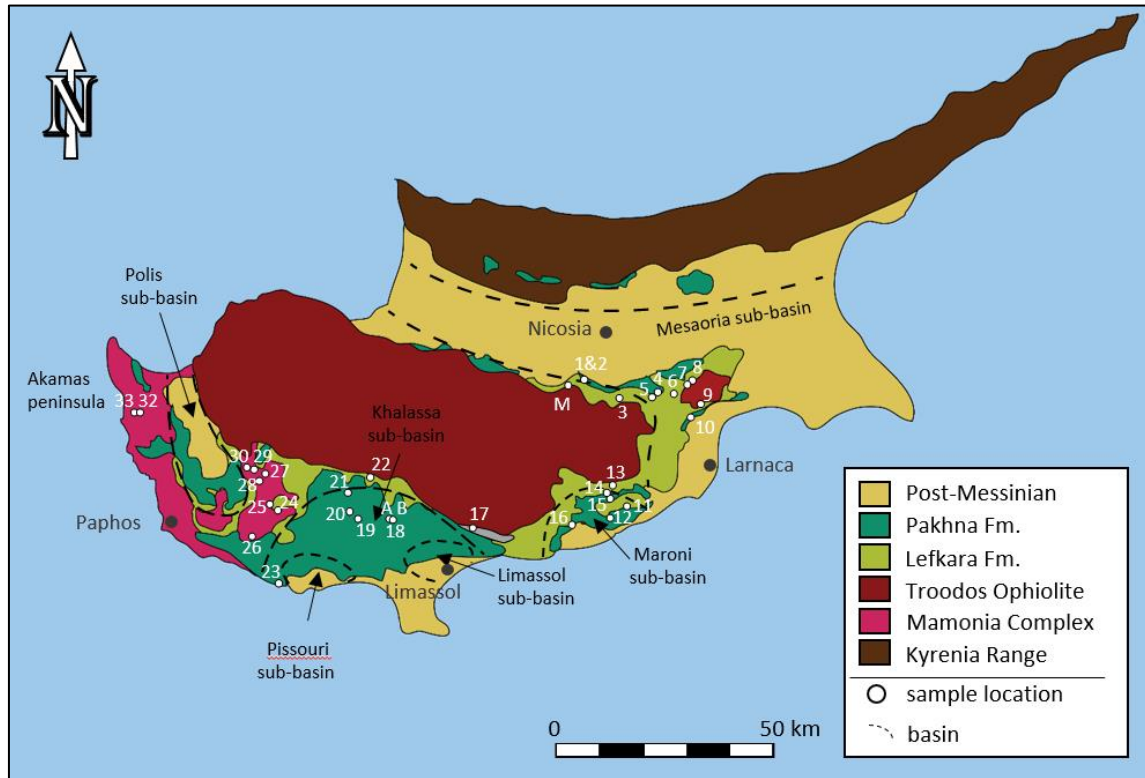


Fig. 2.5 Simplified geological map of Cyprus showing the main important features. White dots represent sample locations.

2.3.1 Circum Troodos Sedimentary Succession

The Circum Troodos Sedimentary Succession spans sediments of Late Cretaceous to Recent age representing the evolution from a deep marine over shallow marine towards a terrestrial environment. During the early Late Cretaceous, around 92 Ma ago, new oceanic crust was created along the spreading axis above a supra-subduction zone, forming the Troodos Ophiolite rocks (Pearce and Robinson, 2010). On top of its upper pillow lavas, Campanian umbers of the Perapedhi Formation and Campanian to Mid-Maastrichtian volcanoclastic sand- to siltstones towards bentonite clays of the Kannaviou Formation were deposited (Morris, 1998; Lord et al., 2000). In some areas reworked material of the Kannaviou Formation is mixed with different exotic blocks of older rocks. These parts are referred to as Moni Formation or Moni M \acute{e} lange. Their deposition is proposed to be Campanian or early Maastrichtian in age and is related to the emplacement of the allochthonous Mamonia Complex in the southwest of the island (Lord et al., 2000).

Still in a deep marine setting, the Lefkara Formation was deposited during a range of 50 Ma from Maastrichtian to Early Miocene and is mainly composed of pelagic marls and white chalks (Lord et al., 2000). Main rock forming components are dominantly biogenic in origin and composed of planktonic foraminifera and calcareous nannofossils with minor radiolarians (Lord et al., 2000). Radiolarians, which are usually siliceous, might have lost their shape due to recrystallation and secondary chert

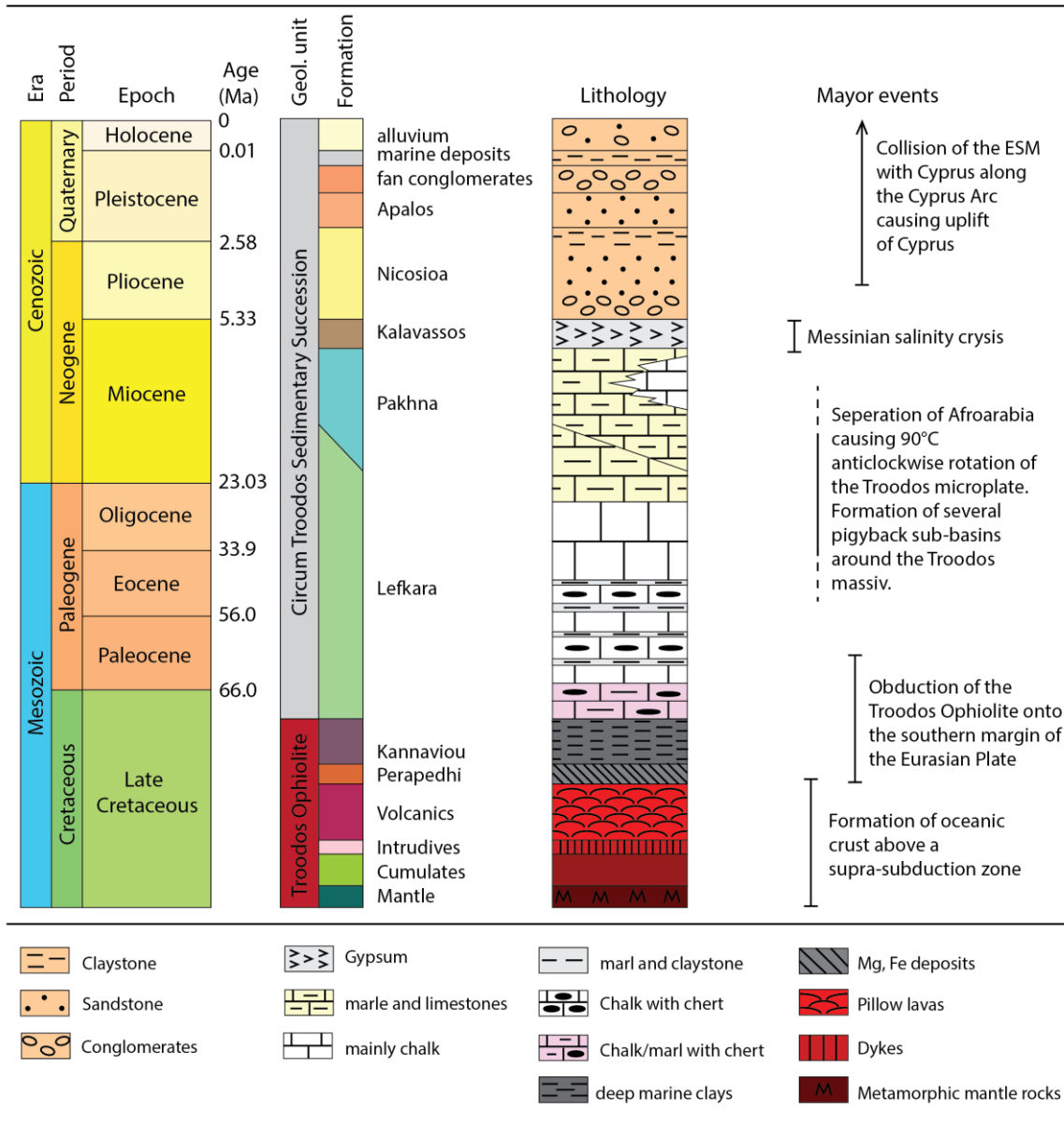


Fig. 2.6 Stratigraphy of Cyprus including the Troodos Ophiolite and its autochthonous Circum Sedimentary Succession. The formation colors refer to the colors of the official geological map of Cyprus.

formation in a proposed water depth of 2000-3000 m, possibly between the carbonate- (CCD) and aragonite compensation depths (ACD)(Kähler, 1994). According to Kähler (1994), the Lefkara Formation can be subdivided into four different lithological units:

(1) The lower marl unit, which is mainly composed of pinkish marls, white chalky marls, rare limestones and interbedded, medium to thick chert layers. The frequency of chert layers increases from bottom to top. Throughout the whole unit burrows and bioturbation can be found as well as turbiditic structures (Kähler and Stow, 1998).

(2) The chalk and chert unit is characterized by regularly bedded, 9-16 cm thick chalks, marly chalks, and thin marls interbedded with silicified micrites and cherts. Turbiditic structures are quite rare whereas bioturbation is more common (Kähler and Stow, 1998).

(3) The pure chalk unit consists of 20-50 cm thick layers that are almost free of cherts. Generally, the bed thickness decreases to the top. Only in the western parts of Cyprus turbiditic structures are recognizable (Kähler and Stow, 1998).

(4) The upper marl unit is completely free of cherts and consists of thin-bedded marls and chalky marls. Overall this unit becomes more calcarenitic towards the top (Kähler and Stow, 1998).

The Lefkara Formation is overlain by the Pakhna Formation, which spans around 16 Ma of hemipelagic deposition and represents gradually shallowing conditions. In the south, the Pakhna Formation lies above exotic Mesozoic lithologies similar to those of the Mamonia Complex. Therefore, the Mamonia Complex might form the basement of the Pakhna Formation in the southern Cyprus coastal and offshore areas (Eaton and Robertson, 1993). The formation is subdivided into two members by Robertson et al. (1993): The (1) lower Terra Member of shallow-water bioclastic carbonates and large benthic foraminifera, indicating a late Oligocene-Early Miocene age and the (2) upper Koronia Member, which is composed of coral reef carbonates dominated by porites, which is dated to be Tortonian in age by Follows et al. (1996). The Pakhna Formation lacks clearly defined lower and upper boundaries. The sediments contain, locally, high amounts of organic material. The terrigenous input clearly increases from bottom to top with the abundance of organic-rich layers containing miospores, leaves and macro-plant debris from the Troodos Island (Lord et al., 2000). Overall, five different facies, from proximal to distal, can be distinguished within the Pakhna Formation (Eaton and Robertson, 1993): (1) the Peripheral Sands Association, (2) the Gullied-slope Association, (3) the Channel-fill Association, (4) the Basin-margin Association, and (5) the Basin-plain Association.

The Peripheral Sands Association consists of amalgamated, massive calcarenites up to 12 m thick, with a bedding, if visible, between 50 and 100 cm thickness. Deposits are characterized by homogeneous, coarse grained bioclastic grainstones. Source of the clastic sediments are (a) marginal shallow water areas, (b) the Troodos Ophiolite in the north, and (c) the allochthonous Mamonia Complex in the south (Eaton and Robertson, 1993).

Within the Gullied-slope Association dominantly hemipelagic successions pass laterally into coarser grained channelized units (Eaton and Robertson, 1993):

Fine Grained Successions: They are mainly composed of bioturbated foraminifera-rich chalks, silty marlstones and laminated calcilutites, becoming more abundant towards the top of the Pakhna Formation. The successions are up to 100 m thick and normally pass downwards into chalks of the Lefkara Formation and upwards into laminated, basinal gypsum of the Kalavassos Formation.

Channel-fill Successions: Channel fills are of two different ages. The larger ones (e.g. at Khirokitia and Amathus) comprise terrigenous muds with calcareous nannoplankton of Late Pliocene age (Houghton et al., 1987).

The Basin Margin Association is characterized by massive, graded and medium- to thin bedded calcarenites, interbedded with chalks and marls. In between clastic packets, the sequence also includes bioturbated marls and chalks, with sporadic, thin to medium-bedded, fine-grained, graded calcarenites.

The lower part of the succession is marked by well-sorted grainstone/packstones with minor silt-sized quartz. From bottom to top, an increasing amount of large shallow-water foraminifera can be recognized, whereas the amount of planktonic varieties decreases. Further, shallow-water bioclastic material can be found and includes bivalve fragments, coralline algae, coral fragments, sponge spicules, echinoids, serpulid worm tubes and large foraminifera (Eaton and Robertson, 1993).

The Basin-plain Association is mainly composed of planktonic foraminifera, nanofossil chalk and marl. Deep-water conditions are indicated by extensive bioturbation, mainly by *Zoophycos*, *Chondrites* and *Planolites*.

At the end of the Miocene, during the Messinian Salinity Crisis (MSC), the regional sea level fall led to the deposition of the Kalavassos Formation. These massive evaporitic gypsum layers can be found throughout the entire island, but are most prominent in the center of the sub-basins around the Troodos mountain.

The post-Messinian reflooding of the area is marked by the Lower Pliocene Nicosia Formation, which comprises mainly fine-grained marine deposits. In the following, the collision with the ESM led to the uplift of the island of Cyprus and the deposition of first shallow marine deposits, followed by widespread erosion and deposition of conglomeratic, fluvial deposits.

2.3.2 Mamonia Complex

The Mamonia Complex represents a complex assemblage of different allochthonous rocks, which were emplaced onto the nowadays southwestern margin of the Troodos Ophiolite (Robertson and Woodcock, 1979). The Mamonia Complex comprises three different groups: (1) The Dhiarizos Group, which comprises magmatic, igneous and extrusive rocks of former oceanic crust; (2) the Ayios Photios Group, which is supposed to represent passive continental margin sediments; and (3) the Ayia Varvara Group, which is mainly composed of metamorphic rocks, which were formed in turn of the emplacement of the complex in the Late Cretaceous. The exact origin of these rocks was and still is highly debated (e.g. Robertson and Woodcock, 1979; Swarbrick, 1993; Bailey et al., 2000; Lapierre et al., 2007). Robertson and Woodcock (1979) suggest that the Mamonia Complex originates from the northwest and was emplaced onto the Troodos microplate before its 90° anti-clockwise rotation, while a more recent

study suggest the former northern passive continental margin of Gondwana as origin (Lapierre et al., 2007).

In terms of potential source rock bearing formations, the Ayios Photios Group is of interest. The Mid to Late Triassic Vlambouros Formation (Robertson and Woodcock, 1979) was deposited on top of the oceanic basement. Lithologies included in this formation are predominantly terrigenous sand and siltstones, and partly calcarenites with intercalated micritic limestones (Bragin and Krylov, 1996). The terrigenous coarser grained units are attributed to a shallow water, probably fluvio-deltaic environment (Robertson and Woodcock, 1979). The sections with higher amounts of calcarenites and marl units, instead, are interpreted as submarine grain flow derived shallow water carbonates (Robertson and Woodcock, 1979).

The highest level of the Ayios Photios Group consists of the Episkopi Formation. It spans an age from Early Jurassic to Mid-Cretaceous and comprises a diverse assemblage of pelagic and hemipelagic siltstones, calcilutites, radiolarian mudstones, as well as sandstones, limestone conglomerates and calcarenites (Robertson and Woodcock, 1979).

2.3.3 *Eratosthenes Seamount*

The sedimentary cover of the ESM is approximately 6 km thick (Montadert et al., 2014), but only the upper 600 mbsf were core drilled during the ODP drilling campaign Leg 160 (Emeis et al., 1996). Undrilled sediments are inferred from seismic reflection and are interpreted to comprise syn-rift sediments (volcaniclastics, carbonates or clastic sediments) which are overlain by a thick post-rift succession of extensive shallow marine carbonate build-ups, intercalated with a sequence of undisturbed, probably fine-grained, marine sediments (Montadert et al., 2014; Papadimitriou, 2017). A schematic overview of the expected lithostratigraphy of the ESM, the Herodotus and the Levant basin, as well as the well-constrained columns of the northern and southern shelf of the Levant Basin are shown in Figure 2.7. Analysis of the drilled intervals from the ODP Leg 160 campaign constrains the interpretation of the depositional environments from the Late Cretaceous onwards (Emeis et al., 1996; Silva et al., 1998; Staerker, 1998). Shallow water carbonate deposition was interrupted during the Cenomanian/Turonian and younger Upper Cretaceous sediments were deposited in a hemipelagic to pelagic environment (Robertson, 1998c). Later, Miocene shallow water carbonate build-ups formed on the ESM. During the Messinian Salinity Crisis (MSC) the sediments of the ESM were most likely exposed and affected by extensive meteoric water flushing, karstification, dolomitization, as well as erosion (Robertson, 1998b). Subsequent drowning of the platform during the Pliocene to Quaternary enabled the deposition of pelagic carbonates and sapropels (Robertson, 1998c).

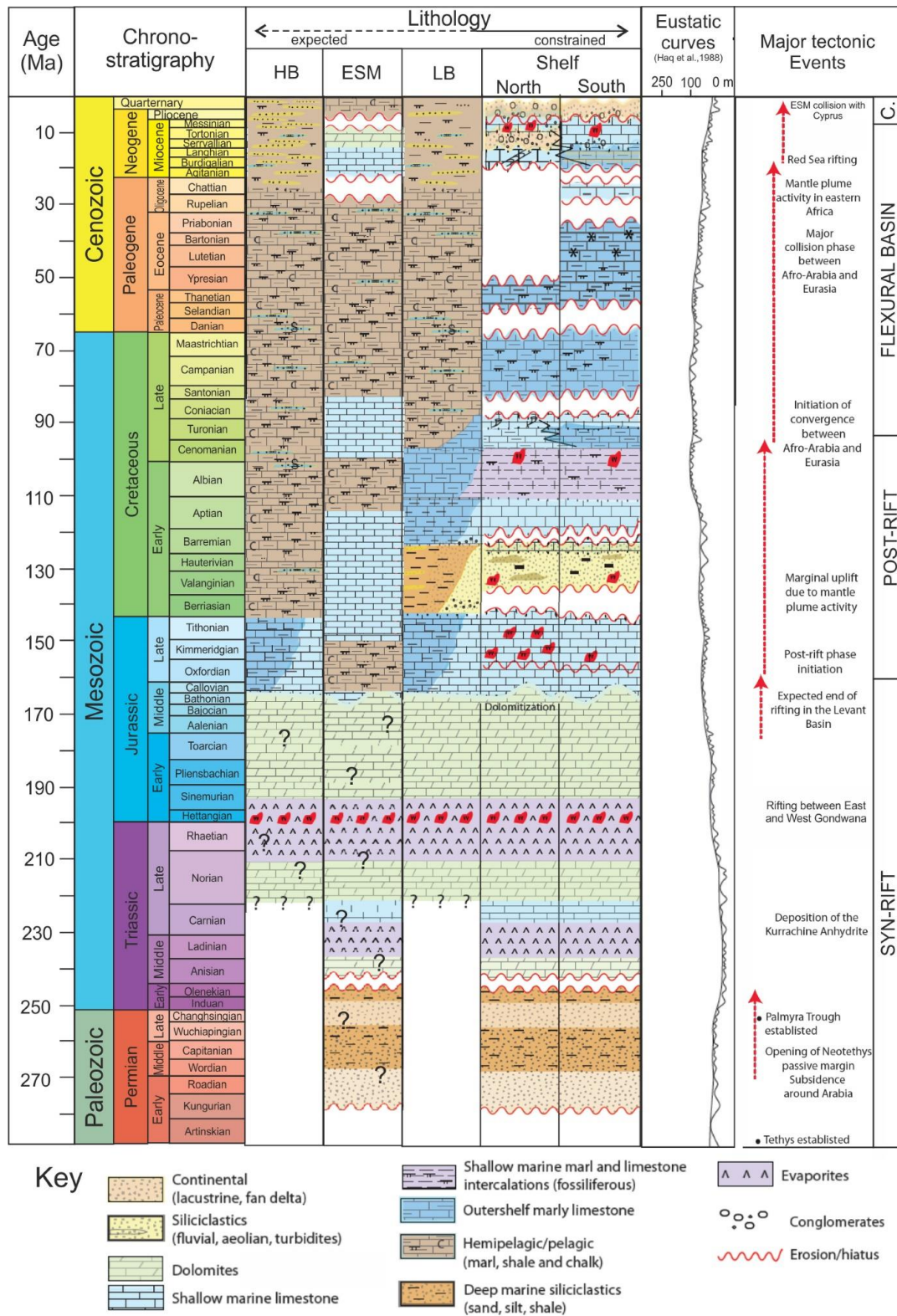


Fig. 2.7 A schematic overview of the expected lithostratigraphy of the Eratosthenes Seamount (ESM), the Herodotus and the Levant basin, as well as the well-constrained columns of the northern and southern shelf of the Levant Basin (modified after Bou Daher 2016).

3 Field campaigns and sample collection

Potential organic-rich intervals were sampled in the greater area of Cyprus in order to study the sedimentary deposition of potential source rocks. In total, 308 samples were collected. Samples from the onshore area of Cyprus were collected during two field campaigns in 2016 and 2017. In addition, offshore samples were retrieved from cores of the ODP Leg 160 wells. The exact outcrop locations are shown in Figure 2.5. Most of the sampled rocks are carbonates and were described following the Dunham (1962) classification (Fig. 3.1).

3.1 First field campaign

3.1.1 Summary

The first field campaign was conducted in November 2016. The aim of the campaign was to gain a first impression on the geology of the island, and to perform a reconnaissance investigation with respect to potential organic-rich intervals throughout formations of late Mesozoic to Cenozoic age. Locations of interest were chosen based on literature review as well as by the help of the Geological

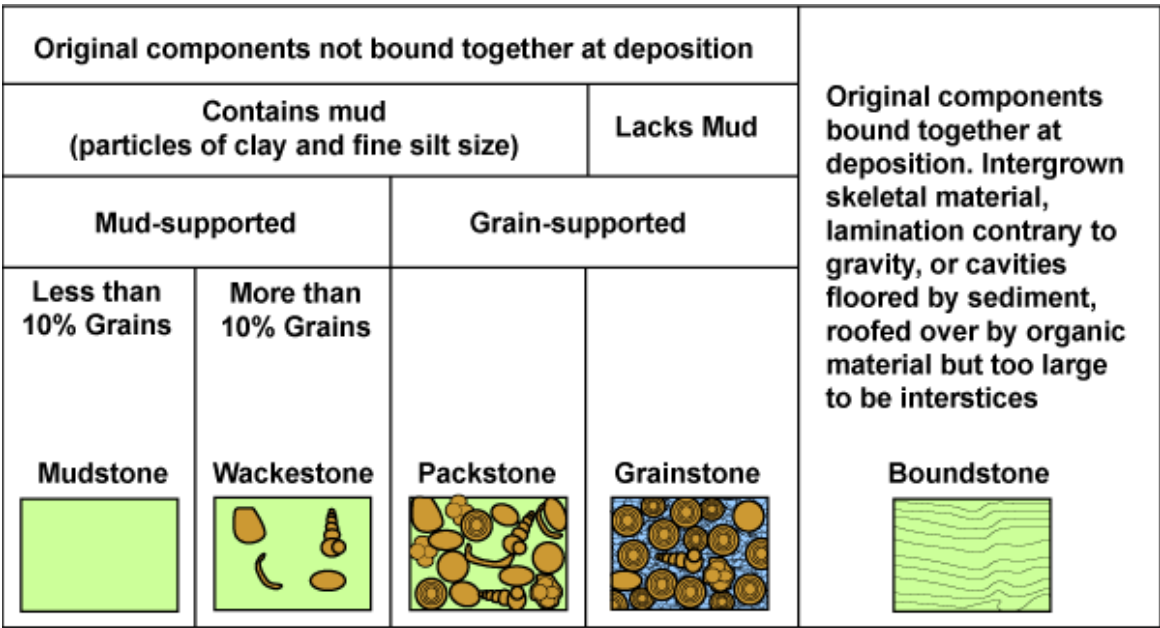


Fig. 3.1 Carbonate classification after Dunham (1962).

Survey Department of Cyprus. Rock samples were mainly chosen based on fine grain size and dark color. To keep weathering effects low, samples were taken from at least 20 cm below the outcrop's exposed surface.

In total 67 samples were collected from 18 locations (Loc.) covering four regional areas (Fig. 2.5): (1) The western margin of the Mesaoria Basin, (2) the western margin of the Maronia Sub-basin, (3) the northern margin of the Kahlassa Basin, and (4) the Mamonnia Complex, mainly around the area of Pera Pedi. The samples comprise the Mid Triassic Vlambouros Fm., the Jurassic Episkopi Fm., the Late Cretaceous to Pleistocene Lefkara Fm., the Miocene Pakhna Fm., and the Pliocene Nicosia Fm.. Appendix Table A lists all samples together with their respective locations, formations and GPS coordinates. The author's sample IDs as well as IFPEN IDs are included. In the following chapters, only the author's sample IDs are used and referred to as "sample".

3.1.2 Outcrop and sample description

3.1.2.1 Circum Troodos Sedimentary Succession

3.1.2.1.1 Lefkara Formation (Late Cretaceous to Paleocene)

The oldest rocks that were sampled within the Circum Troodos Sedimentary Succession belong to the Lower Lefkara Fm., which is of Late Cretaceous to Paleocene age. Samples were taken at five different locations. The outcrop at Loc. 7 (Fig. 3.2 A) shows an interlayering of brown to grey marlstone- and beige grainstone units. Cycles of 2 cm thick, equally alternating layers (Fig. 3.2 B) are separated by four, 15 cm thick grain stone banks in the upper part of the outcrop. The different lithotypes are interpreted to represent changes in the energetic conditions with the marlstones being deposited in the calmer phases. At Loc. 9 (Fig. 3.3) the Lower Lefkara Fm. is juxtaposed to the Troodos Ophiolite along a W-E striking normal fault. A three meter thick unit of dark marlstones with a high amount of foraminifera is followed by whitish chalk at its top. The same darkish mudstone unit crops out at Loc. 22. At Loc. M (Fig. 3.4), white chalk bands are interlayered between grey brown silt- to fine-grained sandstone packages. The lowermost part of the Lefkara Fm., which is in direct contact to the Troodos Ophiolite, can be found at Loc. 3. Pinkish marls with only a low amount of fossils represent a deep marine setting.

3.1.2.1.2 Pakhna Formation (Miocene)

The Pakhna Fm., and mainly its upper section – the Koronia Member, was sampled at four different outcrops. At Loc. 5 (Fig. 3.5), alternating thick chalk banks with thinner interbedded limestones can be observed. A massive, horizontally layered limestone band on top represents a prominent marker horizon, which is located just below the Messinian and can be followed throughout the formation along the entire island. The thinner limestone layers comprise mainly brownish marl- to mudstones of 10 cm thickness.

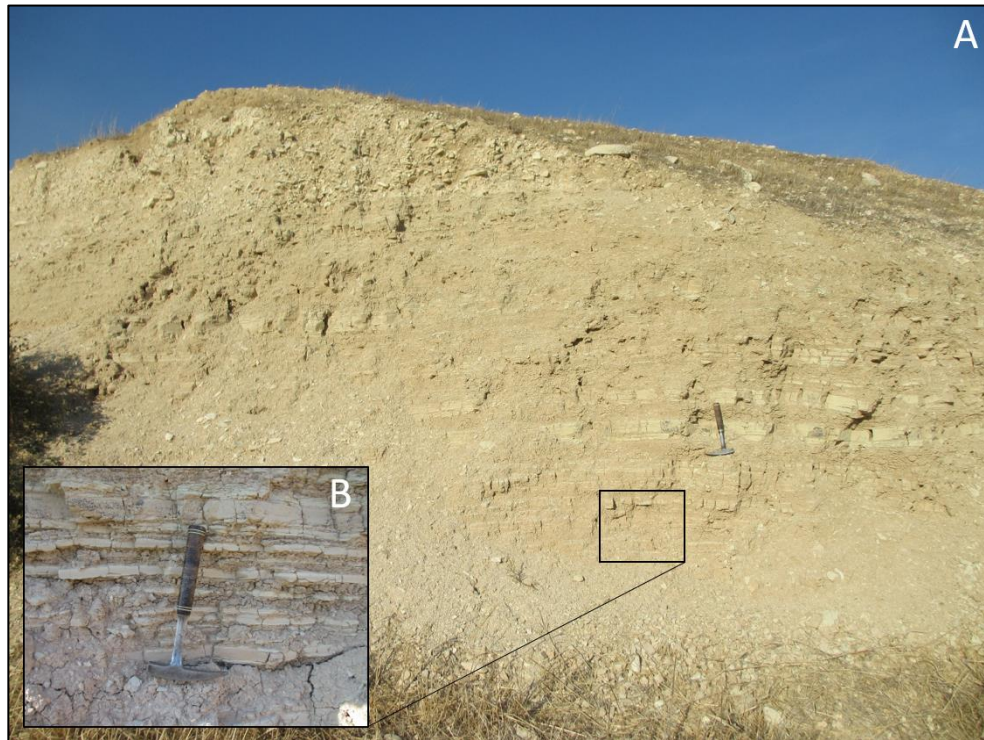


Fig. 3.2 Location 7, Lefkara Formation.



Fig. 3.3 Location 9, Lefkara Formation.

The complete section represents an evolution from deep to shallow marine conditions. A similar setting is observed at Loc. 16. Not directly part of the outcrop, but as part of a large boulder next to it, a massive evaporitic layer can be found (Fig. 3.6 B). Therefore, the outcrop itself is proposed to be located similarly or a few meters deeper in the stratigraphy than at Loc. 5. Thin grey clay layers are interbedded between massive white chalk units (Fig. 3.6 A). Also, recrystallized grainstones, probably representing dolomite can be found. Whereas the clay layers at Loc. 5 are horizontally layered or show no structure,



Fig. 3.4 Location M, Lefkara Formation.

the layers at Loc. 16 show some wavy lamination, indicating marine conditions with higher energetic currents. Loc. 10 (Fig. 3.7) instead, comprises relatively equally thick alternating units of around 25 cm of whitish and dark grey marl- to wackestones. In both lithologies high amounts of ostracods can be observed. Location 21 (Fig. 3.8 A) is supposed to be even deeper located in the stratigraphy. The overall appearance of the rocks is more homogeneous. Only few, very thin brown clay layers are interbedded between large packages of chalk (Fig. 3.8 B). All outcrop locations are located relatively close to the respective basin margins (Fig. 2.3).

3.1.2.1.3 Nicosia Formation (Pliocene)

The Nicosia Fm. was sampled at Loc. 4 (Fig. 3.9). Orange sapropels, probably indicating highly progressed oxidation, are intercalated with whitish grey marlstone layers. The presence of foraminifera and the high abundance of larger shells in the upper layers indicate a marine depositional environment with relatively high energetic conditions. Both, the whitish as well as the darker layers were sampled.

3.1.2.2 Mamonía Complex

3.1.2.2.1 Vlambouros Formation (Mid Triassic)

The Vlambouros Fm. was sampled at two different locations. The outcrop at Loc. 26 comprises fine to medium grained, grey sandstones (Fig. 3.10 A). In the coarser grained parts vuggy pores can be



Fig. 3.5 Location 5, Pakhna Formation.



Fig. 3.6 Location 16, Pakhna Formation.

found with up to 1.5 cm in size (Fig. 3.10 B). In the more fine-grained layers high amounts of brownish black plant remains can be found, which are of rounded to elongated shape, and up to 0.7 cm in size (Fig. 3.10 C).



Fig. 3.7 Location 10, Pakhna Formation.

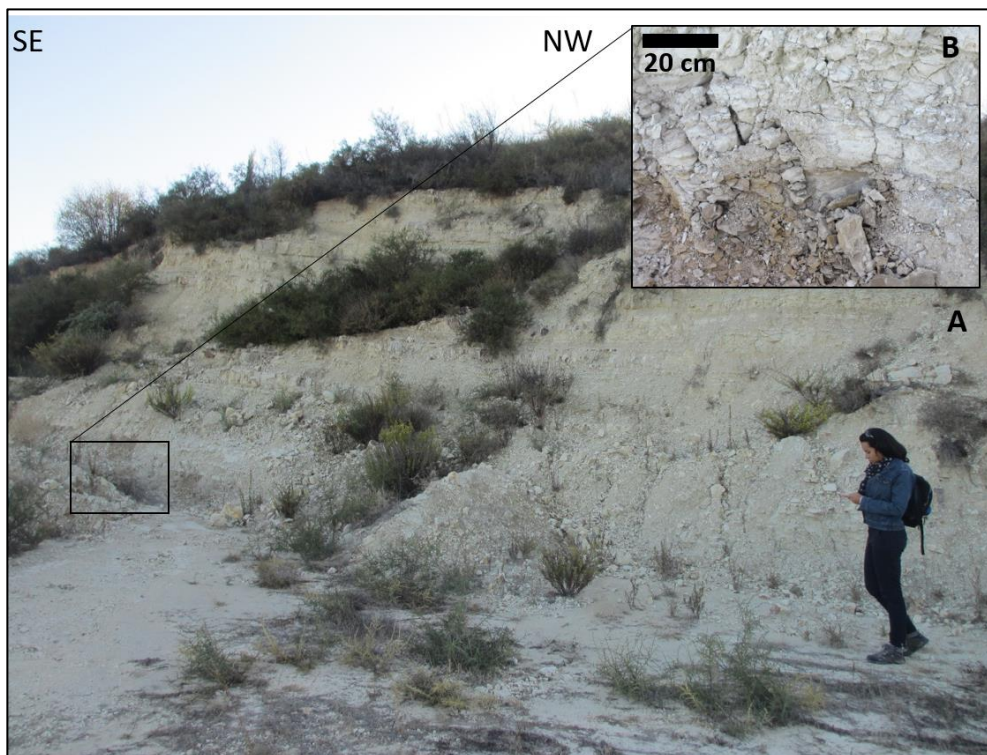


Fig. 3.8 Location 21, Pakhna Formation.

At Loc. 24 thin, dark grey, shaly layers of around 10 cm thickness are interbedded between beige to white massive calcarenites (Fig. 3.11 A). A large number of black, elongated up to 1cm in size plant remains can be found within the shaly layers (Fig. 3.11 B).



Fig. 3.9 Location 4, Nicosia Formation.

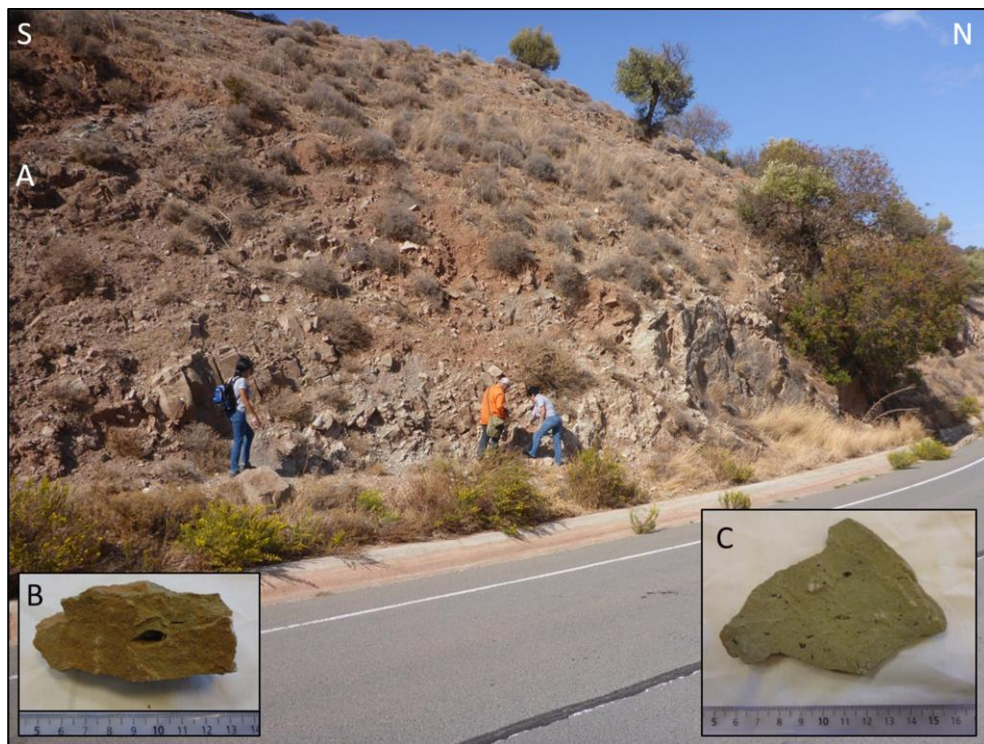


Fig. 3.10 Location 26, Vlambouros Formation.

3.1.2.2.2 *Episkopi Formation (Jurassic)*

The Episkopi Fm. was sampled at four different locations. At the locations 25, 27, 28, 29, it is composed of alternating dark red clay and green, thin bedded mudstones with radiolarian cherts and black manganiferous siltstones. Bright carbonate layers of around 10 to 20 cm thickness are interbedded between the clay layers. Both are strongly folded, possible representing carbonate slump deposits that



Fig. 3.11 Location 24, Vlambouros Formation.



Fig. 3.12 Representative example of large internal folding observed in the Episkopi Formation. The folding is interpreted as syn-depositional slump structures.

were gravity driven transported from shallow into deep-marine water conditions, where they were mixed with the clay (Fig. 3.12).

3.2 Second field campaign

3.2.1 Summary

The second field campaign was conducted in October and November 2017. Based on the results from the first campaign, the aim was to focus mainly on the Pakhna Fm. as well as on parts of the Mamonia Complex. More promising locations were investigated and some of the previous locations were revisited for more detailed sampling. Rock samples were again chosen based on fine grain size and dark color. To keep weathering effects low, samples were taken from at least 20 cm below the outcrop's surface.

In total 80 samples were collected from 16 locations (Fig. 2.3) covering six regional areas: (1) The western margin of the Mesaoria Basin, (2) the Maroni Sub-basin, (3) the Khalassa Sub-basin, (4) the Polis Basin, (5) the Akamas Peninsula, and (6) the Mamonia Complex near the Village of Ayios Fotios. Appendix Table B lists all samples together with their respective locations, formations and GPS coordinates. The author's sample IDs as well as IFPEN IDs are included as well. In the following chapters, only the author's sample IDs are used and referred to as "sample ID". Further, for some locations stratigraphic logs have been taken. They are named according to the respective location. The logs, their assumed correlation to each other as well as the location of the taken samples are shown in Figure 3.13.

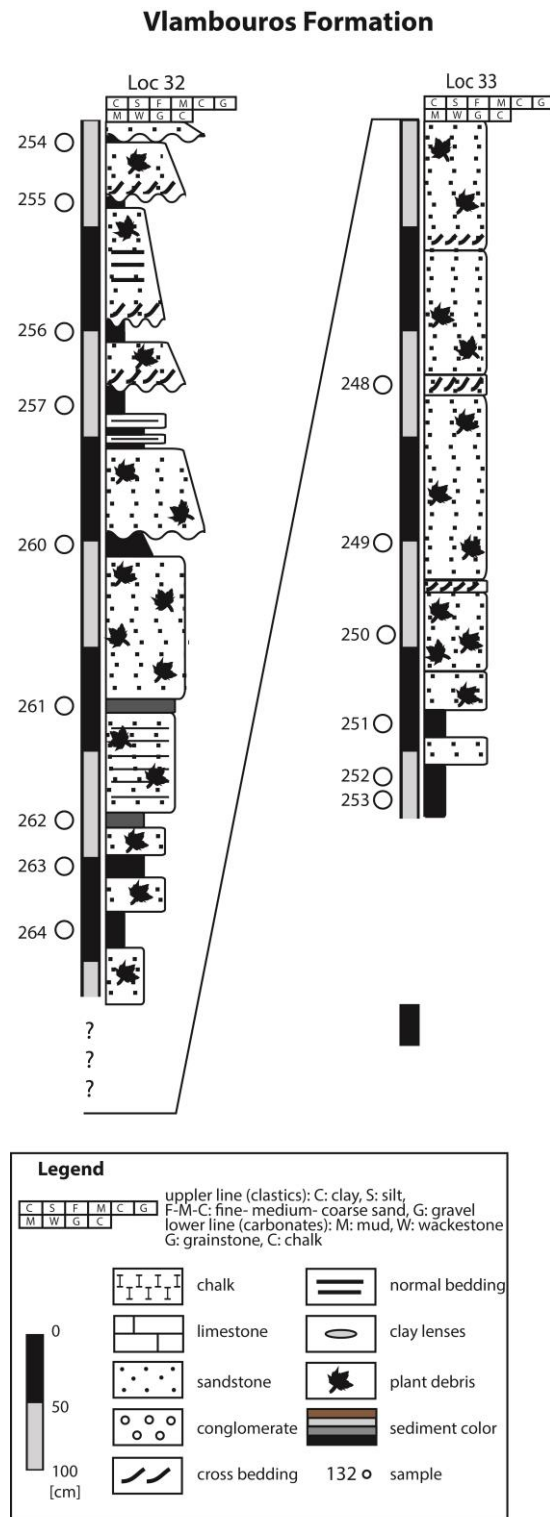


Fig. 3.13 Taken logs of the Vlambouros and the Pakhna Formation showing sample locations. (figure continues on next page...)

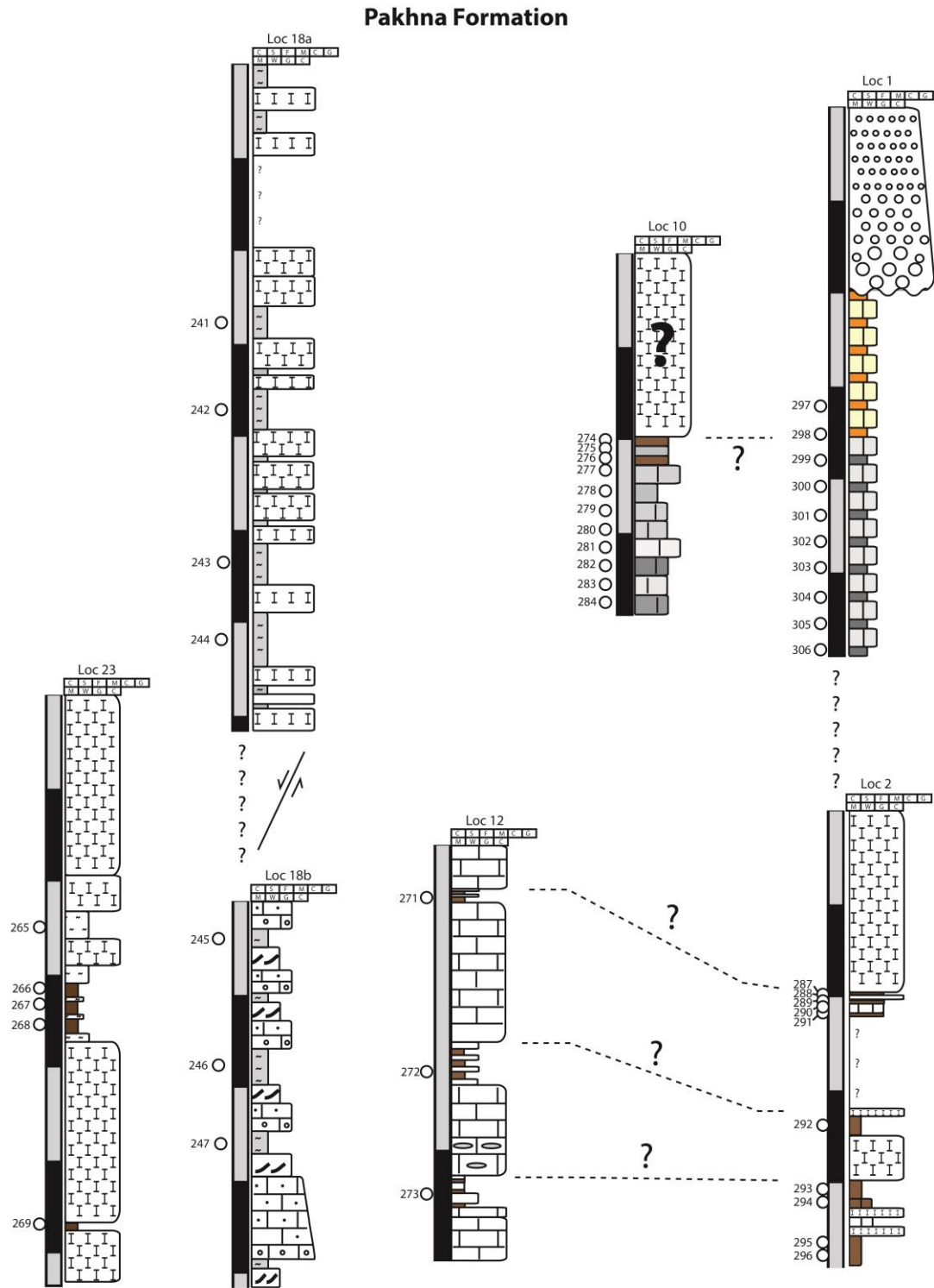


Fig. 3.13 continued.

3.2.2 Outcrop and sample description

3.2.2.1 Circum Troodos Sedimentary Succession

The Pakhna Fm. was sampled at 13 different locations. At 5 locations only one thin dark brown clayish layer is interbedded between massive white chalk units.

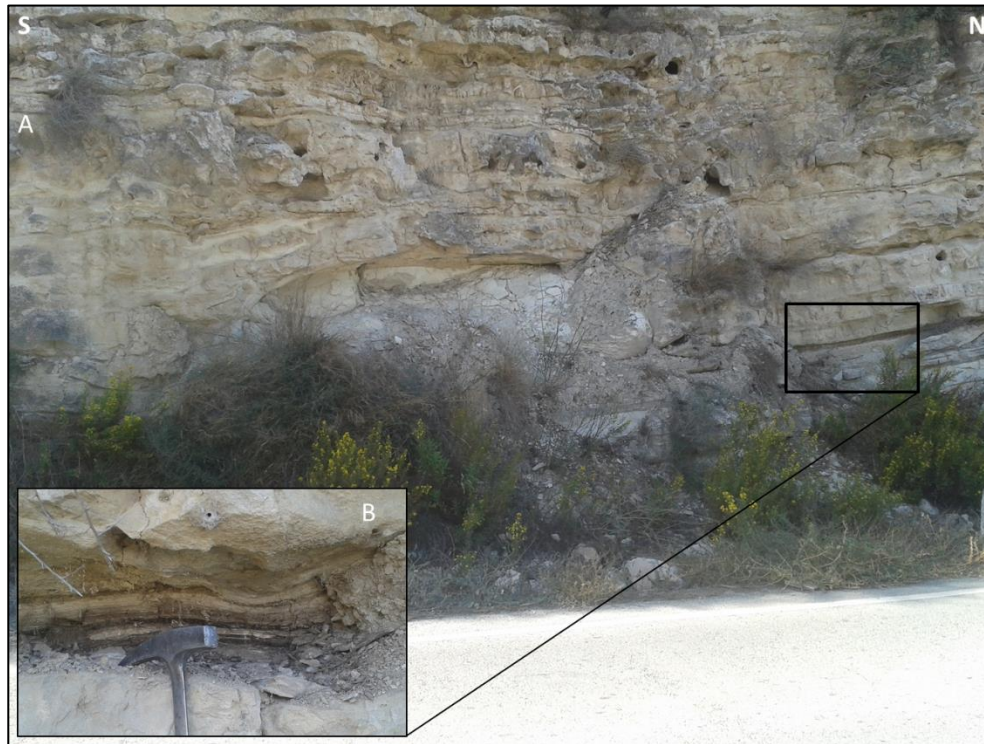


Fig. 3.14 Location 12, Pakhna Formation..

At Loc. 12 (Fig. 3.14) thin mudstone layers of similar brown color are interlayered with beige wackestones forming three observable packages of 10 to 25 cm thickness, which are in turn separated by thick chalk units. In some parts of the whitish chalk units grey clay lenses of up to 2 cm can be observed. A similar pattern is present at Loc. 2 (Fig. 3.15). Similar brownish bands are interbedded between chalk units. The outcrop is largely covered by soil, thus only four small spots could be investigated after removing the soil. Therefore, a clear unambiguous identification was not possible here.

Loc. 18A (Fig. 3.16 A) and 18B (Fig. 3.16 B) are located approximately 50 m away from each other. The outcrop at Loc. 18B is topographically a few meters below Loc. 18A. A quite large normal fault is located between the two outcrops, hindering the determination of the actual vertical, stratigraphic distance. At both outcrops some darkish mudstone to marlstone horizons of 10 to 25 cm thickness are interbedded between banks of calciclastic material. While the calciclastic packages at outcrop 18A are relatively homogenous, the ones at outcrop 18b show clear fining upward structures with pebbles up to 3 cm in diameter in the lower parts just above a partly erosional contact to the mudstone units. Further, cross bedding structures (Fig. 3.17) can be observed in the finer grained sections just below the marl units. Both outcrops are supposed to represent calciclastic turbidite sequences.

A completely different appearance of the Pakhna Fm. can be observed at Loc. 10 (Fig 3.18). Two bands of brownish grainstones are followed by alternating light grey and dark grey to black wacke- to grainstones, which show a high amount of ostracods. The color of the layers seems not to be unambiguously correlatable to the lithology. However, the outcrop is highly brittle and weathered,



Fig. 3.15 Location 2, Pakhna Formation.

inhibiting a clear and detailed investigation. At Loc. 1 (Fig. 3.19) very similar looking dark grey to black wackestones of 10 cm thickness, are interlayered between light grey grainstones of 20 cm thickness. The whole sequence is equally spaced. However, towards the top, the layers change their color to brownish orange for the wacke- and to yellowish for the grainstones. The uppermost part is truncated by Pliocene fluvial channel deposits.



Fig. 3.16 Location 18A (A) and 18B (B), Pakhna Formation.

3.2.2.2 Mamonia Complex

3.2.2.2.1 Vlambouros Formation (Mid Triassic)

The Vlambouros Fm. was sampled along a small canyon at the western coast of the Akamas Peninsula at two outcrops located 300 m away from each other. According to the layering and the topographic evaluation Loc. 33 (Fig. 3.20) should be stratigraphically lower than Loc. 32 (Fig. 3.21). Since the area is highly fractured and faulted a clear correlation is not possible. Both outcrops are composed of large packages of yellow brownish sandstones with partly interbedded dark grey to black, finely laminated clay- to siltstones. Most of the sandstone units comprise large black plant remains similar to those at Loc. 26 (first field campaign). At Loc. 32 the sandstone packages often are deposited on top of an erosional contact cutting into the clay layers. The sand bodies partly show fining upward sequences from coarse to medium sized grains. At their base, the sand bodies often show cross lamination, while the upper, finer grained parts are either massive, structureless, or horizontally laminated. Further, in the closer surrounding to both outcrops, big channel fill structures with pebbles



Fig. 3.17 Location 18A, Pakhna Formation



Fig. 3.18 Location 10, Pakhna Formation.

up to >10 cm in size can be observed (Fig. 3.22). Some of the silty layers show intense crusts of iron-oxides as well as yellowish (probably sulfur) mineral precipitation. The overall system is interpreted to represent a fluvial, probably deltaic system with Loc. 33 representing a more distal and Loc. 32 a more proximal setting.



Fig. 3.19 Location 1, Pakhna Formation.



Fig. 3.20 Location 33, Vlambouros Formation.



Fig. 3.21 Conglomeratic channel fills near Loc. 33 and 32.

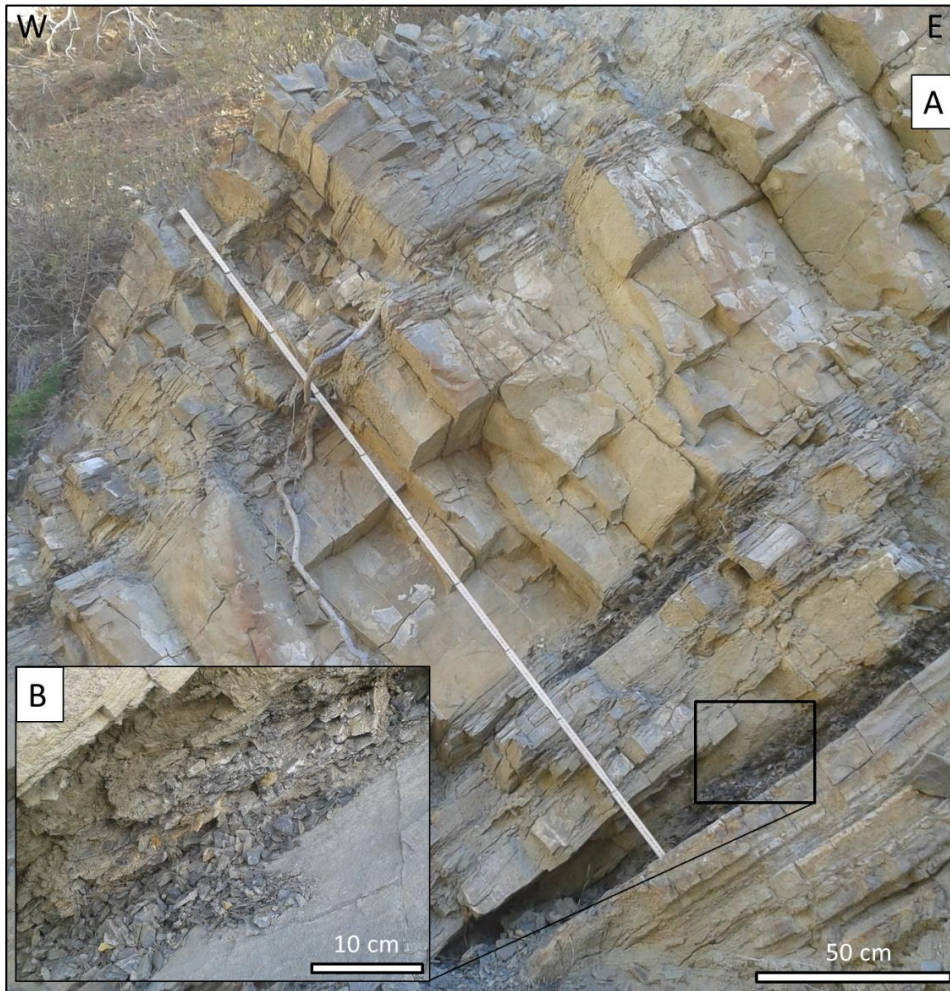


Fig. 3.22 Location 32, Vlambouros Formation.

3.3 Sampling ODP Leg 160 cores at Marum, Bremen, Germany

3.3.1 ODP Leg 160 campaign

The ODP Leg 160 campaign was conducted in 1995 and focused on the northern slope of the ESM (Emeis et al., 1996). The aim of the campaign was to investigate the paleo-oceanographic evolution of the Eastern Mediterranean Sea by analyzing the sedimentary cover of the ESM with its special position, being in collision with Cyprus along the Cyprus arc.

Four sites were drilled (from south to north: 965, 966, 967, 968) and logged during the expedition. The wells transect the ESM platform, its northern slope, and the trench between the ESM and Cyprus (Fig. 3.23). At site 965 and 968 the deepest units reached are of Early Miocene to Pliocene age. Eocene sediments were reached at site 966. At site 967 the deepest well penetrates down to the Upper Cretaceous (600 m). At each site several holes were drilled and partly cored (low recovery rates between 15 to 40

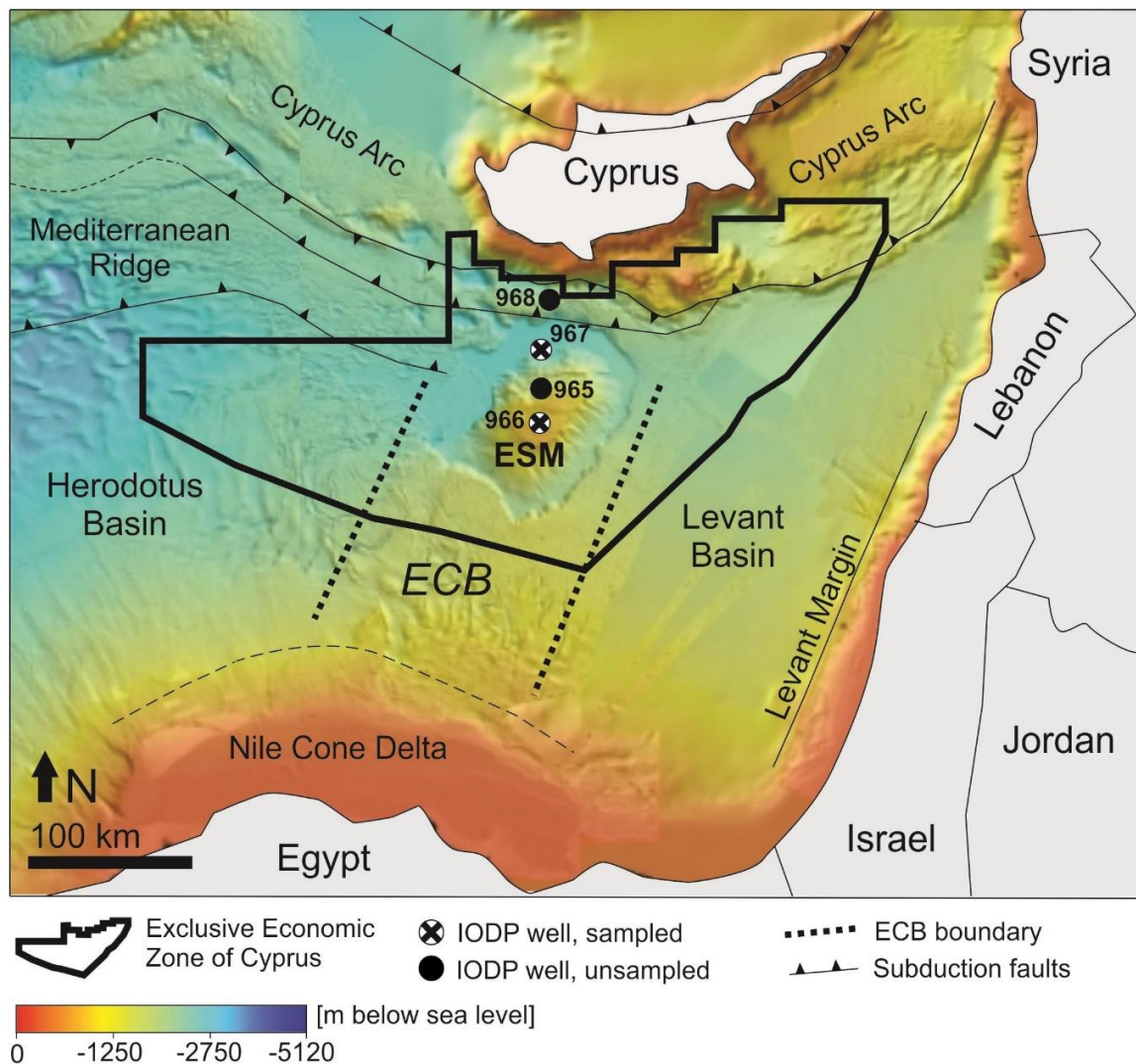


Fig. 3.23 Locations of the ODP Leg 160 wells along the Eratosthenes Seamount (ESM).

%). Core IDs refer to site, hole, core, section (e.g. 967F 26R 2 defines site 967, hole F, 26th core, 2nd section).

The main focus of investigation (and densest coring) was on the Messinian sapropels, which were deposited throughout the Mediterranean Sea. However, for this work, only pre-Messinian sections were sampled.

3.3.2 Sample description

Samples were compiled from Site 966, holes E and F, and Site 967, hole A. In total, 122 samples were taken; 120 samples were collected at irregular distance from brownish-grey to black marls, shaly marls, and carbonates (Fig. 3.24) and two bitumen-impregnated samples were retrieved from light grey marls. A list of all offshore samples including a lithological description is given in Appendix Table C together with the Author's

IDs and the LEK IDs. Biostratigraphic age determination of the cores was conducted by Silva et al. (1998) and Staerker (1998). Their results were adapted to the Chronostratigraphic Chart 2015 for this study; 19 samples are assigned to upper Turonian to Coniacian-, 6 to Santonian-, 11 to Campanian to Maastrichtian-, 3 to Eocene to Miocene, 49 to Ypresian to Lutetian-, 29 to Bartonian to Priabonian-, and 3 samples to the Messinian age.

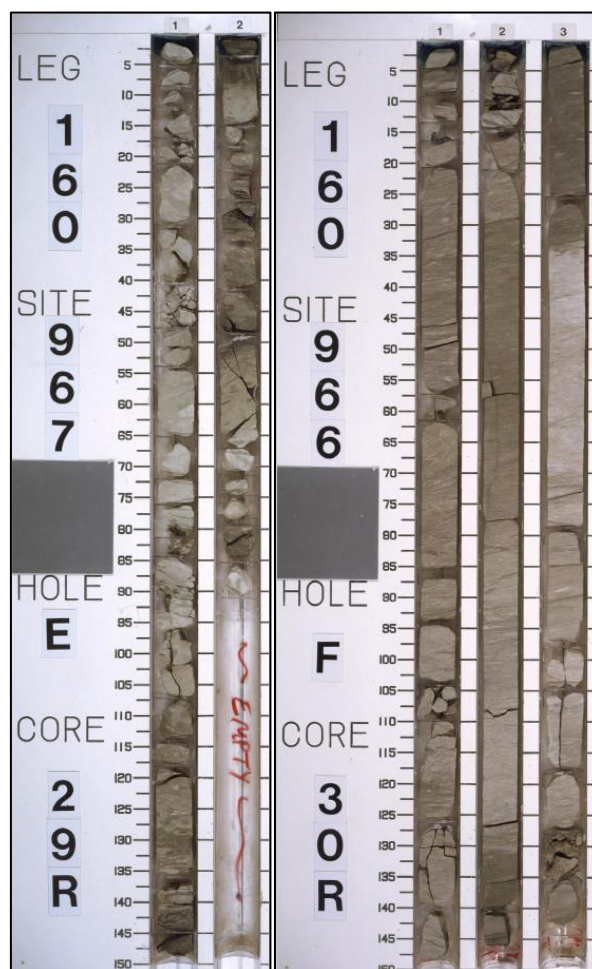


Fig. 3.24 Representative core photos of dark mudstone intervals in the Upper Cretaceous of well 967 E (A) and in the Eocene of well 966 F (B).

4 Source rock characterization of Mesozoic to Cenozoic organic matter-rich marls and shales of the Eratosthenes Seamount, Eastern Mediterranean Sea

An edited version of this chapter was peer-reviewed published as: Grohmann, S., Fietz, S.W., Littke, R., Bou Daher, S., Romero-Sarmiento, M.F., Nader, F.H., Baudin, F. (2018). Source rock characterization of Mesozoic to Cenozoic organic matter-rich marls and shales of the Eratosthenes Seamount, Eastern Mediterranean Sea. Oil and Gas Science and Technology – Rev. IFP Energies nouvelles 73, 49.

Abstract

Several significant hydrocarbon accumulations were discovered over the past decade in the Levant Basin, eastern Mediterranean Sea. Onshore studies have investigated potential source rock intervals to the east and south of the Levant Basin, whereas its offshore western margin is still relatively underexplored. Only a few cores were recovered from four boreholes offshore southern Cyprus by the Ocean Drilling Program (ODP) during the drilling campaign Leg 160 in 1995. These wells transect the Eratosthenes Seamount, a drowned bathymetric high, and recovered a thick sequence of both pre- and post-Messinian sedimentary rocks, containing mainly marine marls and shales. In this study, 122 core samples of Late Cretaceous to Messinian age were analyzed in order to identify organic-matter-rich intervals and to determine their depositional environment as well as their source rock potential and thermal maturity. Both total organic and inorganic carbon analyses (TOC, TIC) as well as Rock-Eval pyrolysis were firstly performed for the complete set of samples whereas total sulfur (TS) analysis was

only carried out on samples containing significant amount of organic matter (>0.3 wt.% TOC). Based on the Rock-Eval results, eight samples were selected for organic petrographic investigations and twelve samples for analysis of major aliphatic hydrocarbon compounds. The organic content is highly variable in the analyzed samples (0 to 9.3 wt.%). TS/TOC as well as several biomarker ratios (e.g. Pr/Ph < 2) indicate a deposition under dysoxic conditions for the organic matter-rich sections, which were probably reached during sporadically active upwelling periods. Results prove potential oil prone Type II kerogen source rock intervals of fair to very good quality being present in Turonian to Coniacian (average: TOC = 0.93 wt.%, HI = 319 mg HC/g TOC) and in Bartonian to Priabonian (average: TOC = 4.8 wt.%, HI = 469 mg HC/g TOC) intervals. A precise determination of the actual source rock thickness is prevented by low core recovery rates for the respective intervals. All analyzed samples are immature to early mature. However, the presence of deeper buried, thermally mature source rocks and hydrocarbon migration is indicated by the observation of solid bitumen impregnation in one Upper Cretaceous and in one Lower Eocene sample.

4.1 Introduction

Significant natural gas discoveries (e.g. Dalit, Tamar, Leviathan, Aphrodite, Zohr and recently Calypso fields) in the last decade have rendered the Levant Basin in the eastern Mediterranean Sea as one of the most promising frontier basins of the world (e.g. Needham, 2013; Ratner, 2016; Eni, 2018) (Fig. 4.1). The reservoir units of these gas plays are Oligocene to Miocene sandstones (Montadert et al., 2014; Bou Daher et al., 2016) and Cretaceous to Miocene shallow water carbonate build-ups (Bertello et al., 2016; Esestime et al., 2016). Onshore studies have identified several events of source rock deposition in the sedimentary succession of the eastern and southern Levant margin which may also extend into the western offshore part of the basin (Beydoun, 1991; May 1991; Vandré et al, 2007; Naylor et al., 2013; Bou Daher et al. 2014, Bou Daher et al., 2015). The potential of working petroleum systems along the western margin of the Levant Basin is inferred from high resolution seismic data indicating sufficient thickness of the sedimentary column, alternating sealing units, as well as direct hydrocarbon indicators, e.g. bright spots and gas chimneys (Roberts and Peace, 2007; Montadert et al., 2014). To date, only south of Cyprus' southern Exclusive Economic Zone, sea bottom sampling in the North East Nile Delta offshore Egypt proves that multiple source rocks participate in thermogenic hydrocarbon charge (Shaaban et al., 2006; Montadert et al., 2014). However, these source rock intervals were drilled in shallow waters close to the coast. Further they are still poorly described, and do not necessarily correlate with the deeper offshore.

Four locations were core drilled in the area of Cyprus by the Ocean Drilling Program (ODP) during the Leg 160 campaign in 1995 (Emeis et al., 1996). The well sites penetrate the northern flank of the Eratosthenes Seamount (ESM) which is located offshore southern Cyprus (Fig. 4.1). Organic matter (OM) rich intervals were noticed in the sedimentary succession of the retrieved cores (Emeis et al.,

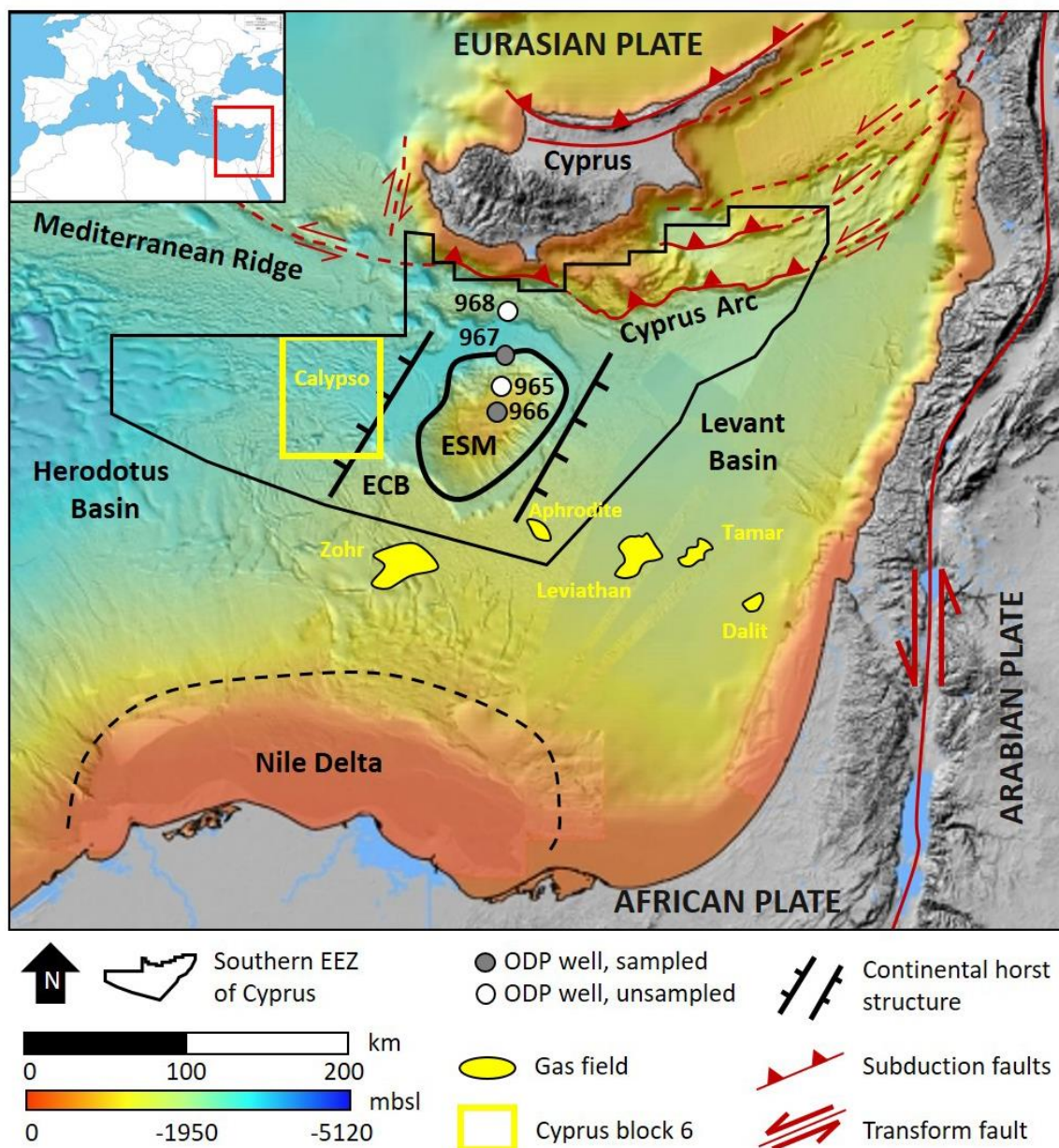


Fig. 4.1 Overview of the study area. Onshore areas colored in grey, subsea bathymetry colored in shades according to scale. Marked gas fields (yellow) represent recent discoveries. The area is mainly controlled by the interplay of the African, Arabian, and Eurasian plates. The Eratosthenes Seamount (ESM) represents a large carbonate platform which is located on the underlying, larger Eratosthenes Continental Block (ECB). The southern Exclusive Economic Zone (EEZ) of Cyprus represents the available blocks for hydrocarbon exploration. The samples of this study were collected from the cores that were drilled along the northern lobe of the ESM during the ODO Leg 160 campaign. Modified after Hawie et al. (2013) and Symeou et al. (2018).

1996). However, barely any detailed organic geochemical analysis has been performed on the pre-Messinian rocks of these cores, hitherto, whereas numerous organic geochemical studies were conducted and published on the young, post-Messinian Mediterranean sapropels. An exception is one sample of middle Eocene age (160-966F-26R-1, 17-22cm) that reveals a TOC value of 5.25 wt.%, Hydrogen and Oxygen Index values of 429 mg HC/g TOC and 63 mg CO₂/g TOC, respectively, as well as a T_{max} of

413°C (Emeis et al., 1996). These results support the assumption that the organic rich intervals in these cores might have significant source rock potential.

For petroleum system perspectives, the purpose of this paper is to provide more potential source rock information about the overall underexplored western margin of the Levant Basin. In this way, sub-Messinian organic-rich rock intervals of the ODP Leg 160 cores were sampled and analyzed in order to investigate the depositional environment, source rock quality as well as thermal maturity of the sedimentary organic matter.

4.2 Geological background

The Eratosthenes Seamount (ESM) is a bathymetric high that rises about 1500 m above its surrounding sea floor with its summit 700 m below sea level (Fig. 4.1) (Galindo-Zaldivar et al., 2001). Its northeast-southwest and northwest-southeast extension reaches approximately 110 km and 80 km, respectively. The ESM is located on the bigger Eratosthenes Continental Block (ECB) which is a continental fragment that was separated from the Afro-Arabian margin during the disintegration of Gondwana. It is believed to have rifted westwards along NNE-SSW oriented transform faults during the Triassic to Early Jurassic (Robertson, 1998a; Gardosh and Druckman, 2006; Netzeband et al., 2006; Segev and Rybakov, 2010, Ghalayini et al., 2014; Montadert et al., 2014). Between the ECB and the Afro-Arabian continental margin, a southern arm of the NeoTethys evolved which later formed the Levant Basin (Gardosh and Druckman, 2006). From the Late Cretaceous onwards, the entire region was affected by the convergence of Eurasia and Afro-Arabia, which resulted in northward subduction and the creation of the Cyprus Arc (Hawie et al., 2013a; Montadert et al., 2014). As a consequence, the ESM is in a state of collision with the island of Cyprus since the Pliocene (Robertson, 1998a; Galindo-Zaldivar et al., 2001).

The sedimentary cover of the ESM is approximately 6 km of thick (Montadert et al., 2014, Papadimitriou et al., 2018). Only the upper 600 meters below the seafloor (mbsf) were cored during the ODP drilling campaign Leg 160 (Emeis et al., 1996). Undrilled sediments are inferred from seismic reflection and are interpreted to comprise syn-rift sediments (volcaniclastics, carbonates or clastic sediments) which are overlain by a thick post-rift succession of extensive shallow marine carbonate build-ups, intercalated with a sequence of undisturbed, probably fine-grained, marine sediments (Montadert et al., 2014). A schematic overview of the lithostratigraphy of the ESM, the Levant Basin, as well as the well-constrained sedimentary pile of the eastern margin of the Levant Basin in northern and southern Lebanon are shown in Figure 4.2. Analysis of the drilled intervals from the ODP Leg 160 campaign constrains the interpretation of the depositional environments of the Upper Cretaceous and younger strata (Emeis et al., 1996; Premoli-Silva et al., 1998; Staerker, 1998). Shallow water carbonate deposition was interrupted during the Cenomanian/Turonian and younger Upper Cretaceous sediments

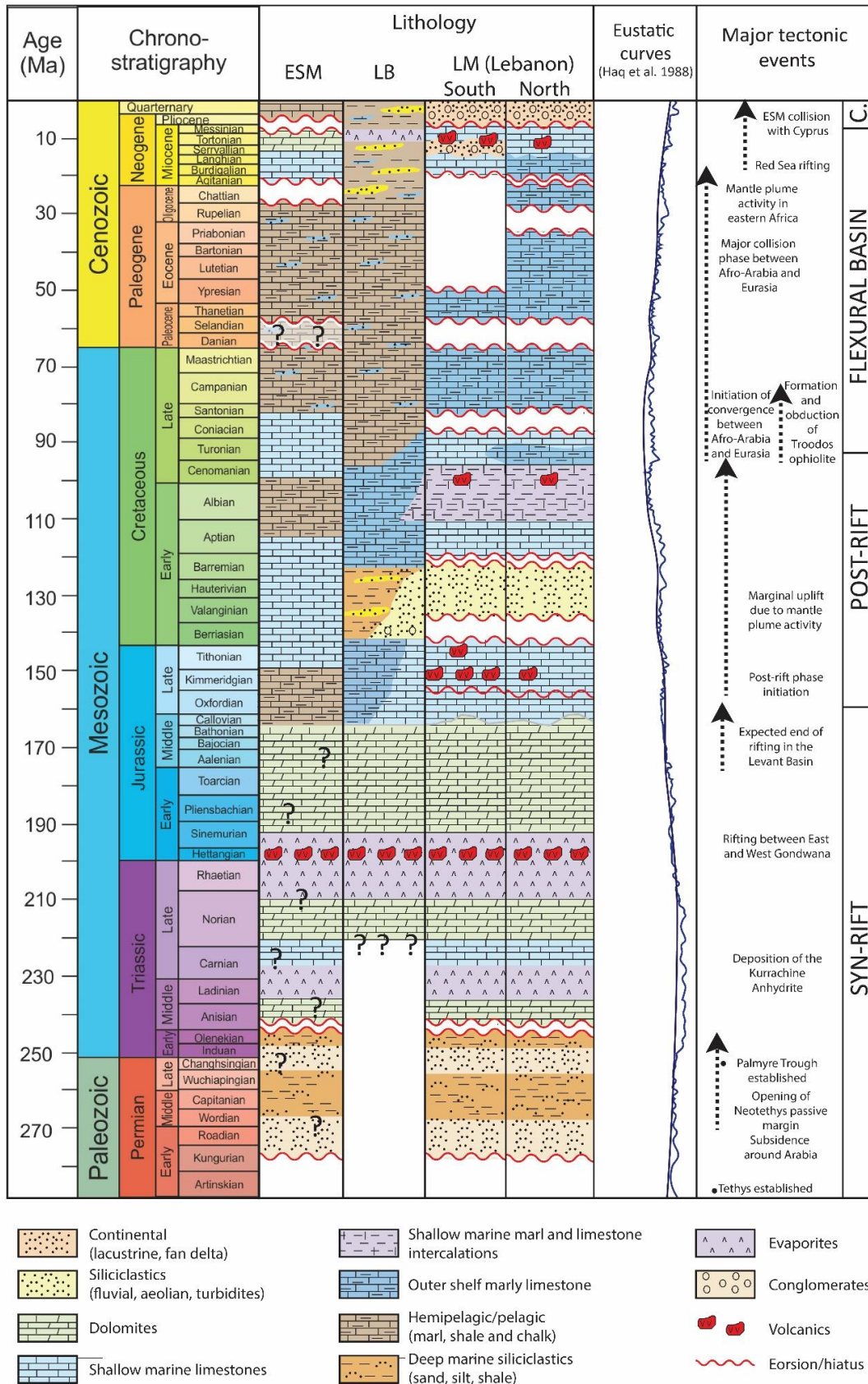


Fig. 4.2 Schematic overview of the sedimentary successions to be found in the Levant Basin (LB), the Eratosthenes Seamount (ESM) and at the Levant margin (LM) along Lebanon. Modified after Bou Daher et al. (2016).

were deposited in a hemipelagic to pelagic environment (Robertson, 1998c). Later, Miocene shallow water carbonate build-ups formed on the ESM. During the Messinian Salinity Crisis (MSC) the sediments of the ESM were most likely exposed and affected by extensive meteoric water flushing, karstification, dolomitization, as well as erosion (Robertson, 1998b). Subsequent drowning of the ESM during the Pliocene to Quaternary enabled the deposition of pelagic carbonates and sapropels (Robertson, 1998c).

4.3 Material and methods

4.3.1 Samples

Samples were collected from Site 966, hole F, and Site 967, holes A and E (Table 4.1). The borehole cores were drilled at the northern slope (Site 967) and the top of the platform (Site 966) of the ESM (Fig. 4.1) by the Ocean Drilling Program (ODP) during the expedition Leg 160 in 1995. Lithology of these cores is described in the initial shipboard scientific results (Emeis et al., 1996). In total, 122 samples were sampled (Table 4.1); 120 samples were collected at irregular intervals from brownish-grey to black marls, shaly marls, and carbonates and two solid bitumen-impregnated samples (15/891 and 15/896; Lower Eocene and Upper Cretaceous, respectively) were retrieved from light grey marls. Biostratigraphic age determination of the cores was previously conducted by Premoli-Silva et al. (1998) and Staerker (1998). Their results were adapted to the Chronostratigraphic Chart 2015 for this study; 20 samples are assigned to upper Turonian to Coniacian, 6 to Santonian, 11 to Campanian to Maastrichtian, 3 to Eocene to Miocene, 50 to Ypresian to Lutetian, 29 to Bartonian to Priabonian, and 3 samples to the Messinian age.

All further processing and analyses of the collected samples were done at the Institute of Geology and Geochemistry of Petroleum and Coal, RWTH Aachen University.

4.3.2 Elemental analysis and Rock-Eval pyrolysis

Total organic (TOC) and inorganic carbon (TIC) measurements were performed on all samples using a liquiTOC II analyzer in order to quantify the amounts of OM and carbonates. The applied "temperature ramp method" enables direct measurement of the carbon content of each sample without previous acidification. The sample powder (100 mg) is heated to 550°C and kept at this temperature for 600 s. Subsequent cooling of the sample to 400°C is followed by a second step of heating until the sample reaches 1000°C where it remains for 400 s. The released CO₂ is detected at each step by an infrared cell (detection limit 10 ppm, relative TOC error 0.6 wt.%, relative TIC error 1.7 wt.%). We already know that thermally less stable carbonates (such as siderite) might decompose already at temperatures around 500°C and might lead to an overestimation of the TOC and an underestimation of

Table 4.1 Samples obtained from the OPD Leg 160 campaign along the Eratosthenes Seamount (offshore Cyprus) and the respective core interval, ordered by age. (Table continues on next page...)

Sample	Site-hole	Core	Depth [mbsf]	Age
15/892	967-A	13	117.38	Messinian
15/893	967-A	13	120.97	Messinian
15/894	967-A	13	122.05	Messinian
17/1679	966-F	26	298.48	Bartonian to Priabonian
15/863	966-F	26	298.53	Bartonian to Priabonian
17/1680	966-F	26	298.56	Bartonian to Priabonian
17/1681	966-F	26	298.61	Bartonian to Priabonian
15/864	966-F	26	298.66	Bartonian to Priabonian
17/1682	966-F	26	298.72	Bartonian to Priabonian
15/865	966-F	26	298.76	Bartonian to Priabonian
17/1683	966-F	26	298.86	Bartonian to Priabonian
15/866	966-F	26	298.90	Bartonian to Priabonian
15/867	966-F	26	299.09	Bartonian to Priabonian
17/1685	966-F	26	299.11	Bartonian to Priabonian
17/1686	966-F	26	299.19	Bartonian to Priabonian
15/868	966-F	26	299.21	Bartonian to Priabonian
15/869	966-F	26	299.28	Bartonian to Priabonian
17/1687	966-F	26	299.35	Bartonian to Priabonian
15/870	966-F	26	299.40	Bartonian to Priabonian
17/1688	966-F	26	299.46	Bartonian to Priabonian
15/871	966-F	26	299.50	Bartonian to Priabonian
17/1689	966-F	26	299.56	Bartonian to Priabonian
15/872	966-F	26	299.59	Bartonian to Priabonian
15/873	966-F	26	299.66	Bartonian to Priabonian
17/1690	966-F	26	299.71	Bartonian to Priabonian
15/874	966-F	26	299.76	Bartonian to Priabonian
17/1691	966-F	26	299.82	Bartonian to Priabonian
17/1692	966-F	26	300.05	Bartonian to Priabonian
15/875	966-F	26	300.84	Bartonian to Priabonian
17/1693	966-F	26	301.03	Bartonian to Priabonian
15/876	966-F	26	301.11	Bartonian to Priabonian
17/1694	966-F	26	301.18	Bartonian to Priabonian
15/877	966-F	27	314.97	Ypresian to Lutetian
17/1696	966-F	28	317.8	Ypresian to Lutetian
17/1698	966-F	28	318.46	Ypresian to Lutetian
17/1699	966-F	28	318.73	Ypresian to Lutetian
17/1700	966-F	28	319.20	Ypresian to Lutetian
17/1701	966-F	28	319.60	Ypresian to Lutetian
17/1702	966-F	28	320.72	Ypresian to Lutetian
17/1703	966-F	28	320.92	Ypresian to Lutetian
17/1704	966-F	28	321.29	Ypresian to Lutetian
17/1705	966-F	28	321.63	Ypresian to Lutetian
17/1706	966-F	28	322.13	Ypresian to Lutetian
17/1707	966-F	28	323.28	Ypresian to Lutetian
17/1708	966-F	28	324.23	Ypresian to Lutetian
17/1709	966-F	29	327.49	Ypresian to Lutetian
17/1711	966-F	29	329.07	Ypresian to Lutetian
17/1712	966-F	29	329.27	Ypresian to Lutetian
17/1715	966-F	29	330.60	Ypresian to Lutetian
15/878	966-F	30	337.10	Ypresian to Lutetian
17/1717	966-F	30	337.18	Ypresian to Lutetian
15/879	966-F	30	337.25	Ypresian to Lutetian
15/880	966-F	30	337.40	Ypresian to Lutetian
15/881	966-F	30	337.50	Ypresian to Lutetian
17/1718	966-F	30	337.51	Ypresian to Lutetian
15/882	966-F	30	337.62	Ypresian to Lutetian
15/883	966-F	30	337.70	Ypresian to Lutetian
15/884	966-F	30	338.03	Ypresian to Lutetian
17/1720	966-F	30	338.12	Ypresian to Lutetian
17/1721	966-F	30	338.40	Ypresian to Lutetian
15/885	966-F	30	338.77	Ypresian to Lutetian
15/886	966-F	30	338.85	Ypresian to Lutetian
17/1722	966-F	30	338.85	Ypresian to Lutetian
15/887	966-F	30	339.32	Ypresian to Lutetian
17/1724	966-F	30	339.55	Ypresian to Lutetian
15/888	966-F	30	339.64	Ypresian to Lutetian
17/1725	966-F	30	339.66	Ypresian to Lutetian
17/1726	966-F	30	339.78	Ypresian to Lutetian
15/889	966-F	30	339.81	Ypresian to Lutetian
17/1727	966-F	30	339.89	Ypresian to Lutetian
15/890	966-F	30	339.94	Ypresian to Lutetian
15/891	966-F	30	340.03	Ypresian to Lutetian
17/1729	966-F	30	340.53	Ypresian to Lutetian
17/1732	966-F	30	341.07	Ypresian to Lutetian
17/1733	966-F	31	346.43	Ypresian to Lutetian
17/1735	966-F	31	347.02	Ypresian to Lutetian
17/1736	966-F	31	347.76	Ypresian to Lutetian
17/1737	966-F	31	347.96	Ypresian to Lutetian
17/1738	966-F	31	348.47	Ypresian to Lutetian
17/1740	966-F	31	348.80	Ypresian to Lutetian
17/1742	966-F	31	349.53	Ypresian to Lutetian

Table 4.1 continued

Sample	Site-hole	Core	Depth [mbsf]	Age
17/1743	966-F	31	349.92	Ypresian to Lutetian
15/895	967-E	6	160.93	Eocene to Miocene
17/1744	967-E	7	167.30	early Oligocene
17/1745	967-E	7	167.79	early Oligocene
17/1746	967-E	8	177.05	Maastrichtian
17/1747	967-E	8	177.32	Campanian
17/1748	967-E	8	177.43	Campanian
15/896	967-E	17	265.49	Campanian
17/1749	967-E	18	273.27	Campanian
17/1751	967-E	18	274.06	Campanian
17/1752	967-E	18	274.36	Campanian
17/1753	967-E	18	274.65	Campanian
17/1754	967-E	18	275.04	Campanian
17/1755	967-E	18	275.55	Campanian
17/1756	967-E	18	276.31	Campanian
17/1757	967-E	25	340.93	Santonian
17/1758	967-E	25	341.34	Santonian
17/1759	967-E	25	342.18	Santonian
17/1760	967-E	25	342.80	Santonian
17/1761	967-E	25	343.11	Santonian
17/1762	967-E	25	344.40	Santonian
15/897	967-E	28	369.44	Coniacian
15/898	967-E	28	370.06	Coniacian
15/899	967-E	28	370.40	Coniacian
17/1763	967-E	29	379.22	Coniacian
15/900	967-E	29	379.71	Coniacian
17/1764	967-E	29	379.87	Coniacian
15/901	967-E	29	379.96	Coniacian
17/1765	967-E	29	379.98	Turonian
15/902	967-E	29	380.28	Turonian
17/1766	967-E	29	380.30	Turonian
15/903	967-E	29	380.36	Turonian
17/1767	967-E	29	380.54	Turonian
15/904	967-E	29	380.77	Turonian
15/905	967-E	29	380.80	Turonian
17/1768	967-E	29	380.94	Turonian
15/906	967-E	29	381.13	Turonian
17/1769	967-E	30	388.46	Turonian
17/1770	967-E	30	388.67	Turonian
17/1771	967-E	30	388.70	Turonian
17/1772	967-E	30	388.82	Turonian

the TIC content, respectively (Pillot et al., 2014). However, the marine carbonates investigated in this study are mostly free of siderite.

CaCO₃ percentage was calculated using $\text{CaCO}_3 = \text{TIC} \cdot 8.333$ (Littke, 1993). Carbonate content of samples from dolomite-dominated intervals was calculated with the equation $\text{CaMg}(\text{CO}_3)_2 = \text{TIC} \cdot 7.8333$ (Bou Daher et al., 2014).

For interpreting the depositional environment and paleo-redox conditions the total sulfur (TS) content was determined for samples containing >0.3 wt.% TOC using a LECO S200 analyzer with an infrared detector (detection limit of 20 ppm, relative error of < 5%).

Rock-Eval pyrolysis (Espitalié et al., 1977) was applied for 122 samples to qualify the hydrogen and oxygen content of the OM and its thermal maturity. However, only 104 samples provided useful results. Measurements were performed on a classic Rock-Eval 6 instrument (Behar et al., 2001) using the standard Basic/Bulk-Rock method described in Espitalié et al. (1977) and Behar et al. (2001). Approximately 120 mg sample powder was taken for samples with TOC values ranging from 0.1 wt.% to 2.0 wt.%, 100 mg powder for samples with TOC values between 2 wt.% and 8 wt.% and 50 mg for samples showing TOC values between 8 wt.% and 20 wt.%. Approximately 50 mg of silica was added to sample quantities of < 50 mg. Standard Rock-Eval parameters like S1, S2, S3, T_{max} as well as

Hydrogen Index (HI), Oxygen Index (OI) and Production Index (PI) were accordingly obtained following procedures also described in Behar et al. (2001).

As described by Katz (1983), Rock-Eval pyrolysis can be effected by additional generation of CO₂ derived from carbonate decomposition even at low temperatures. In order to investigate this effect on the present dataset, 6 samples with 2 g each were decarbonized using 30 ml of hydrochloric acid (10%) at 80°C for 30 min and subsequent neutralizing with distilled water. After settling of the OM overnight and decantation and evaporation at 50°C of the remaining water, Rock-Eval pyrolysis was repeated on these samples.

4.3.3 Organic petrographic analysis

Eight samples were selected for organic petrology analysis based on their age and TOC content (0.52 to 9.33 wt.%) to compare geochemical results with visual investigations like maceral qualification and vitrinite reflectance measurements as a reliable thermal maturity indicator. Thick sections were prepared by embedding sample pieces in a mixture of Araldite XW396 (epoxy resin) and Araldite XW397 (hardener) at a ratio of 10:3 and cutting them perpendicular to the bedding following the preparation procedure described in Sachse et al. (2012). The polished surfaces were analyzed in a dark room with a Zeiss Axio Imager microscope equipped with a tungsten-halogen lamp (12 V, 100 W) for incident white light and a mercury lamp (HXP R120W/45C) for ultraviolet/violet light-excitation of fluorescence. An Epiplan-NEOFLUAR 50x/0.85 oil immersion objective, oil with a refractive index of 1.518, and the calibration standard Klein and Becker Leuco-Saphire (0.592%) were used. Samples were qualitatively analyzed with respect to content of inertinite, vitrinite, liptinite (lamalginite and telalginite), pyrite and fossils (foraminiferas, fish bones, shell fragments). Maceral identification was mainly based on their difference in reflectivity as well as their florescence intensity following procedures described by Littke (1993). Six samples were analyzed for random vitrinite reflectance (%VR_r) . Measurements were processed with the software DISKUS Fossil, v.460.810 (Technisches Büro C. Hilgers, Königswinter, Germany). Details of the microscopical procedure are also described in Sachse et al. (2012).

The maximum paleotemperature (T_{peak}) that was experienced during burial related heating was calculated according to Barker and Pawlewicz (1994):

$$T_{peak} = \frac{\ln(\%VR_r + 1.68)}{0.0124}$$

4.3.4 Molecular geochemistry

Biomarkers can reveal information about specific organic precursor molecules which can help to identify original organic compounds. Further, the chirality of molecules (e.g. steranes) change with increasing temperature and, therefore, can be used as a thermal maturity indicator (Peters et al., 2005). Twelve samples were selected for molecular geochemical analysis by both, gas chromatography (GC) coupled with a flame ionization detector (GC-FID) and GC coupled with a mass spectrometer (GC-MS). Prior to the analysis, maltene fractions were obtained using a *DIONEX ASE 150* instrument (*Thermo Scientific*), which allows a full automatic extraction. Approximately 8 g of powdered rock sample were extracted by 40 ml of dichloromethane (DCM) in a high pressure cell at 100°C and 100 bar during 14 min. All maltene extracts were separated into three fractions by means of silica-gel based liquid column chromatography and eluents of different polarity: 5 ml pentane for the aliphatic fraction, 5 ml pentane/DCM (40:60) for the aromatic fraction, and 5 ml methanol for the polar fraction.

4.3.4.1 GC-FID

A *Carlo Erba Strumentazione HRGC 5300* gas chromatograph equipped with a flame ionization detector was used to investigate the molecular composition of aliphatic fractions. The initial temperature was set to 80°C, kept for 3 min, followed by heating at 5.0°C/min up to 300°C, and held for 20 min. The injection was performed in splitless mode set to 60 s. Compound separation was performed in a 30 m long *Zebron ZB-1* capillary column using hydrogen as carrier gas. The obtained chromatograms were interpreted using the *Atlas CDS* software. Based on the relative abundance of the respective *n*-alkanes, the terrigenous/aquatic ratio (TAR; Bourbonniere and Meyers, 1996), the odd-to-even predominance (OEP; Scalan and Smith, 1970) as well as the carbon preference index (CPI; Bray and Evans, 1961) were calculated as follow:

$$TAR = \frac{(nC_{27} + nC_{29} + nC_{31})}{(nC_{15} + nC_{17} + nC_{19})}$$

$$OEP = \frac{(nC_{21} + 6 * nC_{23} + nC_{25})}{(4 * nC_{22} + 4 * nC_{24})}$$

$$CPI = \frac{2 * (nC_{23} + nC_{25} + nC_{27} + nC_{29})}{(nC_{22} + 2 * (nC_{24} + nC_{26} + nC_{28}) + nC_{30})}$$

Table 4.2 Identified hopane and sterane peaks used in this work.

Peak ID	Hopane m/z = 191	Peak ID	Sterane m/z = 217
A	C ₂₅ tricyclic terpane (22S+R)	a	C ₂₇ β α -diacholestane (20S)
B	C ₂₆ tricyclic terpane (22S)	b	C ₂₇ β α -diacholestane (20R)
C	C ₂₆ tricyclic terpane (22R)	c	C ₂₈ β α -diasterane a (20S)
D	Ts 18 α (H)-trisnorhopane	d	C ₂₈ β α -diasterane b (20S)
E	Tm 17 α (H)-trisnorhopane	e	C ₂₈ β α -diasterane a (20R)
F	C ₂₉ Tm 17 α (H)21 β (H)-norhopane	f	C ₂₈ β α -diasterane b (20R)
G	C ₂₉ Ts 18 α (H)-norneohopane	g	C ₂₇ $\alpha\alpha$ -cholestane (20S)
H	C ₃₀ 17 α (H)-hopane	h	C ₂₇ β β -cholestane (20R)
I	C ₃₀ moretane	i	C ₂₇ β β -cholestane (20S)
J	C ₃₁ 17 α (H)-homohopane (22S)	j	C ₂₇ $\alpha\alpha$ -cholestane (20R)
K	C ₃₁ 17 α (H)-homohopane (22R)	k	C ₂₈ $\alpha\alpha$ -ergostane (20S)
L	C ₃₂ 17 α (H), 21 β (H)-30,31-bishomohopane (22S)	l	C ₂₈ β β -ergostane (20R)
M	C ₃₂ 17 α (H), 21 β (H)-30,31-bishomohopane (22R)	m	C ₂₈ β β -ergostane (20S)
		n	C ₂₈ $\alpha\alpha$ -ergostane (20R)
		o	C ₂₉ $\alpha\alpha$ -stigmastane (20S)
		p	C ₂₉ β β -stigmastane (20R)
		q	C ₂₉ β β -stigmastane (20S)
		r	C ₂₉ $\alpha\alpha$ -stigmastane (20R)

4.3.4.2 GC-MS

Gas chromatography was performed using a Mega Series HRGC 5160 gas chromatograph (Carlo Erba, IT) equipped with a 30 m x 0.25 mm x 0.25 μ m film Zebron ZB-5_MS fused silica capillary column. For specific detection a quadrupol mass spectrometer Trace MS (Thermoquest) was used. 1 μ l of sample was injected by split injection at 80°C. After 3 min isothermal hold, temperature was first increased by 10°C/min up to 160°C, followed by a further temperature increase by 3°C/min up to 320°C, which was held for 20 min. Helium was used as carrier gas with a velocity of 30 cm/s. Hydrocarbons were detected by single ion mode (EI+, 70 eV, measured m/z = 191, 205, 217, 218, 259, 372, 386, 400, 412) with a source temperature of 200°C.

The identification of hopanes and steranes is based on a CHIRON reference standard (Hopane/Sterane Calibration Mix) and by comparison with other reference material. For peak quantification the *Xcalibur* software (ThermoFinnigan) was used. The identified peaks for both hopanes and steranes used in this work for calculated ratios and their respective measured m/z ratios are listed in Table 4.2.

The ratio of steranes to hopanes was calculated according to Peters et al. (2005) by the ratio of C₂₇-C₂₉ regular steranes to C₂₉-C₃₀ 17 α hopanes.

4.4 Results

4.4.1 Elemental analysis and Rock-Eval pyrolysis

Results of the elemental analysis are shown in Figure 4.3 and listed in Table 4.3. TOC contents of the investigated samples range from 0.1 to 9.3 wt.% with an average of 0.83 wt.% with exception of Santonian and Campanian to Maastrichtian samples, where the TOC contents are consistently low, close to the average of 0.25 wt.%. The highest TOC contents are observed in samples of Bartonian to Priabonian age with an average of 4.8 wt.%.

Table 4.3 Results of the elemental analysis and Rock-Eval pyrolysis. TOC = Total Organic Carbon, TIC = Total Inorganic Carbon, TS = Total Sulfur, T_{max} = temperature at the peak of S2, HI = Hydrogen Index (S2/TOC x 100), OI = Oxygen Index (S3/TOC x 100), [---]: not determined. (Table continue on next page...)

Sample	TOC [wt.%]	TIC [wt.%]	TS [wt.%]	S1 [mg HC/g rock]	S2 [mg HC/g rock]	S3 [mg CO ₂ /g rock]	T _{max} [°C]	HI [mg HC/g TOC]	OI [mg CO ₂ /g TOC]
15/892	0.48	5.07	0.17	0.02	0.12	1.31	260	25	273
15/893	0.76	8.02	0.19	0.02	0.17	1.32	260	22	174
15/894	0.96	3.55	0.2	0.02	0.20	1.29	391	21	134
17/1679	5.43	9.20	0.03	0.77	25.23	4.94	415	465	91
15/863	7.12	9.32	1.04	0.63	36.35	1.46	416	511	20
17/1680	5.84	8.99	1.05	0.72	27.67	5.36	415	474	92
17/1681	7.39	8.65	0.99	0.33	24.69	3.69	412	334	50
15/864	7.23	9.42	1.09	0.39	35.74	1.47	412	494	20
17/1682	7.19	8.51	0.15	0.32	27.02	2.11	415	376	29
15/865	9.33	8.68	1.16	0.68	49.70	3.00	413	532	32
17/1683	4.34	5.05	0.66	0.30	11.68	1.60	423	269	37
15/866	3.99	6.20	0.67	0.31	17.72	1.42	421	444	36
15/867	3.55	6.37	0.54	0.18	14.29	1.48	416	402	42
17/1685	4.88	5.79	0.58	0.16	10.24	2.77	415	210	57
17/1686	4.07	4.24	0.62	0.20	11.87	1.66	422	292	41
15/868	3.73	5.25	0.69	0.16	16.87	1.45	421	452	39
15/869	5.08	9.97	0.84	0.18	27.79	1.43	421	547	28
17/1687	6.20	8.22	1.01	0.19	22.52	2.31	416	363	37
15/870	6.16	9.16	0.98	0.24	31.60	1.40	416	513	23
17/1688	4.92	8.69	0.95	0.28	22.56	4.08	415	459	83
15/871	5.85	9.44	0.98	0.22	30.68	1.45	419	524	25
17/1689	4.31	9.09	0.68	0.17	15.69	1.74	420	364	40
15/872	4.80	10.00	0.66	0.17	24.73	1.43	419	515	30
15/873	4.99	9.89	0.78	0.17	25.43	1.43	416	510	29
17/1690	3.80	9.52	0.63	0.17	15.94	3.57	419	419	94
15/874	4.57	10.45	0.59	0.27	23.77	1.51	415	520	33
17/1691	3.13	7.65	0.65	0.22	7.67	1.47	425	245	47
17/1692	0.70	10.32	0.23	0.06	0.64	0.79	423	91	112
15/875	1.19	10.61	0.31	0.07	3.33	1.25	422	280	105
17/1693	1.63	9.34	0.27	0.08	3.49	1.11	428	214	68
15/876	2.35	7.79	0.36	0.15	8.70	1.50	424	370	63
17/1694	1.58	4.65	0.31	0.11	4.12	1.45	421	261	91
15/877	0.67	9.71	0.26	0.04	0.49	1.33	420	73	199
17/1696	0.96	6.81	0.30	0.04	0.45	1.84	423	46	192
17/1698	0.46	10.00	0.20	0.03	0.45	0.66	424	97	143
17/1699	0.58	10.28	0.20	0.03	0.43	0.80	423	74	139
17/1700	0.56	10.04	0.17	0.03	0.54	0.77	425	96	137
17/1701	0.22	1.52	0.11	0.00	0.10	0.74	426	45	332
17/1702	0.94	9.78	0.41	0.03	1.22	0.87	425	129	93
17/1703	0.81	9.80	0.32	0.04	0.75	0.82	426	92	101
17/1704	0.66	10.25	0.20	0.04	0.58	1.12	425	88	170
17/1705	0.33	10.30	0.22	0.00	1.05	1.38	425	318	418
17/1706	0.70	10.14	0.23	0.04	0.88	0.85	423	125	121
17/1707	0.09	10.61	0.16	0.00	0.21	0.75	424	233	833
17/1708	0.12	2.05	0.16	0.01	0.24	0.94	423	200	783
17/1709	0.75	10.58	0.24	0.05	1.07	1.08	424	143	144
17/1711	0.55	10.63	0.29	0.05	0.89	0.71	426	161	130
17/1712	0.40	10.14	0.28	0.04	0.44	0.84	421	110	211
17/1715	1.32	9.21	0.61	0.03	1.89	1.78	428	143	135
15/878	0.62	11.94	0.24	0.03	0.95	1.32	428	153	213
17/1717	0.64	10.95	0.27	0.07	0.71	0.90	429	111	140
15/879	0.70	11.55	0.27	0.04	1.18	1.35	429	169	193
15/880	0.96	11.06	0.30	0.05	1.71	1.36	428	178	142
15/881	0.71	11.78	0.25	0.04	1.09	1.37	427	154	193
17/1718	0.84	10.54	0.26	0.11	0.94	1.12	429	112	133
15/882	0.60	11.88	0.29	0.03	1.04	1.37	428	173	228
15/883	0.82	11.48	0.28	0.04	1.93	1.36	434	235	166
15/884	0.65	11.91	0.19	0.03	0.99	1.40	427	152	215
17/1720	0.09	11.25	0.12	0.00	0.08	0.97	421	89	107
17/1721	0.31	11.53	0.15	0.06	0.58	0.69	430	187	223
15/885	0.95	11.11	0.33	0.04	2.17	1.31	426	228	138
15/886	1.28	11.12	0.31	0.04	2.76	1.31	427	216	102
17/1722	0.58	10.52	0.33	0.01	1.72	1.24	426	297	214
15/887	0.81	10.26	0.32	0.03	1.16	1.35	428	143	167
17/1724	1.13	0.01	0.36	0.04	1.03	1.25	426	91	110
15/888	0.97	10.43	0.36	0.04	1.56	1.29	428	161	133
17/1726	1.45	9.67	0.47	0.03	2.29	1.79	428	158	123
15/889	1.75	10.39	0.43	0.06	4.25	1.30	430	243	74
17/1727	1.85	9.17	0.51	0.04	1.03	1.25	425	56	68
15/890	2.16	10.21	0.41	0.09	6.82	1.63	430	316	75
15/891	1.98	11.03	0.36	0.11	6.81	1.36	423	344	69
17/1729	0.73	10.28	0.22	0.04	0.65	1.03	426	89	142
17/1732	0.84	9.73	0.28	0.04	0.60	0.96	426	72	114
17/1733	0.14	10.71	0.15	0.02	0.36	0.79	425	257	564
17/1735	0.96	9.50	0.34	0.04	0.75	1.45	425	78	151
17/1736	0.30	9.69	0.41	0.00	0.42	1.02	424	140	340
17/1737	0.22	10.50	0.81	0.01	0.19	0.78	417	86	355
17/1738	0.82	9.10	0.81	0.04	0.55	1.03	422	67	125

Table 4.3 continued

Sample	TOC [wt.%]	TIC [wt.%]	TS [wt.%]	S1 [mg HC/g rock]	S2 [mg HC/g rock]	S3 [mg CO ₂ /g rock]	T _{max} [°C]	HI [mg HC/g TOC]	OI [mg CO ₂ /g TOC]
17/1740	0.94	8.90	0.55	0.09	0.68	1.22	421	130	130
17/1742	0.41	11.35	0.18	0.04	0.49	0.81	428	198	198
17/1743	0.47	9.45	0.36	0.03	1.11	1.74	426	236	370
15/895	3.72	9.40	0.27	0.07	9.41	1.54	423	253	41
17/1744	0.03	0.06	---	---	---	---	---	---	---
17/1745	0.70	9.19	0.18	---	---	---	---	---	---
17/1746	0.71	6.16	0.17	---	---	---	---	---	---
17/1747	0.91	7.41	0.17	---	---	---	---	---	---
17/1748	2.29	0.06	0.42	---	---	---	---	---	---
15/896	0.52	11.91	0.19	0.03	0.44	1.30	426	85	250
17/1749	0.48	10.81	0.19	0.03	0.44	1.30	421	59	156
17/1751	0.12	11.00	0.11	---	---	---	---	---	---
17/1752	0.23	11.37	---	---	---	---	---	---	---
17/1753	0.27	11.33	---	---	---	---	---	---	---
17/1754	0.20	11.50	---	---	---	---	---	---	---
17/1755	0.28	11.44	---	---	---	---	---	---	---
17/1756	0.15	11.63	---	---	---	---	---	---	---
17/1757	0.23	11.76	---	---	---	---	---	---	---
17/1758	0.18	11.08	0.16	---	---	---	---	---	---
17/1759	0.22	11.79	---	---	---	---	---	---	---
17/1760	0.27	11.77	---	---	---	---	---	---	---
17/1761	0.26	11.86	---	---	---	---	---	---	---
17/1762	0.04	12.49	---	---	---	---	---	---	---
15/897	0.63	12.15	0.22	0.04	2.19	1.34	427	348	213
15/898	0.95	12.24	0.19	0.06	2.57	1.28	425	271	135
15/899	2.04	11.80	0.36	0.18	9.91	1.58	419	486	77
17/1763	0.38	11.76	0.15	0.04	0.55	1.03	424	183	130
15/900	0.79	12.10	0.25	0.05	2.61	1.31	425	330	166
17/1764	0.88	10.91	0.21	0.08	2.71	0.72	422	308	82
15/901	1.00	12.55	0.22	0.06	3.36	1.30	424	336	130
17/1765	0.55	10.87	0.20	0.02	2.39	0.82	424	435	149
15/902	3.57	11.20	0.51	0.23	20.25	1.57	413	567	44
17/1766	2.48	9.96	0.61	0.16	13.08	2.16	414	527	87
15/903	3.62	10.82	0.54	0.19	20.98	1.57	414	580	43
17/1767	2.19	10.37	0.62	0.16	10.83	2.09	415	495	95
15/904	4.20	11.06	0.56	0.33	23.62	1.59	412	562	38
15/905	2.56	11.49	0.36	0.14	13.48	1.56	418	527	61
17/1768	0.32	11.91	0.13	0.05	0.67	0.54	422	208	169
15/906	2.04	11.58	0.38	0.11	10.61	1.58	416	520	77
17/1769	0.38	11.83	0.11	0.06	1.03	0.49	423	271	128
17/1770	0.36	11.25	0.12	0.02	1.42	0.55	423	394	153
17/1771	0.91	11.70	0.18	0.08	3.13	0.73	423	344	80
17/1772	0.37	11.85	0.10	0.05	1.04	0.47	424	283	128

TIC contents range from 1.4 to 11.9 wt.% with an average of 10.3 wt.%. Calculated carbonate contents show a weak negative correlation with TOC content (Fig. 4.3). Turonian to Santonian samples are (almost) pure carbonates. Some of these rocks contain dolomite rather than calcite; therefore, calculated CaCO₃ contents partly exceed 100%. Ypresian to Bartonian samples contain significant amounts of dolomite rhombs. Therefore, the carbonate content of these intervals was calculated assuming that the TIC content is mainly derived from dolomite. TS values range from 0.03 to 1.16 wt.% with an average of 0.3 wt.%. TS correlates positively with TOC (Fig. 4.3). TS/TOC ratios are low to moderate ranging from 0.01 to 3.66.

Rock-Eval results are shown in Figure 4.3 and listed in Table 4.3. Rock-Eval analysis revealed no meaningful results for the three Messinian, two Eocene to Miocene, and some Campanian and Santonian samples, probably due to oxidation of OM. The remaining 104 samples are marked by low S1 (0.00 to 0.77 mg HC/g rock), but intermediate S2 values (0.08 to 49.70 mg HC/g rock). Both parameters correlate positively with each other and also with their respective TOC content (Fig. 4.3). S3 values are low with only 0.47 to 5.36 mg CO₂/g rock. T_{max} values range from 412°C to 434°C.

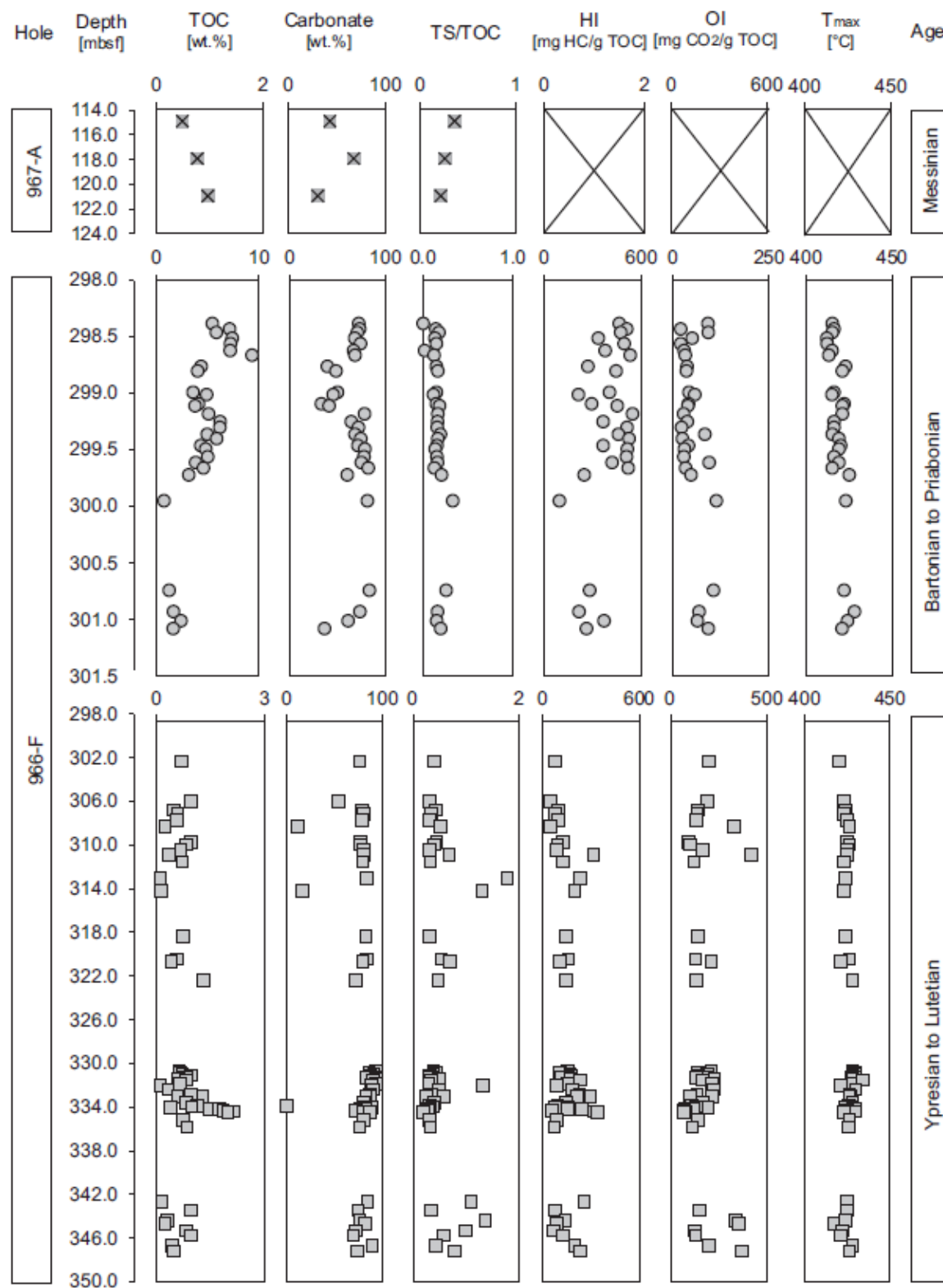


Fig. 4.3 Elemental analysis and Rock-Eval results of ODP Leg 160 core samples that originate from the Eratosthenes Seamount (ESM), southern offshore area of Cyprus. Note that scales vary in the different intervals. Big crosses mark intervals where no results were obtained. (figure continues on next page...)

HI values are relatively high, but vary strongly from 45 to 580 mg HC/g TOC with an average of 240 mg HC/g TOC. OI values vary from 20 to 833 mg CO₂/g TOC with an average of 152 mg CO₂/g TOC. Some extremely high OI values are probably caused by oxygen release from thermally unstable

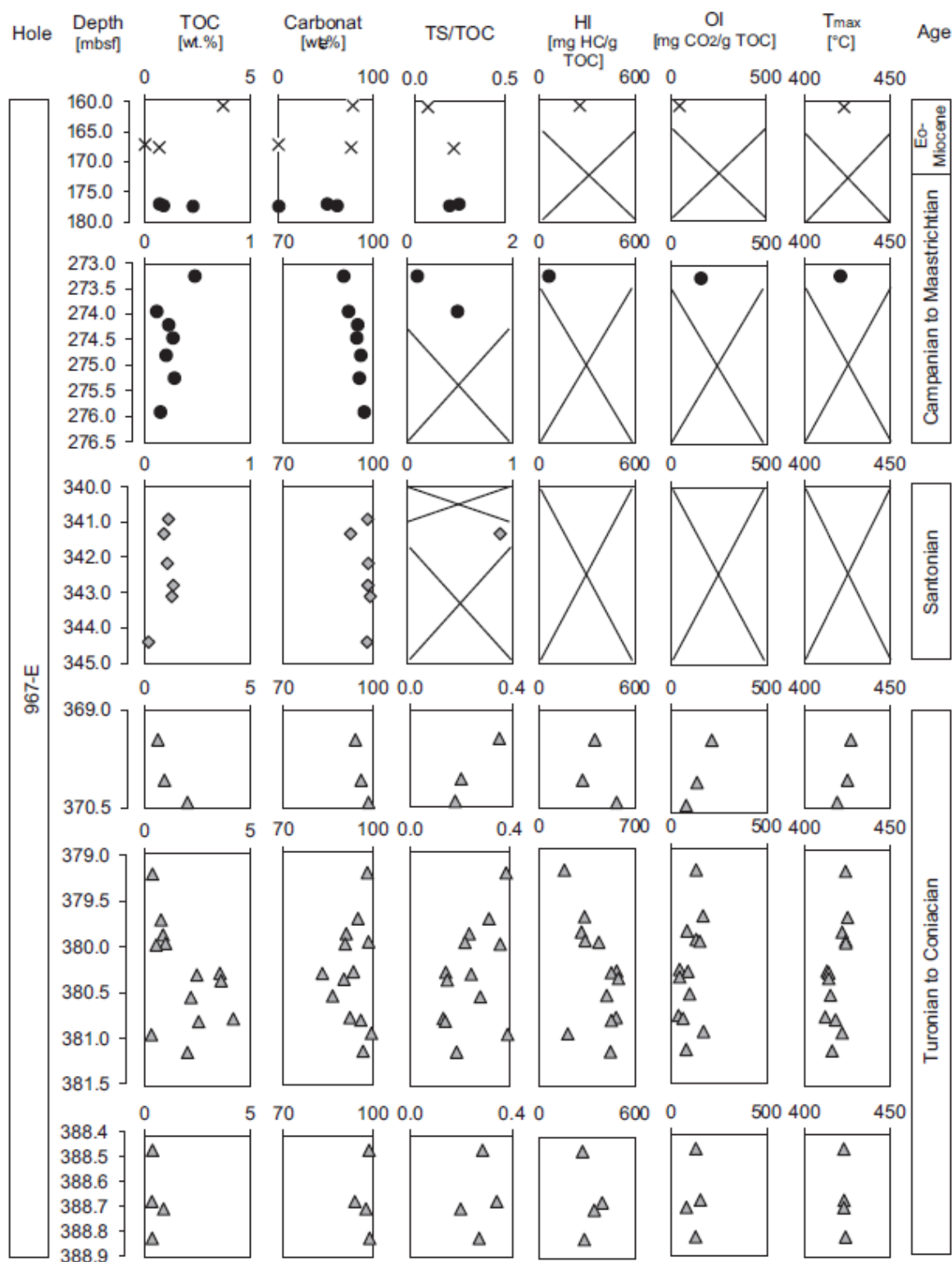


Fig. 4.3 continued.

carbonates (Katz, 1983). OI values correlate negatively with HI values. PI values are very low at 0.01 to 0.12. The two solid bitumen-impregnated samples do not show any significant difference, since the amount of solid bitumen compared to the whole bulk rock volume is very low.

Table 4.4 Comparison of bulk rock and HCl-treated samples. TOC = Total Organic Carbon, TIC = Total Inorganic Carbon, HI = Hydrogen Index ($S_2/TOC \times 100$), OI = Oxygen Index ($S_3/TOC \times 100$).

Sample	Age	TOC [wt.%]	TIC [wt.%]	HI [mg HC/g TOC]	OI [mg CO ₂ /g TOC]
106	Bartonian to Priabonian	7.39	8.65	334	50
106-HCl	Bartonian to Priabonian	31.96	0.12	568	40
110	Bartonian to Priabonian	4.88	5.79	210	57
110-HCL	Bartonian to Priabonian	9.52	0.04	407	39
121	Ypresian to Lutetian	0.96	6.81	46	192
121-HCl	Ypresian to Lutetian	2.31	0.01	159	50
137	Ypresian to Lutetian	0.4	10.14	110	211
137-HCl	Ypresian to Lutetian	2.7	0.02	252	50
188	Turonian to Coniacian	0.3	11.74	348	213
188-HCl	Turonian to Coniacian	5.1	0.03	432	36
192	Turonian to Coniacian	2.19	10.37	495	95
192-HCl	Turonian to Coniacian	23.54	0.09	592	33

The results of the HCl-treated samples are shown in Table 4.4. OI values decrease by a factor between 0.8 and 0.2, while HI values increase by a factor of 1.2 to 3.5 as compared to the bulk rock samples. The strongest mineral matrix effect is observed for samples with low TOC contents.

4.4.2 Petrographic analysis

Most samples, except the two solid bitumen-impregnated samples (15/891, 15/896), contain different macerals in varying amounts (Table 4.5). Vitrinite and inertinite particles occur rarely, are small-sized and often have highly structured surfaces (Fig. 4.4A and B) which hampered random vitrinite reflectance measurements. In contrast, liptinite (lamalginite and telalginite) is very abundant, varies in size and shows yellow-golden fluorescence after ultraviolet-violet light excitation (Fig. 4.4A and B, red arrows). The highest contribution of OM is made up of submicroscopic amorphous liptinites (Fig. 4.4A and B). Pyrite grain size is small and usually occurs in framboidal shape, but almost all samples also contain minor amounts of small, euhedral pyrite (Fig. 4.4C). Foraminifera, fish bones and/or shell fragments occur in all samples and are rather common (Table 4.5). Foraminifera often show recrystallization and blocky cement reduces the intraparticle porosity (classification after Choquette and Pray, 1970). Foraminifera abundance seems to correlate negatively with the OM content and pyrite (Table 4.5). Dolomite rhombs are very rare to absent in the Upper Cretaceous samples and abundant in the Eocene samples (Fig. 4.4B).

Table 4.5 Results from microscopic analysis: Qualitative amounts of analyzed feature (OM = total observable organic matter; V = vitrinite; I = inertinite L = liptinite; Foram = foraminifera; Py = pyrite; Dolo = dolomite) decreases from +++ to +; - indicates that the feature occurs only rarely or not at all.

sample	Age	OM	V	I	L	Foram	Py	Dolo
15/865	Bartonian to Priabonian	+++	++	-	++	+	++	-
15/871	Bartonian to Priabonian	+++	++	-	++	+	++	+++
15/886	Ypresian to Lutetian	++	+	-	+	++	+++	+++
15/890	Ypresian to Lutetian	+++	-	-	+	++	++	+
15/896	Campanian to Maastrichtian	+	-	-	-	+++	+	-
15/898	Turonian to Coniacian	+	-	-	-	++	-	-
15/899	Turonian to Coniacian	++	+	-	++	+++	+	+
15/904	Turonian to Coniacian	++	++	-	+++	++	+	-

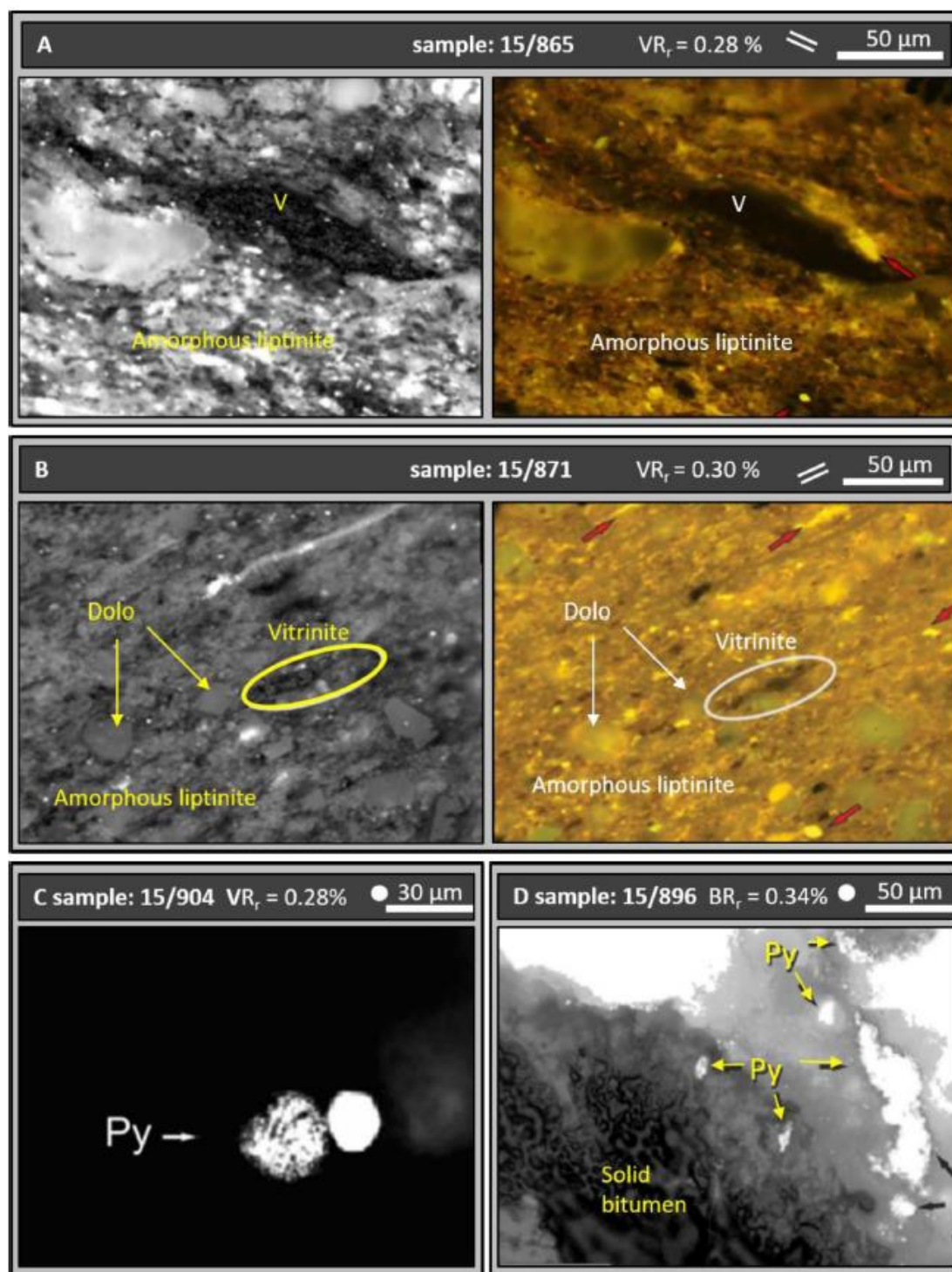


Fig. 4.4 Photomicrographs: || indicate bedding orientation. ● no bedding observable. A: Incident light (left) and ultraviolet light (right). Vitrinite particle with a highly structured surface surrounded by a fine grained matrix and amorphous liptinite. Red arrow marks a lam alginata. B: Incident light (left) and ultraviolet light (right). Vitrinite particle with structured surface (circle) surrounded by fine grained matrix, dolomite rhombs (Dolo), amorphous liptinite and different alginates (red arrows). C: Incident light. The typical occurrence of small framboidal and euhedral pyrite (Py). A large solid bitumen accumulation within a calcareous, organic-rich matrix. Large framboidal pyrite (Py) is observed around its border.

Table 4.6 Results from microscopic analysis: Qualitative amounts of analyzed feature (OM = total observable organic matter; V = vitrinite; I = inertinite L = liptinite; Foram = foraminifera; Py = pyrite; Dolo = dolomite) decreases from +++ to +; - indicates that the feature occurs only rarely or not at all.

Sample	Age	%VR _r	n	Std dev	T _{peak} [°C]
15/865	Bartonian to Priabonian	0.28	52	0.06	33
15/871	Bartonian to Priabonian	0.25	48	0.03	24
15/886	Ypresian to Lutetian	0.30	11	0.03	39
15/890	Ypresian to Lutetian	0.24	3	0.01	20
15/899	Turonian to Coniacian	0.29	22	0.05	36
15/904	Turonian to Coniacian	0.28	31	0.07	33

The solid bitumen-impregnated samples do not contain any vitrinite or inertinite and almost no liptinite. Here, foraminifera are abundant. Solid bitumen occurs as accumulation in cavities and with locally large framboidal pyrite in its close vicinity (Fig. 4.4D).

For 6 samples the vitrinite reflectance could be measured (Table 4.6). However, in only four samples more than 20 vitrinite particles could be measured to generate reliable results (see Barker and Pawlowicz 1993) (Table 4.6). Measured VR_r ranges from 0.25% to 0.3%. Counts and mean values of vitrinite reflectance are listed in Table 4.6.

T_{peak} derived from initial vitrinite reflectance measurements (Table 4.6) ranges from 20 to 39°C for the vitrinite-containing samples indicating that sediments have not reached much higher temperatures or burial depths than at present-day.

4.4.3 Molecular geochemistry

Based on the low thermal maturity as it is indicated by low vitrinite reflectance and Rock-Eval T_{max} values, only aliphatic hydrocarbon fractions were analyzed. Three types of aliphatic distributions were observed: (1) samples showing a clear predominance of medium-chain *n*-alkanes (*n*-C₁₂ – *n*-C₂₀) with almost no long-chain molecules (Fig. 4.5 A); (2) samples showing a predominance of medium-chain *n*-alkanes over abundant long-chain *n*-alkanes (*n*-C₂₀ – *n*-C₃₅) that can even reach tendencies of bimodal distribution (e.g. 15/899; Fig. 4.5B); (3) two exceptions are samples 15/892 and 15/888 which are characterized by a skewed distribution over the full range of detected *n*-alkanes (*n*-C₁₂ – *n*-C₃₅), with a decreasing frequency of shorter/longer chain molecules, respectively. There is no clear correlation between stratigraphy and the type of *n*-alkanes distribution.

Calculated geochemical ratios are shown in Table 4.7. Pristane (Pr)/phytane (Ph) ratios vary between 1.0 and 1.6 with the exception of one Messinian (15/892), one Bartonian to Priabonian (15/868) and one Ypresian to Lutetian (15/888) sample with ratios of 0.50, 0.49 and 0.83, respectively (Table 4.7). Pr/*n*-C₁₇ ratios scatter within a narrow range from 0.24 to 0.54, while Ph/*n*-C₁₈ ratios shows slightly more variability with values between 0.31 and 0.90. TAR values range between 0.06 and 0.69, while only the Messinian sample (15/892) shows a significantly higher value of 1.41. OEP ratios vary between 0.74 and 1.20 and CPI ratios between 0.88 and 1.59, with the majority being above one (Table 4.7).

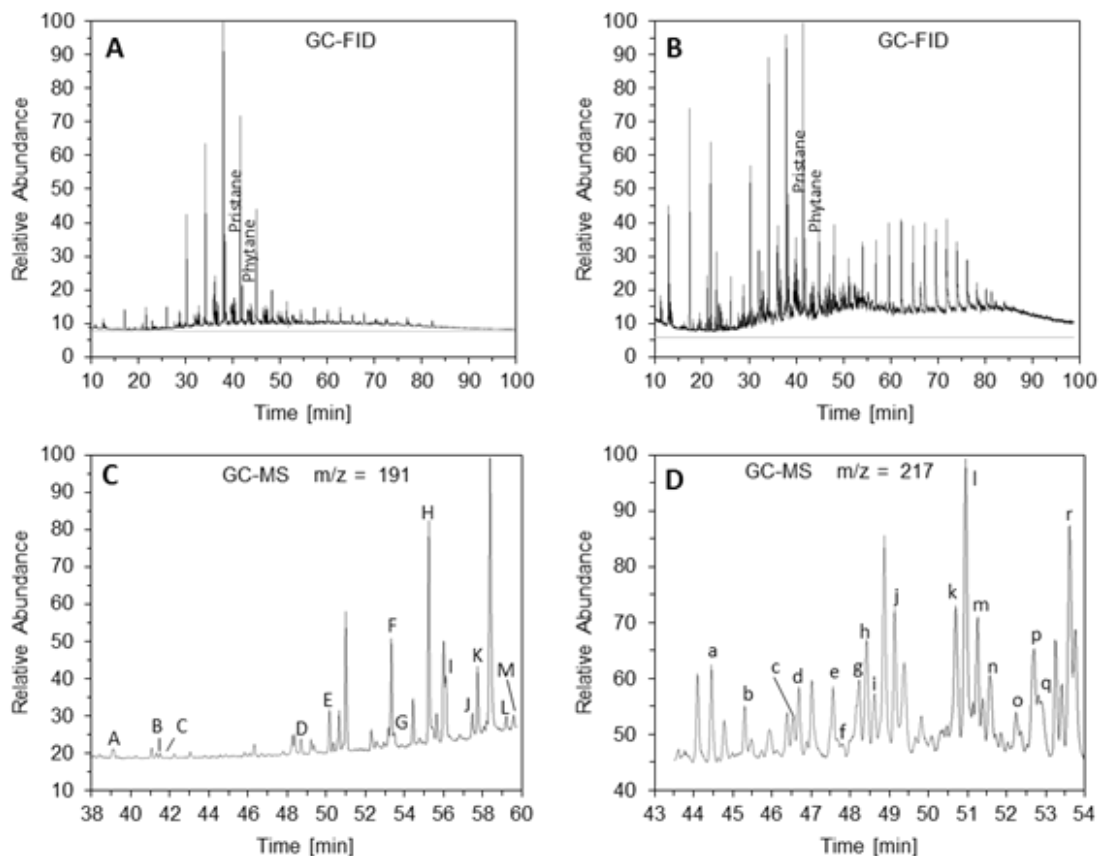


Fig. 4.5 Representative gas chromatographs for the aliphatic hydrocarbon fraction (A) Sample 15/906 shows a clear predominance of medium-chain *n*-alkanes (*n*-C₁₂–*n*-C₂₀) with almost no longer chain molecules. (B) Sample 15/899 illustrates a predominance of medium-chain *n*-alkanes over abundant long-chain *n*-alkanes (*n*-C₂₁–*n*-C₃₅). (C) Partial *m/z* 191 mass fragmentograms showing hopane distributions for sample 15/890. (D) Partial *m/z* 217 mass fragmentograms showing sterane distributions for sample 15/872. Peak identifications are provided on Table 4.2.

Biomarker ratios could be evaluated for 9 of the 12 measured samples. Results are shown in Table 8. Figure 5 provides representative chromatograms (Fig. 4.5 A & B) as well as ion traces (Fig. 4.5 C&D) for hopane (*m/z* = 191) and sterane (*m/z* = 217) identification (see also Table 4.2). The concentration of C₂₈ βαα-steranes is relatively constant for all samples with 35±11% on average. C₂₇ and C₂₉ βαα-steranes concentrations show a slightly larger variation (37±17% and 29±18%, respectively) and seem to be inversely proportional to each other. The Eocene samples (Ypresian to Lutetian and Bartonian to Priabonian) show slightly higher C₂₉ concentrations compared to Turonian to Coniacian and Messinian samples (Fig. 4.6).

The C₃₀ norhopane/hopane ratios are all greater than 1 with the highest value reaching 0.8 in the Messinian. C₂₆/C₂₅ tricyclic terpanes were only evaluated in the Ypresian to Lutetian, the Bartonian to Priabonian and the Messinian samples, varying between 0.68 and 0.95, except for the Messinian with a ratio of 0.13 (Table 4.8). C₃₁R/C₃₀ hopane ratio is generally smaller than 1 with exception of one Bartonian to Priabonian sample (15/872) with a value of 1.42 (Table 4.8). The ratio of steranes over

Table 4.7 Molecular geochemical ratios from GC-FID analysis. Pr = pristane, Ph = phytane, TAR = terrigenous/aquatic ratio, OEP = Odd Even Predominance, CPI = Carbon preference Index.

Sample	Age	Pr/Ph	Pr/n-C ₁₇	Ph/n-C ₁₈	TAR	OEP	CPI
15/892	Messinian	0.50	0.53	0.89	1.41	0.74	0.88
15/895	Eocene to Miocene	1.30	0.50	0.51	0.10	0.76	1.38
15/864	Bartonian to Priabonian	1.49	0.24	0.31	0.07	0.83	1.23
18/867	Bartonian to Priabonian	1.58	0.37	0.49	0.13	1.07	1.41
15/868	Bartonian to Priabonian	0.49	0.33	0.90	0.69	1.16	1.59
15/872	Bartonian to Priabonian	1.25	0.25	0.39	0.22	1.04	1.58
15/888	Ypresian to Lutetian	0.83	0.52	0.73	0.39	0.88	1.29
15/890	Ypresian to Lutetian	1.41	0.36	0.39	0.11	0.85	1.03
15/899	Turonian to Coniacian	1.48	0.54	0.49	0.56	1.11	1.13
15/902	Turonian to Coniacian	1.17	0.38	0.50	0.32	1.20	1.58
15/903	Turonian to Coniacian	1.00	0.31	0.41	0.20	0.99	1.29
15/906	Turonian to Coniacian	1.49	0.32	0.31	0.06	0.94	0.94

Table 4.8 Various biomarker ratios from GC-MS analysis. [---]: not determined.

Sample	Age	Steranes					Hopanes				
		$\beta\alpha\alpha S + \beta\alpha\alpha R$ Steranes %			C ₂₉ Steranes		Steranes/Hopanes	Ts/(Ts+Tm)	C ₃₀ Norhopane/Hopane	Tricyclic terpanes C ₂₃ /C ₂₅	C ₃₁ R/C ₃₀ Hopane
		C ₂₇	C ₂₈	C ₂₉	$\alpha\alpha\alpha$ - 20S/(20S + 20R)	regular- $\alpha\beta\beta/(\alpha\alpha\alpha + \alpha\beta\beta)$					
15/892	Me.	41	30	29	0.34	0.50	0.61	0.08	0.80	0.13	0.39
15/864	B-P	31	33	36	0.14	0.33	0.19	0.33	0.24	0.90	0.28
15/867	B-P	29	30	41	0.05	0.37	0.47	0.25	0.30	0.95	0.32
15/872	B-P	20	46	35	0.14	0.36	0.20	0.29	0.24	0.70	1.42
15/890	Y-L	29	24	47	0.03	0.08	1.36	0.25	0.42	0.68	0.32
15/899	T-C	53	35	12	0.22	0.43	1.63	---	0.56	---	---
15/902	T-C	38	35	27	0.24	0.42	1.00	0.50	0.50	---	0.61
15/903	T-C	38	40	22	0.16	0.38	0.76	0.41	0.48	---	0.68
15/906	T-C	37	39	24	0.24	0.43	0.78	0.43	0.47	---	0.44

hopanes varies between 0.76 and 1.63 in the Turonian to Coniacian and the Ypresian to Lutetian samples and between 0.19 and 0.61 for the Bartonian to Priabonian and the Messinian samples (Table 4.8).

Thermal maturity parameters such as C₂₉ $\alpha\alpha\alpha S_{20}/(20S+20R)$ -, or C₂₉ $\alpha\beta\beta/(\alpha\alpha\alpha + \alpha\beta\beta)$ steranes, and Ts/(Ts+Tm) are all ≤ 0.5 indicating OM of low thermal maturity.

4.5 Discussion

4.5.1 Depositional environment

The 122 analyzed samples of Late Cretaceous to Messinian age are mainly dominated by argillaceous carbonates to almost pure limestones (12 to 99 wt.% carbonate), revealing a high variability in their organic content (0 to 9.3 wt.%) (Fig. 4.3). Samples enriched in OM are mainly attributed to the Eocene (especially to the Upper Eocene, Bartonian to Priabonian) and to the Lower Upper Cretaceous (Turonian to Coniacian) intervals. Petrographic investigations show that the OM in these rocks is mainly composed of alginites and submicroscopic organic matter, which are typically derived from marine

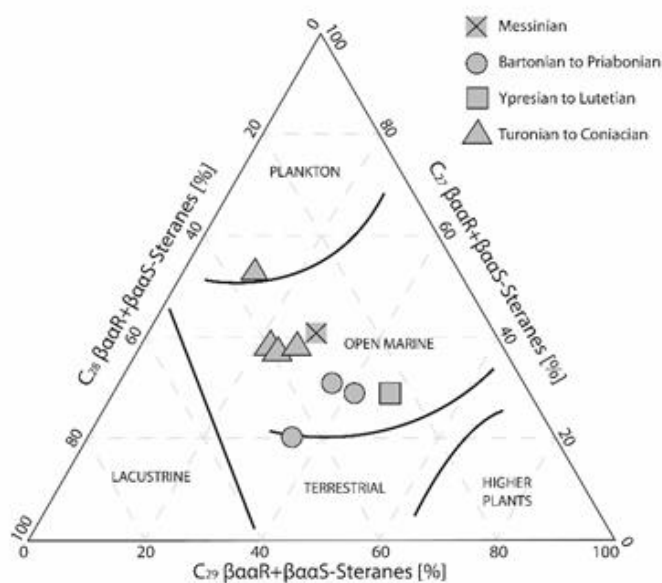


Fig. 4.6 C_{27} to C_{29} $\beta\alpha$ sterane distribution indicating an open marine environment as source for the OM. Eocene samples (Bartonian to Priabonian and Ypresian to Lutetian) show a slightly higher concentration of C_{29} $\beta\alpha$ sterane concentrations. Paleoenvironmental and source interpretation after Hatem et al. (2016) (modified after Huang and Meinschein, 1979).

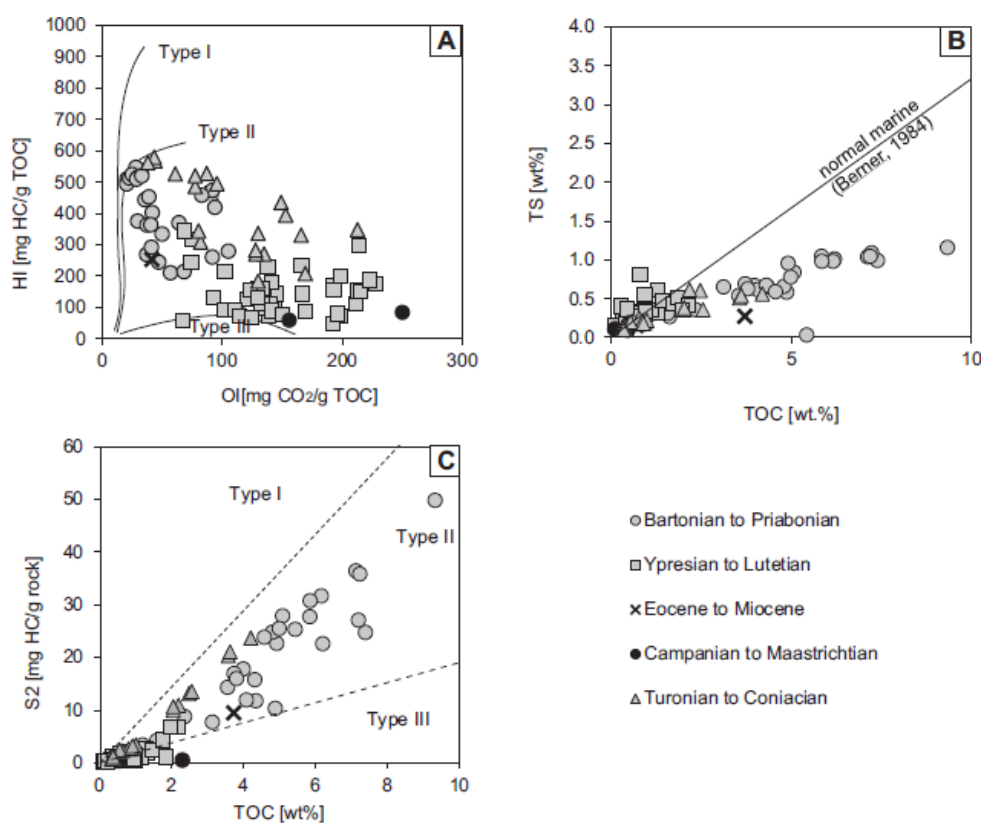


Fig. 4.7 (A) The samples in the pseudo van Krevelen diagram scatter from Type II to Type III. (B) In the TOC vs. S_2 diagram, most samples plot within the Type II area. (C) All samples in the TOC- S_2 diagram show a positive correlation but plot below the normal marine line derived from Berner (1984) indicating a lack of iron to precipitate pyrite.

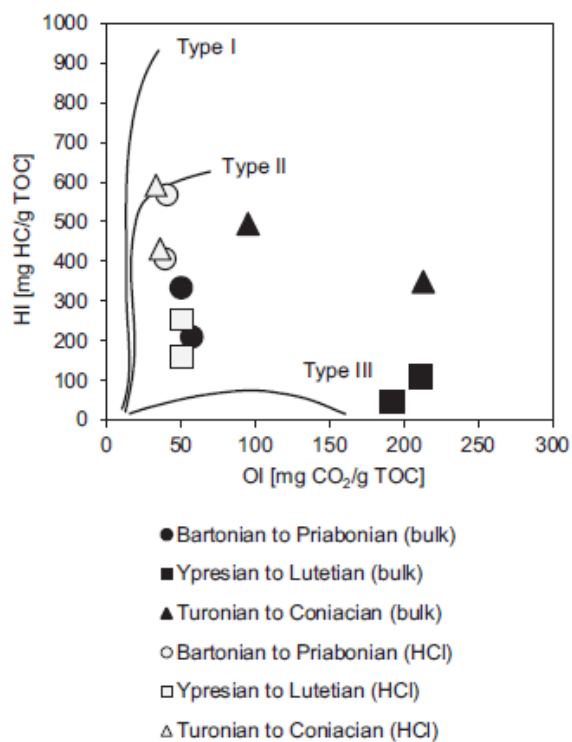


Fig. 4.8 Comparison of bulk and HCl-treated samples in the pseudo van Krevelen diagram. OI values are decreased while HI values are increased. The effect is more prominent for low TOC samples (see Table 4.4).

carbonates (Katz, 1983). The first possibility is assumed to be less likely in this case, since petrographic analysis reveal mainly fresh, unaltered pyrite crystals, which are usually more vulnerable to weathering than OM (Littke, 1993). Alternatively, additional CO₂ generation seems to be a more reasonable explanation, as this effect is known for immature carbonates (Katz, 1983), which are supposed to be present in the analyzed samples. Furthermore, this interpretation is supported by the Rock-Eval results repeated on the HCl-treated samples. As illustrated in Figure 8, these HCl-treated samples have lower OI and higher HI values, show less scattering and plot closer to the Type II kerogen pathway compared to the respective untreated samples. Therefore, results might be inaccurate for low mature, carbonate-rich samples analyzed by bulk rock Rock-Eval pyrolysis only. Although this is the standard technique applied in petroleum exploration, we recommend here to perform Rock-Eval pyrolysis directly on HCl-treated samples to avoid possible bias in the results.

The clear predominance of marine over terrestrial OM is expected based on the rather isolated position of the ESM at present and also during its past, not favoring any large-scale deposition of terrestrial OM. The very rare terrestrial OM which could be observed might originate from the northern African margin, which was the closest landmass in the greater surrounding of the ESM during its past (Robertson et al., 2012). High amounts of clastic, terrestrial material were shed into the Eastern Mediterranean basins by the Nile Delta (Sestini 1989; Hawie et al., 2013a, Nader, 2014).

organisms. These observations are supported by several molecular-geochemical ratios such as TAR and Pr/Ph \ll 2, which are common in marine environments (Peters et al., 2007). Also the relative concentrations of C₂₇ to C₂₈ and C₂₉ $\beta\alpha\alpha$ -steranes (Fig. 4.6) match those observed in open marine environments (Peters et al., 2005).

In view of the predominance of marine OM, many of the analyzed samples show exceptional high OI values measured on bulk rock samples by Rock-Eval pyrolysis, causing a broad scatter between marine Type II and terrestrial Type III kerogen in the modified van Krevelen diagram (after Tissot and Welte, 1984) (Fig. 4.7A). A more clear correlation with Type II kerogen can be observed in the TOC vs. S₂ plot (Fig. 4.7B). This ambiguity can be either caused by oxidized OM or by additional CO₂ generation from the decomposition of

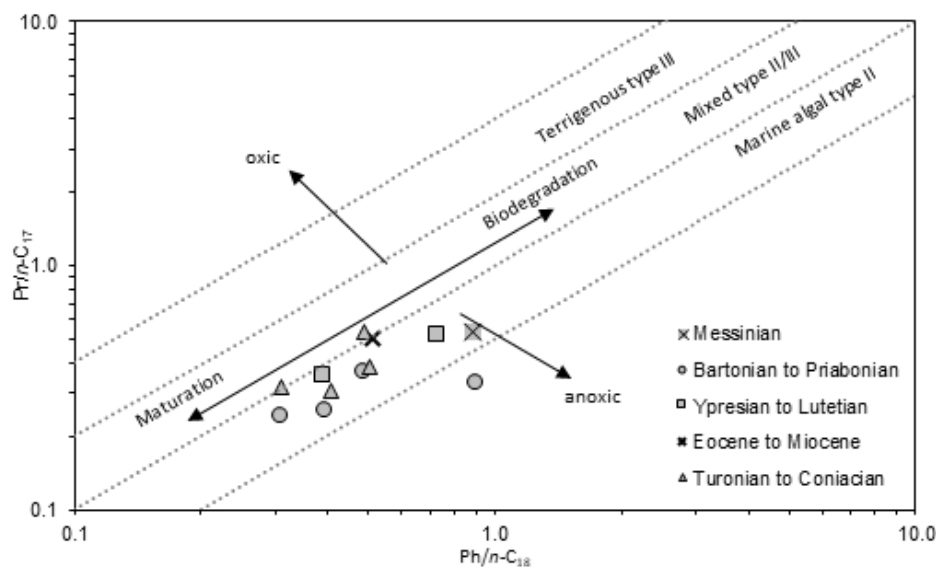


Fig. 4.9 Typical plot of Pr/n-C17 vs. Ph/n-C18 ratios for offshore Cyprus samples indicating marine organic matter deposited under mainly dysoxic conditions (modified from Hunt, 1995).

The positive correlation between TS and TOC (Fig. 4.7C) suggests a dependency of sulfate reduction on the availability of OM, which is usually the case in marine depositional environments. However, all samples plot below the "normal marine line" (Berner, 1984). This observation usually hints to fresh water environments. Sulfur is mainly incorporated into the sediment in the form of pyrite, which requires a distinct amount of reactive iron (Berner, 1984). In highly calcareous systems, such as the ESM, the availability of iron is usually low (Berner, 1984). This assumption is supported by low Fe concentrations which are observed along the ESM ($\ll 1000$ ppm, Emeis et al., 1996). This lack of reactive iron inhibits the formation of pyrite and, therefore, explains the unusual low TS values. Pr/n-C₁₇ vs Ph/n-C₁₈ ratios (Fig. 4.9) suggest a deposition and preservation of OM under dysoxic conditions. The presence of oxygen depleted, yet not completely anoxic bottom waters is further supported by C₃₀ norhopane/hopane ratios < 1 (Peters et al., 2007).

Until the Middle Eocene, the ESM was located within an open oceanic basin (Robertson et al., 2012). Therefore, water stagnation as a control of oxygen depletion, as it is often attributed to restricted basins (Littke, 1993), seems to be highly unlikely for the pre-Eocene strata. Thus, redox conditions might have been controlled by events of increased bio-productivity in the photic zone above the ESM with subsequent export of OM to the seafloor which lead to oxygen depletion through microbial respiration and OM degradation. High bioproductivity leads in such cases to enhanced oxygen depletion and both higher quantities and better preservation of OM (e.g. Littke, 1993). Effects causing such an increased bioproductivity in marine environments may be attributed to upwelling systems, where uprising cold, nutrient-rich waters enhance primary productivity rates (Littke, 1993). High bioproductivity along the eastern Mediterranean shelf has already been documented for the Campanian-Maastrichtian and was attributed to an extensive upwelling system which cause extensive deposition of high quality source rocks (e.g. Bou Daher et al., 2015). However, extent and frequency of organic-rich

intervals on the ESM are rather low and the majority of the sediments show low or no organic matter content. Upwelling systems around seamounts are very sensitive and depend on a complex interplay of e.g. climatic conditions, wind and ocean currents, as well as sea level fluctuations. Thus, their occurrence can be limited to short periods, sometimes only few weeks or even days (Genin and Boehlert, 1985). Such a sensitive, rarely occurring event might have been responsible for the deposition of the present organic-rich intervals. Further, the zone of oxygen-depletion evolving along upwelling regions is quite narrow and located in the upper water column (Suess and Thiede, 1983). Therefore, the extent of the organic-rich intervals is expected to be limited to the surrounding of the ESM as it was shown for the Eastern Levant margin, where organic richness in Cretaceous sediments decreases towards the Levant Basin (Bou Daher et al. 2015).

According to the geochemical results, the Eocene intervals were also deposited under dysoxic conditions, supporting the idea of occasional upwelling-related enhanced bioproductivity being responsible for the deposition of the OM-rich intervals. However, the lateral distribution might extend further towards the surrounding basins. With the ongoing convergence and subduction of Afro-Arabia below the Eurasian plate, the Mediterranean basin became more and more restricted since the Mid-Eocene by narrowing its connection to the Indian Ocean in the east with the final closure and isolation in the Early-Middle Miocene (Robertson et al., 2012). This isolation might have favored the evolution of water stagnation and anoxic bottom waters in the deeper parts of the basin. Thus, primary deposition and/or redeposition of the Upper Eocene intervals (e.g. mass transport deposits such as turbidities) might have led to the deposition and preservation of organic-rich intervals also towards the deeper parts of the basins.

4.5.2 Source rock potential and thermal maturity

Based on the TOC vs. S₂ classification by Peters et al. (2005) and a critical threshold value of 0.3 wt.% TOC for calcareous source rocks (Hunt, 1967) the petroleum generation potential for 46 of the 122 analyzed samples is of at least fair quality (Fig. 4.10). These samples belong mainly to the Turonian to Coniacian intervals containing OM of fair to very good quality (averages: TOC = 0.93 wt.%, S₂ = 2.92 mg HC/g rock, HI = 319 mg HC/g TOC), and the Bartonian to Priabonian samples, which even reach very good to excellent OM quality (averages: TOC = 4.8 wt.%, S₂ = 22.52 mg HC/g rock, HI = 469 mg HC/g TOC). The OM in these rocks is mainly composed of oil-prone Type II kerogen. As mentioned before, Rock-Eval results obtained from untreated immature carbonate samples have to be interpreted with caution as they might lead to an overestimation of the OI values and underestimation of the HI values. Therefore, the quality of OM and the actual source rock potential might be misinterpreted if only based on low mature, carbonate-rich whole bulk rock samples.

All analyzed intervals are thermally immature as it is implied by low S₁ peaks, PI values below 0.1, low T_{max} values of 412°C to 434°C, low VRr of 0.26% to 0.28% and the golden-yellow fluorescence

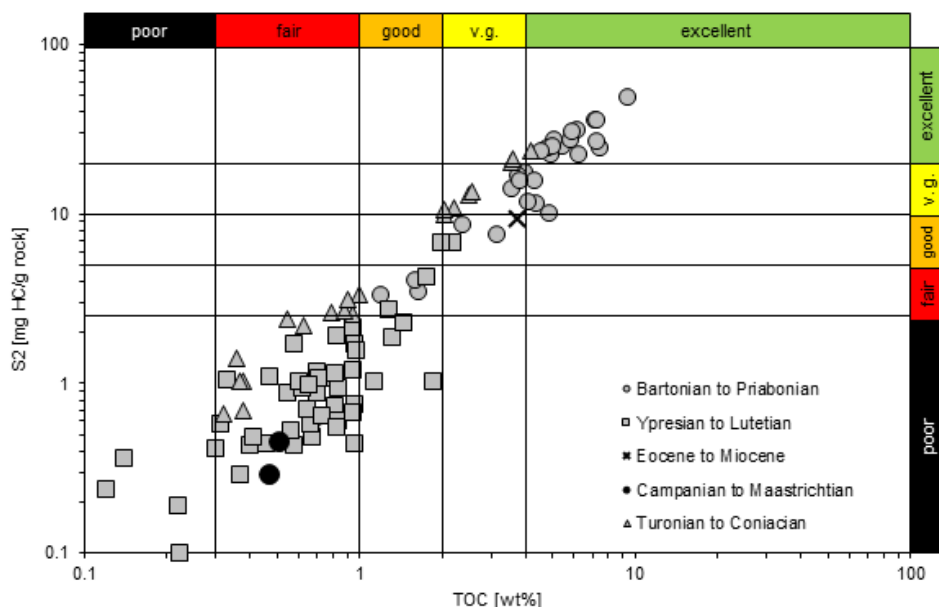


Fig. 4.10 Source rock potential and thermal maturity evaluation based on the TOC vs. S2 classification.

of alginite macerals (Hunt, 1995; Peters, 1986, Peters et al., 2005). These results are further supported by several biomarker ratios such as $Ts/(Ts + Tm) < 0.5$ or the ratio $20S/(20S + 20R)$ $\alpha\alpha\alpha$ -steranes < 0.34 . Maturity differences are too small, so no clear trend of maturity indicators with relative age could be observed. High HI values, especially in the Lower Upper Eocene (Turonian to Coniacian) and Upper Eocene (Bartonian to Priabonian) intervals indicate high potential of yet to be cracked hydrocarbon (HC). However, thermal maturity and HC contribution to working petroleum systems might be enabled for Upper Eocene intervals in deeper parts of the basins (see section 4.4.1), where deeper burial depths of up to 5 km are reached (Montadert et al., 2014).

4.5.3 Implications for petroleum systems

Today, the major gas fields in the Levant Basin, either located in Miocene clastic turbidite reservoirs (e.g. Tamar, Leviathan, Aphrodite) or in Mesozoic shallow water carbonates (Zohr) mainly comprise natural gas of biogenic origin (e.g. Feinstein et al., 2002, Schenk et al., 2010; Bertello et al., 2016). Nevertheless, many reservoirs containing also thermogenic HC accumulations have been proven along the Nile Delta, which are probably charged by mature source rocks of Mid Jurassic to Pre Messinian age. (e.g. Aal et al., 2000; Vandré et al., 2007). Triassic source rocks are known to have sourced oil and gas reservoirs in Syria and Iraq (May, 1991; Lie et al., 2011). Along the eastern Levant margin offshore Israel, thermogenic gas has been proven in Jurassic and Lower Cretaceous intervals (Feinstein et al., 2002). Furthermore, the presence of thermogenic petroleum systems at the eastern margin of the Levant Basin is also indicated by asphalt shows in Upper Cretaceous intervals onshore Lebanon (Nader, 2014). Bou Daher et al (2016) and Nader et al. (2018) have shown that source rocks

of Jurassic-Cretaceous and Cretaceous-Oligo-Miocene age might have reached thermal maturity along the Levant Margin and the deeper parts of the Levant Basin.

For the present study area (offshore Cyprus), potential source rock intervals were proven in the Lower Upper Cretaceous and the Upper Eocene. These immature intervals identified here could be considered as a potential source of biogenic gas, which is produced at shallow burial depths (e.g. Rice and Claypool, 1981; Stolper et al., 2014). Furthermore, the presence of thermally mature source rocks in the sedimentary cover of the ESM or its surrounding is indicated by solid bitumen staining, which could be observed in one Lower Eocene (Ypresian to Lutetian) and one Upper Cretaceous (Campanian) sample. . VR_r reflectance of overlying and underlying sampled intervals is low (0.25% to 0.3%; Table 4.6) and refers to an experienced T_{peak} temperature of only 20°C to 36°C, which is in accordance with present-day burial and temperature conditions. Therefore, these solid bitumens must be derived from deeper buried source rocks, since the thermal maturity in the sampled intervals is too low to allow oil generation. Such mature source rocks might occur, as mentioned above, in deeper parts of the basins or probably in older Mesozoic units, which were not drilled and, therefore, could not be investigated. Nevertheless, as outlined above, onshore investigations have identified several events of source rock deposition in the sedimentary succession along the eastern and southern Levant margin, which might extend towards the deeper Levant Basin. Although the basin ward extent of potential source rocks is unknown, the study conducted by Roberts and Peace (2007) on oil seepage in the Eastern Mediterranean Sea indicates HC generation and potential prospects along the northwestern, northern and southwestern flanks of the ESM. On several seismics e.g., flat spots can be observed which indicate gas accumulations in Upper Cretaceous anticlinal structures (Roberts and Peace, 2007) and, therefore, imply the presence of thermally mature Mesozoic source rocks within the basin.

At the same time, the presence of cavities filling solid bitumen in the immature, otherwise organic-poor samples further demonstrate the existence of a pore interconnectivity allowing hydrocarbon migration from deeper, thermally mature regions up to these shallow intervals. Most investigated samples contain few pyrite grains, but in the vicinity of the solid bitumen accumulations large framboidal pyrite clusters occur (Fig. 4.4). This is an indicator of fluid migration through these rocks at temperatures lower than approximately 80°C, suitable for sulphate reducing, bacterial activity (e.g. Cord-Ruwisch et al., 1987; Schauder and Kröger, 1993). Fluid mobility may also have been enhanced during extensive dissolution of minerals by meteoric water flushing during the subaerial exhumation of the ESM at times of the Messinian Salinity Crisis (MSC) providing potential HC migration pathways.

Potential reservoir structures might be found in turbidites derived from the basin margins and the Nile Cone Delta or within the karstified Mesozoic to Cenozoic carbonates of the ESM (such as Zohr and Calypso). These reservoirs would be sealed by thick Messinian evaporites and trapped by abrupt facies changes along the ESM margins that are inferred from seismic data (Montadert et al., 2014, Papadimitriou et al., 2018).

4.6 Conclusion

The geochemical and petrological data of 122 investigated samples of Late Cretaceous to Messinian age presented in this study adds valuable information on source rock intervals to the underexplored deep water frontier area of the Eratosthenes Seamount (ESM), offshore Cyprus:

- The analyzed samples comprise mainly argillaceous carbonates to pure limestones (12 to 99 wt.% carbonate) with highly varying amounts of marine Type II kerogen (0 to 9.3 wt.% TOC).
- TS/TOC and several biomarker ratios indicate deposition and preservation of OM under dysoxic conditions, which were probably reached during rare and short upwelling events.
- Promising source rock intervals were mainly deposited in the Lower Upper Cretaceous (Turonian to Coniacian; averages: TOC = 0.93 wt.%, HI = 319 mg HC/g TOC) and in the Upper Eocene (Bartonian to Priabonian; averages: TOC = 4.8 wt.%, HI = 469 mg HC/g TOC), and are of fair to good and good to excellent quality, respectively. However, determination of their vertical extent is inhibited by a low core recovery rate.
- Rock-Eval analysis of HCl-treated samples showed here that the kerogen quality might be underestimated if based on bulk rock observations only.
- The Upper Eocene source rocks might continue towards the basins center, if anoxic bottom waters evolved during the isolation of the Eastern Mediterranean since the Mid-Eocene.
- All analyzed samples are immature. However, the presence of thermal mature source rocks in the sedimentary cover of the ESM or its surrounding is indicated by solid bitumen staining, which could be observed in Lower Eocene intervals.
- Karstified Late Cretaceous to Cenozoic carbonates on the ESM or turbidities along its slope might provide potential reservoir structures, which would be sealed by Messinian salt.

Acknowledgements

The authors express their gratitude to the International Ocean Discovery Program and its core repository team in Bremen for granting the access to the ODP Leg 160 cores. The authors would like to thank as well Ms. Lesche for assistance during laboratory analyses at RWTH Aachen. Two anonymous reviewers are also thanked for providing detailed and constructive comments on an earlier draft of this manuscript.

5 Geochemical and petrographic investigation of Triassic and Late Miocene organic-rich intervals from onshore Cyprus, Eastern Mediterranean

An edited version of this chapter was peer-reviewed published as: Grohmann, S., Romero-Sarmiento, M.F., Nader, F.H., Baudin, F., Littke, R. (2019). Geochemical and petrographic investigation of Triassic and Late Miocene organic-rich intervals from onshore Cyprus, Eastern Mediterranean. International Journal of Coal Geology 209, 94-116.

Abstract

In order to improve the understanding of potential petroleum systems in the still underexplored Eastern Mediterranean Sea, two field campaigns were performed to investigate for potential source rocks onshore Cyprus. Elemental data (total organic (TOC) and inorganic carbon (TIC), total sulfur (TS), Fe, Ni, V), Rock-Eval[®] pyrolysis, biomarker and microscopic analysis (organic petrography, random vitrinite reflectance (VR_r), palynofacies) of the obtained Mesozoic to Cenozoic samples have proven the existence of organic matter (OM) rich deposits within the following two geological formations:

(1) The Triassic Vlambouros Formation (Fm.) of the Mamonia Complex comprises frequently occurring, few centimeter thin clay layers interbedded between meter thick sandstone units. The clay layers of this formation are characterized by TOC contents of about 1 wt.% representing a Type III kerogen showing hydrogen index (HI) values of 48 mg HC/g TOC on average. VR_r values of 0.5 to 0.6 % as well as several biomarker ratios indicate early thermal maturity. The formation was deposited at

the northern margin of Gondwana and similar strata might be present in the basement of the Levant Basin and the Eratosthenes Seamount. There, thermal maturity would be higher and such rocks might contribute to thermogenic gas systems.

(2) In the Miocene Pakhna Fm., OM-bearing intervals are mainly present in the upper part of the formation in outcrops east of the Troodos Mountain, while organic-rich intervals are very scarce to absent in the south and southwest of the island. The eastern outcrops show abundant fine-grained, (marly) mud- to wackestones interbedded between coarser-grained carbonates. The fine-grained intervals show TOC contents of about 4 wt.% representing mainly Type II-III kerogen with HI values of 238 mg HC/g TOC on average. The OM is immature as indicated by VR_r values between 0.3 and 0.5 %. $TS/TOC \geq 2.8$ and several biomarker ratios indicate oxygen-depleted, partly even anoxic conditions during deposition. A negative correlation between the TOC and TIC indicates that such conditions were reached during enhanced primary bioproductivity controlled by local and regional clastic derived nutrient input. Similar conditions might have been present along the southeastern margin of the Eratosthenes Seamount, south of Cyprus. Presence of abundant organic matter and high sedimentation rates during the Miocene were favorable for microbial gas generation in the deeper parts of the basins.

5.1 Introduction

During the last decade, several large gas field discoveries were made in the offshore Levant and Herodotus basins (Fig. 5.1A), in the Eastern Mediterranean Sea (Ratner, 2016, Cyprus Mail, 2018). These new fields comprise mainly natural gas of biogenic origin and are located in either Miocene clastic turbidites (e.g. Tamar & Leviathan (Israel), Aphrodite (Cyprus)) or in Mesozoic shallow marine carbonates (Zohr (Egypt), Calypso (Cyprus)). Especially the latter ones set up a new kind of play target for the whole area.

For petroleum system assessments (either thermogenic or biogenic) and the reduction of exploration risks, qualitative as well as quantitative information about the spatial distribution of potential petroleum source rocks is required in order to predict both the type and amount of generated HC. In the Eastern Mediterranean offshore region, the characterization of potential source rocks is not a simple task, since almost no public well data and core samples are available. Therefore, source rock properties and distribution have to be deduced from seismic interpretation and nearby onshore observations. Accordingly, a lot of work has been done for the southern and eastern margins of the Levant Basin (e.g. Abed et al., 2005; El Nady, 2007; Hawie et al., 2013a; Bou Daher et al., 2014; Bou Daher et al., 2015; Ghalayini et al., 2018). Recently Grohmann et al. (2018) showed the existence of potential source rock intervals on the Eratosthenes Seamount (ESM) offshore southern Cyprus. Nevertheless, the western and northern margins of the Levant Basin remains relatively underexplored.

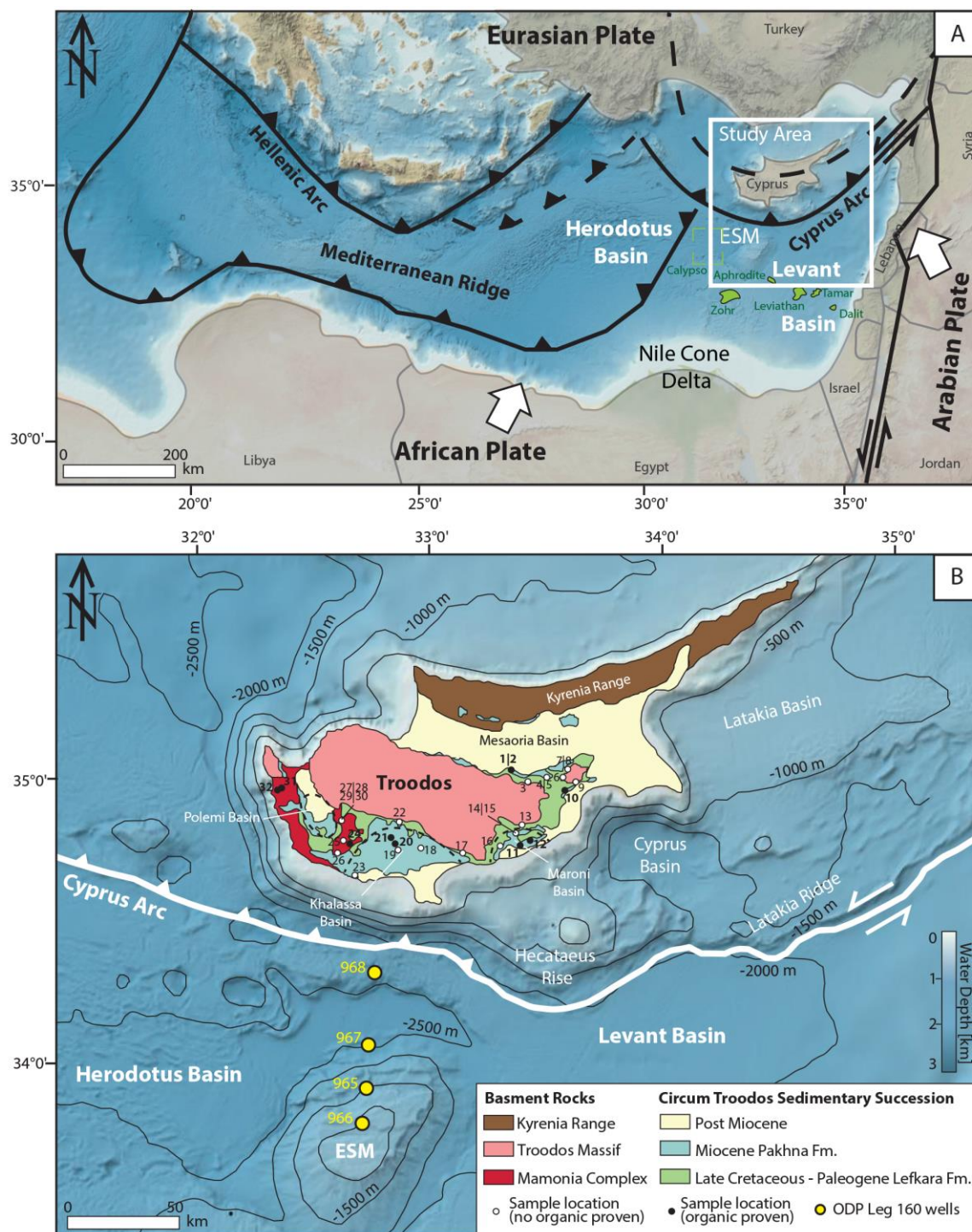


Fig. 5.1 (A) Overview of the Eastern Mediterranean Sea showing the recent tectonic setting. The study area is located at the triple-junction point between the African, the Arabian and the Eurasian plates. White arrows indicate movement orientation of the African and Arabian plates relative to Eurasia (fault location according to Symeou et al., 2018), recent gas field discoveries are delimited in green, ESM=Erasthenes Seamount, (B) Overview of the study area showing a simplified geological map of Cyprus (modified after the official geological map, Cyprus Geological Survey, 1995) and the surrounding basins and the ESM. Yellow dots show the Ocean Drilling Program (ODP) Leg 160 wells (see Grohmann et al. (2018) for respective offshore samples). White (TOC < 0.3 wt%) and black dots (TOC > 0.3 wt%) show onshore sample locations. (For all locations and GPS coordinates, see Table 5.1.) Bathymetric and topographic maps taken from the National Oceanic and Atmospheric Administration (2018) Bathymetric Data Viewer. Fm=Formation.

In this context, we present here a review of potential petroleum source rocks in the Eastern Mediterranean Sea and enhance the current, available data base by new geochemical and petrographic

results obtained from Triassic and Late Miocene organic-rich rocks from the onshore area of Cyprus. In this study, two consecutive field campaigns were carried out in 2016 and 2017 to collect potential source rock intervals from onshore Cyprus. These rocks were investigated with respect to both the quantity and quality of sedimentary organic matter (OM), their source rock potential, the thermal maturity and the corresponding depositional environment. All this information is used to discuss the possible mechanisms of source rock deposition and petroleum systems in the greater area of Cyprus.

5.2 Geological setting

The evolution of the Eastern Mediterranean Sea began in Late Paleozoic time and is until today mainly determined by the interplay of the African, Arabian and Eurasian plates (Fig. 5.1A). During the Pangaea breakup, the area was located at the northern margin of Gondwana (Robertson et al., 2012). Several, mainly northwest-southeast oriented rifting phases in Jurassic and Triassic time caused the disintegration of Gondwana and the evolution of the Neo-Tethys Ocean (Segev and Rybakov, 2010; Hawie et al., 2013a; Ghalayini et al., 2014). During these rifting phases, the Herodotus and the Levant Basin were formed and separated by the Eratosthenes Continental Block (ECB) (Montadert et al., 2014). The Herodotus Basin is unambiguously floored with oceanic crust (e.g. Makris and Stobbe, 1984; Granot, 2016), whereas there are different hypothesis for the crustal style of the Levant Basin: Gardosh and Druckman (2006) proposed an oceanic crust, whereas recent studies have indicated that the basin's basement is made up by thin (~8 km), stretched continental crust (Granot, 2016; Inati et al., 2016, Inati et al., 2018). The ECB between these two basins presented a permanent bathymetric high. On its top, the ESM (Fig. 5.1A and B), a huge, up to 6 km thick, isolated carbonate platform evolved (Montadert et al., 2014; Papadimitriou et al., 2018). The basins, however, comprise thick sedimentary fills of 14-16 km in the Herodotus Basin and 12-14 km in the Levant Basin (Montadert et al., 2014).

During the Late Cretaceous, the tectonic regime changed from an extensional setting to a compressional one. Afro-Arabia started to move northwards and a north-verging subduction zone evolved along the southern margin of Eurasia (Hawie et al., 2013a; Montadert et al., 2014). In the Turonian, between 90 and 92 Ma, slab-pull related extension along the southern Eurasian margin caused the formation of new oceanic crust above the subduction zone (Regelous et al., 2014). Consecutively, in the Maastrichtian (~70 Ma) parts of this new oceanic crust were obducted onto the northern Afro-Arabian margin (Garfunkel, 2004). One of these ophiolitic complexes is the Troodos Ophiolite, today representing the basement of the island of Cyprus (Henson et al., 1949; Swarbrick and Robertson, 1980; Lord et al., 2000). At the time of initial obduction, Cyprus was still in a deep marine setting (2000-3000 m water depth) far away from any continental margins. This is well illustrated by white chalk and chert deposits of the Late Cretaceous to Early Miocene Lefkara Formation (Fm.) (Fig. 5.1B and 5.2) (Kähler, 1994; Kähler and Stow, 1998; Lord et al., 2000).

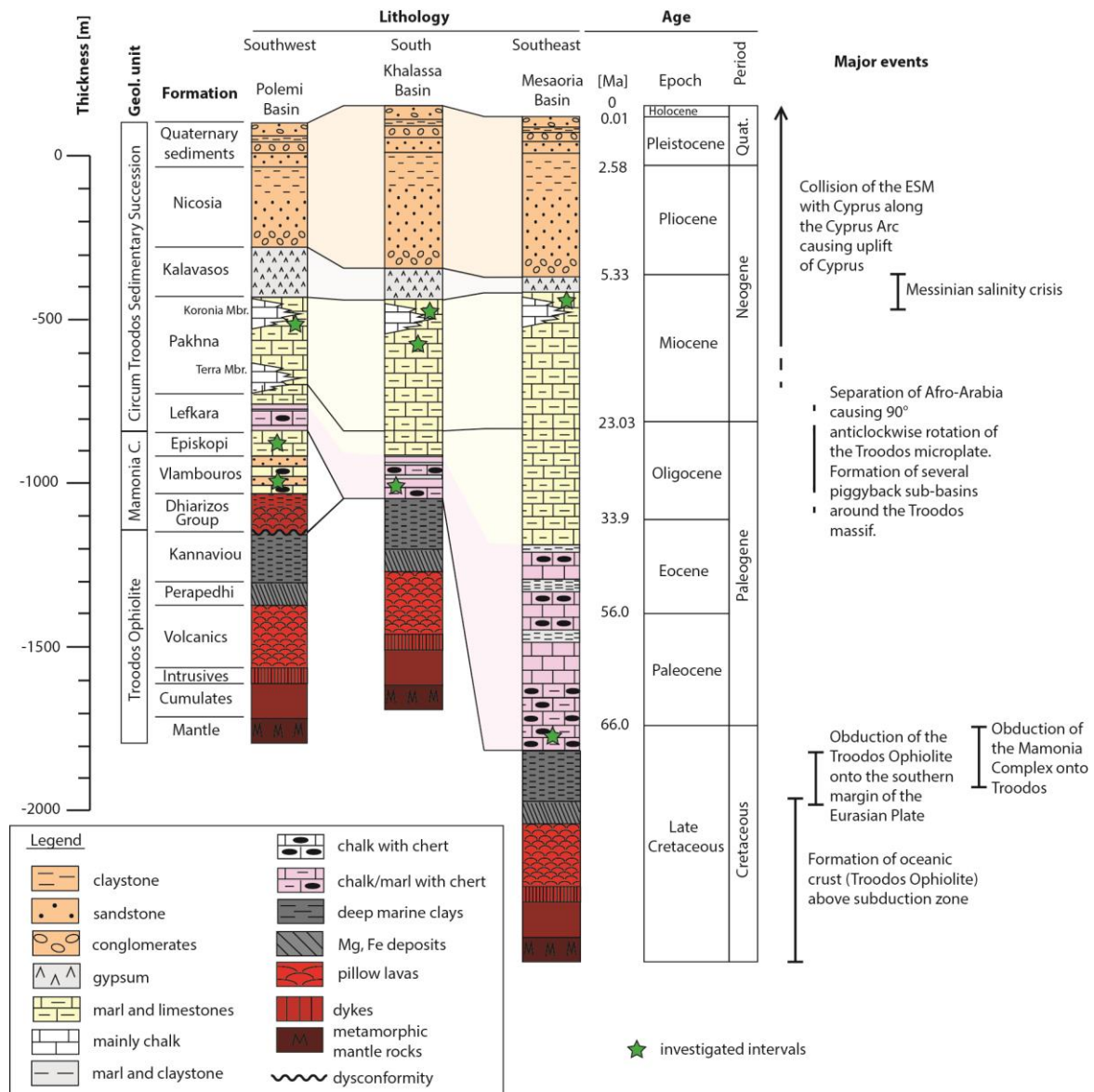


Fig. 5.2 Simplified lithostratigraphy of southern Cyprus as it can be observed within the different sub-basins (modified after Kinnaird et al., 2011) and the main tectonic events. Proposed estimated thicknesses are speculative and must be treated with caution as they can vary throughout each basin. Note that the Mamonia Complex (C.) does not apply to the time scale, as it represents an allochthonous melange that was overthrust onto the Troodos Ophiolite (its rocks span ages from Triassic to Late Cretaceous). Green stars mark sampled intervals.

In the Oligocene, the evolution of an active hot spot caused the breakup of Afro-Arabia with an accelerated northward drift of the Arabian plate. Consequently, the Levant Margin experienced a strong uplift, causing erosion and the incision of canyons along the margin and high input of clastic material into the Levant Basin (Gardosh et al., 2008; Nader, 2014). Since the Mid Eocene, the shrinking Neo-Tethyan Ocean became continuously separated from the Indian Ocean in the east with the final isolation of the Eastern Mediterranean Sea in the Early-Middle Miocene (Robertson et al., 2012). During the Latest Miocene, the Mediterranean Basin was also cut off from the Atlantic Ocean resulting in the Messinian Salinity Crisis (MSC) (Hsü et al., 1977; Krijgsman et al., 2002; Meilijson et al., 2018). Throughout almost the entire Mediterranean Basin thick sequences of salt (up to 2 km) were deposited

while the ESM was exposed above sea-level and subjected to meteoric water flushing (Robertson, 1998), before the whole area was reflooded again in the Pliocene (Hsü et al, 1977; Krijgsman et al., 2002).

Since the Early Miocene, the ESM is in a state of collision with the Troodos Ophiolite along the Cyprus Arc (Fig. 5.1). This caused a strong uplift of the area and the rise of Cyprus above sea level (Robertson, 1998b; Galindo-Zaldivar et al., 2001). During the Miocene, this ongoing convergence in combination with transpressional forces related to the faster movement of the Arabian plate caused the formation of several, separately tectonically controlled sub-basins, as they can be observed around the rising Troodos Mountain (Fig. 5.1B) and throughout the offshore area along the Cyprus Arc (Reiche et al., 2016; Symeou et al., 2018). These sub-basins were partly restricted from the open sea (Eaton and Robertson, 1993). The sedimentation during this period is represented by the carbonate deposits of the Pakhna Fm. (Fig. 5.1B and 5.2), which is divided into the lower Terra Member (shallow water bioclastic carbonates) and the Upper Koronia Member (coral reef carbonates) (Eaton and Robertson, 1993; Lord, 2000). The different tectonic regimes led to varying accumulated thicknesses. While the formation's thickness spans approximately 250 m in the Polemi Basin in the west (Fig.5.1B and 5.2), it reaches up to 400 m in the Khalassa Basin in the south and in the Mesaoria Basin in central Cyprus, respectively (Kinnaird et al., 2011).

Most of the shallow water environments around the Troodos Mountain were also affected by the MSC, which is indicated by the gypsum deposits of the Kalavassos Fm. (Fig. 5.2) (Krijgsman et al., 2002).

5.3 Petroleum source rocks in the Eastern Mediterranean

Whether OM is accumulated and preserved in the sedimentary pile or not depends on several factors such as (a) elevated primary bioproduction of OM, (b) enhanced preservation due to anoxic bottom waters, (c) burial rate, which determines for how long the OM is subjected to oxidation if no anoxic bottom waters are present, as well as (d) specific decomposition kinetics depending on the type of OM (Bohacs et al., 2005; Katz, 2012). Often it is an interplay between these factors, controlling the formation and quality of petroleum source rocks. Throughout the geological history of the Eastern Mediterranean Sea, several periods provided conditions that favored the deposition and preservation of OM and led to the formation of major regional petroleum source rocks.

During the syn-rift phase in the Early to Middle Mesozoic, extension related subsidence led to the flooding of the area. With ongoing subsidence, first shallow water carbonate platforms evolved, which later evolved into deep marine carbonate environments (Barrier and Vrielynck, 2008). In this setting, organic-rich rocks are believed to have been deposited along the passive continental margin. In northern Egypt, Mid-Jurassic source rocks are believed to be present deeply buried below the Nile Delta and to be responsible for thermogenic generation of oil and gas (Wigger et al., 1997; Shaaban et al., 2006).

Also in the area of Lebanon, Triassic to Mid-Jurassic OM-rich limestones are considered as potential source rock intervals (Ghalayini et al., 2018). In Israel, thermogenic hydrocarbons (HC) are present in Jurassic and Cretaceous reservoirs, although no specific source could be assigned (Feinstein et al., 2002).

With the change to a compressional regime at the end of the Mesozoic, the whole region was located in a slope to basinal clastic marine environment, with exception of the ECB and the Troodos Ophiolite, on which deep marine carbonate platforms began to evolve (Barrier and Vrielynck, 2008; Papadimitirou et al., 2018). During the Late-Cretaceous to Early-Cenozoic, a large-scale upwelling system affected the southern shallow epicontinental shelf of the Tethyan Ocean (Levant margin) providing cold and nutrient-rich waters (Almogi-Labin et al., 1993). Consequently, increased bio-productivity led to the formation of extensive source rock intervals, as they are reported as fine grained limestones of Turonian to Lower Maastrichtian age with total organic carbon (TOC) contents up to 11 wt.% in Lebanon (Bou Daher et al., 2014; Bou Daher et al., 2015) or phosphatic oil shales and bituminous limestones of Late Maastrichtian to Paleocene age with TOC contents up to 22 wt.% in Jordan (Abed et al., 2005). These source rocks comprise mainly Type II or Type II-S kerogen and are of low thermal maturity in the onshore area. Bou Daher et al. (2015) observed that TOC contents decrease towards the deeper parts of the Levant Basin. Nevertheless, with the assumption that source rocks are still present in the deeper basin, Bou Daher et al. (2016) demonstrated that the oil-window thermal maturity is reached in the offshore area and thermogenic HC generation is likely to have occurred between 34 and 16 Ma in Upper Cretaceous source rocks.

The separation of the African and the Arabian plates (see above) in the Oligocene-Miocene caused a major uplift of the Levant area leading to an increased influx of sediments derived from the Nile Delta as well as from the Levant margin (Inati et al., 2018). As a result, the environment changed from a carbonate to a more siliciclastic-dominated setting at the Early/Late Oligocene boundary (Roberston et al., et al., 2012). For this period, organic-rich intervals are expected to have developed in the Nile Delta in the Oligocene to Miocene. They are believed to be responsible for natural gas and condensate accumulations, which might be partly of biogenic origin (Wigger et al., 1997). Also at the southeastern Levant margin, offshore Israel, the geochemical analysis of different oil and gas samples indicates different sources of biogenic gas. Corresponding source rocks might be located in the Eocene, Oligo-Miocene, and Plio-Pleistocene (Feinstein et al., 2002). Furthermore, Bou Daher et al. (2016) and Schneider et al. (2016) suggested that Oligo-Miocene source rocks potentially present in the offshore area of Lebanon are likely to have produced biogenic gas, similar to the gas, which is present in the Tamar and Leviathan fields offshore Israel.

Through the Late Mesozoic until Mid Cenozoic geological history, the area of Cyprus was located far away from any continental margins and, thus, exposed to different depositional conditions compared to the Levant Margin (Barrier and Vrielynck, 2008). In the southern offshore area of Cyprus, Grohmann et al. (2018) investigated Late Cretaceous to Messinian intervals along the ESM. The studied sections comprise mainly argillaceous carbonates to pure limestones with low organic contents (average TOC

around 0.2 wt.%). More clay-rich sections with increased amounts of Type II kerogen (TOC contents up to 5 wt.%) and, in general, good hydrocarbon generation potentials are present in the lower Upper-Cretaceous (Turonian to Coniacian) and Upper Eocene (Bartonian to Priabonian) intervals. While the older source rock intervals are likely to be restricted to the closer surroundings of the ESM, organic-rich post-Mid-Eocene units might extend also in the deeper parts of the Levant Basin.

Onshore Cyprus, evidences for the existence of organic-rich intervals are reported for the Paleogene Lefkara Fm. (Kähler and Stow, 1998) and within the Miocene Pakhna Fm. (Eaton and Robertson, 1993). Furthermore, bituminous sandstones are observed in Triassic and Jurassic formations within the Mamonia Complex (Lapierre, 1975; Robertson and Woodcock, 1979). However, all these evidences are based on rock descriptions without any modern geochemical investigations. Therefore, the main objective of this work is to investigate these formations in greater detail by means of geochemical and petrographic analysis to better identify and characterize the potential source rock intervals throughout the onshore Cyprus region, and to better understand their implications on offshore HC exploration.

5.4 Samples and methods

5.4.1 Sampling representative outcrop rocks: Onshore Cyprus

A total of 147 samples, which were suspected to be enriched in OM (chosen mainly by fine grain size and dark color), were collected from the onshore area of Cyprus. Samples were taken from at least 30 cm below the outcrop surface in order to reduce the risk of major weathering effects. Figure 5.1B shows a simplified geological map of the island. Sample locations are widespread throughout the southern island (Fig. 5.1B, Table 5.1).

In the Mamonia Complex (a *mélange* of autochthonous rocks that were over-thrusted onto the Troodos Ophiolite during the Late Cretaceous), samples originate from both the Triassic Vlambouros and the Jurassic Episkopi formations. The Vlambouros samples originate from thin shaly clay intervals which are interbedded between thick sandstone successions at Location (Loc.) 31 and 32 (Fig. 5.1B and 5.3). Large (> 1mm) plant remains can be recognized in both, the clay-rich as well as in the sandstone units. Similar organic-rich clay layers can be observed at Loc. 24 (Fig. 5.1B), where they are interbedded between massive calcarenites. All three outcrops are likely to be part of a passive continental margin, fluvio-deltaic environment. Loc. 31 and 32 represent a more clastic, proximal setting while Loc. 24 should represent a more distal calcareous system.

The Episkopi samples are mainly dark, reddish-deep brown claystones, which are referred to deep marine slump deposits.

Table 5.1 List of investigated locations and the respective formation, taken samples and GPS coordinates. Locations where organic matter could be proven are marked by *. Locations are shown on the geological map (Fig. 5.1) and in the lithostratigraphic column (Fig. 5.2).

Loc.	Formation	Age	Latitude	Longitude
1*	Upper Pakhna	Upper Miocene	35°01'58.27"N	33°20'35.56"E
2*	(Upper?) Pakhna	(Upper) Miocene	35°01'57.25"N	33°20'39.12"E
3	Lower Lefkara	Late Cretaceous	34°59'53.20"N	33°25'29.39"E
4	Nicosia	Pliocene	35°00'52.41"N	33°30'36.96"E
5	Upper Pakhna	Upper Miocene	35°00'23.91"N	33°30'25.53"E
6	Lower Lefkara	Late Cretaceous	35°00'50.45"N	33°33'24.35"E
7	Lower Lefkara	Late Cretaceous	35°01'47.35"N	33°35'42.05"E
8	Lower Lefkara	Late Cretaceous	35°02'02.35"N	33°35'58.67"E
9	Lower Lefkara	Late Cretaceous	34°59'47.69"N	33°36'51.27"E
10*	Upper Pakhna	Upper Miocene	34°57'29.54"N	33°34'43.13"E
11*	Pakhna	Miocene	34°48'08.56"N	33°26'08.74"E
12*	Pakhna	Miocene	34°46'38.21"N	33°23'56.29"E
13	Pakhna	Miocene	34°50'13.50"N	33°23'58.10"E
14	Pakhna	Miocene	34°49'40.04"N	33°23'29.82"E
15	Pakhna	Miocene	34°49'04.70"N	33°23'37.92"E
16	(Upper?) Pakhna	(Upper) Miocene	34°45'53.18"N	33°18'03.91"E
17	Moni Melange	Triassic to Cretaceous	34°45'14.58"N	33°06'23.90"E
18	Pakhna	Miocene	34°45'51.40"N	32°55'52.38"E
19	Pakhna	Miocene	34°45'43.12"N	32°50'35.95"E
20*	Pakhna	Miocene	34°46'25.23"N	32°49'55.88"E
21*	(Upper?) Pakhna	(Upper) Miocene	34°48'55.58"N	32°49'27.02"E
22	Lower Lefkara	Late Cretaceous	34°51'22.39"N	32°52'16.77"E
23	Pakhna	Miocene	34°39'37.84"N	32°39'08.18"E
24*	Vlambouros	Middle Triassic	34°47'39.67"N	32°39'22.08"E
25	Episkopi	Middle Jurassic	34°48'12.56"N	32°38'43.71"E
26	Vlambouros	Middle Triassic	34°44'05.05"N	32°35'54.18"E
27	Episkopi	Middle Jurassic	34°52'08.85"N	32°36'25.95"E
28	Episkopi	Middle Jurassic	34°51'58.19"N	32°36'10.41"E
29	Episkopi	Middle Jurassic	34°52'29.37"N	32°35'48.04"E
30	Episkopi	Middle Jurassic	34°52'34.04"N	32°35'38.65"E
31*	Vlambouros	Middle Triassic	34°58'54.70"N	32°19'09.44"E
32*	Vlambouros	Middle Triassic	34°58'50.01"N	32°19'00.37"E

In the Circum Troodos Sedimentary Succession (autochthonous sediments around the Troodos Ophiolite) samples are described according to Dunham (1962) although some of the samples contain elevated amounts of fine grained argillaceous material. Samples were collected from the Late Cretaceous-Paleocene Lefkara Fm. comprising greyish mudstones, and from the Miocene Pakhna Fm. In the Khalassa (Loc. 20 and 21) and Maroni (Loc. 11 and 12) basins (Fig. 5.1B), the collected Pakhna samples are representative of few, thin dark brown mudstone layers, which are interbedded between massive limestones. More towards the northeast, in the Cyprus (Loc. 10) and Mesaoria (Loc. 1) Basins, instead, two thick successions of greyish black mud- to wackestones relatively regularly interlayered between wacke- to grainstones were sampled in greater detail (Fig. 5.4).

5.4.2 Sample preparation

Prior to the organic geochemical and microscopic investigations, all collected samples were dried over night at 50°C. Grinded rock powder was prepared from large bulk rock pieces being representative of the whole sample lithology using a disc mill to ensure homogeneity of the samples.

Additionally, total organic matter (TOM) concentrates were prepared for the more organic-rich samples of the Vlambouros and Pakhna Fm. for further detailed analysis. Approximately 10 g of sample were crushed to a grain size of 1-2 mm by using a quartz mortar, in order to avoid destruction of organic particles. TOM isolation was performed following the standard non-oxidizing acid treatment and drying procedures described by Durand and Nicaise (1980). The crushed material was filled into plastic beakers

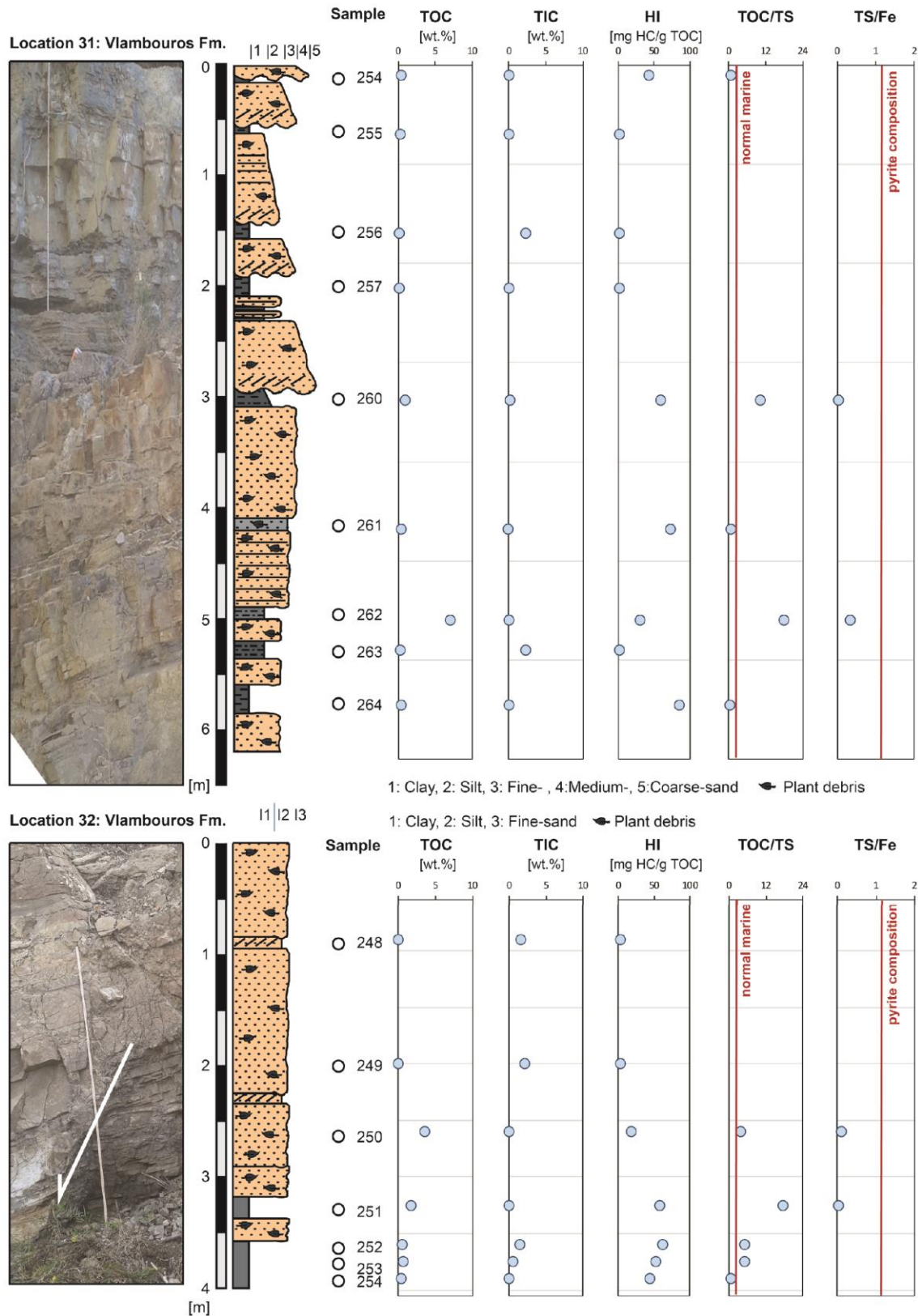


Fig. 5.3 Sedimentological and geochemical logs of the Mid Triassic Vlambouros Formation (Fm). at location 31 and 32 (For locations see Fig. 1 and Table 1). Colors of the lithological column indicates observed rock color. Horizontal lines indicate recognizable normal lamination, while inclined lines indicate cross bedding. Although the clay-rich sections partly show elevated total organic carbon (TOC) contents, the source rock quality is poor due to low hydrogen index (HI) values < 50 mg HC/g TOC on average. Total sulfur (TS)/TOC ratios indicate oxic conditions during deposition (Bernier, 1984). TS/Fe ratios indicate that most sulfur is bound to pyrite. White line and arrow indicates small normal fault observed in the outcrop.

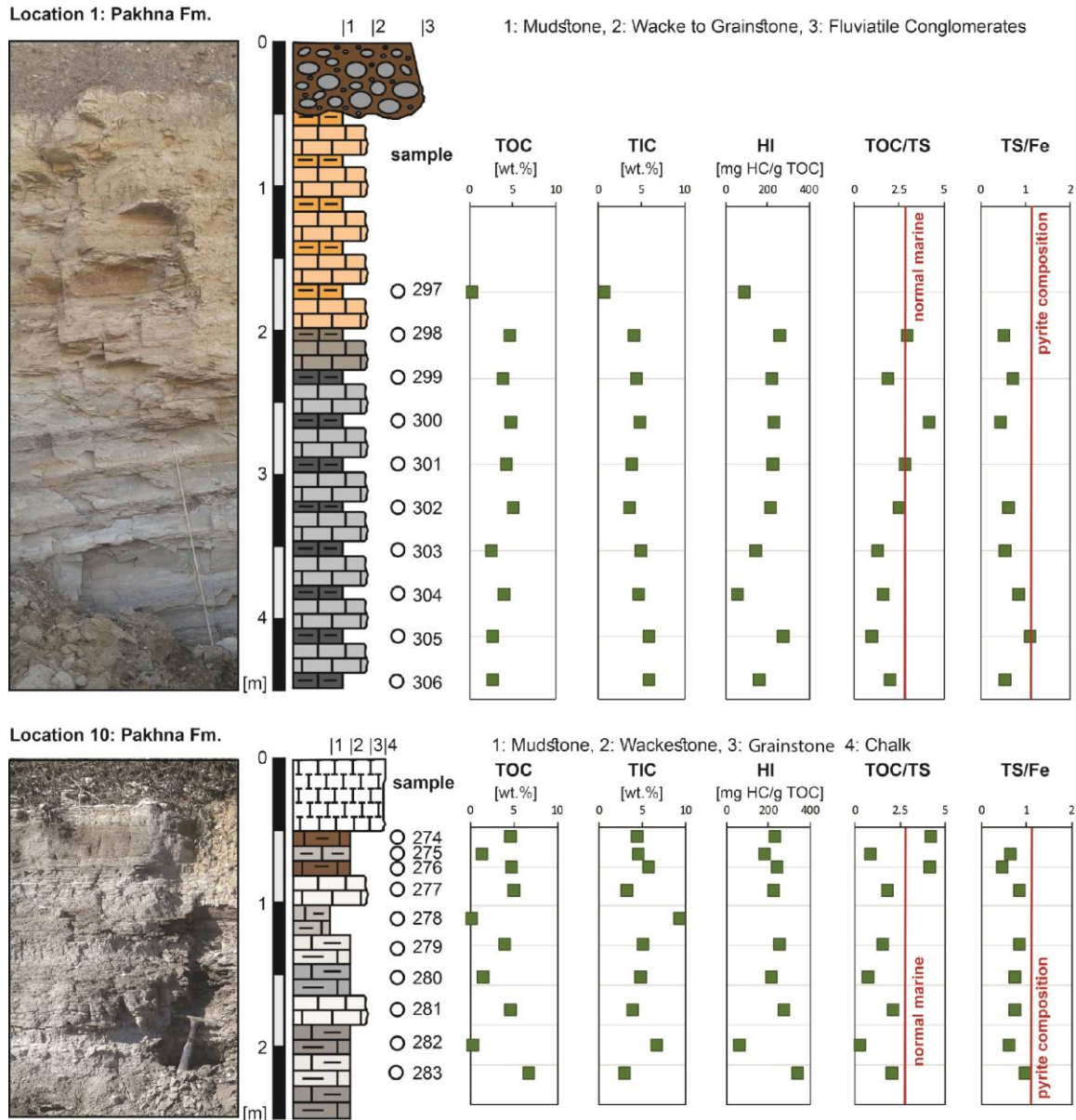


Fig. 5.4 Sedimentological and geochemical logs of the Late Miocene Upper Pakhna Formation at location 1 and 10 (for locations see Fig. 1 and Table 1). Colors of the lithological column indicates observed rock color. Total organic (TOC) and inorganic carbon (TIC) contents and hydrogen index (HI) values indicate good source rock quality. Total sulfur (TS)/Fe ratios show that all sulfur is bound to pyrite. TS/TOC ratios are mainly lower than those observed under normal marine conditions, suggesting a deposition under anoxic conditions (Bernier, 1984).

and treated with 150 ml of HCl (35%) to destroy carbonate minerals. After the reaction ceased, boiling water was added to enable the destruction of dolomite. When all particles settled down, the water was removed and the beaker refilled with fresh deionized water. For subsequent silicate removal, the samples were treated with 150 ml of HF (75%) for 15 hours, followed by two washing steps with deionized water. 150 ml of boiling HCl (35 %) were used to decompose minerals probably formed during the HF attack, such as fluorosilicates. At the end, the organic residue was washed with hot, distilled water until a neutral pH value was reached. A centrifuge run at 3500 rotations/min was used to settle all the organic matter and enable the removal of water by decantation. One part of the sample material was kept in

water for later preparation of slices for palynofacies analysis. The other part was dried in an oven at 50°C to evaporate the remaining water.

5.4.3 Elemental analysis

5.4.3.1 Bulk rock (TOC, TIC, TS, Fe, Ni, V)

For quantification of the carbon content, a *LiquiTOC II* device equipped with a module for solid analysis (*Elementar*) was used. The total organic (TOC) and inorganic carbon (TIC) contents were directly determined by measuring the amount of CO₂ evolving from 100 mg of powdered sample during combustion at 550 and 1000°C, respectively, by an IR detector (detection limit 10 ppm, TOC error 0.6%, TIC error 1.7%).

The total sulfur (TS) content was determined for all bulk rock samples using a *LECO S-200* instrument. 100 mg of powdered rock sample were combusted in a ceramic crucible at 1800°C. Oxygen was used as carrier gas and for sulfur oxidation to SO₂, which was measured by an IR detector (detection limit 20 ppm, error < 5%).

In addition, the iron (Fe), nickel (Ni) and vanadium (V) contents were measured for 37 bulk rock samples with significant TS contents via X-ray fluorescence. Measurements were performed on thick, homogenized pellets of 8 g pulverized (<63 μm) bulk rock mixed with 2 g of a *Fluxene CEREON* wax using a *SPECTRO XEPOS ED(P)-RFA* instrument (detection limit ≤ 1.4 ppm; error for Ni and V < 2%, error Fe < 0.2%).

5.4.3.2 Total organic matter (C, H, N, TS, O)

Carbon (C), hydrogen (H), nitrogen (N), and total sulfur (TS) concentrations were determined on ten TOM aliquots using a *FLASH 2000 Organic Elementar Analyzer* by *ThermoFischer SCIENTIFIC*. Aliquots of 1 to 2 mg were filled into soft tin crucibles together with a small amount of vanadium pentoxide (V₂O₅), acting as a catalyst. Combustion was performed at 1600 °C resulting in the formation of CO₂, H₂O, SO₂, SO₃, and NO_x. The latter two molecules were reduced to SO₂ and N₂ and remaining O₂ was fixed to copper. The generated molecules are transported by a helium flux, separated by gas chromatography and detected by thermal conduction detector (TCD) with a lower detection limit of < 0.5 μg and an accuracy of ± 0.2%.

The oxygen (O) content was determined using the same device. Sample material was capped in small, soft silver crucibles without adding any catalyst. Instead of combustion, the sample was pyrolyzed at 1065 °C under a helium atmosphere. Pyrolysis products are N₂, H₂, CH₄, and CO (representing the

oxygen contained in the sample), which were again separated by gas chromatography and detected by the TCD with a lower limit of $\leq 1 \mu\text{g}$ and an accuracy of $\pm 0.2\%$.

5.4.4 Rock-Eval pyrolysis

In order to evaluate the source rock potential of the analyzed rocks, Rock-Eval[®] analysis (Espitalié et al., 1977) was performed using a Rock-Eval[®] 6 Complete Analysis – Serial Process device (Vinci Technologies). The IFP Basic/Bulk-Rock Method for Source Rocks was applied on 50 mg of powdered sample following the procedures described in Behar et al. (2001). The sample was heated under a nitrogen atmosphere at isothermal 300°C for 3 min with consecutive temperature increase by 25°C/min up to 650°C. In this study, the Hydrogen (HI) and Oxygen Index (OI) were determined from the Rock-Eval[®] S2 and S3 peaks in relation to the TOC content determined by the elemental analyzer.

Additionally, ten TOM concentrates (5 mg) of the Pakhna Fm. were analyzed using the IFP Pure Organic Matter Method also described in Behar et al. (2001), following the same heating program but reaching a final pyrolysis temperature of 800°C. It is assumed that all generated CO and CO₂ are in this case of organic origin.

5.4.5 Biomarker analysis

15 samples were selected for molecular geochemical analysis to cover each outcrop. For outcrops with numerous samples low and high TOC samples were chosen. Maltene extracts were first obtained by accelerated solvent extraction (ASE) using a DIONEX ASE 150 instrument (ThermoFischer SCIENTIFIC), which allows a full automatic extraction. Approximately 4 g of pulverized bulk rock sample were extracted by 40 ml of dichloromethane (DCM) in a high pressure cell at 100°C and 100 bar during 14 min. The maltene extracts were separated into three fractions by means of silica-gel based liquid chromatography and eluents of different polarity: 5 ml of pentane to obtain the aliphatic fraction, 5 ml pentane/DCM (40:60) for the aromatic fraction, and 5 ml methanol for the polar fraction. Only the first fraction was selected for further analysis, due to the expected low thermal maturity of the samples.

5.4.5.1 GC-FID

For the relative determination of *n*-alkanes as well as the isoprenoids pristane (Pr) and phytane (Ph), a Carlo Erba Strumentazione HRGC 5300 gas chromatograph equipped with a flame ionization detector (GC-FID) was used. The starting temperature was set to 60 °C and kept for 3 min. Afterwards, the temperature was increased by 5 °C/min up to 310 °C and held for 20 min. 1 μl of concentrated sample was injected in splitless mode set to 60 s. Compound separation was achieved using a 30 m long

Zebron ZB-1 capillary column and hydrogen as carrier gas. The obtained chromatograms were interpreted using the *Atlas CDS* software.

5.4.5.2 GC-MS

For the analysis of hopanes and steranes gas chromatography coupled with mass spectrometry (GC-MS) was performed using a *Mega Series HRGC 5160* gas chromatograph (*Carlo Erba, IT*) equipped with a 30 m x 0.25 mm x 0.25 μ m film *Zebron ZB-5_MS* fused silica capillary column. For specific detection a quadrupole mass spectrometer Trace MS (*Thermoquest*) was used. 1 μ l of sample was injected by split injection at 80°C. After 3 min isothermal hold, temperature was first increased by 10°C/min up to 160°C, followed by a further temperature increase by 3°C/min up to 320°C, which was held for 20 min. Helium was used as carrier gas with a velocity of 30 cm/s. Hydrocarbons were analyzed in single ion mode (EI+, 70 eV, measured m/z = 58, 85, 191, 205, 217, 218, 259, 372, 386, 400, 412) with a source temperature of 200°C.

Hopanes and steranes were evaluated based on m/z = 191 and m/z = 217, respectively. The identification of different compounds is based on a CHIRON reference standard (Hopane/Sterane Calibration Mix) and by comparison with other reference material. For peak quantification the *Xcalibur* software (*ThermoFinnigan*) was used.

5.4.6 Organic petrography and palynofacies analysis

Organic petrography was performed for 21 samples covering the most organic rich samples (> 1wt.% TOC, where possible) from all investigated outcrops. Polished sections were prepared by embedding bulk rock pieces in a two compounds epoxy resin and consecutively polishing perpendicular to their bedding planes. For maceral analysis, a Zeiss Axio Imager.M2m microscope equipped with both a 50x/1.0 Epiplan-NEOFLUAR Oil Pol objective and a PI 10x/23 ocular lenses was used. Maceral identification was mainly based on their difference in reflectivity as well as their fluorescence intensity under ultra-violet light following procedures described by Taylor et al. (1998). Random vitrinite reflectance (VR_r) was measured under a Zeiss Axioplan microscope equipped with a 50x/1.0 EC-Epiplan-NEOFLUAR Oil Pol objective lense and a PI 10x/23 ocular lenses. Calibration was performed on a Leuco-Saphir standard with a reflexivity of 0.932%. VR_r values were calculated as the mean of at least 50 measured single vitrinite grains. More details of the preparation and microscopic analysis are described in Sachse et al. (2011).

Twenty-one TOM concentrates were chose for palynofacies analysis according to the same criteria as for organic petrography. The analysis was performed following procedures described in Tyson (1995). Aliquots of the TOM were sieved (> 10 μ m) and mounted on glass slices for the microscopical

analysis. The quantitative determination of the palynological compounds was based on the sieved kerogen fraction larger than 10 μm . Counting was performed under normal transmitted light using a 40x magnification objective and an ocular with a 10x10 grid to determine the relative areal abundance of the different components.

5.5 Results and interpretation

5.5.1 Organic matter-richness and carbonate content

The TOC content is widely used as an indicator of the quantity of OM in sedimentary rocks (Peters, 1986). A minimum of 0.3 wt.% of TOC is required for (calcareous) sediments to be considered as potential source rocks (Hunt, 1967). 60 of the 147 investigated samples exceed this threshold (Table 5.2) and will be discussed in the following. These samples are assigned to the Triassic Vlambouros Fm. and the Miocene (mainly Upper) Pakhna Fm.

The organic-rich samples of the Vlambouros Fm. are characterized by average TOC contents of around 1 wt.% with one exception of sample 262 showing a TOC content of 7 wt.%. The TIC contents in these samples are very low with 0.02 wt.% on average at Loc. 31 and 32 (Fig. 5.1 B and Fig. 5.3) and higher at Loc. 24 with an average of 2.7 wt.% (Fig. 5.1 B).

Carbon contents of the Pakhna samples vary strongly between the different locations with 0.3 to 6.7 wt.% of TOC and 0.7 to 8.7 wt.% of TIC. The higher TOC contents are observed at the northeastern outcrops at Loc. 1 and 10 (Fig. 5.4) with 4.4 wt.% on average, while the southwestern outcrops (Fig. 5.1 B) show average values of 1.6 wt.%.

In the TOM concentrates of the Pakhna samples, the TOC contents vary between 31 and 57 wt.%. A TOC content of about 70 wt.% is to be expected for immature marine kerogen (Stock et al., 2017). Thus, the organic matter content ranges from about 71 to 81 % for the Pakhna TOM concentrates with the exception of one sample (44 %) proving that these are relatively clean total organic matter plus pyrite concentrates.

5.5.2 Source rock quality and thermal maturity

Based on the Rock-Eval[®] results (Table 5.2), the Vlambouros samples are characterized as terrestrial, gas-prone Type III kerogen in the pseudo- van Krevelen diagram (Fig. 5.5 A) with HI values between 18 and 73 mg HC/g TOC and OI values between 21 and 150 mg CO₂/g TOC. The Pakhna samples scatter somewhere between the marine, oil/gas prone Type II to and Type III kerogen pathways (Fig. 5.5 A), with HI values ranging from 21 to 384 mg HC/g TOC and OI values ranging from 35 to 319 mg CO₂/g TOC.

Table 5.2 Total organic (TOC) and inorganic carbon (TIC) and Rock-Eval® results for bulk rock samples > 0.3 wt.% TOC. For locations (Loc.) see Fig. 1 and 2. Fm. = Formation, P = Pakhna; V = Vlambouras, [---] = T_{max} was not determined due to bad resolution of the S2 peak. HI = hydrogen index, OI = oxygen index, T_{max} = temperature at S2 peak.

Sample	Loc.	Fm.	TOC [wt.%]	TIC [wt.%]	S1 [mg HC/g rock]	S2 [mg HC/g rock]	S3 [mg CO ₂ /g rock]	HI [mg HC/g TOC]	OI [mg CO ₂ /g TOC]	T _{max} [°C]
11	10	P	4.44	4.91	0.28	15.26	4.69	344	106	421
12	10	P	4.36	3.2	0.22	12.33	4.92	283	113	419
13	10	P	5.12	3.77	0.29	15.85	5.72	310	112	421
15	10	P	4.64	4.27	0.32	17.82	5.01	384	108	424
16	10	P	1.25	6.65	0.04	2.51	2.01	201	161	426
17	10	P	3.94	4.58	0.2	11.16	4.87	283	124	421
18	10	P	4.64	4.79	0.25	14.55	5.18	314	112	419
19	10	P	4.69	4.34	0.25	15.34	5.15	327	110	426
20	10	P	5.02	3.34	0.22	14.52	5.65	289	113	421
21	10	P	4.29	3.43	0.17	11.51	5.17	268	121	423
33	21	P	0.58	7.29	0.01	0.6	1.34	143	319	429
227	12	P	3.66	6.07	0.14	11.80	2.75	322	75	429
228	11	P	1.57	1.03	0.06	2.33	1.93	148	123	434
233	20	P	0.51	4.93	0.04	0.50	1.05	97	206	433
271	11	P	3.05	5.22	0.10	7.05	1.80	231	59	434
272	11	P	2.23	6.68	0.10	6.45	1.34	289	60	433
273	11	P	0.41	8.75	0.04	0.27	0.69	65	166	434
274	10	P	4.69	4.45	0.20	10.81	2.55	230	54	420
275	10	P	1.43	4.63	0.08	2.57	0.98	180	69	---
276	10	P	4.75	5.69	0.21	11.48	3.50	241	74	414
277	10	P	5.08	3.19	0.27	11.35	3.20	224	63	420
279	10	P	4.04	5.11	0.19	10.23	2.87	253	71	421
280	10	P	1.44	4.79	0.09	3.09	1.06	214	73	425
281	10	P	4.68	3.97	0.20	12.78	3.22	273	69	423
282	10	P	0.32	6.74	0.05	0.20	0.63	63	193	---
283	10	P	6.71	3.01	0.31	22.71	2.34	338	35	420
285	10	P	5.25	2.44	0.19	12.63	2.23	241	42	420
286	2	P	3.73	3.16	0.16	5.81	2.88	156	77	428
287	2	P	1.17	2.77	0.07	0.30	3.34	26	285	---
288	2	P	1.27	4.74	0.08	0.32	3.21	25	252	---
289	2	P	1.31	2.56	0.09	0.28	3.86	21	295	---
290	2	P	1.06	4.95	0.08	0.30	1.87	29	176	---
291	2	P	0.71	3.61	0.06	0.25	2.10	36	297	---
292	2	P	1.52	3.43	0.09	1.80	1.50	119	99	427
293	2	P	4.15	3.14	0.17	9.14	2.93	220	70	421
294	2	P	2.70	3.89	0.14	7.00	2.00	259	74	424
295	2	P	3.27	5.25	0.21	5.87	3.38	179	103	427
296	2	P	1.46	2.51	0.09	1.23	2.51	84	171	428
297	1	P	0.31	0.71	0.12	0.27	0.88	88	286	---
298	1	P	4.66	4.20	0.21	11.97	2.52	257	54	424
299	1	P	3.93	4.40	0.16	8.70	2.13	221	54	423
300	1	P	4.85	4.81	0.19	11.14	2.30	230	47	422
301	1	P	4.24	3.93	0.17	9.68	2.18	228	51	422
302	1	P	5.01	3.72	0.19	10.81	2.33	216	47	421
303	1	P	2.50	4.99	0.10	3.62	1.70	144	68	428
304	1	P	3.95	4.66	0.08	2.22	1.79	56	45	424
305	1	P	2.71	5.97	0.18	7.46	2.26	276	83	427
306	1	P	2.71	5.97	0.12	4.27	2.08	158	77	425
56	24	V	1.08	1.66	0.00	0.50	0.98	41	81	440
57	24	V	0.62	4.01	0.00	0.26	0.8	40	123	442
58	24	V	0.37	2.73	0.00	0.12	0.54	33	150	441
250	32	V	3.55	0.02	0.03	0.65	1.91	18	54	---
251	32	V	1.75	0.02	0.03	1.00	0.72	57	41	---
252	32	V	0.47	1.48	0.03	0.30	0.43	62	91	---
253	32	V	0.63	0.54	0.03	0.33	0.38	52	61	---
254	31	V	0.42	0.02	0.03	0.18	0.56	43	134	---
260	31	V	1.03	0.18	0.04	0.60	0.22	59	21	437
261	31	V	0.44	0.01	0.03	0.32	0.09	73	21	---
262	31	V	7.07	0.03	0.06	2.12	2.69	30	38	434
264	31	V	0.41	0.02	0.00	0.50	0.98	86	48	---

It is known that the Pakhna Fm. was deposited in a marine environment (e.g. Eaton and Robertson, 1993). Although it is not uncommon to find terrigenous organic matter/type III kerogen in marine settings, some of the OI values seem to be exceptionally high while some of the HI values seems to be too low for OM deposited in a marine setting. In the HI vs. T_{max} diagram (Fig. 5.5 B) the scattering is less prominent, but still some of the samples tend towards Type III. These unexpected results can be explained as follows:

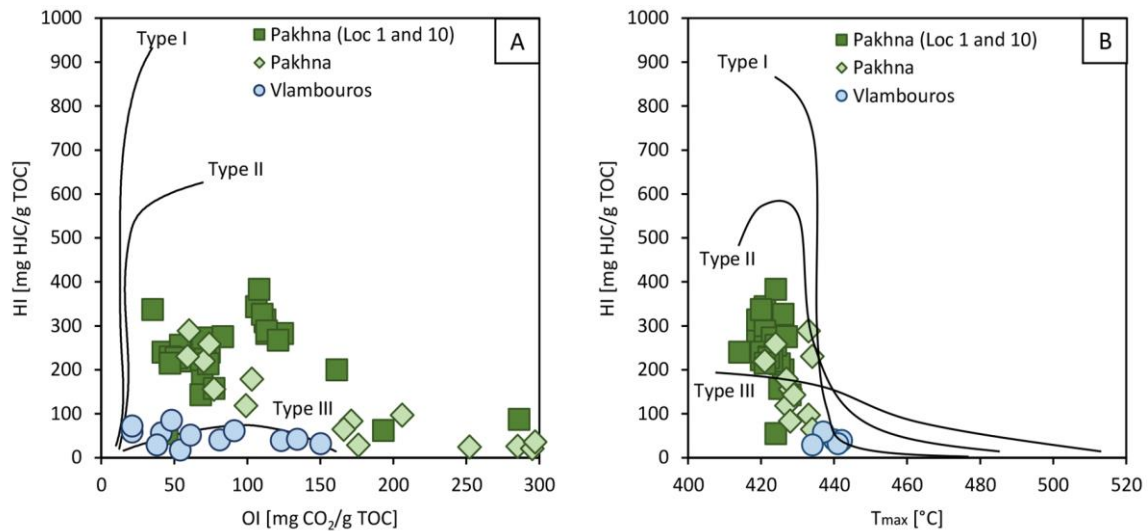


Fig. 5.5 Rock-Eval® results for all >0.3 wt% total organic carbon (TOC) samples. (A) Pseudo-van Krevelen diagram (Hydrogen Index (HI) vs. Oxygen Index (OI)) after Espitalie et al. (1986) showing high OI values. (B) Rock-Eval® HI vs. T_{max} plot to avoid misinterpretation in kerogen typing related to probably inaccurate OI values. In both plots, the majority of the Pakhna samples is interpreted as Type II kerogen while the Vlambouros samples are Type III. However, some Pakhna samples (mainly from Location (Loc.) 2, 11, 20, and 21) also plot as Type III kerogen, although their depositional setting is supposed to be marine.

Samples originating from outcrops are affected by weathering and potentially oxidation of the OM, which would lead to increased OI and T_{max} values (Littke, 1993).

During pyrolysis, some instable, immature carbonates might decompose already at low temperatures. Also, organic acids can be generated during pyrolysis, which dissolve parts of the carbonate. Both produce additional CO₂, which would cause an overestimation of the OI (Katz, 1983). This case has been already observed for organic-rich carbonates along the ESM, offshore Cyprus (Grohmann et al., 2018).

For samples containing low TOC contents, HC generated during pyrolysis can be retained to different extends depending on the type and amount of clay minerals contained in the mineral matrix, leading to a decrease of the recorded S2 peak and, therefore, to a reduced HI value (Espitalié et al., 1984).

Table 5.3 Comparison of Rock-Eval® results obtained from bulk rock samples and the respective total organic matter concentrates. TOC = total organic carbon, HI = hydrogen index, OI = oxygen index, T_{max} = temperature at S2 peak.

Sample	Bulk rock				Total organic matter			
	TOC [wt.%]	HI [mg HC/g rock]	OI [mg CO ₂ /g rock]	T _{max} [°C]	TOC [wt.%]	HI [mg HC/g rock]	OI [mg CO ₂ /g rock]	T _{max} [°C]
11	4.44	344	106	421	57.26	596	88	406
12	4.36	283	113	419	49.66	500	96	398
13	5.12	310	112	421	50.07	528	81	404
15	4.64	384	108	424	50.67	609	81	406
16	1.25	201	161	426	31.48	430	91	405
17	3.94	283	124	421	49.91	536	91	402
18	4.64	314	112	419	48.08	505	85	398
19	4.69	327	110	426	53.97	539	83	401
20	5.02	289	113	421	49.49	512	93	397
21	4.29	268	121	423	50.78	526	91	401
33	0.58	143	319	429	46.69	457	120	414

Table 5.4 Average random vitrinite reflectance (VR_r) for each outcrop based on one or several samples (n_{samples}). Fm. = Formation (P = Pakhna, V = Vlambouros); Loc. = Location; n_{total} = total amount of measured vitrinite particles per outcrop; Std dev = standard deviation.

Fm.	Loc.	samples	VR _r	n _{samples}	n _{total}	Std dev
P	1	302, 306	0.43	2	85	0.08
P	10	11, 12, 13, 15, 16, 17, 18, 19, 20, 21	0.33	10	479	0.05
P	11	228, 271	0.44	2	41	0.07
P	21	33	0.48	1	57	0.07
V	24	56, 57, 58	0.51	3	148	0.07
V	31	262	0.51	1	97	0.03
V	32	250, 251	0.63	2	165	0.06

Table 5.5 Various molecular ratios calculated from the saturated hydrocarbon fraction. Loc. = Location, Fm. = Formation (P = Pakhna, V = Vlambouros).

Sample	Loc.	Fm.	Pr/Ph ^a	Pr/n-C ₁₇	Ph/n-C ₁₈	TAR ^b	CPI ^c	OEP ^d
17	10	P	1.91	1.27	0.59	8.57	2.56	1.59
18	10	P	1.03	0.43	0.53	3.01	3.35	1.84
19	10	P	1.07	0.76	0.82	10.29	3.08	1.91
20	10	P	0.63	0.26	0.32	3.98	2.53	1.43
33	21	P	1.08	0.37	0.54	4.98	2.23	1.22
233	20	P	1.40	0.37	0.23	8.59	2.34	1.17
272	11	P	0.98	0.47	0.43	2.72	2.56	1.25
286	2	P	1.27	0.36	0.26	3.82	3.08	1.49
296	2	P	2.05	0.58	0.46	6.72	4.39	1.45
297	1	P	1.19	0.27	0.29	1.25	1.78	0.43
302	1	P	1.26	0.34	0.37	0.66	2.91	2.08
306	1	P	0.98	0.39	0.41	7.40	3.35	1.29
56	24	V	2.09	0.83	0.46	1.44	0.49	0.95
250	32	V	3.44	1.13	0.28	0.04	0.43	0.10
262	31	V	2.50	0.77	0.31	0.51	0.93	1.26

^apristane/phytane, ^bTerrigenous Aquatic Ratio = $(n-C_{27} + n-C_{29} + n-C_{31}) / (n-C_{15} + n-C_{17} + n-C_{19})$

^cCarbon Preference Index = $((2 * (n-C_{23} + n-C_{25} + n-C_{27} + n-C_{29})) / (n-C_{22} + 2 * (n-C_{24} + n-C_{26} + n-C_{28}) + n-C_{30}))$

^dOdd Even Predominance = $(n-C_{21} + 6 * n-C_{23} + n-C_{25}) / (4 * n-C_{22} + 4 * n-C_{24})$

Table 5.6 Hopane and sterane ratios obtained from the saturated fraction. [---] = no results obtained. Loc. = Location, Fm. = Formation (P = Pakhna, V = Vlambouros).

Sample	Loc.	Fm.	Regular steranes					Hopanes					
			C ₂₇ [%]	C ₂₈ [%]	C ₂₉ [%]	20S/ (20S+20R)	αβ/ (αα+αββ)	Ts/ (Ts+Tm)	GI*	C ₂₂ /C ₂₁	C ₂₄ /C ₂₃	C ₂₆ /C ₂₅ tricyclic	C ₂₉ /C ₃₀
17	10	P	33	31	36	0.22	0.35	0.28	0.27	0.39	0.60	0.52	0.46
18	10	P	39	27	33	0.28	0.29	0.18	0.55	0.31	0.48	0.65	0.44
19	10	P	37	28	34	0.14	0.28	0.12	0.23	0.37	0.58	0.94	0.41
20	10	P	42	26	31	0.21	0.32	0.17	0.04	0.35	0.44	0.64	0.34
33	21	P	33	27	40	0.14	0.39	0.20	0.72	0.40	0.54	0.76	0.41
233	20	P	34	22	44	0.15	0.36	0.29	0.40	0.51	0.51	0.62	0.02
272	11	P	37	25	39	0.06	0.25	0.06	0.37	0.42	0.48	0.82	0.44
286	2	P	39	27	34	0.23	0.41	0.24	0.33	0.39	0.52	0.80	0.47
296	2	P	38	30	32	0.33	0.39	0.25	0.78	0.42	0.50	0.80	0.54
297	1	P	41	22	37	0.25	0.38	0.31	0.88	0.37	0.48	0.82	0.91
302	1	P	37	29	34	0.14	0.29	0.20	0.49	0.27	0.51	0.91	0.43
306	1	P	36	31	34	0.31	0.45	0.25	0.54	0.48	0.54	0.73	0.37
56	24	V	---	---	---	---	---	---	---	---	---	---	---
250	32	V	39	27	34	0.30	0.33	0.14	1.42	0.45	0.50	0.74	0.48
262	31	V	38	21	40	0.28	0.37	0.19	0.28	0.38	0.47	0.77	0.00

*Gammacerane Index = $(10 \times \text{gammacerane}) / \text{C30 hopane}$

In the present case, the first effect is considered to be of less importance, since the microscopic investigation of the samples show mainly fresh pyrite (Fig. 5.6 A and C), which is usually more vulnerable to weathering than OM (Littke, 1993). Only one sample with intensely weathered pyrite could be observed (Fig. 5.6 G and H).

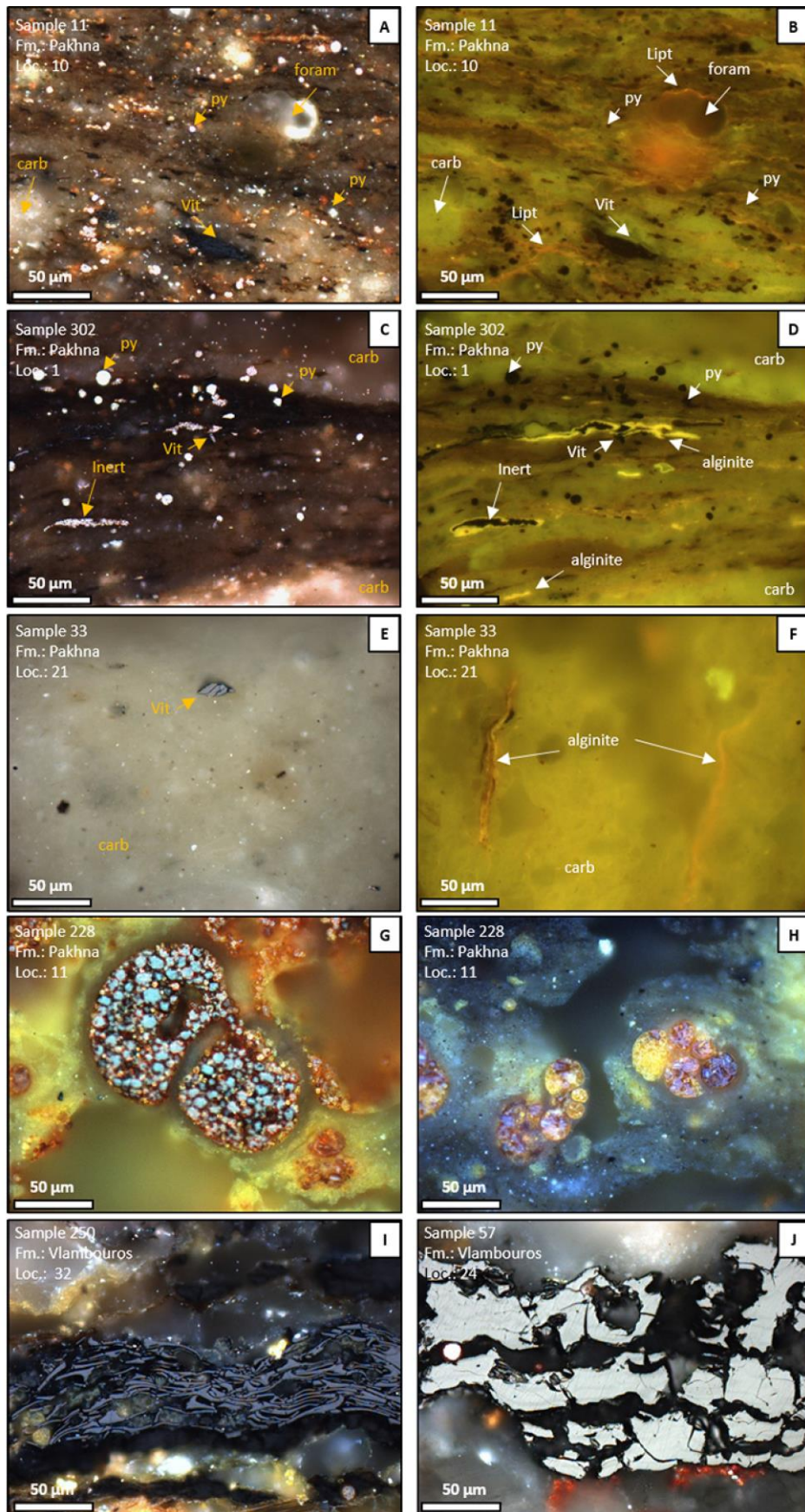


Fig. 5.6 figure caption on next page

Caption Figure 5.6 Reflected light (A, C, E, G, H, I, J) and fluorescence (B, D, F) microphotographs. (A and B) Representative sample for the organic-rich sections of the Pakhna Formation (Fm.) from location (Loc.) 10. The sample is composed of a fine-grained siliciclastic matrix with patchy carbonate (carb). Pyrite (py) is mainly present as framboids. Organic matter (OM) is mainly present as fine, disseminated liptinites (Lipt) as indicated by the yellowish background fluorescence (B). Only small amounts of terrestrial particles such as vitrinites (Vit) can be observed. The OM as well as the pyrite framboids seem to be more abundant in the more siliciclastic parts, while foraminifera (foram) can rather be observed in the more calcareous parts. (C and D) Representative sample for the organic-rich sections of the Pakhna Fm. from Loc. 1. Additionally to liptodetrinite, alginites can be observed parallel to the bedding planes. Many pyrite framboids show diameters $>5 \mu\text{m}$. OM seems to be related to the more clastic parts. (E and F) Representative sample of the less organic-rich samples of the Pakhna Fm. from the southwestern outcrops (Loc. 11, 12, 20, 21). The samples are characterized by more calcareous deposits and a reduced abundance of amorphous liptinites. Alginites can still be observed but are here also present in the calcareous parts (F). (G and H) Sample 228 is the only sample from the Pakhna Fm. where intense pyrite weathering could be observed. The pyrite is partly present as pore filling within foraminifera. I & J) Large vitrinite (Vit) and inertinites (Inert) particles with recognizable cell structures in the Vlambouros Fm. at Loc. 32 and 24, respectively.

To investigate the other two possible effects, Rock-Eval[®] results obtained from 11 representative bulk rock samples of the Pakhna Fm. were compared with their corresponding TOM concentrates (Table 5.3). Figure 5.7 A and B illustrate the Rock-Eval[®] pyrograms for the bulk rock and TOM aliquotes of one high (Fig. 5.7 A) and one low TOC (Fig. 5.7 B) sample normalized by the TOC content and the sample weight. It can be seen that a high proportion of thermovaporized and pyrolyzable HC is retained by the mineral matrix. The effect is stronger in the sample with the lower bulk TOC content (Fig. 5.7 B). This effect causes higher HI values for the TOM concentrates (Table 5.3). At the same time, the OI values are lower (Table 5.3). Both, the increase in the HI and the decrease in the OI seem to be more pronounced if the bulk rock samples show low TOC contents (Fig. 5.7 C). As a result of both effects, the TOM concentrates plot closer to the kerogen Type II pathway than the respective bulk rock samples (Fig. 5.7 D) and are in accordance with the classical kerogen classification based on the H/C vs. O/C atomic ratios (Fig. 5.7 E). Although Rock-Eval[®] analysis for bulk rock samples is a standard technique in petroleum exploration, the HC generation potential might be severely underestimated, especially for samples with low-moderate TOC content if measured on bulk rock.

Thermal maturity of sedimentary OM is another crucial parameter for the characterization of source rocks since their hydrocarbon generation potential changes with thermal maturation and the related loss of functional groups (e.g. Peters et al., 2005; Zieger et al., 2018). Thermally, the Vlambouros samples are marginally mature as indicated by Rock-Eval[®] T_{max} values between 434 and 442°C and VR_r values of 0.51 to 0.63% (Table 5.2 and 5.4; Fig. 5.8 A). The Pakhna samples are thermally immature as indicated by T_{max} values between 424 and 428°C and VR_r values of 0.33 to 0.48% (Table 5.2 and 5.4; Fig. 5.8 A). The very low thermal maturity in both formations is further supported by the predominance of odd-numbered *n*-alkanes (Fig. 5.9 A) expressed by a carbon preference index (CPI) or odd-even

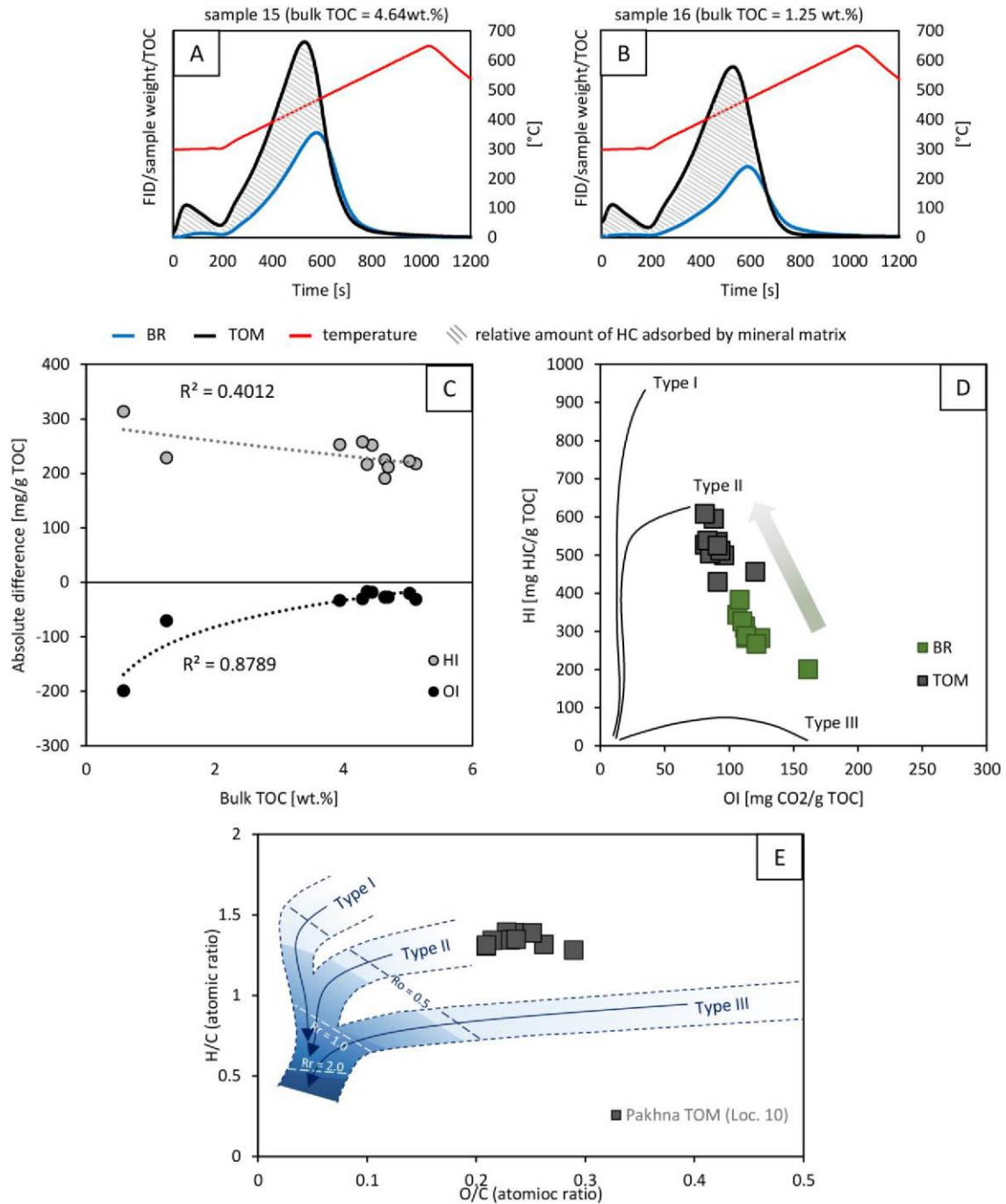


Fig. 5.7 (A and B) Comparison of Rock-Eval® pyrograms for the bulk rock (BR) and the respective total organic matter (TOM) concentrates of two Pakhna samples. For comparison, the curves are normalized to the sample weight and the respective total organic carbon (TOC) content. (A) It can be seen that a large proportion of the thermovaporized and pyrolyzable hydrocarbon (HC) is retained by the mineral matrix. (B) The effect is even more prominent if the bulk TOC is lower. (C) The absolute difference between bulk and TOM HI and OI in the Pakhna samples seems to decrease with increasing bulk TOC content. (D) The Pakhna TOM concentrates plot closer to the kerogen Type II pathway than the respective bulk rock samples in the pseudo van Krevelen diagram and correlate better with the elemental results (E). Loc.=Location.

predominance (OEP) mostly > 1 (Table 5.5) as well as by the preference of 20R- and $\alpha\beta$ -configuration of the analyzed steranes (Fig. 5.8 B, Table 5.6) (Bray and Evans, 1961; Peters et al., 2007).

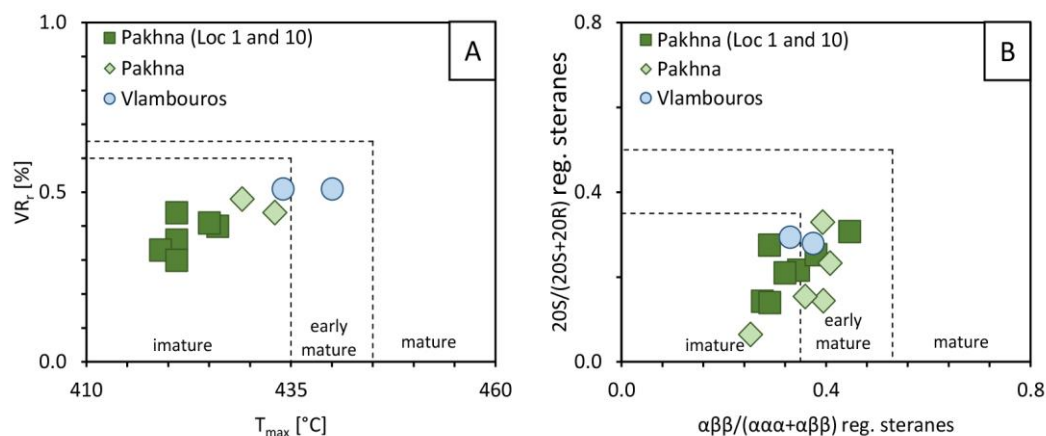


Fig. 5.8 Several thermal maturity parameters. (A) Random vitrinite reflectance (VRr) and Rock-Eval® T_{max} values indicate an immature state of organic matter with only the Vlambouros samples reaching up to early maturity. (B) The configuration of 20S/(20S+20R) and $\alpha\beta/(\alpha\alpha+\alpha\beta)$ regular steranes indicates an immature to early mature state for all samples.

All analyzed parameters indicate thermal immaturity of the Pakhna samples. Thus, it can be assumed that the obtained results represent the initial quality of the OM. The samples of the Vlambouros Fm. are marginal mature, so that the initial HC generation potential might have been slightly higher. Nevertheless, the HC generation potential of the Vlambouros samples is very low and the organic-rich intervals are only a few centimeters thick (Fig. 5.3). Therefore, this formation cannot be considered as a typical petroleum source rock.

The Pakhna samples, instead, especially the northeastern successions at Loc. 1 and 10 are of very good quality according to the classification by Peters et al. (2005). Furthermore, the actual HC potential might be even higher, due to the observed mineral matrix effect. However, it should be noted that the total observable thickness for this formation at the outcrop scale ranges between 10 to 20 meters, which is at the lower limit for high-quality source rocks.

5.5.3 Origin of organic matter and paleo-redox conditions

Petrographic (Fig. 5.6 I and J) and palynological observations (Fig. 5.10 D and 5.11) show that the OM in the Vlambouros Fm. is almost exclusively composed of large terrestrial particles. This is in accordance with the Rock-Eval® results (Fig. 5.5). Most of the woody particles are characterized as highly oxidized palynomacerals (PM) of Type 4 and 1 (Fig. 5.10 D and Fig. 5.11) pointing towards a deposition under oxygenated conditions (Tyson, 1995).

The investigated Pakhna samples are characterized by a fine grained siliciclastic and/or calcareous matrix (Fig. 5.6 A and C) comprising mostly disseminated, submicroscopical liptinites, which are identified by their green-yellowish fluorescence color under ultra-violet light excitation (Fig. 5.6 B and D). Also relatively abundant are larger liptinites like alginites, which are oriented parallel to the bedding (Fig. 5.6 D and F). Terrestrial macerals like vitrinites and inertinites are less common in all Pakhna

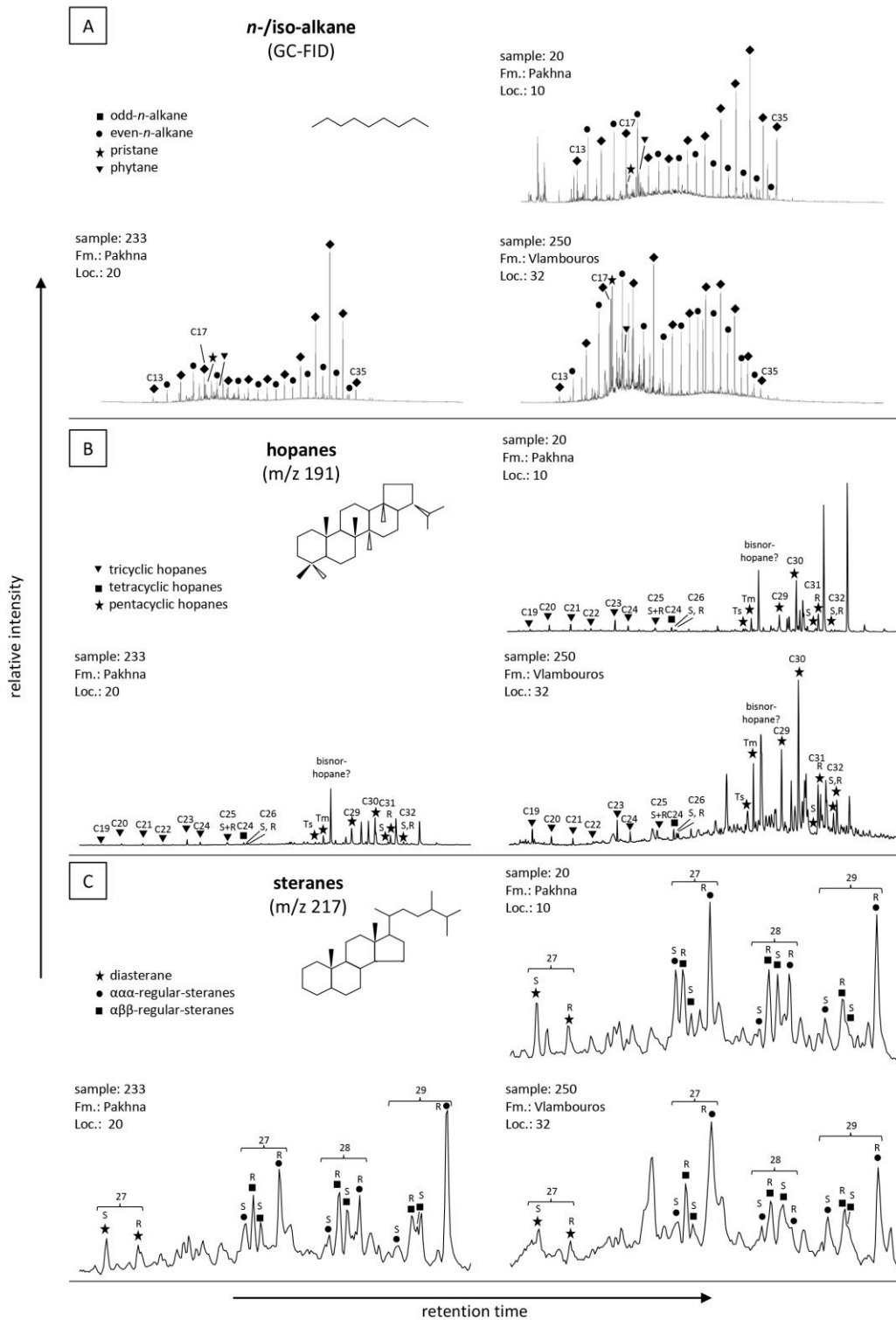


Fig. 5.9 Distribution of organic molecular compounds in the aliphatic fraction of representative samples of the Pakhna Formation (Fm.) from location (Loc.) 1 and 10 in the northeast (sample 20), and from the southwest (sample 233), and of the Vlambouros Fm. (sample 250). (A) Representative full chromatograms (GC-FID) showing distribution of *n*-alkanes and pristane (Pr) and phytane (Ph). (B) Mass chromatograms *m/z* 191 of the aliphatic fraction showing distribution of hopanes. (C) Mass chromatograms *m/z* 217 showing distribution of steranes.

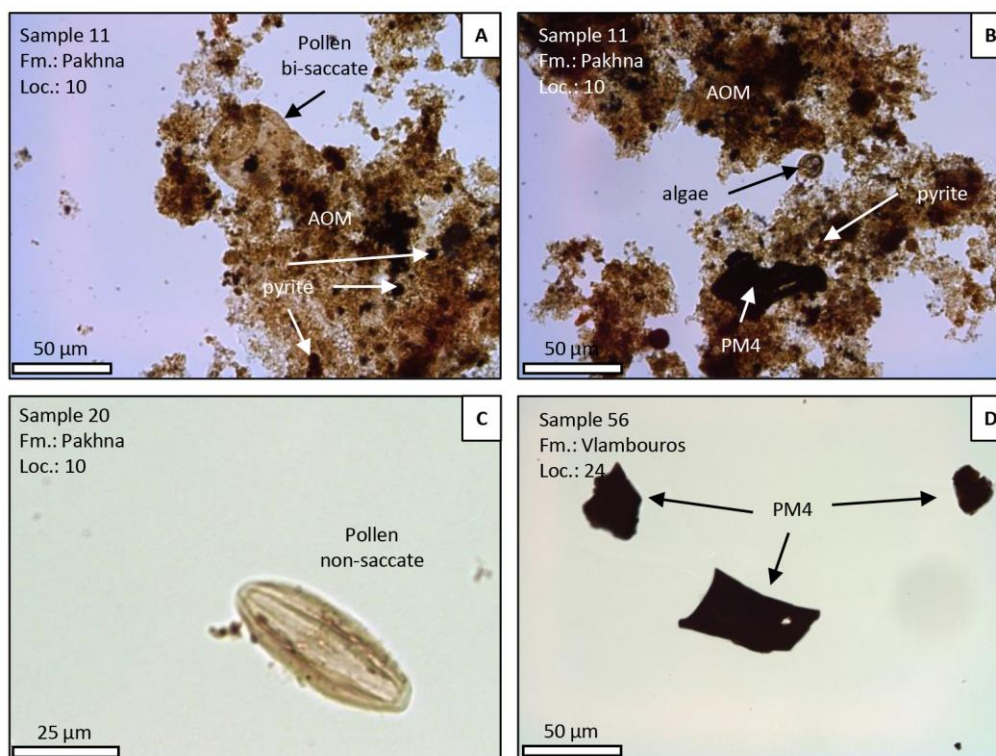


Fig. 5.10 Transmitted light microphotographs of palynological components. The general palynofacies of the Pakhna samples is represented by A and B: The largest percentage (up to >90%) is made up by amorphous organic matter (AOM) of dark brownish color which forms large, clumpy aggregates. Minor components include different types of pollen (A and C), highly oxidized palynomacerals (PM4) and algae. The Vlambouros samples are almost exclusively characterized by oxidized PM (D). For the statistical overview of the different compounds see Fig. 5.11.

samples. Especially in the samples from outcrops with thinner and less organic-rich intervals (mainly in the southwest) their abundance is low (Fig. 5.6 E).

Pyrite occurs mainly as epigenetic pore filling crystals in foraminifera in the samples from the outcrops with thinner and less organic-rich intervals (mainly in the southwest) (Fig. 5.6 G and H). In the samples of the thicker and more organic-rich intervals (Loc. 1 and 10, northeast) instead, syngenetic pyrite is highly abundant, often as large framboidal aggregates. Some of these framboids show diameters larger than 5 μm and a homogenous distribution of the individual crystals (Fig. 5.6 C). Under normal marine conditions pyrite growth starts in the anoxic pore waters below the sediment water interface resulting in crystals larger than 5 μm, while under anoxic conditions pyrite growth occurs in the water column resulting in crystals not larger than 5 μm. (Wilkin and Barnes, 1996; Wilkin et al. 1997). Thus, the depositional redox conditions of the Pakhna samples are interpreted to be dys- to partly anoxic.

In general, both OM as well as framboidal pyrite in the Pakhna samples are more abundant in the more siliciclastic parts of the rocks and less common in the more calcareous intervals. This observation can also be made at the outcrop scale. Hence, the original sediment composition before bacterial sulfate reduction was roughly calculated according to Littke (1993) (Fig. 5.12, see figure caption for detailed description). For the Pakhna samples, the amount of OM seems to increase with increasing silicate and

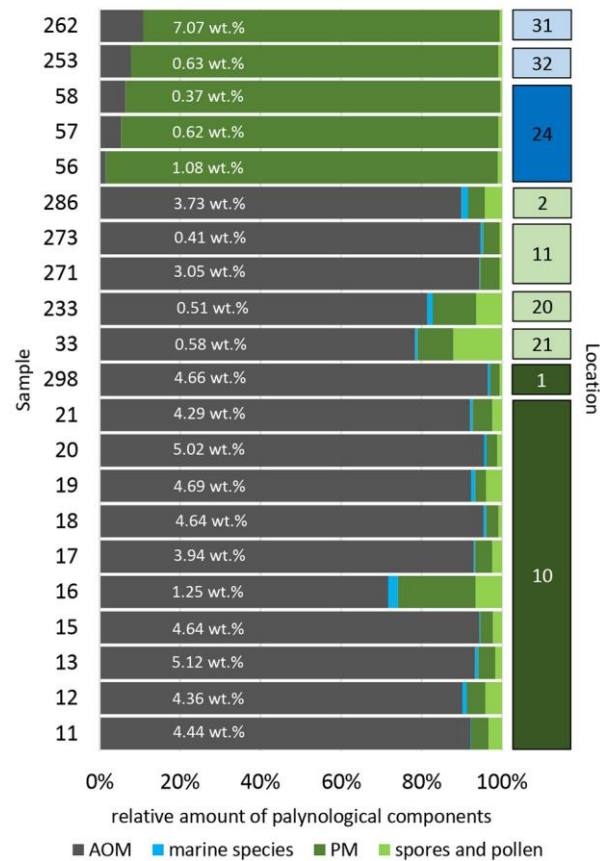


Fig. 5.11 Results of the palynological observations. Values expressed in wt% indicates the total organic carbon (TOC) content of the respective sample. The Pakhna samples are mainly (up to >90%) composed of amorphous organic matter (AOM). Terrestrial particles like palynomacerals (PM) are highly oxidized (mainly PM4 and PM1). Other terrestrial and marine constituents like spores, pollen, algae, and foraminifera are relatively constant to each other. Samples containing low TOC show also a decrease in the percentage of AOM. In the Vlambouros samples the OM is almost exclusively (> 90%) composed of highly oxidized PM.

decreasing carbonate content, indicating that nutrient supply and thus bioproductivity were positively affected by the deposition of siliciclastic material (Ricken, 1993).

Further parameters useful for the interpretation of paleo-redox conditions can be obtained from the abundance of TS, Fe, Ni, and V. Their concentrations are shown in Table 5.7. Bacterial sulfate reduction is controlled by the availability of OM. Thus formation of pyrite results under normal marine conditions in a positive correlation of TOC and TS values, with ratios varying around 2.5 (Berner, 1984). This is also the case for many of the Pakhna samples from southwestern Cyprus (Fig. 5.13 A). Oxygen depletion in the bottom water promotes bacterial sulfate reduction already in the water and leads to TOC/TS ratios lower than 2.5, as it can be observed for many Pakhna samples from eastern Cyprus (Fig. 5.13 A). Sulfate-depleted freshwater environments result in significantly larger TOC/TS ratios, as observed for most of the Vlambouros samples (Fig. 5.13 A).

Another redox indicator is the ratio of $V/(V + Ni)$. For the Pakhna samples, these ratios are quite high (Fig. 5.13 B) representing Eh conditions that are only reached under conditions of enhanced bacterial sulfate reduction (Lewan, 1984). To verify whether the measured TS originates from pyrite

Table 5.7 Elemental concentrations in the bulk rock samples. [---] = not measured. Loc. = Location, Fm. = Formation (P = Pakhna, V = Vlambouros), TS = total sulfur, Fe = iron, Ni = nickel, V = vanadium.

Sample	Loc.	Fm.	TS [wt.%]	Fe [wt.%]	Ni [ppm]	V [ppm]
11	10	P	2.54	2.67	128	225
12	10	P	2.77	3.73	163	315
13	10	P	3.73	4.15	164	235
15	10	P	2.85	3.28	152	244
16	10	P	1.17	2.00	101	122
17	10	P	2.86	3.48	138	245
18	10	P	2.64	3.14	140	213
19	10	P	2.62	3.43	139	245
20	10	P	3.19	3.93	172	246
21	10	P	2.76	3.39	135	233
33	21	P	0.07	1.33	90	367
271	11	P	0.48	---	---	---
272	11	P	0.33	---	---	---
273	11	P	1.05	0.49	45	31
274	10	P	1.10	---	---	---
275	10	P	1.66	2.65	89	101
276	10	P	1.13	2.52	107	166
277	10	P	2.77	3.31	148	204
279	10	P	2.55	2.99	125	179
280	10	P	1.9	2.55	74	167
281	10	P	2.18	2.93	125	207
282	10	P	1.16	1.91	49	85
283	10	P	3.2	3.3	146	263
285	10	P	3.08	4.07	170	235
286	2	P	0.69	---	---	---
287	2	P	0.10	---	---	---
288	2	P	0.14	---	---	---
289	2	P	0.14	---	---	---
290	2	P	0.19	---	---	---
291	2	P	0.14	---	---	---
292	2	P	0.36	---	---	---
293	2	P	1.89	---	---	---
294	2	P	1.96	3.62	157	283
295	2	P	0.81	---	---	---
296	2	P	0.77	---	---	---
297	1	P	6.20	---	---	---
298	1	P	1.55	2.98	175	325
299	1	P	2.08	2.91	120	272
300	1	P	1.15	2.71	127	280
301	1	P	1.47	---	---	---
302	1	P	1.97	3.16	144	285
303	1	P	1.94	3.56	128	231
304	1	P	2.42	2.88	119	152
305	1	P	2.77	2.49	116	240
306	1	P	1.34	2.52	94	202
56	24	V	0.24	2.50	162	70
57	24	V	0.25	1.95	325	66
58	24	V	0.21	1.94	326	62
250	33	V	0.90	11.05	32	160
251	33	V	0.10	3.52	184	114
252	33	V	0.09	---	---	---
253	33	V	0.12	---	---	---
254	32	V	0.57	---	---	---
260	32	V	0.10	2.89	44	149
261	32	V	0.48	---	---	---
262	32	V	0.39	1.21	51	145
264	32	V	0.80	---	---	---

and is not to a major percentage of organic origin, TS and Fe contents were compared (Dean and Arthur, 1989). For the analyzed set of samples, TS/Fe ratios smaller than 1.15 indicate that sulfur is mainly present in the form of iron sulfide, in agreement with other interpretations (Fig. 5.13 C). Thus, all elemental data indicate dys- to anoxic conditions for the Pakhna samples and oxic- to dysoxic freshwater conditions for the Vlambouros samples.

Another set of data are specific biomarker ratios which are useful to interpret the origin of OM and the redox conditions during deposition (Tables 5.5 and 5.6, Fig. 5.14 and 5.15). The ratio of Ph/*n*-C₁₈ vs Pr/*n*-C₁₇ (Fig. 5.14 A and B) confirms a mainly terrestrial type of OM deposited under oxic conditions for the Vlambouros samples. In contrast, C₂₇-steranes (Fig. 5.14 C and 5.15) indicate for two samples

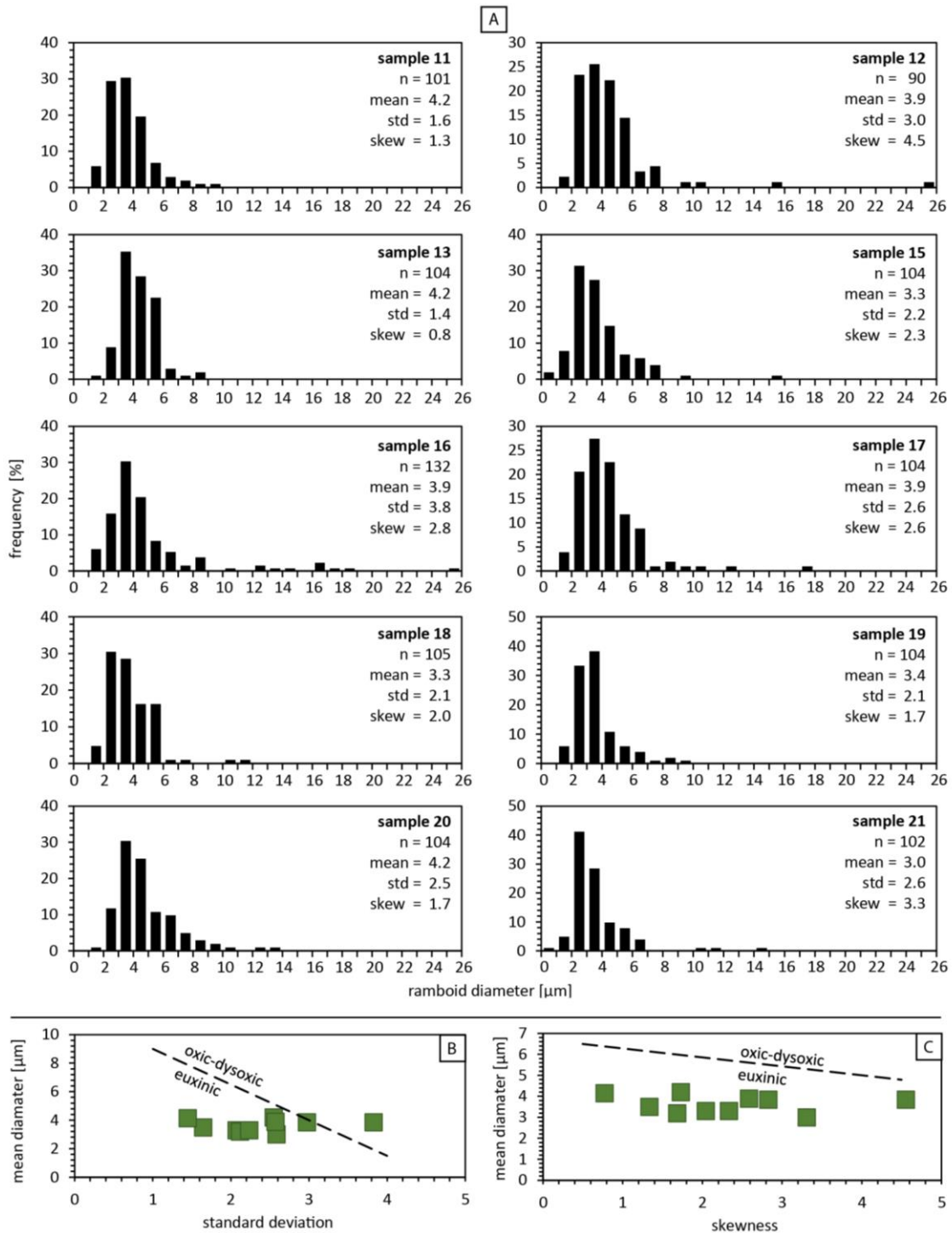


Fig. 5.12 Results of the pyrite framboid size distribution in Pakhna samples originating from location 10. (A) Histograms showing the distribution of pyrite framboid diameters (bin size=1 µm). n=number of measured framboids, mean=mean framboid diameter, std.=standard deviation to mean value, skew=skewness of distribution. (B) and (C) plot of the mean framboid diameters vs. the standard deviation and skewness of the distribution, respectively, pointing towards euxinic/anoxic conditions (plots after Wilkin and Barnes, 1996).

also a contribution of marine OM, which, however seems reasonable, as a deltaic environment is assumed for this formation.

Biomarker ratios indicate a marine to mixed type of OM for most Pakhna samples and the redox conditions are interpreted as oxygen depleted (Fig. 5.14 A, B, C). The ratio of C₂₇-, C₂₈-, and C₂₉ regular

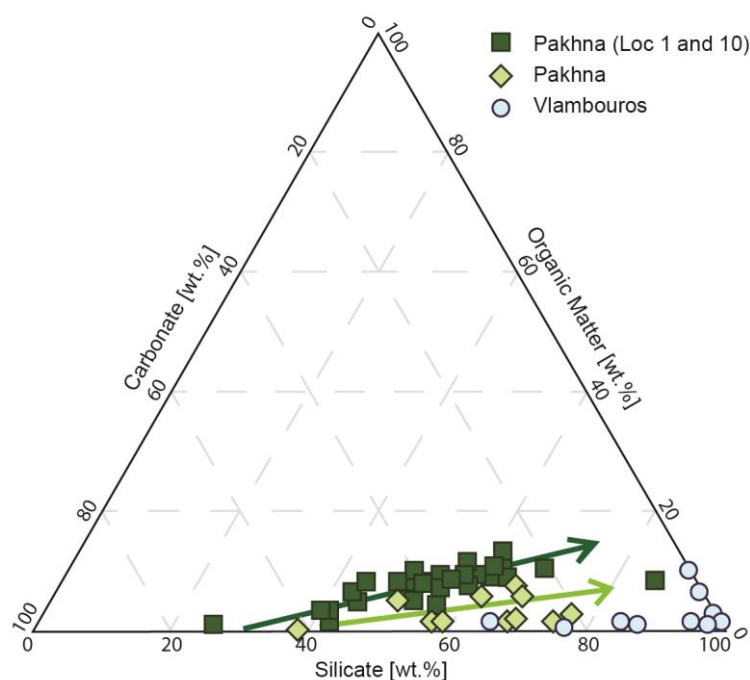


Fig. 5.13 Ternary diagram showing the original sediment composition calculated according to Littke (1993) under the assumption that all sulfur now present as pyrite/marcasite is derived from early diagenetic sulfate reduction and organic carbon oxidation. 2 mol carbon are lost in order to create one mole of (reduced) sulfur: $TOC^* = TOC \times 2S \times (MC/MS)$ with TOC^* : TOC (total organic carbon) before bacterial sulfate reduction, S : sulfur content, MC and MS : Mmolar mass of carbon and sulfur, respectively. $M^* = TOC^* \times (COM)$ with OM^* =original organic matter, COM : carbon percentage in the OM (here an average of 70% is assumed for marine organic matter; see Stock et al., 2017). In the Littke plot, the carbon (Carb) content is determined based on the elemental carbon analysis and the silicate (Sil) content is calculated as $Sil = 100 - \%OM^* - \%Carb$. The Pakhna samples (especially samples from the northeastern locations (Loc.) 1 and 10) show a tendency to increasing OM with increasing silicate and decreasing carbonate content, respectively, while the OM in the Vlambouros samples shows no correlation.

steranes confirms a marine environment (Fig. 5.16). Furthermore, very low (<1) Gammacerane Index values disagree with high salinity, i.e. there was no high salinity event before the Messinian salinity crisis. Tricyclic hopanes C_{22}/C_{21} vs. C_{24}/C_{23} (Fig. 5.14 D) indicate carbonate-dominated to siliciclastic marine conditions, in accordance with lithological and petrological observations.

5.6 General discussion and hypothesis on the offshore area

The integrated geochemical and petrographic analysis of 147 Mesozoic to Cenozoic outcrop samples from onshore Cyprus prove the existence of organic-rich intervals in the Triassic Vlambouros Fm. as well as in the Miocene Pakhna Fm.

Samples of the Vlambouros Fm. comprise early mature gas-prone Type III kerogen, which was deposited under oxic conditions. These samples are mainly representative of thin, clay-rich layers interbedded between massive sandstone packages. However, even in some of the sandstones, terrestrial organic particles could be proven, leading to elevated concentrations of TOC in these intervals.

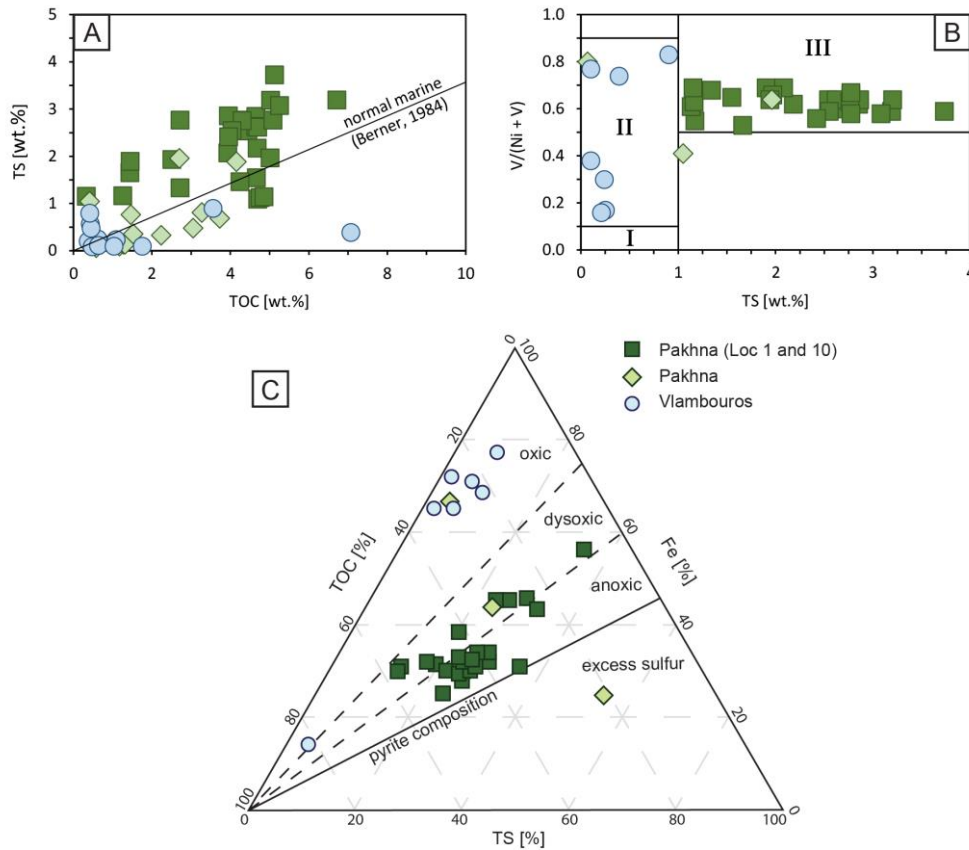


Fig. 5.14 Various elemental ratios to interpret paleo-redox conditions. (A) D) Total sulfur (TS) vs. total organic carbon (TOC) contents (Berner, 1984). (B) TS vs. vanadium-nickel fraction ($V/(Ni+V)$). The three fields with the roman numbers correspond to the stability regimes of different species as proposed by Lewan (1984). (C) Ternary diagram showing the relative concentration of total organic carbon (TOC), total sulfur (TS) and iron (Fe). Diagram after Dean and Arthur (1989) and Racka et al. (2010). For samples which have excess iron, it can be assumed that most sulfur is incorporated in pyrite. In total, the Pakhna samples are interpreted as dys- to anoxic conditions, while the samples of the Vlambouros Fm. are related to oxic, sulfate-depleted conditions.

Samples of the Pakhna Fm. reveal immature, medium to high quality, marine, oil- and gas-prone Type II kerogen. However, biomarker analysis shows that also subordinate terrestrial material is present. The following sections present a first depositional concept for the larger area, which could explain why the Miocene organic-rich deposits are present east of the Troodos Mountain and almost absent in the southern parts of the island.

5.6.1 Mechanisms of source rock deposition (Pakhna Fm.)

The distribution of OM within the Pakhna Fm. is proposed to be the result of (1) the tectonic setting combined with (2) paleo-climatic, and (3) local and regional paleo-geographic conditions during the Late Miocene:

- 1) The collision of the ESM with the Troodos Ophiolite during the Miocene caused the formation of several small piggy-back basins along the Cyprus Arc. Simultaneously, the Cyprus area experienced a strong uplift, with the strongest uplift occurring in the southern-central part of the island (Symeou et al., 2018).

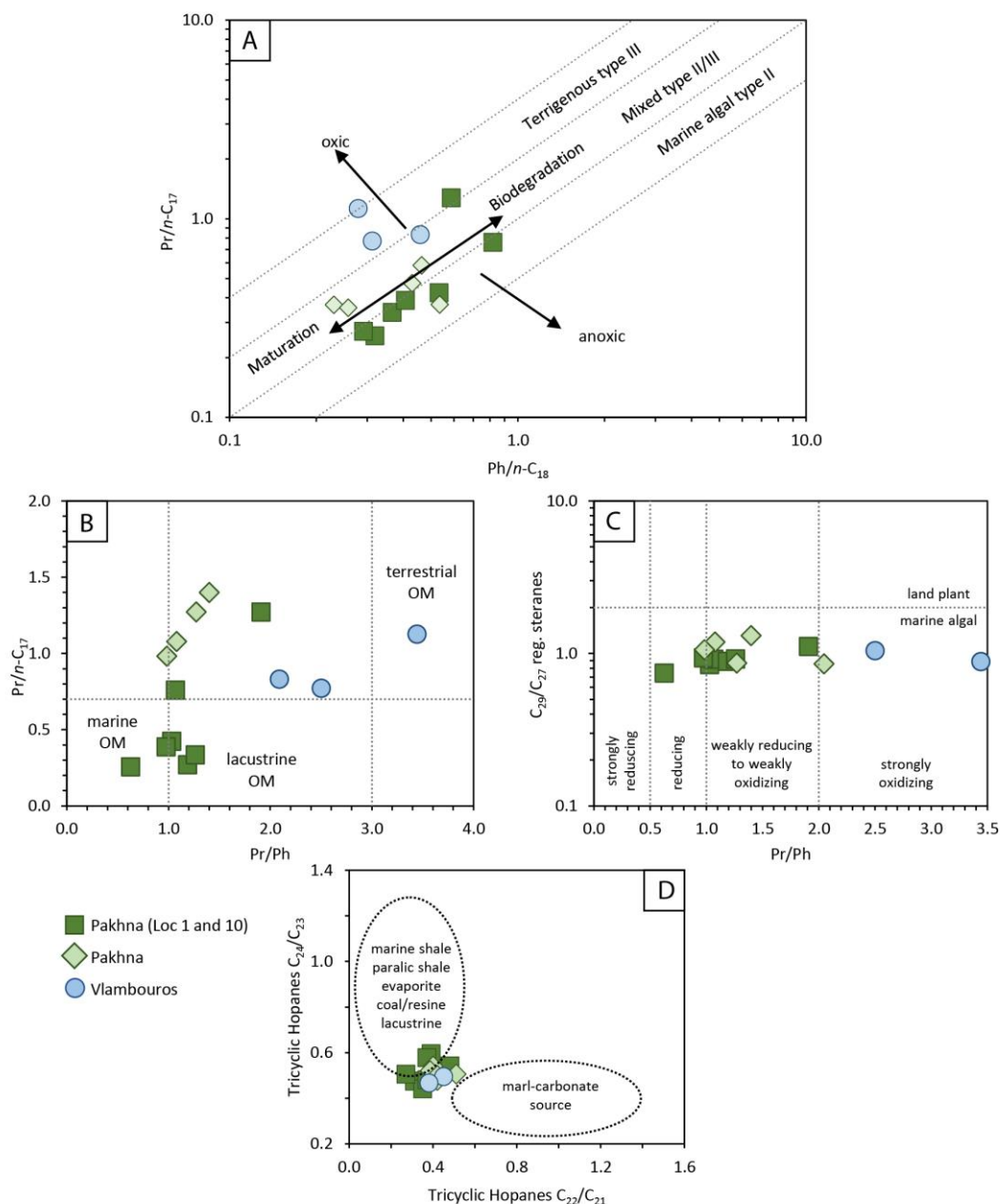


Fig. 5.15 Various biomarker ratios to determine source of organic matter (OM) and paleo redox-conditions. (A) Pristane (Pr) over *n*-C17 vs. Phytane (Ph) over *n*-C18 indicating oxygen depleted conditions for the Pakhna samples. Samples from Location (Loc.) 1 and 10 seem to be slightly more oxygen depleted than samples from the other outcrops. The samples of the Vlambouros Formation (Fm.) indicate more oxic conditions. (B) Pr/*n*-C17 vs. Pr/Ph indicating a mainly marine/aquatic source of OM for Pakhna samples from Loc. 1 and 10, while the other Pakhna samples as well as the Vlambouros samples indicate also a contribution of terrestrial OM. (C) The ratio of C29 to C27 regular steranes, however, indicates for all samples a mainly marine algal source. (D) According to the ratio of tricyclic hopanes C24/C23 vs. C22/C21 the depositional setting is to interpret as somewhat between a marly-carbonaceous source and a more marine or freshwater dominated environment. Loc.=Location.

- 2) Climatic conditions during the Late Miocene, with mainly west to east oriented ocean and wind currents, were comparable to those that can be observed today in the Mediterranean region (Kouwenhoven and van der Zwaan, 2006; Rohling et al., 2015). However, during the Late Miocene (already before the MSC), the sea level was significantly lower than today (Haq et al., 1988). Under this low sea level, the uprising island of Cyprus, the ESM, as well as the large

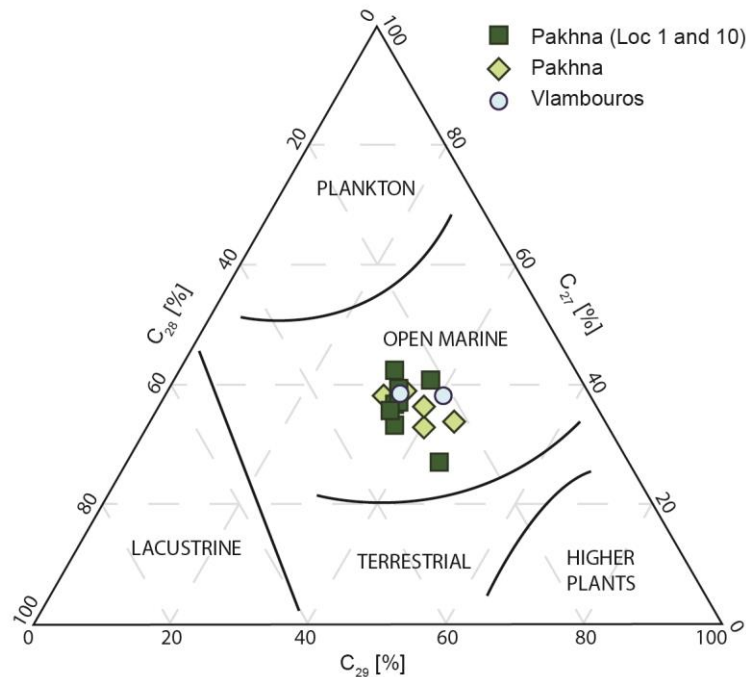


Fig. 5.16 Relative distribution of C27 to C29 regular steranes showing a mainly marine source of organic matter (OM) for the Pakhna samples and partly increased terrestrial influence in the Vlambouros samples. Paleoenvironmental and source interpretation after Huang and Meinschein, 1979). Loc.=Location.

Nile Cone Delta might have acted as barriers protecting the easternmost part of the Eastern Mediterranean Sea from high energy water currents. A consequence would have been calmer water bodies, where less mixing took place enhancing the chance of oxygen depletion, as shown by the presented data.

- 3) Bioproductivity largely depends on the availability of nutrients (Nixon et al., 1986), which are usually derived from terrestrial sources together with clastic material (Van der Zwaan and Jorissen, 1991). Related to the paleo-geographic and topographic setting during the Late Miocene, the input of nutrients into the Mesaoria and Cyprus basins is likely to have been significantly higher than into basins located south of the Troodos Mountain. While the local terrestrial supply towards the Khalassa and Maroni Basin was restricted to the Troodos as source area, the Mesaoria and Cyprus basins were also fed by the already emerged Kyrenia Range in the north. More regional sources for terrestrial input at that time were the Nile Cone Delta in the south, the uprising Levant Margin in the east (Nader, 2014), and probably also the Latakia region at the northeastern edge of the Levant Basin (Hawie et al., 2017). Favored by the isolated, calm water environment, plumes of fine sediments and nutrients might have propagated over long distances towards the (south-) eastern rim of the barrier. Therefore, local as well as regional nutrient supply would have favored an increased bio-productivity in basins east of the Troodos.

Thus, a high bio-productivity together with calm waters might have led to oxygen depletion and the formation of dysoxic (to probably even anoxic) bottom waters and finally to the deposition and preservation of OM-rich intervals as they are described here for the eastern Paghna outcrops.

5.6.2 Implications on petroleum systems in the Eastern Mediterranean Sea

Due to the general lack of publically available well data in the Eastern Mediterranean Sea, any extrapolation from on- to offshore areas, especially in the Cyprus Arc region, is hard to accomplish. However, some assumptions can be made as follows:

Lapierre et al. (2007) suggest that the Late Triassic sediments of the Mamonia Complex represent remnants of the old northern passive continental margin of Gondwana. Hence, these sediments would correlate with those underlying the ESM in the southern offshore area of Cyprus, as well as the Levant Basin in general. Triassic rocks under the ESM are buried by 6 km of overlying strata and they are interpreted to be at depths of around 11 km in the deepest part of the Levant Basin (e.g. Montadert et al., 2014; Bou Daher et al., 2016). At such depths, similar gas-prone Type III kerogen bearing clay- and sandstone intervals like those observed in the Vlambouros Fm. might have produced thermogenic gas enriched in ethane, which was announced to be present in the recently discovered Calypso 1-field in Cyprus offshore block 6 (CyprusMail, 2018).

During the Late Miocene, increased bio-productivity and preservation of OM seem to have been restricted to the basins east of the Troodos Mountain, since almost no OM-rich deposited can be found in the southern area. This scenario is in accordance with the observations made by Grohmann et al. (2018), who could not prove any OM-bearing intervals within Miocene sections along the central and northern ESM. Respecting the above-explained local and regional factors (barrier effect of Troodos and ESM, calm water conditions, long distance transport of fine sediments and nutrients from Nile and northern Levant area), it can be assumed that similar constellations allowed the deposition of source rocks also at the northern and western margins of the Levant Basin. These locations, in particular, might be the southern flank of the Hecateus Rise and Latakia Ridge, as well as the southern and eastern flank of the ESM (Fig. 5.1). Hence, OM production would be mainly increased in front of these barriers. TOC contents might be similar to those observed onshore eastern Cyprus, but are expected to gradually decrease towards the deeper parts of the basin, depending on the extend of the created oxygen minimum zone.

Middle to Late Miocene clastic sediments, derived either from the Nile Cone Delta or from the Levant Margin, are described as fan and turbidite deposits reaching far into the northern Levant Basin (Hawie et al., 2013b). Their distal, sandy lobes are stacked over each other and are intercalated with more clay- (Hawie et al., 2013b; Hawie et al. 2017) and probably organic-rich deposits. Furthermore, numerical simulations performed by Schneider et al. (2016) have shown that sedimentation rates,

especially in the Middle and Upper Miocene, were favorable for biogenic gas generation almost throughout the whole deeper parts of the basin. With these assumptions, the Middle – Late Miocene successions would represent self-charging reservoirs, which are sealed by the Messinian salt.

For future perspective works, all geochemical results and the proposed conceptual depositional models presented here, can be tested and used by extending previous numerical depositional models (Hawie et al., 2017) towards the western margin of the Levant Basin. This will allow a better prediction of the lateral extent of potential source rocks in the Eastern Mediterranean Sea. Such source rock models in combination with biogenic as well as thermogenic petroleum system modeling (such as Schneider et al., 2016; Bou Daher et al., 2016) can provide an integrated approach, which can help to better understand and predict HC generation and accumulation in this underexplored frontier area.

5.7 Conclusion

The geochemical and microscopic investigation of a great number of Mesozoic to Cenozoic samples could prove the existence of organic-rich deposits onshore Cyprus. Such intervals were found within (1) the Triassic Vlambouros Fm. and (2) the Miocene Pakhna Fm. and can help do get a better idea of potential source rocks at the northwestern margin of the Levant Basin:

(1) Respective intervals in the Vlambouros Fm. are composed of thin clay layers, containing about 1 wt.% TOC in the form of terrigenous, gas-prone Type III kerogen. The OM shows early thermal maturity. The formation represents an extended depositional system formed at the northern continental margin of Gondwana, which is also to be expected in the basement of the ESM and the Levant Basin. There, similar gas-prone intervals might contribute to thermogenic gas, which was announced to be present in the Calyso 1 field, offshore Cyprus.

(2) Promising source rock intervals in the Pakhna Fm. are restricted to the upper part of the formation and were only observed east of the Troodos Mountain. Frequently occurring mud- to wackestone layers show TOC contents of about 4 wt.%. Rock-Eval HI values of 238 mg HC/g rock on average indicate presence of Type II and III kerogen. The OM is immature as indicated by VR_r values between 0.3 and 0.5 %. Comparison with TOM concentrates, biomarker analysis, and microscopic observations indicate that kerogen quality determined by Rock-Eval[®] pyrolysis on whole rock powders might be severely underestimated for immature rock samples containing low-moderate TOC contents.

The restriction of potential source rock intervals to the eastern basins around the Troodos might be related to local and regional tectonic and paleo-geographic conditions, favoring enhanced bio-productivity in that area. Comparable situations might have also been present along the southeastern flank of the ESM. These young source rocks were definitely affected by strong biogenic gas generation during and after the Messinian. Such gas has high preservation potential due to its young state of generation and the presence of excellent cap rocks.

Acknowledgements

We thank the Ministry of Energy, Commerce, Industry and Tourism and the Geological Survey Department of Cyprus for the field work permission and their help in organization. Further, we gratefully acknowledge the support of Dr. Zomenia Zomeni and Dr. Efthymios Tsiolakis who assisted us during our field work and provided an excellent introduction into the regional geology of Cyprus. We thank the technical staff of IFPEN, Sorbonne Université and RWTH Aachen University, especially Dr. Alireza Baniasad, who provided helpful assistance with respect to analytical work. Finally, we want to thank Dr. Nikolaus Papadimitriou and Dr. Vasilis Symeou for fruitful discussions, which helped to better understand the geological history of Cyprus and two anonymous reviewers, who provided important and constructive comments on an earlier draft of this manuscript.

IFP Energies nouvelles provided financial support for the doctoral research of S. Grohmann.

6 Characterization of Late Cretaceous to Miocene source rocks in the Eastern Mediterranean Sea: An integrated numerical approach of stratigraphic forward modeling and petroleum system modeling

An edited version of this chapter was peer-reviewed and accepted as: Grohmann, S., Fietz, S., Nader, F.H., Romero-Sarmiento, M.F., Baudin, F., Littke, R. (in press). Characterization of Late Cretaceous and Miocene source rocks in the Eastern Mediterranean Sea: An integrated numerical approach of stratigraphic forward modeling and petroleum system modeling. Basin Research.

Abstract

Stratigraphic forward modeling was used to simulate the deposition of Upper Cretaceous, Eocene, and Oligo-Miocene source rocks in the Eastern Mediterranean Sea and, thus, obtain a process-based, 3D prediction of the quantity and quality distribution of organic matter (OM) in the respective intervals.

Upper Cretaceous and Eocene models support the idea of an upwelling related source rock formation along the Levant Margin and the Eratosthenes Seamount (ESM). Along the margin, source rock facies form a narrow band of 50 km parallel to the paleo shelf break, with high total organic carbon (TOC) contents of about 1 to 11%, and HI values of 300 to 500 mg HC/g TOC. On top of the ESM, TOC contents are mainly between 0.5 and 3% and HI values between 150 and 250 mg HC/g TOC. At both locations, TOC and HI values decrease rapidly towards the deeper parts of the basin. In the Oligo-Miocene intervals, terrestrial OM makes up the highest contribution to the TOC content, as marine organic matter (OM) is diluted by high sedimentation rates. In general, TOC contents are low (<1%), but are distributed relatively homogeneously throughout the whole basin, creating poor quality, but very thick source rock intervals of 1 to 2 km of cumulative thickness.

The incorporation of these source rock models into a classic petroleum system model could identify several zones of thermal maturation in the respective source rock intervals. Upper Cretaceous source rocks started petroleum generation in the late Paleocene/early Eocene with peak generation between 20 and 15 Ma ca. 50 km offshore northern Lebanon. Southeast of the ESM, generation started in the early Eocene with peak generation between 18 and 15 Ma. Eocene source rocks started HC generation approximately 25 Ma ago between 50 and 100 km southeast of the ESM and reached the oil to wet gas window at present day. However, until today they have converted less than 20% of their initial kerogen. While the Miocene source rocks are mostly immature, Oligocene source rocks lie within the oil window in the southern Levant Basin and reached the onset of the wet gas window in the northern Levant Basin. However, only 10 to 20% of their initial kerogen have been transformed to date.

6.1 Introduction

The eastern Mediterranean Sea (Fig. 6.1) evolved to one of the world's most important hydrocarbon (HC) frontier exploration areas, after the discoveries of several large gas fields during the last decade. Next to the Nile Delta Cone, the eastern Mediterranean Sea features the Levant and the Herodotus basins, where the recent discoveries are either located in Miocene turbidites (such as the fields of Tamar and Leviathan offshore Israel, and the Aphrodite field offshore Cyprus) or in Mesozoic to Cenozoic shallow water carbonates (Zohr field offshore Egypt or Calypso and Glaucus offshore Cyprus). Both types are reported to be mainly sourced by gas of biogenic origin, although it is speculated that thermogenic petroleum systems exist in the region as well (e.g. Al-Balushi et al., 2016; Bou Daher et al., 2016; Barabasch et al., 2018).

In such new offshore frontier exploration areas, scientific as well as industrial challenges relate to high uncertainties and risks, which are associated to the general lack of well and core data. Seismic reflection data, which today are available for large parts of the eastern Mediterranean Sea, can certainly help to identify potential reservoir structures, yet the characteristics of reservoir rocks and sealing units

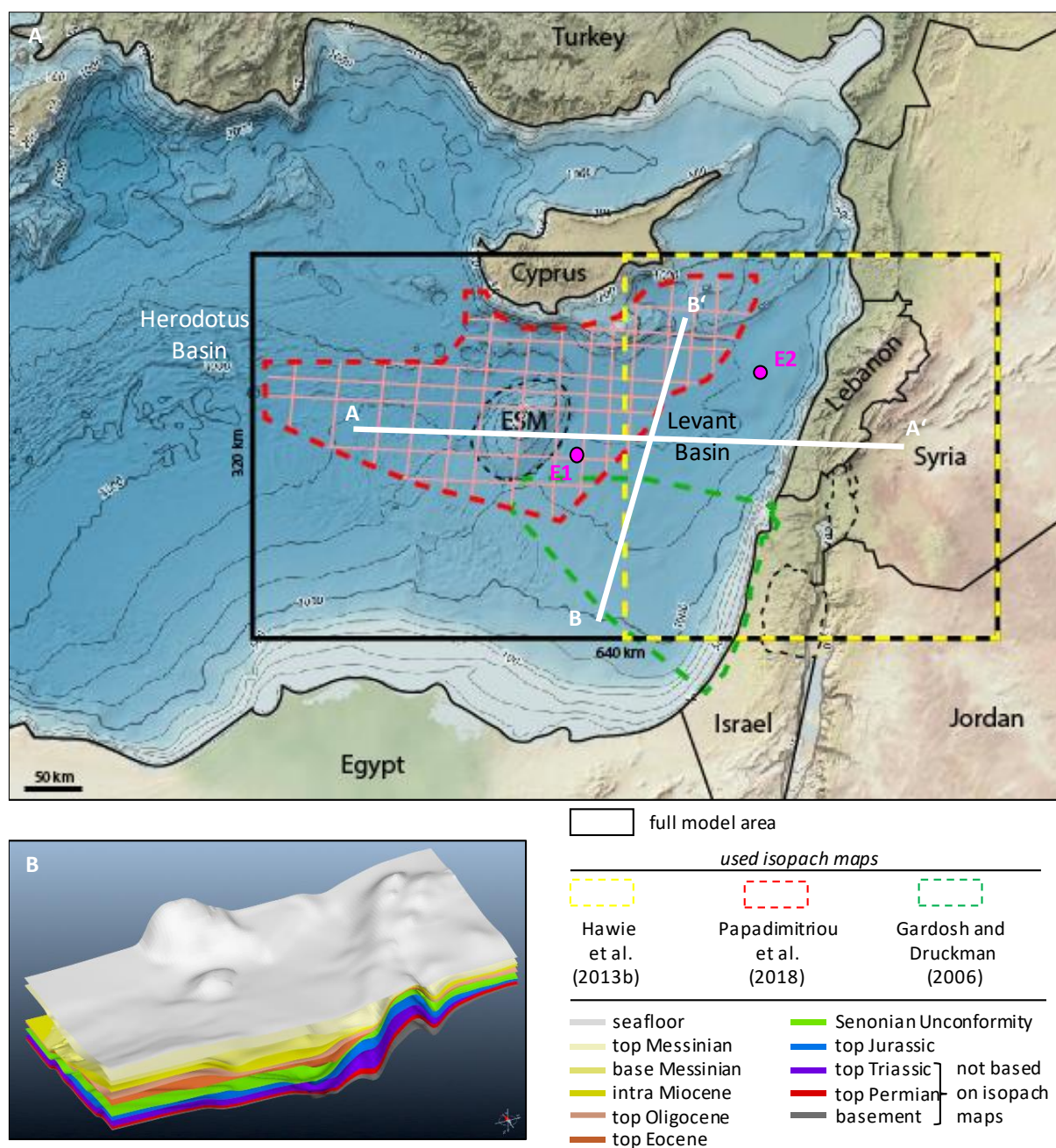


Fig. 6.1 A) Overview of the Eastern Mediterranean. Black rectangle showing the model area. Yellow and green dashed polygons show the zones where isopach maps provided by Hawie et al. (2013b) and Gardosh and Druckman (2006) were used to construct the eastern part of the static model. Red dashed polygon shows the area with new isopach maps of the Eratosthenes Seamount, provided by Papadimitriou et al. (2018). Profiles A-A' and B-B' of the respective petroleum system model are shown in Figure 9D and E. The burial history of locations E1 and E2 (pink dots) are illustrated in Figure 13. B) Depth horizons providing the base structure for the static model.

are hardly predictable based on seismic data only. Another crucial element of potential petroleum systems is the distribution, quality, and thickness of source rocks. Although there are possibilities to estimate the total organic carbon (TOC) content of a potential source rock based on special seismic reflection characteristics (Eastwell et al., 2018), a precise lateral and vertical prediction of the quantity and quality of sedimentary organic matter (OM) requires measured geochemical data and geological modeling. Therefore, additional information needs to be acquired from adjacent on- and offshore areas.

Potential Upper Cretaceous and Upper Paleocene source rock intervals have been proven along the eastern margin of the Levant Basin (e.g. Almogi-Labin et al., 1993; Bou Daher et al., 2014; Bou Daher et al., 2015) and in the Upper Paleocene (Bou Daher et al., 2016). At the southern margin, source rocks are present in Jurassic to Miocene intervals in northern Egypt (Shaaban et al., 2006). At the western margin of the basin, Upper Cretaceous and Upper Eocene source rock units occur within the sedimentary cover of the Eratosthenes Seamount (ESM) south of Cyprus (Grohmann et al., 2018). Onshore eastern Cyprus, thermally immature OM-rich have been identified within an Upper Miocene succession (Grohmann et al., 2019).

Simulation results from Bou Daher et al. (2016) demonstrate that present-day oil generation only takes place at great depth of more than 4,300 m in the center of the Levant Basin, within Paleogene and older sedimentary strata. Therefore, in terms of thermogenic petroleum systems, the basin-ward extent in quantity and quality of OM is the crucial uncertainty, which determines whether these sediments can be considered as actual HC producing source rocks. In addition, the lateral distribution of OM throughout the basin has to be known in order to achieve meaningful predictions of biogenic HC generation, which largely depends on a narrow temperature window and specific sedimentation rates (Schneider et al., 2016).

One way to address these uncertainties can be provided by stratigraphic forward modeling (e.g. Granjeon and Joseph, 1999), which allows the simulation of sedimentary processes and, hence, to generate a process based model of spatial and temporal distribution of the sedimentary infill of a basin. Such models have recently been provided for the Miocene (Hawie et al., 2017) and for the whole Mesozoic to Cenozoic geological history of the Levant Basin (Barabasch et al., 2018). However, both models focus on the general sedimentary infill of the basin and do not consider the distribution of OM. Further, both models include only the central part of the basin and its eastern margin, but not the western and southwestern margins, featuring the ESM and the Nile Delta Cone area, respectively.

For an accurate petroleum system evaluation in the Eastern Mediterranean, missing information on source rocks distribution and their properties is an essential knowledge gap. Therefore, the scope of this contribution is to present one large-scale numerical model including both the eastern and western margin of the Levant Basin, the latter covering the greater area of the ESM. In addition to the distribution of clastic and carbonate sediments, the production and sedimentation of OM is simulated for Upper Cretaceous to Miocene periods. The resulted models provide a quantitative estimation of the lateral and vertical distribution of source rock quality. They are also incorporated into a classic petroleum system model in order to identify zones of thermal maturation and determine where thermogenic petroleum might occur. The integration of stratigraphic forward modeling and petroleum system modeling on a unique numerical platform allowed a comprehensive understanding of the source rocks distribution as well as their varying capability to generate hydrocarbon. Hence, the approach presented in this contribution helps in de-risking exploration and could be applied on similar frontier hydrocarbon provinces.

6.2 Geological setting

The geodynamic evolution of the Eastern Mediterranean region started with the Pangea breakup in the Late Paleozoic with the disintegration of Gondwana and the opening of the Neotethys Ocean in the north of the Afro-Arabian plate (Fig. 6.2; Robertson et al., 2012). The initial rifting phase is proposed to have started in the Triassic followed by a main rift-drift event during the Early Jurassic (Segev and Rybakov, 2010; Hawie et al., 2013a; Hawie et al., 2013b; Ghalayini et al., 2014) leading eventually to the formation of the Herodotus Basin in the west and the Levant Basin in the East (Fig. 6.1). While the Herodotus Basin is believed to be floored with oceanic crust (Granot, 2016), the basement of the Levant Basin is supposed to consist of thin, stretched continental crust (Inati et al., 2016, 2018). Both basins are separated by a thick fragment of continental crust, the Eratosthenes Continental Block (ECB). On its top the Eratosthenes Seamount (ESM) evolved, which represents a huge carbonate platform (Emeis et al., 1996). Time-equivalent shallow water carbonate deposits have also been documented along the Levant Margin (Hawie et al., 2013a).

In the Late Cretaceous, the overall extensional setting changed to a compressional one when the Afro-Arabian plate moved northwards and a north-verging subduction zone evolved along the southern

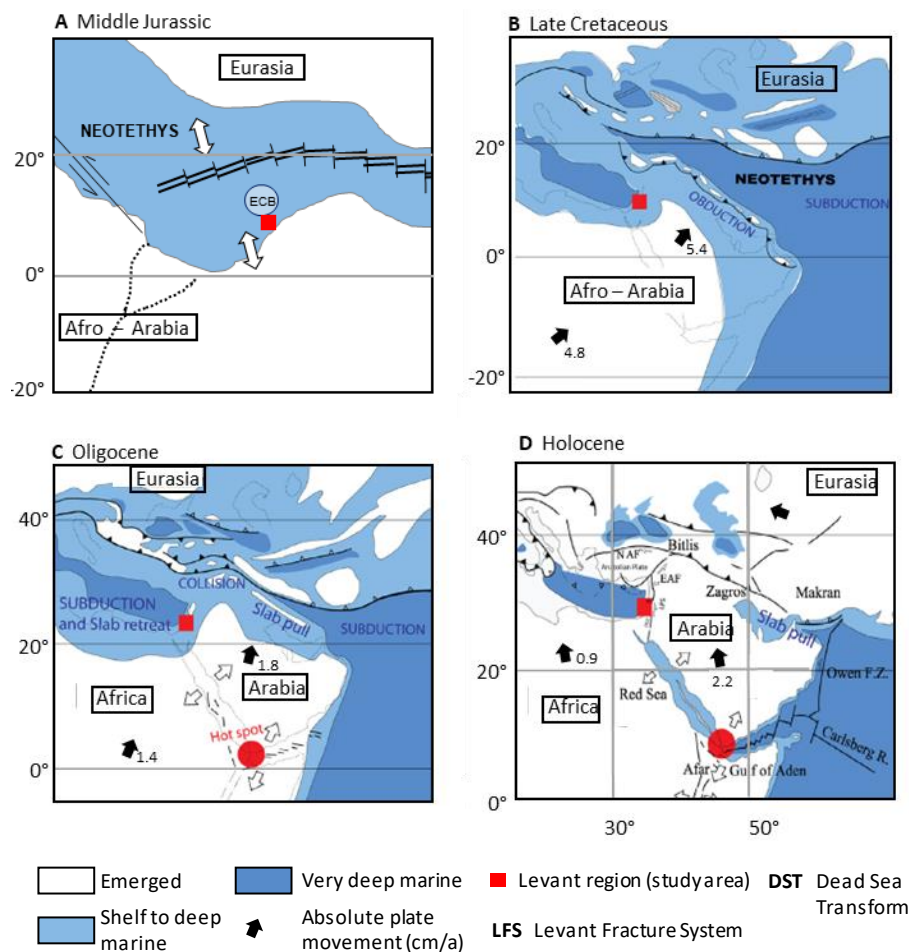


Fig. 6.2 Geological and tectonic evolution of the greater realm of the Eastern Mediterranean since the Middle Jurassic. (modified after Hawie et al., 2017 and Symeou et al., 2018).

margin of Eurasia (Hawie et al., 2013a; Montadert et al., 2014). Slab-pull related forces along the southern Eurasian Margin caused the formation of new oceanic crust and the obduction of several ophiolitic complexes (Fig. 6.2), such as the Troodos Ophiolite, which today represents the basement of the island of Cyprus (Pearce and Robinson, 2010). However, at that time, Cyprus was in a deep marine environment. A general sea level rise in the Late Cretaceous together with post-rift subsidence caused the drowning of the ESM as well as the whole Levant region leading to a more pelagic carbonate sedimentation throughout the area. Further, a large scale upwelling system affecting the whole Levant region is proposed to be responsible for the deposition of Upper Cretaceous source rocks along the Levant Margin (Almogi-Labin et al., 1993; Bou Daher et al., 2014; Bou Daher et al., 2015) and the ESM (Grohmann et al., 2018). Besides, upwelling-like processes above the ESM are believed to have taken place in the Eocene, resulting in the deposition of source rock intervals around the seamount (Grohmann et al., 2018).

In the Oligocene, the breakup of Afro-Arabia with an accelerated northward drift of the Arabian Plate initiated the ultimate isolation of the Mediterranean Basin and caused a strong uplift of the Levant Margin; thereby changing the overall carbonate dominated towards siliclastic-dominated depositional environments (e.g. Gardosh et al., 2008; Nader, 2014). Huge amounts of fine and coarse-grained clastic material were shed into the basin forming stacked turbidite features reaching far into the Levant Basin (Hawie et al., 2017). Mainly Oligocene but also Miocene source rocks are believed to be mainly responsible for the biogenic gas which was discovered during the last decade in the Eastern Mediterranean Sea. Since the Miocene, the ECB is in collision with the Troodos Ophiolite, which caused a strong local uplift and the rise of Cyprus above sea level (Robertson, 1998a; Galindo-Zaldivar et al., 2001).

6.3 Workflow

In the present study, *DionisosFlow*® and *TemisFlow*® software packages (*Beicip Franlab*) were used for stratigraphic forward and petroleum system modeling, respectively. For the 3D, present day structural representation of the model area, 3D depth maps are used (Fig. 6.1B). For the eastern Levant Basin and the onshore Levant Margin these maps are derived from seismic interpretation by Gardosh and Druckman (2006) and Hawie et al. (2013b) and new 3D maps of the greater ESM area are provided by Papadimitriou et al. (2018). The geometrical construction of the northern part of the Nile Cone Delta interpolated from a schematic cross section (Tassy et al., 2015).

6.3.1 Stratigraphic forward modeling

Stratigraphic forward modeling is based on the “source to sink” principle, where the spatial and temporal transport and deposition of sediments can be simulated per distinct time intervals on an initial paleo bathymetry (Fig. 6.3). The available net accommodation space for sediment deposition is provided by the combination of sea floor subsidence and the variations in paleo sea level (as provided by Haq et al., 1988). Subsidence maps are calculated based on the initial and final bathymetry of a simulated seismic package as well as its thickness. For the present model, a lateral resolution of 5 km x 5 km was chosen, while the vertical resolution represents time steps of 0.5 Ma. In the model, different sediments are defined by distinct properties, such as grain size, density, and their transport behavior expressed by an empirical diffusion equation, which vary between continental and marine environments, as well as between gravitational or fluvial driven transport:

$$Q_s = \left(\frac{K_{s_i}}{\nabla h} \right) - K_{w_i} Q_w^m S^n \quad [1]$$

Q_s : sediment flux (km²/a); k_{s_i} and k_{w_i} : diffusion coefficient for different processes (km²/a), and i referring to the respective sediment; h : elevation (m); Q_w : local water discharge in each cell (dimensionless); S : slope gradient in each cell; n and m : constant, between 1 and 2 (Tucker and Slingerland, 1994).

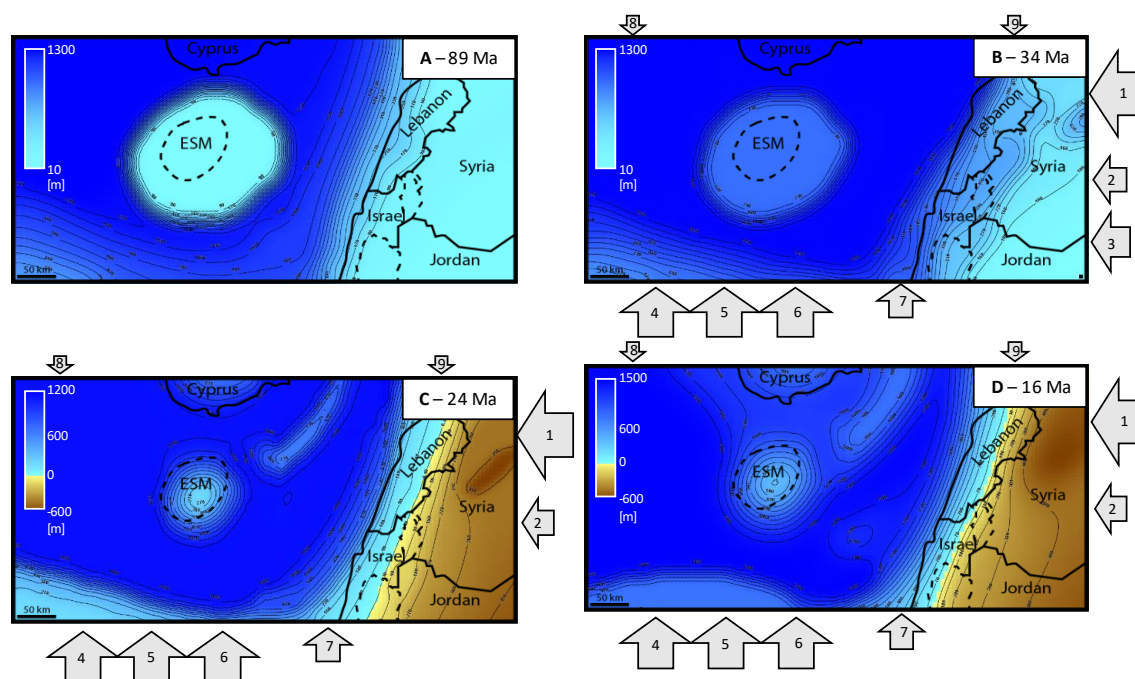


Fig. 6.3 Used paleo-bathymetry maps for the Upper Cretaceous to Eocene (A), Oligocene (B), Lower Miocene (C), and Upper Miocene (D) intervals. The color scale indicates water depth (negative values above sea level) The arrows in B-D represent sediment input sources defined in the Oligocene and Miocene intervals: 1 to 3: Sediment originating from the Arabian Plate in the east, 4 to 7: sediments originating from the Nile, 8: sediment input from the western Anatolian Plate, 9: sediment input from the Latakia region.

Table 6.1 Definition of the simulated sediments in the stratigraphic forward model.

sediment	grain size [mm]	Density [g/cm ³]	diffusion coefficient ² [km ² /ka]				
			gravity driven		water driven		waves
			cont. ³	mar. ⁴	cont. ³	mar. ⁴	
clay*	0.04	2.5	5.5-6.0	0.55-0.6	40-42	5.0-6.5	10
sand*	20	2.7	4.6-5.0	0.46-0.5	32-35	3.2-3.5	2-3
carbonate mud	0.04	2.5	0.01-0.02	0.01-0.02	8	4	0.04
carbonate grains	10	2.5	0.01	0.01	5	3	0.04
marine OM ¹	0.1	1.3	1.0-5.5	0.1-0.55	30-40	3-4	6-9
terrestrial OM ¹	0.1	1.8	5.8	0.58	41	4.1	10

*Grain sizes for "clay" and "sand" are based on DionisosFlow® standard values and are higher than in common definitions. Thus "clay" includes silt and "sand" includes conglomerates.

¹ organic matter, ² parameter is adjusted for each model within the given range, ³ continental environment, ⁴ marine environment

Six different sediment types and sediment components were simulated, which are grouped into three classes: 1) carbonates 2) clastics, and 3) OM. While grain size and density are kept constant, the diffusion coefficient is individually adjusted for each simulation. The respective sediment characteristics are shown in Table 6.1. Diffusion coefficients throughout the literature range from <0.01 km²/ka (Gawthorpe et al., 2003) to > 10⁷ km²/ka (Burgess et al., 2006). These diffusion coefficients are chosen to represent different transport behaviors of each sediment class relative to each other, rather than representing real physical parameters. Clay for example is easier transported than sand grains and thus has a higher diffusion coefficient. For numerical simplification, each seismic package was simulated individually. Compaction of these packages was simulated based on present burial depths without considering any density differences of the overburden lithological column and thus has to be considered as only a rough approximation.

6.3.1.1 Simulating carbonate production

The relative production of carbonate takes place *in situ* as a function of water depth (Fig. 6.4), while the absolute production can vary throughout the geological history and is used as calibration parameter. However, absolute production rates (Table 6.2) were chosen in a way to account for changing climatic (temperature) conditions during the simulation, so that there is e.g. a significant increase in the production rate towards the Oligo- and mainly Miocene, when the climate in the Mediterranean Region was significantly warmer (Gatt and Gluyas, 2012). For the present model, two different types of carbonate were simulated: 1) Carbonate mud, representing mainly pelagic carbonate sedimentation with the highest production rate between 100 and 200 m water

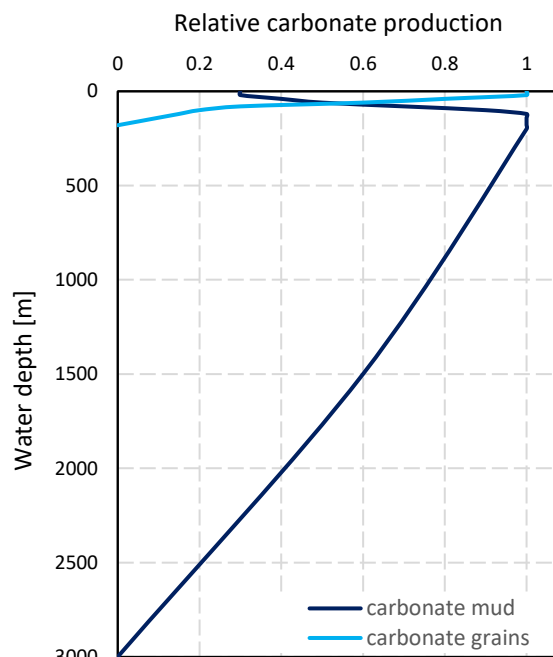


Fig. 6.1 Assigned carbonate production law as a function of water depth for carbonate mud and carbonate grains in the present model.

depth and an exponential decrease down to 3000 m; and 2) carbonate grains representing shallow water, platform carbonates with the highest production rate between 20 and 40 m water depth and no production below 180 m.

6.3.1.2 Simulating siliciclastic sediment input

Siliciclastic sediments enter the model via sediment input sources (Fig. 6.3B-D), which are placed at the model's border. In the model, only riverine sources are considered, whereas aeolian input of fine clastic material is neglected. Nine sediment sources were defined to simulate the clastic input during the Oligo-Miocene (Fig. 6.3B-D): Source 1, 2, and 3: sediments originating from the Arabian Plate in the east; source 4, 5, 6, and 7: a broad sediment input originating from an adjacent Nile river(s) in the southwest of the model. Note, that the model area does not include the onshore area in the south. Therefore, the Nilotic sediment sources were set relatively broad, to avoid a punctual, radial sediment distribution around these sources. Further, a source 8 was placed at the northwestern boarder of the model to simulate the sediment input derived from the western Anatolian area, and a source 9 was placed at the northeastern boarder to simulate the sediments originating from the Latakia region since the Upper Miocene.

The sediment supply (in km^3/Ma) is composed of a defined percentage of different sediments and determines the total amount of provided sediment, while the fluvial discharge (in m^3/s) influences the transport distance. Both parameters were chosen according to global drainage relationships (Fig. 6.5) and expected sediment volumes inferred from isopach maps.

Table 2 Absolute carbonate production rates used in the stratigraphic forward model.

age [Ma]	absolute production [m/Ma]	
	carbonate mud	carbonate grains
16 – 6	60	70
24 – 16	40	40
34 – 24	20	15
85 – 34	30	15
89 – 85	30	35
144 – 89	10	22

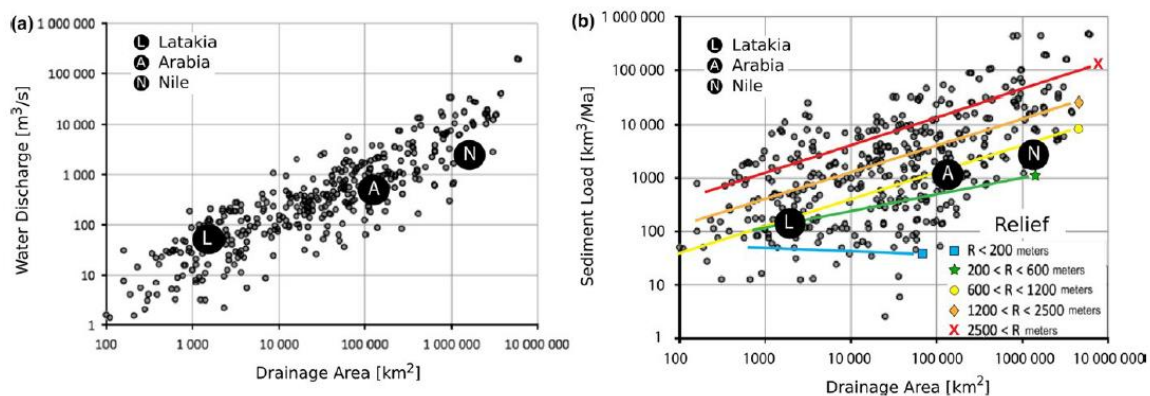


Fig. 6.5 Global relationship between (A) drainage area and water discharge and (B) drainage area and sediment load. Estimated conditions for the Latakia (L), Arabian Plate (A) and Nile (N) area are indicated for the Miocene. (Figure from Barabsch et al., 2018, modified after Hawie et al., 2015. Datasets based on Dai and Trenberth, 2002 and Milliman and Syvitski, 1992).

6.3.1.3 Simulating production and preservation of organic matter

Two different types of OM were defined in the model: 1) Terrestrial OM, which is treated like any other clastic sediment and enters the model as a fraction of the total sediment supply via the input sources. Hydrogen index (HI) values of terrestrial OM are predefined and do not change throughout the simulation. 2) Marine OM is assumed to be derived mainly from phytoplankton, which is produced *in situ* according to specific primary production (PP) laws at the water surface and is defined as the mass of produced organic carbon over one square meter per year ($\text{gC m}^{-2}\text{a}^{-1}$). In order to respect different possible scenarios of marine OM production, three different “sub-classes” for marine OM were created: a) “normal-marine-OM”, where the PP is defined as a function of distance to the shoreline, b) “upwelling-marine-OM”, where an increased PP is attributed to an upwelling zone defined around a specific bathymetry (Fig. 6.6), and c) “defined-marine-OM”, where the PP zones are defined manually by productivity maps. The latter one can be used to test different scenarios where increased PP rates are expected in specific areas. The relative PP rate for each sub-class can vary for different ages allowing a separated or combined use of all three scenarios. It has to be mentioned here, that upwelling systems are complex systems that are affected by many factors. Wind and ocean current might affect the location and the shape of upwelling areas, especially if these are located above isolated seafloor features, such as the ESM. However, for simplification, no wind- or ocean currents are simulated here, and thus the simulated outcomes represent only the rough area of upwelling and thus the zone of increased primary productivity.

Only a small fraction of the OM that is produced at the water surface is expected to reach deeper environments (Grabowski et al., 2019). Once the marine OM is generated at the water surface, it is transported by the carbon flux (e.g. Berger, 1987; Honjo et al., 2008) towards the sediment water interface (SWI). The exported fraction of PP reaching the SWI (CF) is calculated according to Martin et al. (1987):

$$CF = 0.409PP^{1.41} \left(\frac{Z}{100} \right)^{-n} \quad [2]$$

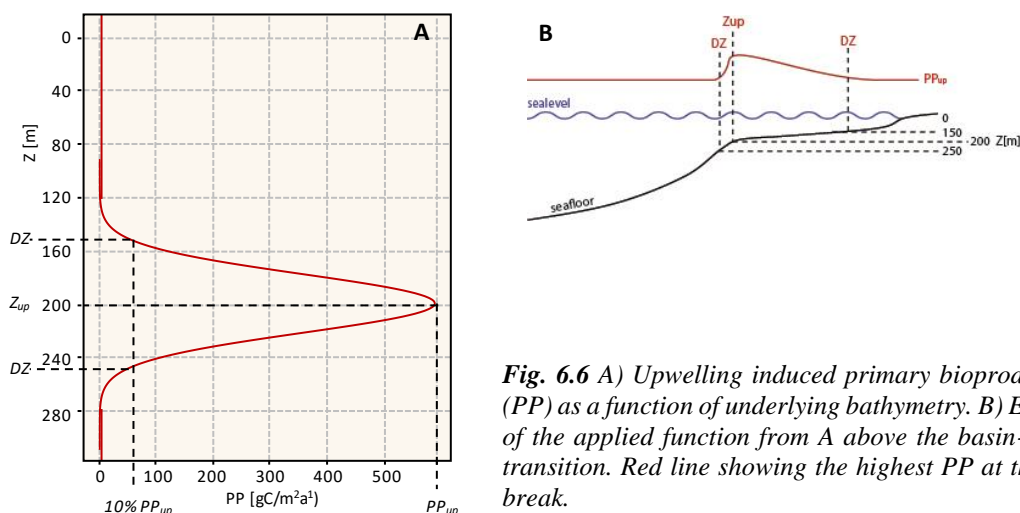


Fig. 6.6 A) Upwelling induced primary bioproductivity (PP) as a function of underlying bathymetry. B) Example of the applied function from A above the basin-margin transition. Red line showing the highest PP at the shelf break.

with CF being the exported organic flux ($\text{gC}/\text{m}^2\text{a}$), PP the primary productivity ($\text{gC}/\text{m}^2\text{a}$), z the water depth (in m), and n assumed to be constant and equal to 0.86.

The degradation (decrease of HI) of the marine OM is simulated in relation to the dissolved oxygen content in the water column. To calculate the oxygen concentration, a mass balance equation between oxygen consumption and oxygen renewal is used after Mann and Zweigel (2008). A purely vertical (1D) relationship is assumed for the present model:

$$dOx_z(z) = A_z(z) \times Ox_{REF} - D_z \times Ox_z(z) \quad [3]$$

with Ox_z as the oxygen level at the sea floor (no dimensional between 0 = anoxic and 1 = oxic), $A_z(z)$ as the mixing rate coefficient, Ox_{REF} the reference oxygen level and $D_z(z)$ the oxygen consumption linked to the OM degradation by organisms. In the present model the mixing rate is constant, thus the oxygen level is depending on bathymetry and PP only.

Another parameter controlling the preservation of marine OM in the first few meters in the sediment is the burial efficiency, which depends on the sedimentation rate and the oxygen concentration at the SWI (Betts and Holland, 1991; Tyson, 1995). The respective equation is:

$$\frac{dC_{org}}{dt} = -kC_{org}^n \rightarrow S \frac{dC_{org}}{dz} = -kC_{org}^n \quad [4]$$

with C_{org} as the available organic carbon (in wt.%), k the degradation coefficient (function of the burial depth into the sediment, $k = k_0 e^{-z/z_0}$) and S the sedimentation rate (in m/Ma).

By combining these different equations, an initial marine TOC content is calculated during the early diagenesis stage. Note that no thermal degradation of OM is taken into consideration at this point (this is done in the petroleum system model).

The simulated bulk TOC is then the sum of marine TOC plus the terrestrial TOC. In the following paragraphs, the term “simulated TOC” will be used to describe the modeling results (expressed in %), while the term “TOC” refers to the total organic carbon content measured on actual rock samples (expressed in wt.%).

More detailed descriptions of the above mentioned processes and their numerical implementation are described in Chauveau and Granjeon (2013) and Bruneau et al. (2017).

6.3.1.4 Model calibration

The calibration of the model was achieved in two steps. First, the thickness of each simulated interval was compared to the actual thickness obtained from the respective isopach maps. In a second step, the sediment distribution was compared qualitatively to gross-depositional-environment maps from the literature (Barrier and Vrielynck, 2008; Hawie et al., 2013b).

For calibration, the above-mentioned parameters for carbonates and clastics were tested in a reasonable range until one best-fit model was achieved. On this best-fit model, the deposition of OM was simulated.

6.3.2 Petroleum system modeling

6.3.2.1 Geological framework/static model

The export of the *DionisosFlow*® results to *TemisFlow*® is one crucial part in this integrated workflow. The *DionisosFlow*® stratigraphic forward model is first used to provide a general distribution of the different simulated sediment classes throughout the model area, rather than simulating precise internal sedimentary architectures. For the *TemisFlow*® petroleum systems modeling, however, specific facies maps are required, which are correlated to distinct physical properties rather than sediment distribution maps (*TemisFlow*® output). Therefore, based on specific threshold values, the different sediment compositions in the *DionisosFlow*® model are grouped to facies types, which can be read by *TemisFlow*® (using a common facies library – i.e. same lithological characteristics). For the present model, 13 different facies were created (based on standard, predefined *TemisFlow*® facies types). Their respective threshold values and physical properties are shown in Table 6.3.

The second choice that needs to be made addresses the vertical resolution of the *TemisFlow*® model. In *DionisosFlow*®, 0.5 Ma intervals were simulated. However, regarding the scarce availability of well data, this temporal resolution is too detailed and could not raise a claim of representing reality. Hence, the *DionisosFlow*® model was investigated for sequences where significant changes in facies and/or OM content are observed. In *TemisFlow*®, the main seismic packages are defined by 3D depth maps obtained from seismic interpretations (Gardosh and Druckman, 2006; Hawie et al., 2013a; Tassy et al., 2015; Papadimitiou et al., 2018). The *DionisosFlow*® grouped sequences are then used to split

Table 3 Overview of the facies properties with their sediment composition in the stratigraphic forward *DionisosFlow* model and their petrophysical properties in the petroleum system *TemisFlow* model.

type	name	sediment composition in <i>Dionisos</i> ®				petrophysical properties in <i>Temis</i> ®				
		mud [%]	carbo grains [%]	shale [%]	sand [%]	ρ^1 [g/cm ³]	θ^2 [%] at 0 m	θ^2 [%] at 10 km	Λ^3 W/m ² °C]	C ⁴ [J/kg ² °C]
carbonates	Marl	> 70	-	-	-	2.67	57	3	2.76	815
	Limestone	-	> 40	-	-	2.71	38	7	3.57	795
	30lms_70mrl	60 - 90	10 - 40	-	-	2.69	55	3	2.98	809
clastics	sandstone	-	-	-	> 90	2.67	36	5	6.32	700
	90sa_10sh	15 - 5	-	20 - 10	80 - 90	2.67	35	5	5.67	710
	70sa_30sh	35 - 15	-	40 - 20	60 - 80	2.66	35	5	4.56	740
	50sa_50sh	55 - 35	-	60 - 40	40 - 60	2.66	35	5	3.67	765
	30sa_70sh	75 - 55	-	80 - 60	20 - 40	2.65	32	4	2.95	790
	Shale	-	-	> 70	-	2.64	40	4	2.37	815
	023_70sa-30sh_TURB_LOBE	-	-	-	60 - 80 *	2.66	36	4	4.6	740
	mix	20lmst20sh	10 - 30	10 - 30	10 - 40	10 - 40	2.67	47	4	3.26
20sa20si20mrl		20 - 40	-	10 - 30	5 - 25	2.67	19	4	3.14	785
15sa15si20ch30mrl		20 - 40	-	10 - 30	5 - 25	2.67	19	4	3.14	785
50mrl_50sh		40 - 60	-	40 - 60	-	2.66	22	4	2.56	815

* sand fraction combined with the turbidity indicator of the *Dionisos Flow*® software

¹ density, ² porosity, ³ thermal conductivity, ⁴ heat capacity

the *TemisFlow*® packages according to the proportion of each sequence relative to the total simulated thickness in *DionisosFlow*®. The facies of each sequence were determined considering the dominant facies in the included simulation steps, while the TOC and HI values were calculated as the average of each sequence.

The selected sequences providing the base for the *TemisFlow*® model are shown in Table 6.4. The Lower Cretaceous consist of four sequences, where the two oldest ones represent the clastic input from the southwest during the Early Cretaceous. The two younger ones represent changes in the paleo coastline, and therefore a shift from pelagic to shallow water carbonates along the margin-basin transition. The Upper Cretaceous to Eocene interval was subdivided into nine sequences. The four oldest ones represents lateral and vertical changes in the extent of deposited source rock intervals. The following groups reflect lateral changes of pelagic and shallow water carbonates along the Levant

Table 6.4 Layers of the petroleum system model. Shaded rows represent seismic horizons (Fig. 1B), while the subdivisions are interpolated from the stratigraphic forward mode.

layer	geological unit	age [Ma]	thickness [m]			Source rock interval
			ESM	basin	margin	
43	Pliocene-Quaternary	0	1	825	1	
Top Messinian						
42	Messinian	5.3	1	1910	23	
Base Messinian						
41	Upper Miocene	6.0	4.5	94	30	✓
40	Upper Miocene	6.5	4.5	94	30	✓
39	Upper Miocene	7.0	4.5	94	30	✓
38	Upper Miocene	7.5	4.5	94	30	✓
37	Upper Miocene	8.0	4.5	94	30	✓
36	Upper Miocene	8.5	9	188	60	✓
35	Upper Miocene	9.5	9	188	60	✓
34	Upper Miocene	10.5	9	188	60	✓
33	Upper Miocene	11.5	9	188	60	✓
32	Upper Miocene	12.5	4.5	94	30	✓
31	Upper Miocene	13.0	4.5	94	30	✓
30	Upper Miocene	13.5	9	188	60	✓
29	Upper Miocene	14.5	13.5	282	90	✓
Intra Miocene						
28	Lower Miocene	16.0	18	233	30	✓
27	Lower Miocene	17.0	18	233	30	✓
26	Lower Miocene	18.0	18	233	30	✓
25	Lower Miocene	20.5	18	233	30	✓
24	Lower Miocene	22.5	18	233	30	✓
Top Oligocene						
23	Oligocene	24.0	18	169	47	✓
22	Oligocene	25.0	18	169	47	✓
21	Oligocene	26.5	18	169	47	✓
20	Oligocene	27.5	18	169	47	✓
19	Oligocene	28.5	18	169	47	✓
18	Oligocene	29.5	18	169	47	✓
Top Eocene						
17	Eocene	34.0	5	249	55	✓
16	Eocene	41.0	2	124	27	
15	Eocene	44.5	2.5	142	31	
14	Eocene	48.5	2	124	27	
13	Eocene	52.0	2.5	142	31	
12	Eocene	56.0	6.5	355	78	
11	Upper Cretaceous	66.0	2	107	24	✓
10	Upper Cretaceous	69.0	12	622	137	✓
9	Upper Cretaceous	86.5	1.5	89	20	✓
Senonian Unconformity						
8	Lower Cretaceous	89.0	90	130	225	
7	Lower Cretaceous	100.0	180	260	450	
6	Lower Cretaceous	121.0	90	130	225	
5	Lower Cretaceous	132.5	90	130	225	
Top Jurassic						
4	Jurassic	144.0	700	900	2480	
3	Triassic	201.0	150	260	780	
2	Triassic	220.0	150	260	780	
1	Permian	251.0	150	170	1200	
0	basement	299.0	-	-	-	

Margin coastline. Further, one extra group was chosen to represent the Upper Eocene source rocks. For the Oligocene, Lower- and Upper Miocene, 6, 5, and 13 groups were defined, respectively. The intercalation of more fine-grained and more coarse-grained intervals in the basin center as well as along the margin were maintained to represent reservoir heterogeneities as well as intercalations of source and reservoir rocks.

The two youngest intervals (Messinian 6-5.3 Ma, and Pliocene to Quaternary 5.3-0 Ma) were drawn manually, since no detailed information on the post-salt sequences is required for the purpose of this work. For the Messinian, pure salt was assigned to the whole basin. To the margin, sandstones were assigned, and on top of the ESM and the Latakia Ridge limestone was favored. For the Quaternary, a mix of 30% sand and 70% shale is assigned to the onshore Levant Margin and the Island of Cyprus, while the transition to the basin composes a mix of platform and pelagic carbonates. The ESM is composed of pelagic carbonate while the basin and the Nile Delta area are composed of sand, which is mixed with clay and mud towards the deeper basin.

Based on this static model, 3D simulations were performed considering compaction, pressure, thermal maturation, and kerogen transformation. HC migration was not taken into account in this model. Classical backstripping techniques were used to reconstruct the basin structural evolution. No faults are included in the present model.

6.3.2.2 Geochemical properties/source rocks

Since the exact onset of thermal cracking of kerogen and, thus, the beginning of HC generation depends on the type of OM (Tissot and Welte, 1984), the correct assignment of source rock specific kinetic parameters is of great importance in petroleum system modeling. For the present model, non-compositional kinetic parameters were adopted from Bou Daher et al. (2016) for the Upper Cretaceous (mainly Type II/IIS kerogen) and Eocene/Paleocene (Type II/III kerogen) source rock intervals. The latter one was also used for Oligocene-Miocene source rocks, as these source rocks show also a mixed Type II and Type III kerogen composition. Initial TOC and HI values were taken from the respective intervals in the stratigraphic forward model.

6.3.2.3 Boundary conditions

In the *TemisFlow*® software, the upper thermal boundary is defined by paleo surface temperature maps. For the present model, respective temperatures were calculated according to Wygrala (1989) based on the paleo latitude and surface temperatures of the Arabian plate and respective paleo water depths (taken from the *DionisosFlow*® model) for the offshore areas.

For the lower thermal boundary, the basement, the lower crust, and the upper mantle are simulated with a heat source of 1333 °C at the upper mantle (Allen and Allen, 2013). Thickness values for these intervals are adopted from the model by Bou Daher et al. (2016) and slightly modified according to Inati et al. (2018).

6.3.2.4 Model calibration

Model calibration is mainly based on the near-shore well, and pseudo well data published in Bou Daher et al. (2016) for the Levant Margin. Note that these used pseudo wells are based on an independent study, where calibration with real onshore data was achieved and independent crustal-tectonic modeling was used to deduce the evolution of heat flow (Halstenberg, 2014). For the area of the ESM, borehole temperatures are taken from the initial ODP Leg 160 reports, precisely from well 967E (Emeis et al., 1996). Vitrinite reflectance values from the ODP wells (Grohmann et al., 2018) were also used for calibration in this part.

6.4 Results and discussion

6.4.1 Stratigraphic forward modeling

The stratigraphic forward modeling results are illustrated in Figures 6.7, 6.8, 6.9, 6.10, and 6.11. They are representative for the carbonate dominated (Late Cretaceous to Eocene) and the clastic dominated (Oligo-Miocene) depositional environments. Figure 6.12 shows the thickness error maps for the Late Cretaceous to Eocene, the Oligocene, the Lower and the Upper Miocene.

6.4.1.1 Upper Cretaceous to Upper Eocene

For the Upper Cretaceous to Upper Eocene interval, a sea level increase combined with post-rift subsidence (on average: 15 m/Ma at the margin; 69 m/Ma in the northern and 36 m/Ma in the southern basin, respectively; 9 m/Ma at the basin-margin transition, and 15 m/Ma at the ESM) could simulate the drowning of the area. Platform carbonates change towards a mix of pelagic and coarse grained carbonates on top of the ESM, and carbonate buildups along the Levant Margin retreat landwards, while the basin parts are dominantly characterized by pelagic carbonate sedimentation (Fig. 6.7A). The platform carbonates along the margin are interrupted by a mix of platform and deeper marine carbonates in the area of central to northeastern Lebanon, related to the southwestern extent of the Palmyra Basin (Fig. 6.7A). In order to obtain any sedimentation on top of the ESM, an almost flat initial bathymetry had to be used, which is different compared to its present day anticlinal shape. In addition, the paleo-diameter of the platform had to be larger than today. Both observations are in accordance with the

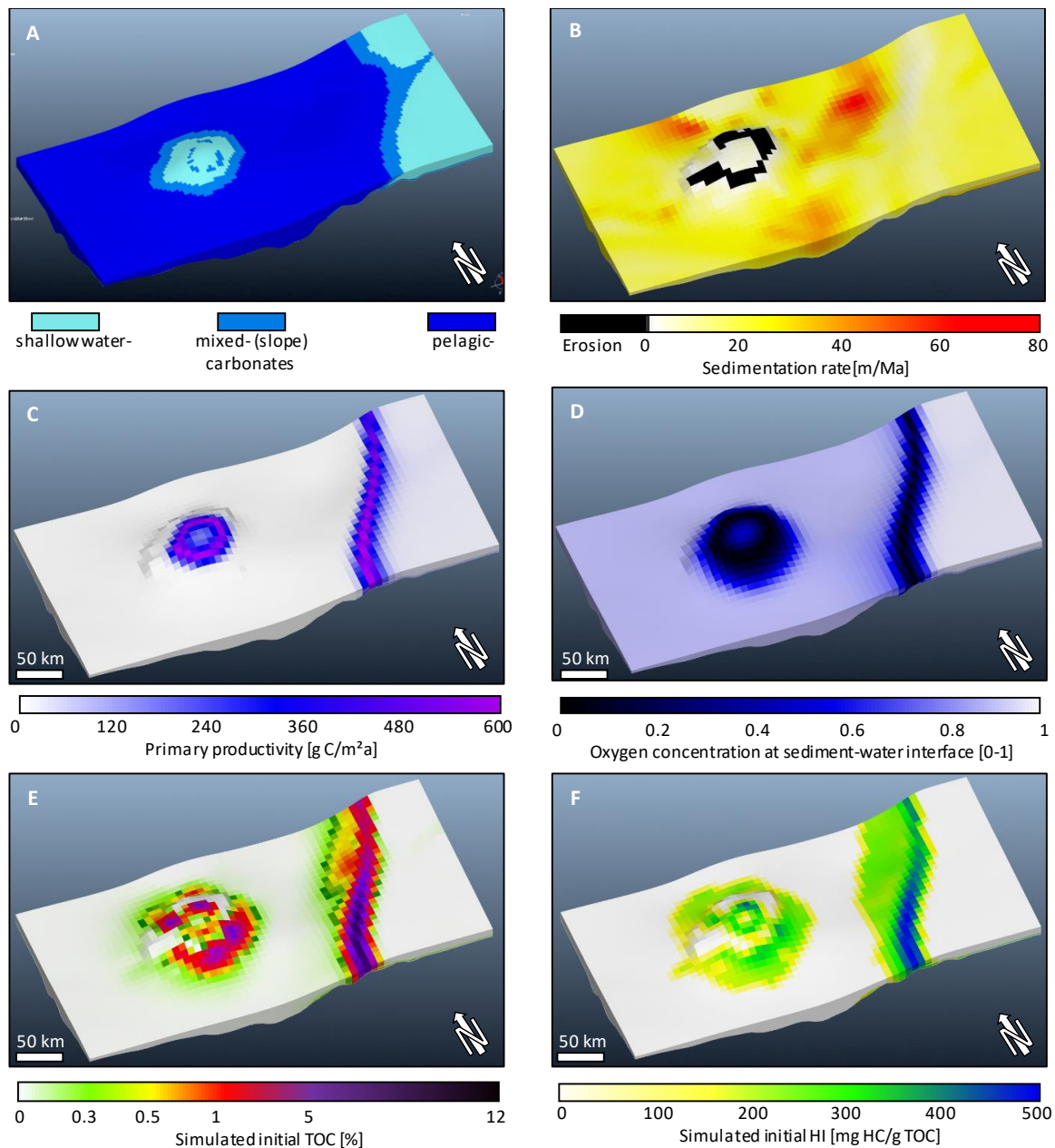


Fig. 6.7 Stratigraphic forward modeling results of the Upper Cretaceous (89 to 65 Ma). A) Facies distribution, B) sedimentation rate (black cells indicate erosion), C) simulated primary productivity caused by upwelling, D) oxygen concentration at the sediment water interface (0 = anoxic, 1 = oxic), E) simulated initial total organic carbon (TOC) content, F) simulated initial bulk hydrogen index (HI). Levant Margin on the right (eastern) side, ESM in the center-left.

tectonic history of the ESM, which underwent significant folding and faulting of its flanks since the Cretaceous and mainly during the Miocene collision of the ESM and the Cyprus Arc (Papadimitriou et al, 2018). It is important to note that the ESM is characterized by relatively steep flanks, resulting in erosion and resedimentation of platform carbonates creating a ring of a mixed carbonate facies and mass-transport deposits around the seamount (Fig. 6.7A).

In terms of simulated thickness (Fig. 6.12A and B), good results are achieved in the basin, and along the margin (100 to 140% of actual thickness). On the other hand, locally on top of the ESM and at the southern basin-margin transition, too large thickness values are obtained (140 to >300% of actual

thickness based on seismic data interpretation). On top of the ESM these spots with a too large thickness are related to areas where the actual thickness of the isopach maps is very low ($\ll 10$ m), which explains these high percentage values. In general, these patchy thickness errors, especially on top of the ESM emphasize the importance of a well-defined initial paleo-bathymetry for such specific seafloor features, which can differ a lot compared to the present day state.

For OM simulation, three different types of marine OM production were used for the Upper Cretaceous to Eocene interval. From 89 to 66 Ma, the “upwelling-marine-OM” was used in order to simulate the upwelling system that was active during the Upper Cretaceous (e.g. Almogi-Labin et al., 1993; Bou Daher et al., 2015). The PP was defined with the highest rate occurring at a bathymetry of 200 m water depth with DZ of ± 50 m and a maximum productivity of $600 \text{ g C m}^{-2}\text{a}^{-1}$ (Fig. 6.4), which is in accordance with primary productivity rates that are observed in recent continental upwelling areas (Lalli and Parson, 1997). In this way, the deposition of Upper Cretaceous source rocks could be simulated along the Levant Margin as well as on top of the ESM (Fig. 6.7E). In the simulation, PP values reach the maximum of $600 \text{ g C m}^{-2}\text{a}^{-1}$ close to the margin, while PP rates above the ESM are lower with 100 to $500 \text{ g C m}^{-2}\text{a}^{-1}$ (Fig. 7C). These production rates result in the formation of an oxygen minimum zone between 100 and 500 m water depth.

Along the Levant Margin, simulated TOC contents average around 1 to 2% in the northernmost part, around 3 to 4% in the central part and around 11 to 12% in the southern part, respectively (Fig. 6.7E). These values are in good agreement with the measured organic carbon contents of the immature source rocks in northern (Fig. 6.9A) and southern Lebanon (1.5 wt% TOC and 3.8 wt% TOC

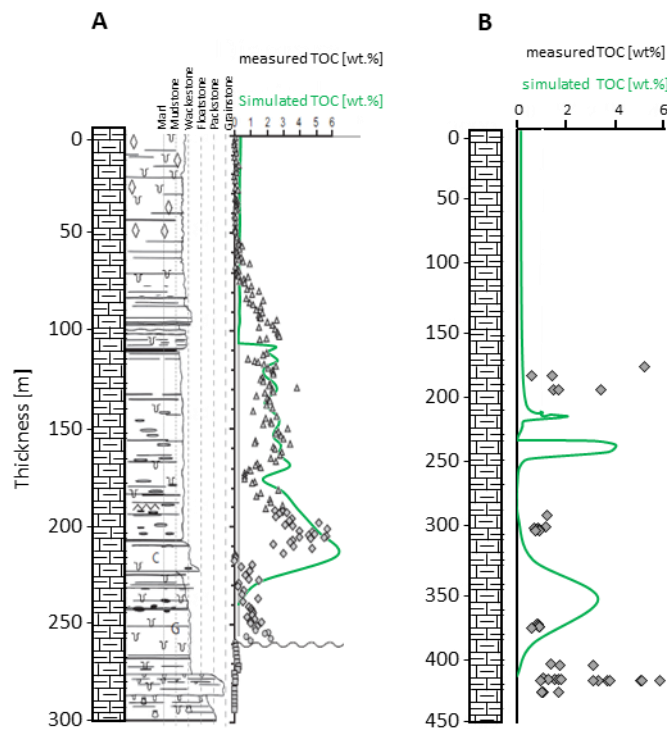


Fig. 6.9 Comparison of simulated with measured TOC contents at (A) the Chekka region in Lebanon (modified after Bou Daher et al., 2014) and at ODP Leg 160 well 967 (Geochemical data from Grohmann et al., 2018)..

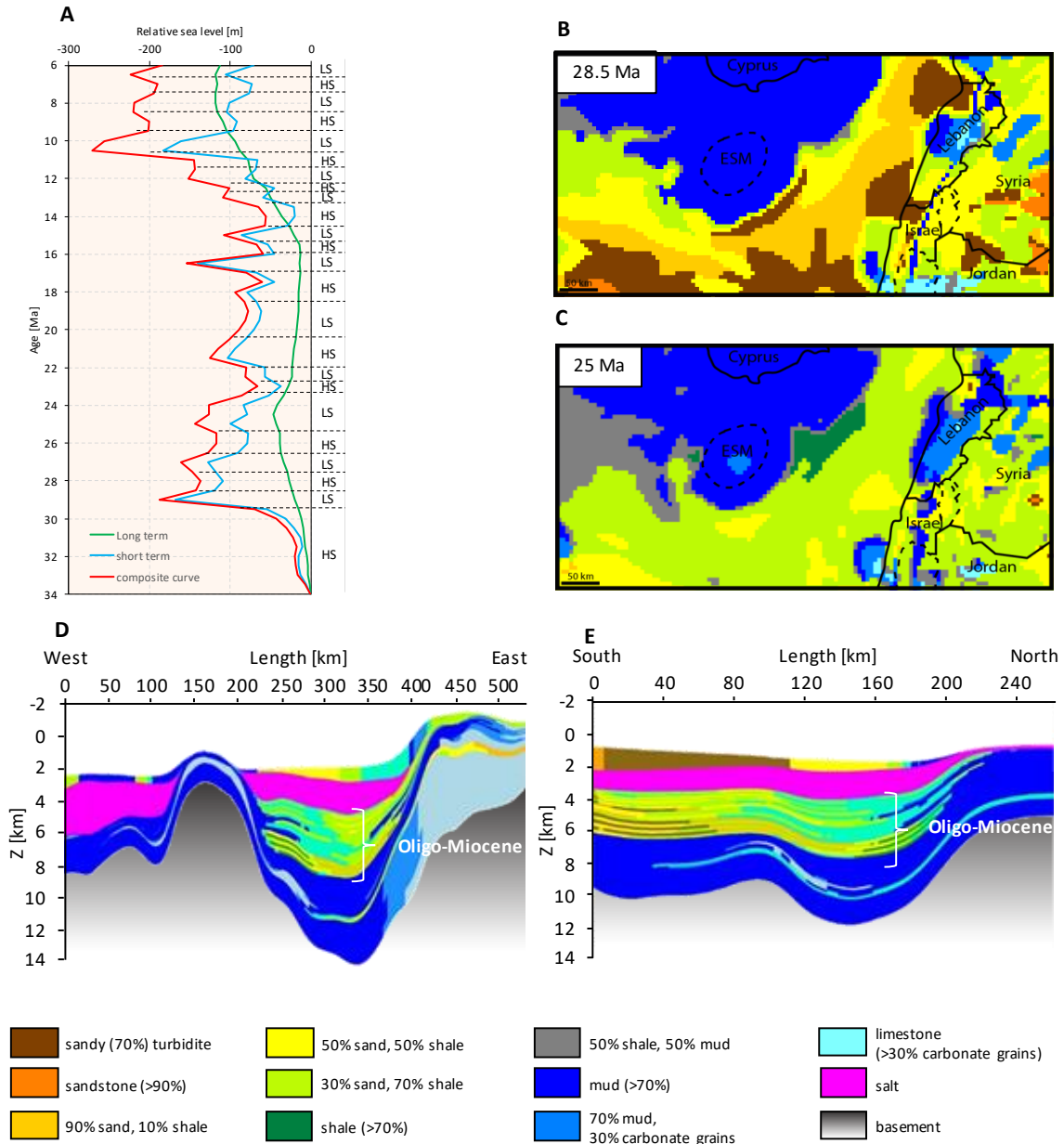


Fig. 6.10 A) Long- (green) and short-term (blue) sea level curves after Haq et al. (1987) and the composite curve (red), which is used for the present model. High stand (HS) and low stand (LS) periods are indicated, which are used to define the relative clastic sediment composition during the oligo-Miocene period. LS periods bring more coarse grained material into the basin (B), while HS periods are defined by more fine grained deposits (C). Fig. D and E show the resulting intercalation of fine and coarse grained intervals in the basin at present day burial. For location of the profiles, see Figure 1.

on average, respectively; Bou Daher et al., 2014; Bou Daher et al., 2015) and in Israel (6.8 wt% to 14 wt% TOC, Almogi-Labin et al., 1993). Simulated HI values (Fig. 6.7F) average around 300 to 400 mg HC/g TOC in Lebanon and around 500 mg HC/g TOC in Israel. The highest simulated TOC contents and HI values are found at water depths between 150 and 350 m and are thus located within the center of the oxygen minimum zone. Below the oxygen minimum zone (max. 600 m water depth) only very low simulated TOC and HI values can be found. These results are comparable to Quaternary organic-rich sediments related to a recent upwelling system offshore Peru, where highest TOC contents (4.5 wt.% on average) and HI values (418 mg HC/g TOC) are observed at a water depth of about 460 m (ten Haven et al., 1990). Along the Levant Margin, these simulated intervals span a thickness of 200 to 300

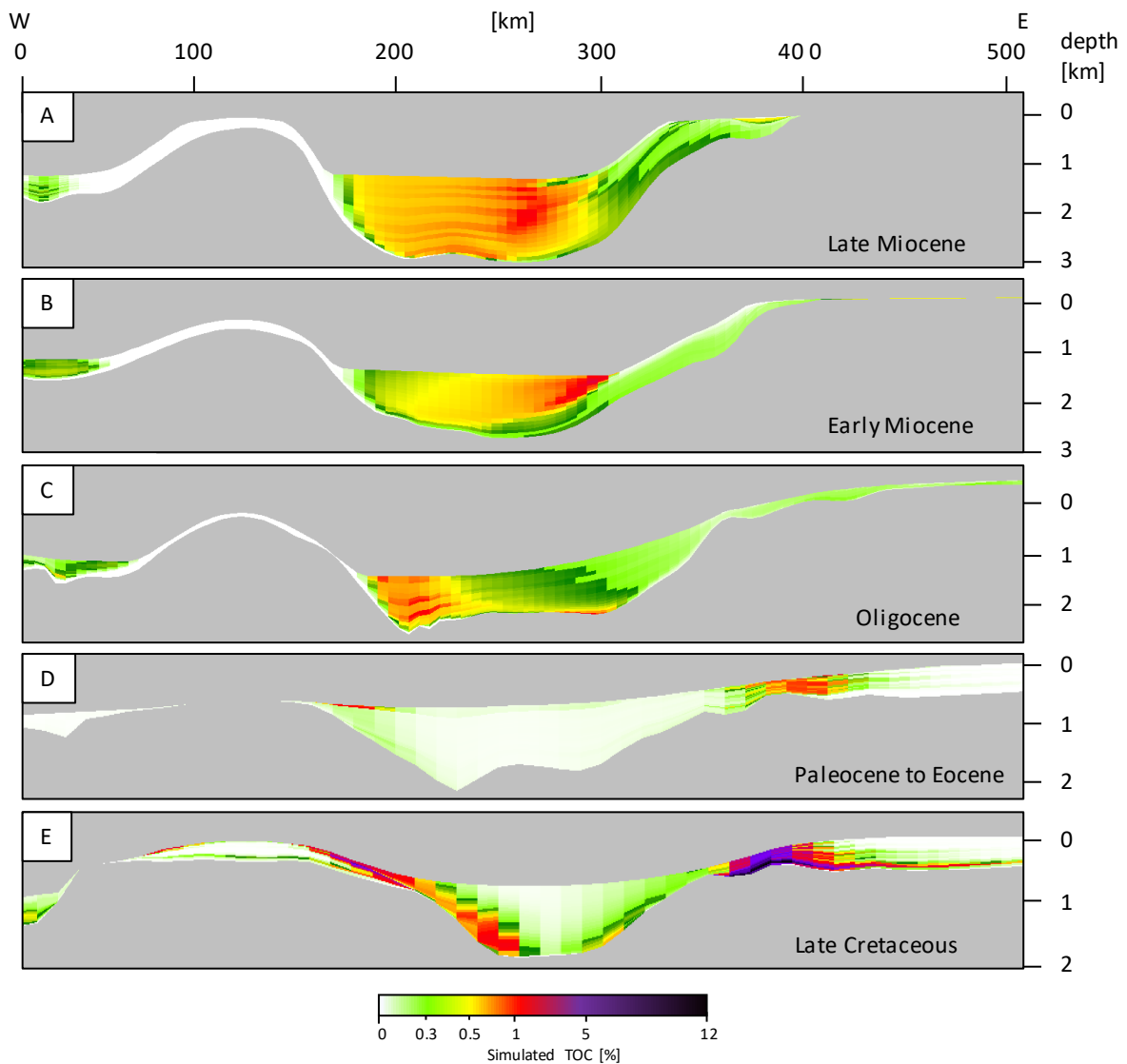


Fig. 6.11 Distribution of simulated total organic carbon (TOC) contents during the different intervals. The location of the cross section corresponds to the profile A-A' (Fig. 1A).

m, while the deeper, basin-ward extents (which show much lower simulated TOC contents and HI values) reach up to 1000 m, without considering compaction at present day burial (Fig. 6.11D and E). Simulated TOC contents decrease within the Upper Cretaceous from bottom to top (Fig. 6.11E), but are still higher and wider distributed than in the Eocene (Fig. 6.11D).

On top of the ESM, OM is preserved along the outer rim of the seamount, with simulated TOC contents mainly between 0.5 and 3%, which is in agreement with measured TOC contents for the Upper Cretaceous interval in ODP Leg 160 well 967 (0.9 wt% TOC on average, Grohmann et al., 2018). At the location of well 967, simulated organic-rich intervals show similar, irregular spacing with comparable TOC contents, although the exact location does not fit as well as at the margin (Fig. 6.9B), pointing out again the importance of the initial paleo bathymetry and its influence on the depositional conditions on top of the seamount. Simulated HI values are between 150 and 250 HC/g TOC and are in good agreement with the geochemical data, as well. Uncompacted thickness of the organic-rich interval

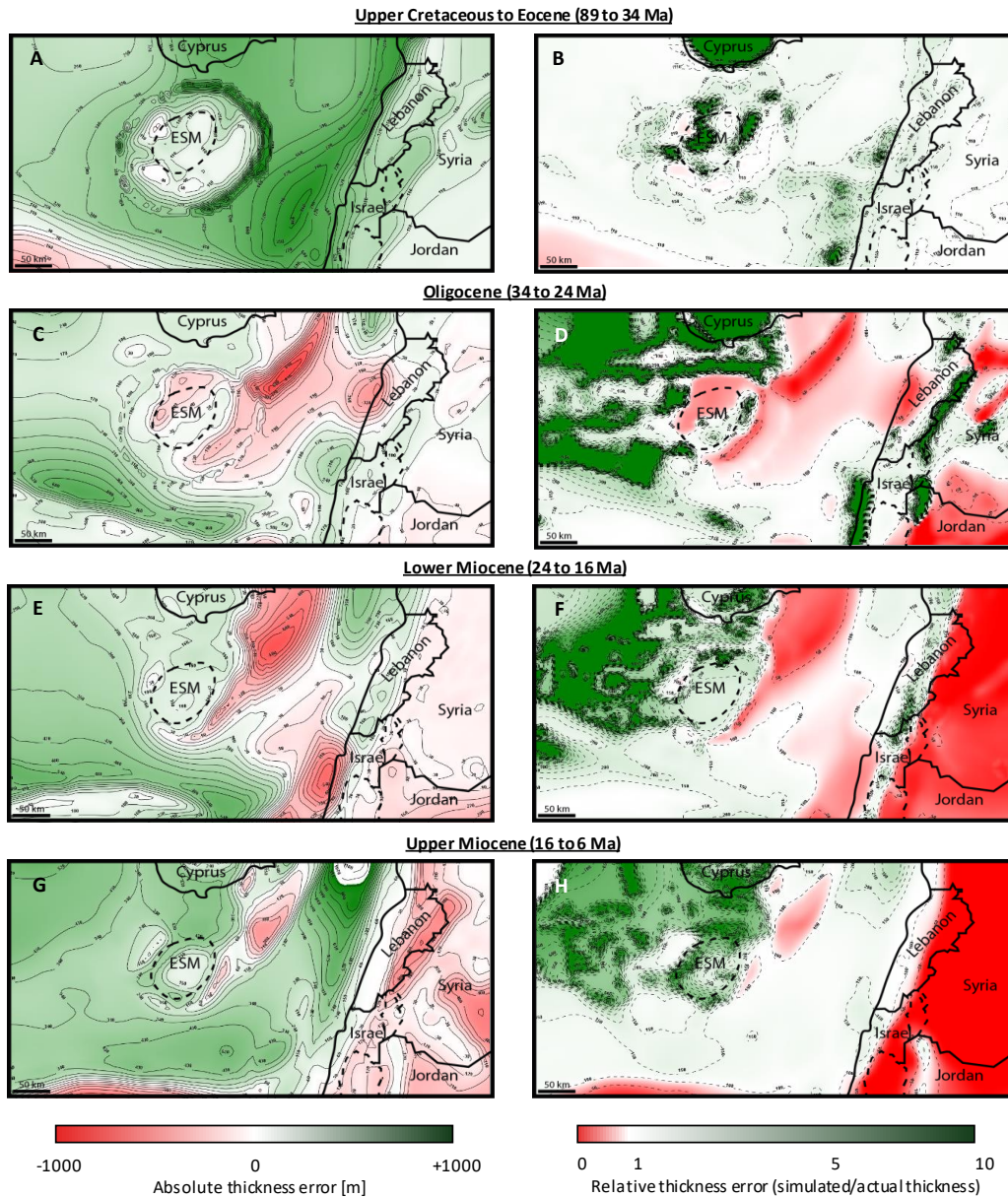


Fig. 6.12 Absolute and relative thickness errors maps for the Upper Cretaceous to Eocene (A and B), the Oligocene (C and D), the Lower Miocene (E and F) and the Upper Miocene (G and H) intervals. For the relative thickness error “0” means 0% of the actual thickness (from isopach maps) was reproduced by the numerical simulation. This means that the model resulted in no sediment deposition at this location. “1” means perfect match of simulated and actual thickness values. “2” means simulated thickness value is two times larger than the actual thickness value at this location. The figure caption was changed for clarification.

is locally about 100 to 200 m on top of the ESM and reaches values > 300 m in the outer rim again with much lower TOC contents, (Fig. 6.11D and E).

At all locations, a sharp decrease in simulated TOC and HI towards the deeper basin can be observed (Fig. 6.7C, E, and F). Figure 6.7D indicates that the oxygen concentration is almost zero directly below the main PP zone, and much higher in the bottom water of the deeper basin. In addition, Figure 6.7B and E show that locations, where OM is accumulated, are characterized by low

sedimentation rates. In turn, for instance in the northern part of the basin/slope, some OM was deposited as well, but sedimentation rates are very high, so that the OM is diluted resulting in low TOC contents.

6.4.1.2 Oligocene to Miocene

The simulation of several sediment input sources (Arabia, Nile, Western Anatolia, Latakia, see 3.1.2) illustrates the change from carbonate towards clastic dominated sedimentation along the Levant Margin and within the basin (Fig. 6.8A). Small and patchy accumulations of a mix of pelagic and shallow water carbonates along the Levant Margin remain only in local spots, where no clastic sediments reach the basin (Fig. 6.8A). The ESM and the area of Cyprus remain carbonate dominated with mainly pelagic carbonate sediments, mixed with some shallow water carbonates on top of the ESM (Fig. 6.8A).

With the stepwise establishment of the Levant Fracture system from south to north (e.g. Bartov et al., 1980; Ghalyini et al., 2014), sediments coming from the east were blocked and did not further feed the basin. Hence, the sediment input sources 1 to 3 (Fig. 6.3) were successively deactivated from south to north during the Oligocene to Miocene: 34 to 22.5 Ma – sources 1, 2, and 3 active; 19 to 7 Ma – sources 1 and 2 active, 7 to 6 Ma – source 1 active. This approach could produce a shift of the depocenter from south to north from the Oligocene, over the Lower-, to the Upper Miocene, which is in accordance with the isopach maps of the respective intervals. Consequently, the sediment supply coming from the Nile had to be increased with each deactivated source in order to still fill the complete basin. Sediment supply as well as fluvial discharge were mainly adopted from Hawie et al. (2017) and Barabasch et al. (2018).

The sediment supply delivered by either fluvial systems or by the erosion of an uprising margin is not constant over geological periods and depends on several factors, such as climatic conditions (precipitation), tectonic activities, or sea level fluctuations (e.g. Einsele et al., 1996; Mulder and Syvitski, 1995). Changes in these conditions can affect the total amount of transported sediment, as well as the composition of the sediment load. Therefore, such changes can affect the frequency of occurring mass flow events, such as turbidites. For a rough consideration of this relationship, total sediment supply and fluvial discharge were adjusted by +10% during sea level low stands, and by -10% during sea level high stands (Fig. 6.10A). The sediment composition changes from 40% sand, 59.5% clay, and 0.5% terrestrial OM during high stands to 80% sand, 19.5% clay, and 0.5% terrestrial OM during low stands, respectively. In that way, stacked sand bodies that are intercalated with more clay-rich units could be produced (Fig. 6.10B to E), which is in accordance to seismic interpretation of the offshore area (e.g. Hawie et al., 2013b).

In terms of simulated thickness, good results are achieved within the basin, with 90 to 110% of the actual thickness (Fig. 6.12C to H). Best results for the deeper basin part are obtained for the Upper Miocene interval (Fig. 6.12G and H). For this interval, representing the period with the strongest uplift

of Mount Lebanon (e.g. Hawie et al., 2013b), it is important to mention that a relatively thick substratum is required, which can be eroded during the uplift and fill the accommodation space towards the northwest. Sediment supply only from the sediment input sources could not fill this gap. Nevertheless, one area with a large thickness deficit of 200 to 600 m occurs at the northern basin margin along the Latakia Ridge in the Oligocene as well as in the whole Miocene (Fig. 6.12C, E, G), which represents 20 to 80% of the actual thickness in the Oligocene and Upper Miocene, respectively (Fig. 6.12D, F, H). This is reasonable, since *DionisosFlow*® does not consider any structural deformation, which, however, is to be expected along the ridge since the Oligocene (Hall et al., 2005).

The area of the ESM shows moderately good results. In the Oligocene, it shows a deficit of -50 m in the northwestern and a too large thickness of +50 m in the southeastern part (Fig. 6.12C), which are between 60 and 200% of the actual thickness (Fig. 6.12D). In addition, there are some spots with high relative additional thicknesses along the Levant Margin in the Oligocene (Fig. 6.12D), which can be explained by a too high carbonate buildup in these areas. Running the simulation with different carbonate production rates has shown that these buildups do not significantly affect the overall sediment distribution within the Basin. They do, however, affect sediment structures within the surrounding clastic deposits, which would affect e.g. reservoir bodies and properties in these intervals. These reservoir properties are not the focus of this work and are, thus, not considered problematic in this workflow. In the Lower and Upper Miocene, the ESM shows higher thicknesses with 200 to partly 300% of the actual thicknesses (Fig. 6.12F and H), which, however, represents an additional average thickness value of less than 100 m (Fig. 6.12E and G).

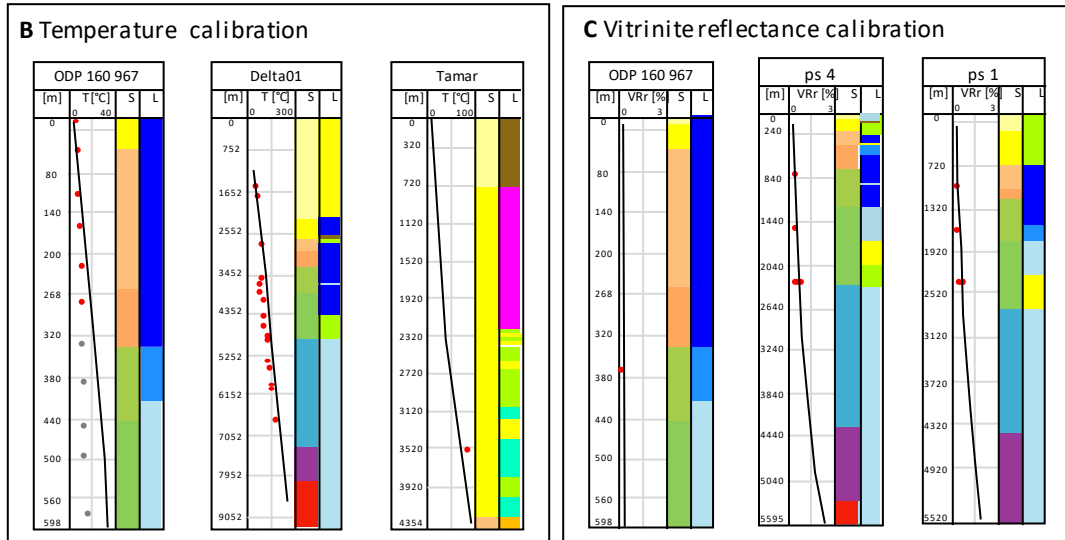
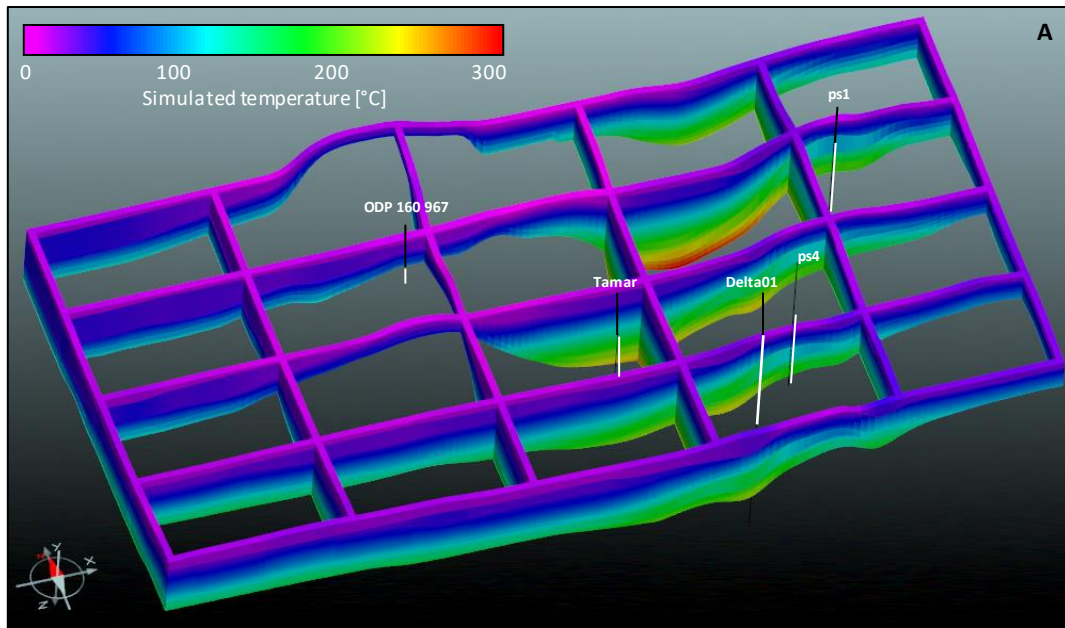
Oligocene and Miocene source rock samples from the Nile Delta Cone show that OM in these samples is either composed of kerogen Type III or a mix of Type II and III (Shaaban et al., 2006). Hence, a combination of “specific-marine-OM” as well as the input of terrestrial-OM via the sediment input sources (0.5% of total sediment supply) was chosen. Since the production of marine OM is usually controlled by nutrients derived from clastic input, the PP of “specific-marine-OM” was related to the sediment distribution from the input sources, with PP decreasing from $200 \text{ g C m}^{-2}\text{a}^{-1}$ at the coast towards $50 \text{ g C m}^{-2}\text{a}^{-1}$ in the offshore area (Fig 6.8C). The input of terrestrial OM as 0.5% of the total sediment supply could produce good results in comparison to the literature values. The simulated TOC contents are generally $\ll 1\%$ throughout the basin (Fig. 6.8 and 6.11A-C). While the initial PP of marine OM is relatively high, clastic sedimentation rates within the basin are also high and dilute the preserved marine OM. Furthermore, the vertical distribution of terrestrial TOC is rather homogenous, showing only minor differences between more clay or more sand rich intervals (Fig. 6.11A-C), which is in accordance to observations within the Nile Delta, where thick (up to >1000m) Oligocene intervals of sand- and siltstones with relatively homogenous TOC contents are observed (Rasoul and Khaled, 2019).

6.4.2 Petroleum system model

The main focus of the integrated petroleum system model was to investigate if the simulated source rock intervals reach far enough into the basin to be affected by thermal maturation, and hence, if they might contribute to viable thermogenic petroleum systems in the Levant Basin. It has to be emphasized here, that the simulation of source rock maturation mainly depends on the maximum temperatures reached during the burial history of a source rock. Next to the spatial source rock distribution, the temperature simulation represents one of the major uncertainties in the presented model. Due to the limited amount of available calibration data for both the present day as well as paleo temperatures, the results presented in the following paragraphs have to be updated as soon as new calibration data becomes available for the offshore area. Further it has to be noted here, that only Easy%Ro (Sweeney and Burnham, 1990) was used for simulating the vitrinite reflectance which has been the standard calculation scheme for almost three decades. Other recently developed algorithms, such as Basin%Ro (Nielsen et al., 2017) or Easy%RoDL (Burnham et al., 2016) will lead to different maturity ranges. Recently, all three algorithms were compared in the context of petroleum generation kinetics for coal/type III kerogen (Froidl et al., 2020).

Figure 6.13 shows the present day simulated temperature throughout the model area (Fig. 6.13A) as well as the temperature (Fig. 6.13B) and vitrinite (Fig. 6.13C) calibration, while Figure 14 shows the burial history for two representative locations, one offshore northern Lebanon (Fig. 6.14 C-D) and one southeast of the ESM (Fig. 6.14 A-B). Temperatures at the top basement are around 120 °C along the onshore Levant area. In the basin, the temperature is around 200 °C in the southern part and reaches up to > 300 °C in the northern Basin, where the deepest burial of about 14 km is reached. At the ESM, instead, temperatures at the top basement are very low with values < 100 °C. The thermal evolution, as well as the resulting simulated vitrinite reflectance during the burial history are shown in Figure 12 for two respective sites in the basin (one at the eastern flank of the ESM, and another one offshore northern Lebanon).

For calibration, simulated present day temperature (Fig. 6.13B) and vitrinite reflectance values (Fig. 6.13C) were initially compared to measured data from wells as published in Bou Daher et al. (2016). These well locations are mainly restricted to the on- and shallow offshore area along the Levant Margin (Fig. 6.13A). For the western part of the model, simulated values were compared to those obtained from ODP Leg 160 wells 966 and 967. It is believed that the ESM was uplifted by about 1 km during the Miocene (Robertson, 1998b). However, vitrinite reflectance measurements of the Upper Cretaceous source rocks that are present along the ESM (Grohmann et al., 2018) show that the maximum burial depth cannot have been much deeper than today. Hence, no uplift/erosional event was considered in this model. Overall, good fits were obtained for all calibration points in the model (Fig. 6.13B and C).



S = stratigraphy

- Pliocene to Holocene
- Miocene
- Oligocene
- Paleocene to Eocene
- Upper Cretaceous
- Lower Cretaceous
- Jurassic
- Triassic
- Permian

L = lithology

- Salt
- Sandy turbidite
- 90% sand 10% shale
- 50% sand 50% shale
- 30% sand 70% shale
- Carbonate mud
- 70% mud 30% carbo grains
- Carbonate grains

Fig. 6.13 A) Simulated present day temperature. For calibration, wells and pseudo wells provided by Bou Daher et al. (2016) plus ODP Leg 160 well 967E (Emeis et al., 1996) are used. Note that the grey temperature dots (B) represent most likely inaccurate temperature measurements (see Emeis et al., 1996). B) Temperature calibration, C) vitrinite reflectance calibration. Depth given in meters below sea level. In (B) and (C) depth values represent meters of burial, relative to the sediment surface.

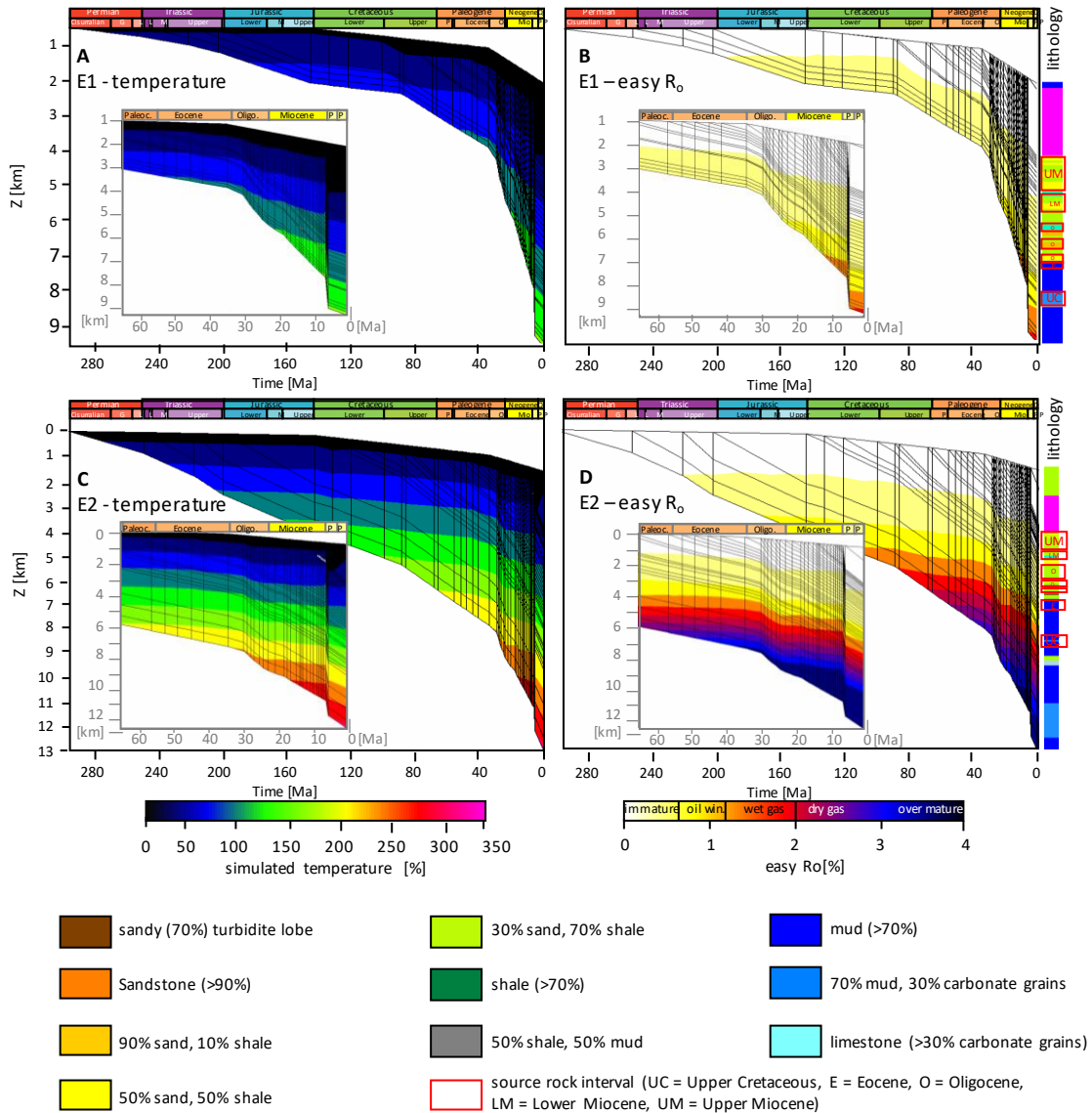


Fig. 6.14 Burial plot showing simulated temperature and Easy R_o evolution through time extracted from location E1 (A and B) and for location E2 (C and D). See Figure 1 for locations E1 and E2.

6.4.2.1 Upper Cretaceous source rocks

Figure 6.15 illustrates the lower (Fig. 6.15 A, C, E) and upper (Fig. 6.15 B, D, F) boundary of the Upper Cretaceous source rock interval at present day burial. Along the Levant Margin, source rocks with high simulated TOC contents ($\gg 1\%$) form a narrow, continuous band of about 50 km parallel to the margin. At the ESM, highest simulated TOC contents form a patchier, halo-like distribution around the summit of the seamount. At both locations the source rocks reach farther into the basin at the lower boundary of the interval compared to the upper boundary (Fig. 6.15A and B).

In terms of temperature, Figure 6.15C and D show that the highest values are reached in the deepest parts of the basin, which is located offshore northern Lebanon. Temperatures reach $250\text{ }^\circ\text{C}$ at the lower boundary and around $210\text{ }^\circ\text{C}$ at the upper boundary. Along the margin, temperatures are much lower

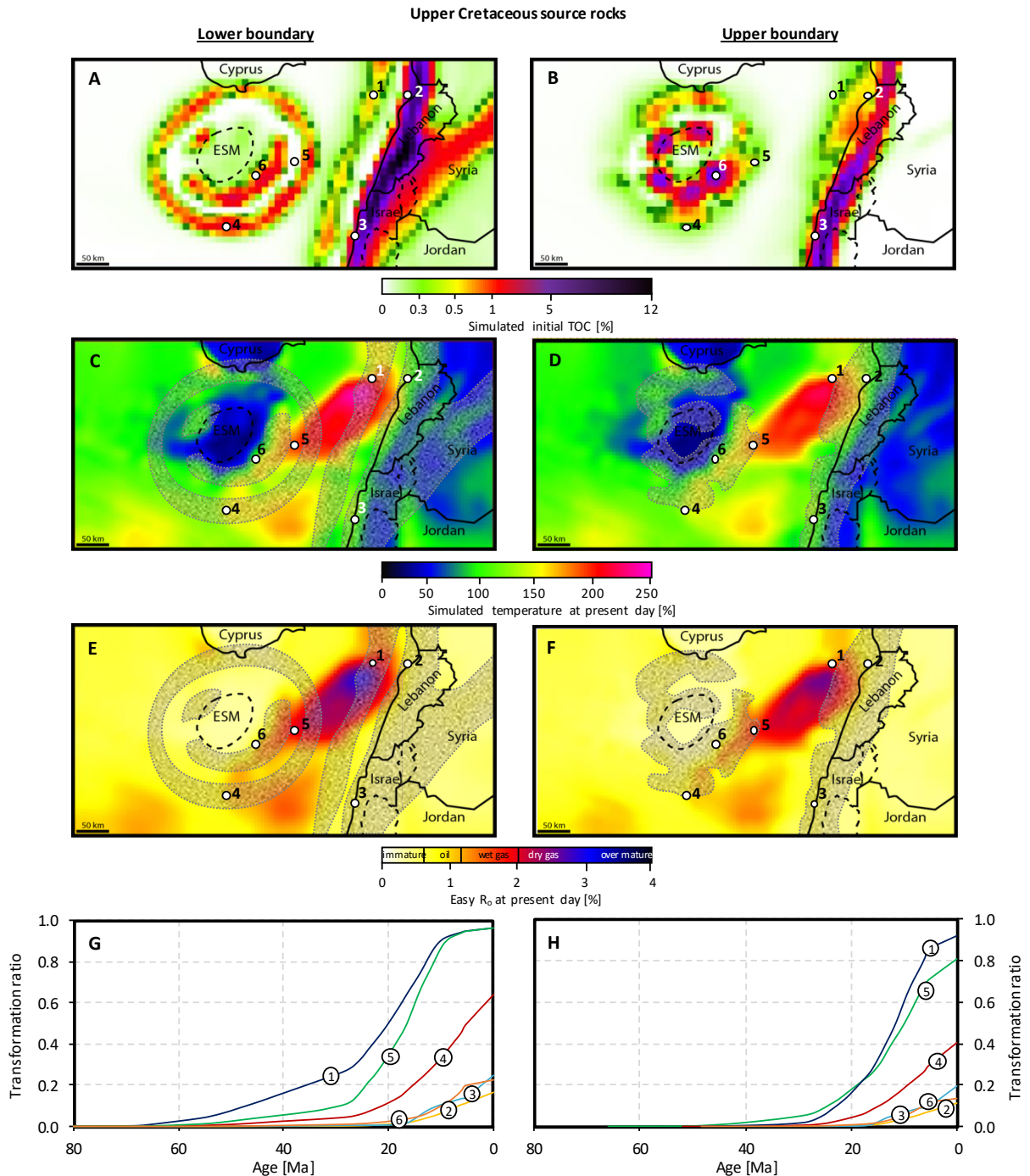


Fig. 6.15 Extracted maps from the petroleum system model showing the initial distribution of the total organic carbon (TOC) content at the lower (A) and upper boundary (B) of the Upper Cretaceous source rock interval. C and D showing the simulated present day temperature at the lower and upper boundary. E and F showing the simulated present day vitrinite reflection at the lower and upper boundary. Shaded areas in C to F indicate source rocks with TOC contents > 0.3%. G and H showing the evolution of the kerogen transformation ratio for different locations (see location numbers. Location 1 and 6 correspond to the extracted burial plots E2 and E1 (Fig. 1 and 13) at the lower and upper boundary, respectively. The cumulative thickness of the source rock at the respective six locations is as follows: 1 = 1000 m, 2 = 300 m, 3 = 260 m, 4 = 470 m, 5 = 600 m, 6 = 400 m.

with 70 °C on average while the ESM is even colder with <50 °C. Comparing the resulting Easy Ro values (Fig. 6.15E and F) with the simulated TOC distribution (Fig. 6.15A and B) shows that the high quality parts (>1% TOC) of the source rocks are not affected by thermal maturation or are, if at all, early mature (Fig. 6.15E and F, location 2 and 3). Nevertheless, the basin ward, low TOC (<1%) source rock

facies reaches higher maturities. These zones are located approximately 50 km offshore northern Lebanon, where both the lower and upper boundary reach into the late dry gas window (Fig. 6.15E and F, location 1), approximately 100 km east of the ESM, where early dry gas maturity is reached (Fig. 6.15E and F, location 5 and 6), and approximately 150 km south of the ESM, where the outermost parts of the source rocks reach into late wet gas window (Fig. 6.15E and F, location 4). Solid bitumen can be found in Upper Cretaceous intervals onshore northern Lebanon (Bou Daher et al., 2015), as well as in Upper Cretaceous and Eocene intervals of the ESM (Grohmann et al., 2018), supporting the model outcome of deeper located HC kitchen areas adjacent to these two locations.

Figure 6.14 shows the burial history for two locations, one offshore northern Lebanon and one southeast of the ESM. In addition, Fig. 6.15G and H show the evolution of the kerogen transformation ratio through time for six specific locations (see above). The high simulated TOC source rocks (>1% TOC) along the margin, which are only slightly affected by thermal maturation, started to generate HC 20 Ma ago and have converted less than 20% of its initial kerogen up to now (Fig. 6.15G and H, locations 2 and 3).

Offshore northern Lebanon, petroleum generation started at the lower source rock boundary in the late Paleocene/early Eocene (approximately 60 Ma) and during the middle Eocene at the upper boundary (Fig. 6.15G and H, location 1). This is approximately 15 to 20 Ma earlier than proposed by Barabasch et al. (2018) or Bou Daher et al. (2016), who, however, did not distinguish between the lower and upper boundary of these source rocks. Source rocks falling into this zone of maturation have converted 50% of its initial kerogen between 20 and 15 Ma, and almost 100% at present day (Fig. 6.15G and H, location 1).

Approximately between 50 and 100 km east of the ESM (Fig. 6.15G and H, location 5) petroleum generation started at the lower source rock boundary in the early Eocene around 50 Ma ago and before 40 Ma at the upper boundary. They have converted 50% of its kerogen between 18 and 15 Ma ago and reach a transformation ratio of 1 and 0.8 at present day. South of the ESM (Fig. 6.15G and H, location 4), temperatures are lower, resulting in a slightly later initiation of petroleum generation and a transformation ratio of 0.6 and 0.4 at the lower and upper boundary, respectively.

Based on the distribution of TOC and the area of maturation, migration pathways in the eastern part of the basin are (without considering any faults) expected towards the direction of the Levant Margin, as well as towards the Latakia Ridge. With respect to potential reservoirs offshore Lebanon, anticlinal structures of the Syrian Arc might be considered as potential targets. These folds formed during late Turonian to early Eocene time (Eyal, 2011) and were, thus, already present before the main phase of hydrocarbon generation.

In the area around the ESM, migration should be either vertical or, depending on the availability of potential impermeable layers, towards the seamount. This interpretation fits well to the presence of solid

bitumen, which was observed in the Upper Cretaceous intervals in the ODP Leg 160 wells (Grohmann et al., 2018).

6.4.2.2 Eocene source rocks

For the Eocene interval (Fig. 6.16) temperatures along the margin and the ESM are almost the same as in the Upper Cretaceous interval. In the northern basin, temperatures reach values of 150 to 170 °C. There is no significant difference between the lower and the upper boundary.

Along the margin, the main parts of the source rocks are immature (Fig. 6.16A and C, location 1). At the northern margin-basin transition only rocks with very low simulated TOC contents (< 0.3%), which are not considered as thermogenic source rocks (Hunt, 1967), reach into the zone of oil and wet gas generation (Fig. 6.16A and C).

For the source rocks along the ESM, most zones with simulated TOC contents > 0.3% are immature. Only the southern- and eastern-most extents reach into the onset of the oil- and early wet gas window, respectively (Fig. 6.16A and C, location 2, 3, and 4). At these locations, petroleum generation started approximately 25 Ma ago. Up to today, they have converted less than 20% of their kerogen. As

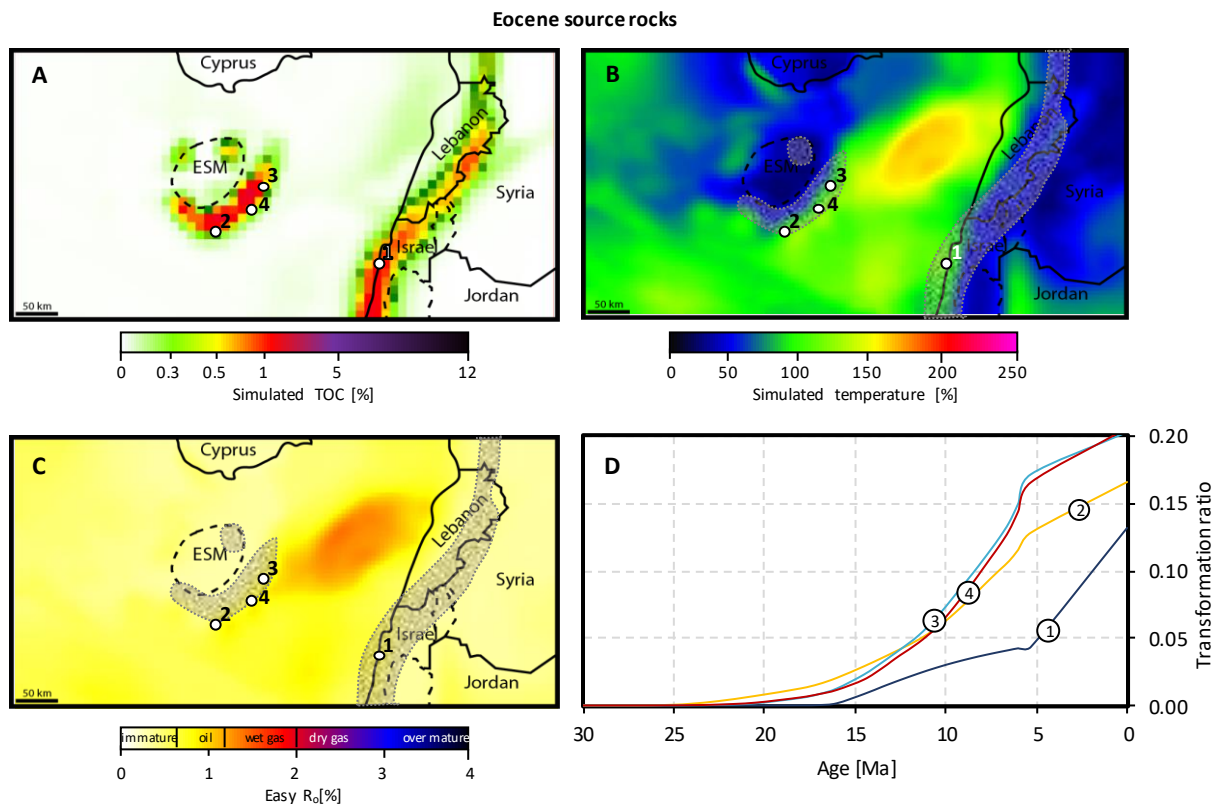


Fig. 6.16 Extracted maps from the petroleum system model showing the initial distribution of the total organic carbon (TOC) content in the Eocene source rocks. B showing the simulated present day temperature. C showing the simulated present day vitrinite reflectance. Shaded areas in B and C indicate source rocks with TOC contents >0.3%. D showing the evolution of the kerogen transformation ratio for different locations (see location numbers, Location corresponds roughly to the burial plot of E1 (Fig. 1 and.13). The cumulative thickness of the source rock at the respective six locations is as follows: 1 = 60 m, 2 = 130 m, 3 = 100 m, 4 = 100 m.

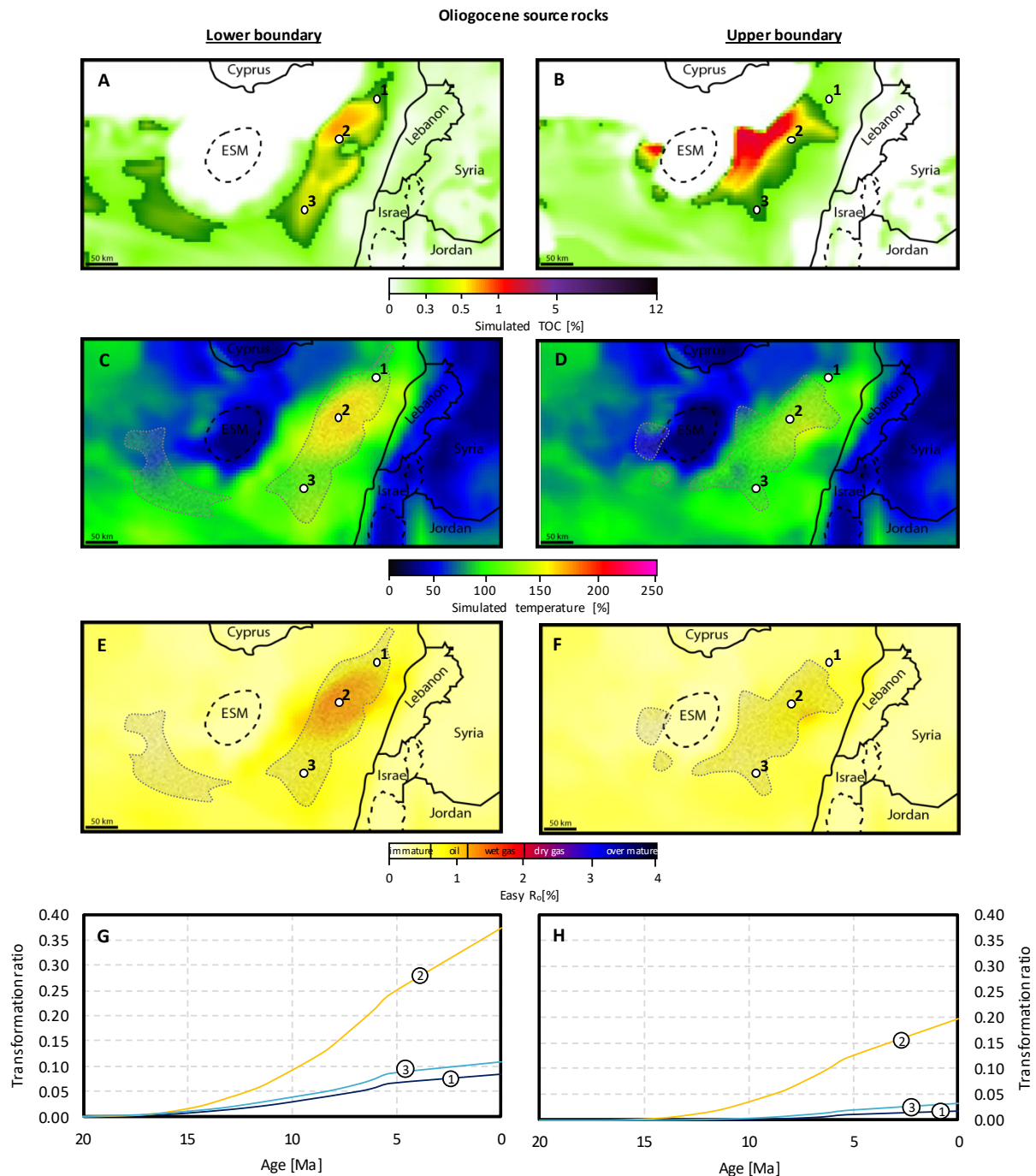


Fig. 6.17 Extracted maps from the petroleum system model showing the initial distribution of the total organic carbon (TOC) content at the lower (A) and upper boundary (B) of the Oligocene source rock interval. C and D showing the simulated present day temperature at the lower and upper boundary. E and F showing the simulated present day vitrinite reflection at the lower and upper boundary. Shaded areas in C to F indicate source rocks with TOC contents > 0.3%. G and H showing the evolution of the kerogen transformation ratio for different locations (see location numbers, location 1 corresponds roughly to the burial plot E2 (Fig. 1 and 13)) at the lower and upper boundary, respectively. The cumulative thickness of the source rock at the respective six locations is as follows: 1 = 1300 m, 2 = 1100 m, 3 = 1100 m, 4 = 100 m.

seen in Figures 6.14 and 6.16D, enhanced thermal maturation was reached after the Messinian salt was deposited, increasing the chance of HC trapping under the salt. Potential reservoir structures might be present as structural traps that are related to the formation of the Levant Fracture System during the late Miocene.

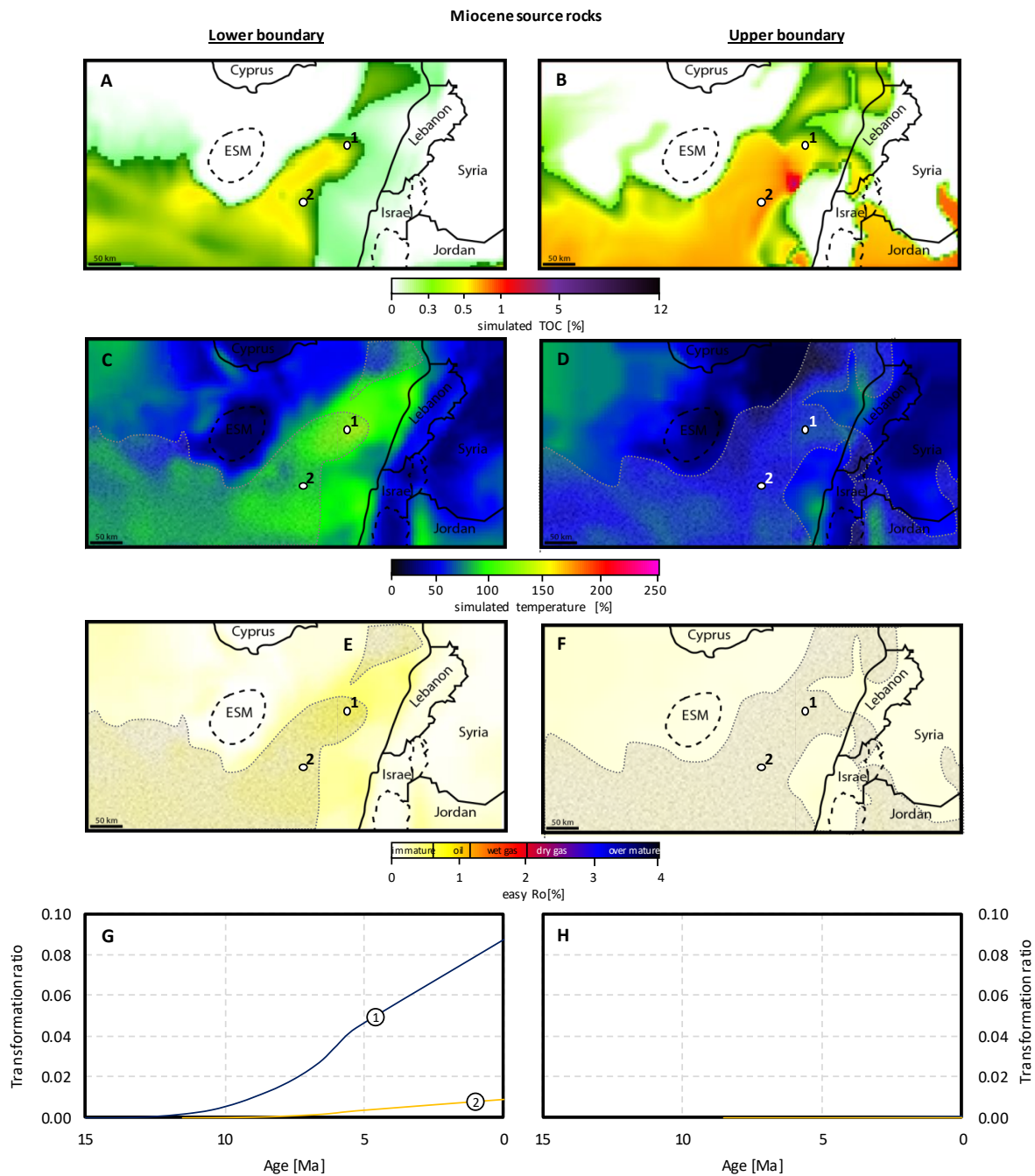


Fig. 6.18 Extracted maps from the petroleum system model showing the initial distribution of the total organic carbon (TOC) content at the lower (A) and upper boundary (B) of the Miocene source rock interval. C and D showing the simulated present day temperature at the lower and upper boundary. E and F showing the simulated present day vitrinite reflection at the lower and upper boundary. Shaded areas in C to F indicate source rocks with TOC contents > 0.3%. G and H showing the evolution of the kerogen transformation ratio for different locations (see location numbers) at the lower and upper boundary, respectively. The cumulative thickness of the source rock at the respective six locations is as follows: 1 = 3000 m, 2 = 2000 m.

6.4.2.3 Oligo-Miocene source rocks

Present day temperatures in the Oligocene to Miocene intervals are clearly lower than in the underlying intervals. Temperatures in the basin are around 100 °C reaching up to 150 °C in the deepest, northern part in the lowest Oligocene source rock interval (Fig. 6.17D), around 100 °C in the lowermost Miocene (Fig. 6.18C), and 50 to 70 °C in the uppermost Miocene source rock interval (Fig. 6.18D).

Generally, it has to be mentioned that sedimentation rates during the Oligo-Miocene were high, which can have significant effects on temperature equilibrium in sediments, especially if sedimentation is non-uniform or when overpressures are generated leading to pulsed fluid flow. Most pronounced transient effects occur in subduction zones, where sediments are brought to great depth 10-100 times faster than in fast subsiding basins. This leads to significant temperature disequilibrium (Lutz et al. 2004). A detailed treatment of such effects was, however, beyond the scope of this study due to the limited calibration data.

Oligocene as well as Miocene source rocks occur almost throughout the entire basin, but show mainly very low simulated TOC contents $\ll 1\%$ (Fig. 6.17A and B; Fig. 6.18A and B). Oligocene source rocks lie within the oil window in the southern model area with their lowermost boundary reaching into the onset of the wet gas window in the northern part of the basin (Fig. 6.17C and D). Miocene source rocks, instead, just entered the onset of the oil window at their lowermost boundary in the northern part of the basin (Fig. 6.18C and D).

Oligocene source rocks started petroleum generation around 15 Ma ago (Fig. 6.17G and H). In the deepest part of the basin, only 10 to 20% of the initial kerogen have been converted before the deposition of the Messinian salt (Fig. 6.17G and H). Thus, further HC generation, which might be still ongoing today, is likely with a good chance of trapping under the salt. However, as these intervals are also believed to be the source for biogenic gas generation (Schneider et al., 2016), it is uncertain how much of the initial TOC is left for thermogenic generation. Miocene source rocks instead, have generated almost no thermogenic HC until today, and are, therefore, primarily interesting as biogenic source rocks.

6.5 Conclusion

The present stratigraphic forward model provides for the first time a process-based, 3D prediction of Upper Cretaceous, Eocene, and Oligo-Miocene source rocks in the Eastern Mediterranean region (Levant Margin and Eratosthenes Seamount). Simulated TOC contents and HI values are in good agreement with published geochemical data of the respective, immature source rocks.

Upper Cretaceous and Upper Eocene source rock models support the idea of upwelling induced enhanced primary bioproductivity, consequent oxygen depletion and deposition and preservation of OM along the Levant Margin, as well as on top of the ESM. Source rocks along the margin form a narrow band of approximately 50 km parallel to the paleo shelf break. Within this narrow band, simulated TOC contents and HI values are high with 1 to 11%, and 300 to 500 mg HC/g TOC, respectively and decrease rapidly towards the deeper basin. At the ESM, OM accumulations show a more patchy distribution and are restricted to the top of the seamount and its closer vicinity. Simulated TOC contents are between 0.5 and 3% and HI values between 150 and 250 mg HC/g TOC, and show as well a rapid decrease towards the deeper basin.

Inferred Oligo-Miocene source rocks show that marine OM is diluted by high sedimentation rates in most locations of the basin. The highest contribution to the simulated TOC content, which occurs relatively homogeneously throughout the entire basin but is mostly $\ll 1\%$, is made up by terrestrial OM which is brought into the basin via the sediment input sources. This leads to low quality, but thick kerogen Type III source rocks with a cumulative thickness of 1 to 2 km.

The incorporation of these simulated source rocks into a classical burial history model shows that some parts of these source rocks are affected by thermal maturation and, hence, suggests the presence of several thermogenic petroleum systems in the Levant Basin:

- Upper Cretaceous source rocks started petroleum generation in the late Paleocene/early Eocene with peak HC generation between 20 and 15 Ma approximately 50 km offshore northern Lebanon. Southeast of the ESM, such source rocks started petroleum generation in the early Eocene with peak generation between 18 and 15 Ma. At both locations these source rocks show a transformation ratio of almost 1.
- Eocene source rocks started HC generation approximately 25 Ma ago between 50 and 100 km southeast of the ESM and reach into the oil to wet gas window at present day. However, until today they have converted less than 20% of their initial kerogen.
- While the Miocene source rocks are mostly immature, Oligocene source rocks lie within the oil window in the southern Levant Basin and reach into the onset of the wet gas window in the northern Levant Basin. However, only 10 to 20% of their initial kerogen has been transformed yet.

Although the presented results are in good agreement with onshore observations and seismic interpretations of the offshore area, it has to be emphasized here that this is still a highly conceptual model, based on many assumptions. Such models of the Eastern Mediterranean region have to be updated according to new information, which will come up in the future. With respect to the presented model, among others, simulated source rock distribution as well as simulated temperatures represent major uncertainties. Certainly, new offshore well data would provide valuable information in this context. A highly recommended well location, in terms of gaining new insights on the offshore area, would be close-shore, offshore Lebanon, with a depth reaching at least down to the Upper Cretaceous. Presence, thickness, TOC and HI data for the source rock intervals would provide data of great relevance for understanding the petroleum system, improving the presented stratigraphic forward model. Maturity (vitrinite reflectance) data would allow a better paleo temperature calibration. In addition, information on the younger strata could provide evidence on gas generation and also provide information on the quality of the Oligo-Miocene reservoir intervals.

Acknowledgements

We thank *Beicip Franlab* for providing the licenses for *DionisosFlow*® and *TemisFlow*®. Further, we thank Benoit Chauveau and Renaud Traby who supported us with the technical aspects of using the respective software packages. We also thank Samer Bou Daher and Nicolas Hawie for interesting, modeling-related discussion about the Eastern Mediterranean Sea. Last but not least, the three reviewers Cedric Griffiths, Gabor Tari and Andy Mort are deeply acknowledged for useful and constructive comments on the manuscript.

7 Conclusion

This PhD thesis was the latest of several previous projects launched and organized by the IFPEN in collaboration with several universities, which aim to enhance the geological knowledge about the Eastern Mediterranean sedimentary basin with a special focus on the petroleum systems in that area. The geochemical analysis of rock samples from onshore Cyprus and from the ODP Leg 160 wells drilled at the Eratosthenes Seamount presented in this thesis prove the existence of formally unknown source rock intervals at the northwestern margin of the Levant Basin. Stratigraphic forward modeling results support the proposed depositional models for the here presented intervals, as well as for other source rocks in the greater Eastern Mediterranean Sea. These models further provide a process based, quantitative estimation of the lateral, basin-ward extent of these source rocks. The incorporation of these source rock models into a petroleum system model can further evaluate areas where thermal maturation might be high enough in order to allow the generation of hydrocarbons.

7.1 Summary

7.1.1 *Source rock characterization*

More than 300 samples of potentially OM-rich rocks were collected during two field campaigns onshore Cyprus and from the ODP Leg 160 cores. The geochemical and petrographic analysis of these samples proves the existence of potential source rock intervals in mainly four different geological units: Onshore Cyprus, these units are the Triassic Vlambouros Fm. and the Miocene Paghna Fm.; offshore Cyprus, along the ESM, these units are the Upper Cretaceous, and the Lower and Upper Eocene. All collected samples are immature or early mature ($\leq 0.6\% \text{ VR}_T$). Therefore, the results of their geochemical analysis are supposed to represent the original characteristics of these rocks.

In the offshore area, very dark, OM-rich mudstones are identified in Upper Cretaceous intervals in well 967 and in Eocene intervals in well 966. The Upper Cretaceous source rocks can be observed in three intervals, which comprise a total cumulative thickness of about 11 m. Due to the low core recovery rate in these wells, the exact thickness cannot be determined. However, the gamma ray logs of this respective well suggests that the actual vertical extent of these source rocks might be higher. In the Eocene, a cumulative thickness of around 30 m of potential source rock intervals can be observed, where the best properties in terms of quantity and quality of OM are found in the uppermost 3 m, which are attributed to the Upper Eocene.

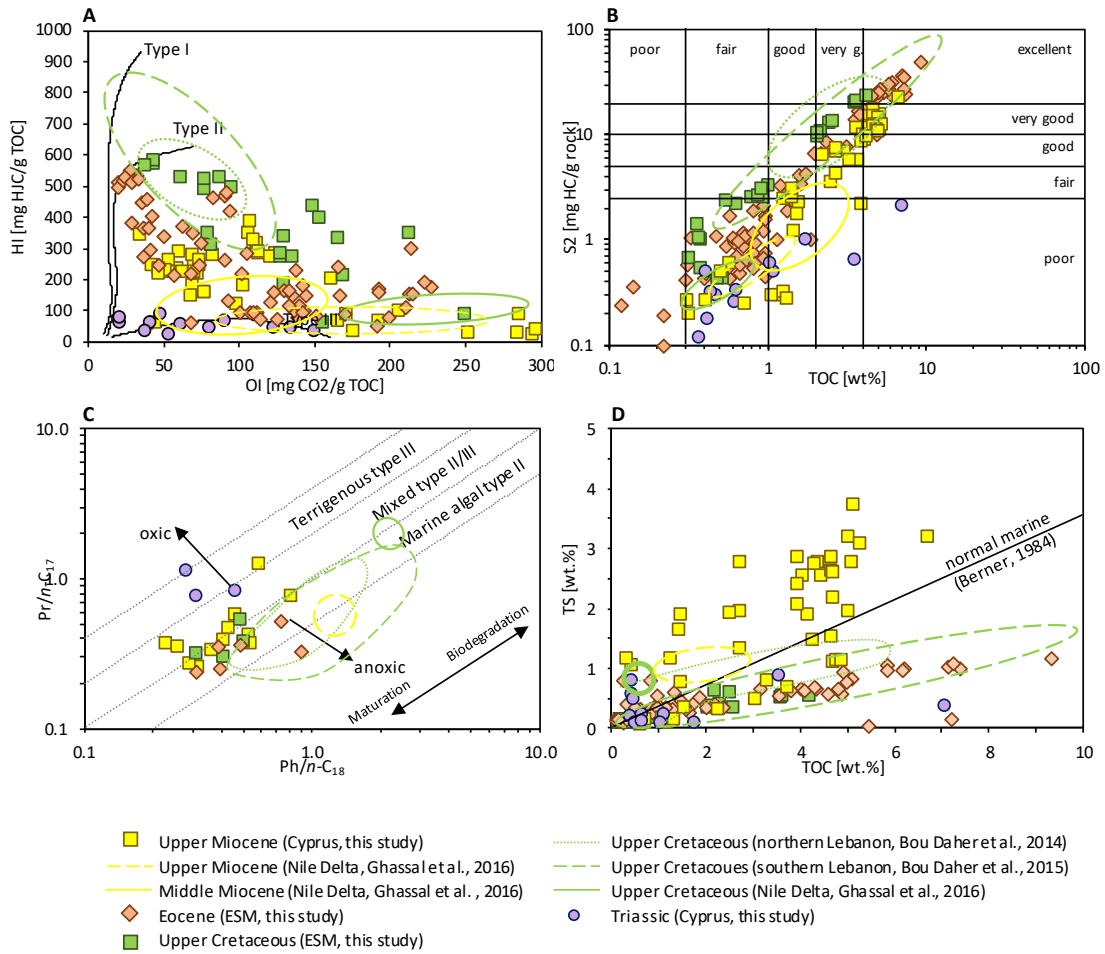


Fig. 7.1 Comparison of several Triassic to Miocene source rocks in the greater area of the Levant Basin. A) Pseudo van Krevelen diagram for kerogen interpretation based on oxygen index (OI) vs. hydrogen index (HI), B) source rock quality based on total organic carbon (TOC) content and hydrocarbon generation potential (S₂), C) TOC vs. total sulfur (TS) content for aquatic environment interpretation, D) Phytane (Ph) over n-C₁₈ vs. Pristane (Pr) over n-C₁₇ ratio for interpretation of paleo redox conditions.

The elemental analyses (TOC, TIC, TS) of these offshore samples indicate an almost exclusive calcareous composition with very little siliciclastic contribution. Rock-Eval pyrolysis (Fig. 7.1 A, Fig. 4.7 A), organic petrography (Fig. 4.4) and biomarker analysis (Fig. 4.5) further indicate that the OM in these rocks is mainly of marine origin. The very low contribution of terrestrial material, a strong positive correlation between the TOC and TS content (Fig. 4.7 B), as well as the oxygen depleted conditions referred from Pr/Ph ratios (Fig. 4.9) suggest that source rock deposition on top of the ESM was the result of upwelling induced enhanced primary bioproductivity, and the consequent formation of an extended oxygen minimum zone. This interpretation is in accordance with the proposed Late Cretaceous upwelling event which affected the Levant Margin and caused the formation of extensive, high quality source rocks for example in Lebanon or Israel. Further, this interpretation is supported by simulations by Rosing (2017), which show that such upwelling events must not be exclusively restricted to the shelf area, but can also occur above topographic heights on the seafloor. In the open ocean, however, such upwelling processes are very sensitive to sea level and ocean current fluctuations, explaining the irregular occurrence of the observed organic-rich intervals along the ESM. Nevertheless,

in terms of type of OM, the Upper Cretaceous source rocks of the ESM are well comparable to their age equivalent onshore Lebanon (Bou Daher et al., 2014, Bou Daher et al., 2015), which is expressed by very similar TOC/S₂ ratios, indicating a similar kerogen type (Fig. 7.1 B), and thus supporting the idea of a related upwelling system. However, total amounts of TOC are clearly lower on average than in Lebanon (Fig. 7.1 B) or Israel, suggesting that the upwelling system, and thus the overall primary productivity was less strong above the seamount than at the Levant Margin. This is further supported by Pr/Ph ratios, which indicate slightly lower oxygen depletion for the samples of the ESM compared to the Levant Margin (Fig. 7.1 C). Both locations are, hence, interpreted as representing normal marine, yet oxygen depleted conditions, which are indicated by the positive correlation between the TOC and the TS content. However, the carbonate-dominated environments at both locations with an expected lack of available reactive iron, causes the samples from the ESM as well as from Lebanon to plot significantly below the normal marine line (Fig. 7.1 D).

Onshore Cyprus, OM-bearing intervals are proven within the Triassic Vlambouros Fm. and in the Miocene Pakhna Fm (Fig. 5.3 and Fig. 5.4). No OM-rich rocks could be found in deposits of Late Cretaceous age, although this was one of the main targets. This can be explained by the geographical location and the depositional environment of Cyprus during the Late Cretaceous, when the island was still in a deep marine environment. Therefore, this area was not affected by the late Cretaceous upwelling event. Also the area was located far away from any continental margin and outside the reach of any OM input.

The Vlambouros Fm. was deposited at the former passive continental margin of Gondwana and was obducted together with the Mamonia complex on the Troodos Ophiolite during the Late Cretaceous. Hence, this formation does not represent depositional conditions that were present in the Levant Basin. Nevertheless, since similar strata is expected in the basement of the Levant Basin or below the ESM, information about potential source rocks within this formation can increase the knowledge about petroleum systems in the area as well. Thin clay stone intervals are interbedded with thick sandstone packages. OM comprising almost exclusively gas-prone type III kerogen (Fig. 7.1 A, Fig. 5.5) is concentrated in the clay layers, but can also be found throughout the sandstone intervals. Although TOC contents are low on average, such sequences reach thicknesses of several tens of meters, and, therefore, might serve at least as minor contributors to thermogenic gas generation at deep burial in the Levant Basin or below the ESM.

In the Miocene Pakhna Fm., which was deposited in several, tectonically controlled sub-basins around the Troodos Ophiolite, OM-bearing intervals are found mainly in the eastern part of the island. Towards the southwestern basins, the frequency and quality of the OM-bearing layers decreases and in the westernmost part of the Pakhna Fm. such layers are absent. Although some terrestrial material can be found within these samples, OM is interpreted to be mainly composed of marine Type II kerogen (Fig. 7.1 A). Biomarker analysis (Fig. 7.1 C, Fig. 5.14 and 5.15) indicates mainly dysoxic depositional conditions, while for the easternmost, high TOC intervals, TOC/TS ratios (Fig. 7.1 D, Fig. 5.14 A), as

Conclusion

well as pyrite framboid size distributions (Fig. 5.12) indicate even anoxic conditions. A positive correlation of the calculated initial amount of OM with the amount of siliciclastic material (Fig. 5.13) suggests that the primary bioproductivity was enhanced by the input of clastic material, which usually provides also nutrients into the system. In the proposed depositional model, these fine grained clastics are either derived from the uprising Troodos Mountain or from the Kyrenia Range in the north of the Island. As more regional sources, the Nile Cone Delta, the uprising Levant Margin, and the Latakia area are considered. All sources would rather reach towards the eastern basins around the Troodos than towards the southwestern ones. This pattern would explain the higher frequency and quality of OM-rich intervals in this eastern part of the island. However, comparing these samples to source rock samples of similar age from other parts of the Levant Basin, e.g. to the Oligocene in Lebanon (Bou Daher et al., 2016) or to the Oligocene-Miocene of the Nile Delta (e.g. Ghassal et al., 2016; Rasoul and Khaled, 2019), shows that the Cyprus area seems to represent a completely different depositional environment compared to the rest of the Levant Basin. While the Miocene Cyprus samples are mainly composed of marine OM, Oligocene and Miocene from the southern and eastern margin of the Levant Basin are almost exclusively composed of Type III kerogen (Fig. 7.1 A). Furthermore, the Cyprus samples contain quite high amounts of carbonates, while in the other areas samples comprise almost exclusively fine grained clastics. However, at all locations, oxygen depleted conditions were reached, which led to the accumulation and partly preservation of OM (Fig. 7.1 C).

In terms of general source rock evaluation based on Rock-Eval pyrolysis, the here presented analysis has shown that there can be a significant difference in HI and OI values obtained from bulk rock samples compared to TOM concentrates (Fig. 7.2). According to older literature, this effect was mainly observed for samples with low TOC contents (e.g. Katz, 1983; Espitalié et al., 1984), whereby the quantity of “low” is not precisely defined. The here presented results confirm that these differences are most prominent, if the TOC content is low. However, even for samples with TOC contents of 4 to 5 wt.% there are still some significant differences. Especially in immature carbonates, unstable carbonates might either decompose already at low temperatures or get dissolved by organic acids, which are generated during pyrolysis, leading to an overestimation of the OI value. On the other hand, clay minerals might retain hydrocarbons that are generated during pyrolysis leading to an underestimation of the HI value. These differences between bulk rock samples and either only decarbonated samples (here for the offshore samples) and TOM concentrates (here for the onshore samples) are in agreement to observations made by Stock et al. (2017). They observed as well pronounced differences between bulk rock samples and concentrated organic matter for samples of the Posidonia Shale (Fig. 7.2). These samples are characterized by high bulk rock TOC contents (4 to 13 wt.%) as well. Comparing their results to those of the Miocene Pakhna samples from Cyprus a less strong difference in the OI values can be observed. However, this can be explained with the lower carbonate contents in the Posidonia samples (2.5 wt.% TIC on average compared to 4.6 wt.% TIC in the Cyprus samples). Furthermore, Stock et al. (2017) observed a decrease in the difference between bulk rock and TOM concentrate with

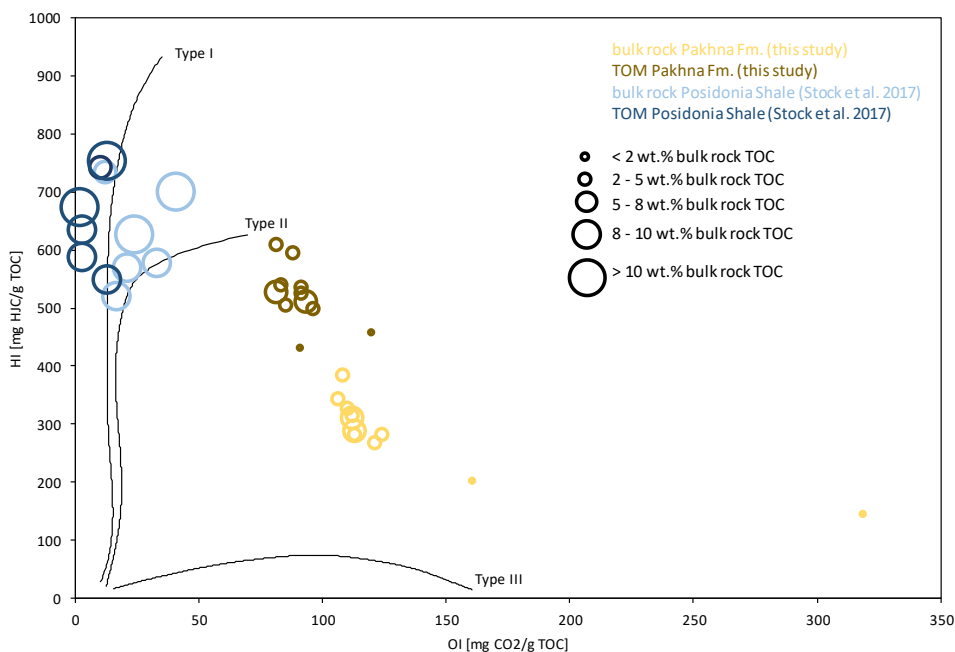


Fig. 7.2 Comparison of Rock-Eval results of bulk rock samples vs. total organic matter (TOM) concentrates obtained from samples of the Miocene pakhna Fm. (onshore Cyprus) from this study with samples of the Posidonia Shale (Stock et al., 2017).

increasing thermal maturity, which fits to the strong differences observed in the Miocene Cyprus samples, which are all completely immature.

7.1.2 Simulation of source rock deposition

Stratigraphic forward modeling and the simulation of a high, upwelling induced primary bioproductivity could generate the Late Cretaceous and Eocene source rocks along the ESM as well as their time equivalents along the Levant Margin. Simulated TOC and HI contents are in good agreement to those values measured on the here presented rock samples, and to those that are published for different locations along the Levant Margin, such as in Lebanon and Israel. Thus, the model is able to support the presented depositional concept for these source rocks and can provide a process based, quantitative estimation of their lateral distribution (Fig. 6.7). The model shows that source rocks along the Levant margin are aligned in a narrow, approximately 50 km wide band parallel to the margin and follow the present day onshore coast line. Best source rock qualities occur in Israel and, in general, quantity and quality of the organic content decrease rapidly outside the simulated oxygen minimum zone. Almost no OM is found in the deeper offshore area, only offshore northern Lebanon, low TOC rocks ($\ll 1\%$) reach up to 50 km towards the basin center. Above the ESM, the lateral source rock extent is also restricted by the extent of the oxygen minimum zone. In contrast to the Levant Margin, however, source rocks are accumulated in topographic lows on the seamounts top and flanks leading to an overall more patchy distribution rather than forming one continuous layer. Some resedimented OM can also be found as halo

Conclusion

like structures around the seamount's flanks. However, these organic-rich sediments do not reach farther than a few kilometers towards the basin.

For the Oligo-Miocene period, the stratigraphic forward model indicates a depositional environment through the Levant Basin that is determined by the deposition of clastic material and terrestrial OM, which form thick sequences of low TOC ($\ll 1\%$) gas prone source rocks. This is in good agreement with published data for the Oligocene in the Nile Delta (reference). However, these clastic sediments derived from all three regional sources, the Nile, the Levant Margin, and the Latakia area, do not reach far into the Levant Basin, but are blocked by the Latakia Ridge, and do not reach up to the island of Cyprus. Hence, the presented model can not confirm the depositional hypothesis for the Miocene source rock onshore Cyprus. Further, the model shows, that even in areas of high primary marine bioproduction, clastic sedimentation rates are too high and dilute any accumulated marine OM. Consequently, source rock deposition around the Cyprus Island had to be controlled by local factors, rather than by regional ones. Hence, as indicated by the comparison to Miocene samples from the Nile Delta, the Miocene source rocks found onshore Cyprus might be more representative of the Miocene as it might be present within the Cyprus- and Latakia Basin, rather than the Levant Basin. However, as the direct area of Cyprus was not properly modeled in this study, this interpretation remains speculative and has to be tested in further studies.

7.1.3 Simulation of source rock maturation

The incorporation of the simulated source rock intervals into a classic petroleum system model could answer the question whether these source rocks are affected by thermal maturation and might contribute to thermogenic petroleum systems in the area. The model shows that for the simulated Upper Cretaceous and Eocene source rock intervals, along the Levant Margin as well as around the ESM, the major parts and especially the zones of high quality (high TOC and HI) are not affected by thermal maturation. However, at two locations the outermost extents of these source rocks, which show low amounts of TOC ($\ll 1\%$) and low HI values, fall into the zone of thermal petroleum generation. These locations are approximately 50 km offshore northern Lebanon and in close vicinity southeast of the ESM. Offshore Lebanon, the Upper Cretaceous source rocks entered the oil window during the middle to late Eocene and might therefore be considered as a potential charge for anticlinal structures which were formed during the Sirian Arc formation. Today, these source rocks lie within the zone of wet gas generation and have transformed almost their entire generation potential. Southeast of the ESM, Late Cretaceous as well as Eocene source rocks reached the zone of oil or even wet gas generation after the deep burial during the Messinian and are likely to have just started their kerogen transformation.

Oligocene source rocks just entered the oil window after the deep burial during the Messinian. Only in the northern part of the Levant Basin burial is deep enough to reach the onset of wet gas generation. However, as the OM in these source rocks is mainly type III kerogen, a production of oil from these

source rocks in unlikely. Reservoir structures, which might be charged by eventually generated gas could be represented by structural, fault associated traps, which were formed during the establishment of the Levant Fracture System in the late Miocene. Miocene source rocks, however, are immature throughout the whole area. Nevertheless, regarding the thick and relatively homogenous distribution of TOC, both, Oligocene and Miocene intervals might serve as good source rocks for biogenic gas generation, since geothermal gradients in the area are low. Sedimentation rates would than be

7.2 Perspective

The integrated approach of extensive field work, geochemical analysis, and numerical simulation provides the first detailed characterization of source rocks in terms of distribution of quantity and quality of OM. Nevertheless, some aspects of the petroleum system need to be studied further. Some interesting follow up research topics are suggested in the following:

- In the present model, only thermal maturation of source rocks was investigated. However, the main HC contribution within the known reservoirs is of biogenic origin. Therefore, it would be interesting to classify zones in the model that are suitable for biogenic generation (based on temperature gradient and sedimentation rates) and combine these zones with the here provided 3D source rock models. In that way, assumptions could be made about regions where the highest biogenic production has occurred and where enough OM material is present to allow the highest amounts hydrocarbons to be generated.
- The simulation of Upper Cretaceous and Eocene source rocks, especially at the ESM, has shown that one very crucial parameter is the shape of the bathymetry and its evolution through time. Hence, more detailed 3D depth maps, which could be obtained from high resolution seismics, and a closer spacing between the seismic lines, could help to produce a more detailed model of the ESM. Also a smaller model, focusing on the ESM alone would help to investigate and calibrate different parameters in a more accurate way in order to better investigate the influence of sea level fluctuations, wave impact, and the interplay between deposition, erosion, and resedimentation of carbonate particles on such an isolated carbonate platform.
- For the Upper Cretaceous upwelling system, constant primary productivity over time was assumed. However, it is known that the intensity of the upwelling varied through time and had a gradual beginning and a gradual termination phase. These variations could be better simulated in a single stratigraphic forward model, focusing on that specific time period.
- A more detailed model for the area of Cyprus would be required in order to better investigate and understand the northeastern part of the Eastern Mediterranean Sea. As the results of the

Conclusion

geochemical analysis as well as the stratigraphic forward modeling have shown that the source rocks offshore Cyprus seem to represent a depositional system, which is at least not directly related to the Levant Basin, a detailed model of the Cyprus area and its eastern offshore area might help to identify regions, where similar source rocks could be present.

- The comparison of Rock-Eval results of bulk source rock samples and their respective total organic matter concentrates has shown that there are significant differences in the obtained HI and OI values. This effect is most prominent for samples with low TOC contents, but appears still for samples with TOC contents up to 5 wt.%, which was not reported in that way in the literature before. A more detailed, systematic study of a larger set of samples with different types and concentrations of OM, different mineral compositions and different maturities could bring new insights into the limitations of Rock-Eval pyrolysis for the classification of kerogen types.

Bibliography

- Aal, A.A., El Barkooky, A., Gerrits M., Meyer, H., Schwander, M., Zaki, H. (2000). Tectonic evolution of the Eastern Mediterranean Basin and its significance for hydrocarbon prospectivity in the ultradeepwater of the Nile Delta, *The Leading Edge* 19, 1086-1102.
- Abed, A.M., Arouri, K.R., Boreham, C.J. (2005). Source rock potential of the phosphorite–bituminous chalk–marl sequence in Jordan. *Marine and Petroleum Geology* 22, 413-425.
- Al-Balushi, A.N., Neumaier, M., Fraser, A.J., Jackson, C.A. (2016). The impact of the Messinian salinity crisis on the petroleum system of the Eastern Mediterranean: a critical assessment using 2D petroleum system modelling. *Petroleum Geoscience* 22, 357-379.
- Allen, P.A., Allen, J.R., (2013). *Basin analysis: Principles and Application to Petroleum Play assessment*. Third edition. John Wiley & Sons, Ltd.
- Almogi-Labin, A., Bein, A., Sass, E. (1993). Late Cretaceous upwelling system along the southern Tethys margin (Israel): interrelationship between productivity, bottom water environments, and organic matter preservation. *Paleoceanography* 8, 671-690.
- Bailey, W. R., Holdsworth, R. E., Swarbrick, R. E. (2000). Kinematic history of a reactivated oceanic suture: the Mamonia Complex Suture Zone, SW Cyprus. *Journal of the Geological Society*, 157, 1107-1126.
- Bar, O., Gvirtzman, Z., Feinstein, S., Zilberman, E. (2013). Accelerated subsidence and sedimentation in the Levant Basin during the Late Tertiary and concurrent uplift of the Arabian platform: Tectonic versus counteracting sedimentary loading effects. *Tectonics*, 32, 334-350.
- Barabasch, J., Ducros, M., Hawie, N., Daher, S. B., Nader, F. H., Littke, R. (2018). Integrated 3D forward stratigraphic and petroleum system modeling of the Levant Basin, Eastern Mediterranean. *Basin Research*, 31, 228-252.
- Barker, C.E., Pawlewicz, M.J. (1993). An empirical determination of the minimum number of measurements needed to estimate the mean random vitrinite reflectance of disseminated organic matter, *Organic Geochemistry* 20, 643-651.
- Barker, C.E., Pawlewicz, M.J. (1994). Calculation of Vitrinite Reflectance from Thermal Histories and Peak Temperatures - A Comparison of Methods, in: Mukhopadhyay P.K., Dow W.G. (eds), *Reevaluation of Vitrinite Reflectance*. ACS Symposium Series 570, pp. 216-229.
- Barrier, E., Vrielynck, B. (2008). *Atlas of Paleotectonic maps of the Middle East (MEBE Program)*. – CCGM – CGMW. - Atlas of 14 maps.

Bibliography

- Bartov, Y., Steinitz, G., Eyal, M., Eyal, Y. (1980). Sinistral movement along the Gulf of Aqaba—its age and relation to the opening of the Red Sea. *Nature* 285, 220.
- Behar, F., Beaumont, V., Pentead, H.D.B. (2001). Rock-Eval 6 technology: performances and developments, *Oil Gas Science and Technology – Rev. IFP* 56, 111-134.
- Berger, W. H. (1987). Productivity and organic carbon flux. Part I. Overview and maps of primary production and export production. *Scripps Institution Oceanography* 67.
- Berner, R.A. (1984). Sedimentary pyrite formation: an update, *Geochimica et Cosmochimica Acta* 48, 605-615.
- Bertello, F., Harby, H., Brandolese S. (2016). Egypt: Zohr, an Outstanding Gas Discovery in a New Deep-Water Hydrocarbon Play, in: 8th Mediterranean Offshore Conference and Exhibition, Alexandria, Egypt.
- Betts, J.N., Holland, H.D., (1991). The oxygen content of ocean bottom waters, the burial efficiency of organic carbon, and the regulation of atmospheric oxygen. *Global Planetary Change* 97, 5–18.
- Beydoun, Z.R. (1991). Arabian Plate Hydrocarbon Geology and Potential - A Plate Tectonic Approach, *AAPG Studies in Geology* 33, 77.
- BMWi (2017), Erneuerbare Energien in Zahlen – Nationale und internationale Entwicklung im Jahr 2016. Bundesministerium für Wirtschaft und Energie.
- Bragin, N.Y., Krylov, K.A. (1996). Stratigraphy and lithology of the Upper Triassic deposits of southwestern Cyprus (Vlambouros Formation). *Stratigraphy and Geological Correlation* 4, 132-140.
- Bohacs, K.M., Carroll, A.R., Mankiewicz, P.J., Miskell-gerhardt, K.J., Schwalbach, J.O.N.R., Wegner, M.B., Simo, J.A.T. (2005). Production, destruction, and dilution—the many paths to source-rock development. in: Harris, N.B. (Ed.), *The Deposition of Organic-carbon-rich Sediments: Models, Mechanisms and Consequences*. Special Publications of SEPM, pp. 61-101.
- Bou Daher, S., Nader, F.H., Strauss, H., Littke R. (2014). Depositional environment and source-rock characterization of organic-matter rich Upper Santonian-Upper Campanian carbonates, northern Lebanon, *Journal of Petroleum Geology* 37, 5-24.
- Bou Daher, S., Nader, F. H., Müller, C., Littke, R. (2015). Geochemical and petrographic characterization of Campanian–Lower Maastrichtian calcareous petroleum source rocks of Hasbayya, South Lebanon, *Marine and Petroleum Geology* 64, 304-323.
- Bou Daher, S., Ducros, M., Michel, P., Hawie, N., Nader F.H., Littke R. (2016). 3D thermal history and maturity modelling of the Levant Basin and its eastern margin, offshore–onshore Lebanon, *Arabian Journal of Geosciences* 9, 440.

-
- Bourbonniere, R.A., Meyers, P.A. (1996). Sedimentary geolipid records of historical changes in the watershed and productivities of Lake Ontario and Erie, *Limnology and Oceanography* 41, 352-359.
- Bray, E.E., Evans, E.D. (1961). Distribution of n-paraffins as a clue to recognition of source beds, *Geochimica et Cosmochimica Acta* 22, 2-15.
- Bruneau, B., Chauveau, B., Baudin, F., Moretti, I. (2017). 3D stratigraphic forward numerical modelling approach for prediction of organic-rich deposits and their heterogeneities. *Marine and Petroleum Geology* 82, 1-20.
- Chauveau, B., Granjeon, D., Huc, A.Y. (2013). Depositional Model of Marine Organic Matter Coupled With a Stratigraphic Forward Numerical Model (DIONISOS): Application to the Devonian Marcellus Formation (Abstr.). In: AAPG Hedberg Conference Petroleum Systems: Modeling the Past, Planning the Future abstracts. American Association of Petroleum Geologists.
- Choquette, P.W., Pray, L.C. (1970). Geologic nomenclature and classification of porosity in sedimentary carbonates, *AAPG bull.*54, 207-250.
- Cord-Ruwisch, R., Kleinitz, W., Widdle, F. (1987). Sulfate-reducing bacteria and their activities in oil production, *Journal of Petroleum Technology* 39, 97-106.
- Cyprus Geological Survey, 1995. Geological map of Cyprus, [http://www.moa.gov.cy/moa/gsd/gsd.nsf/All/43CA34467BC412EAC2256FB30035287E/\\$file/GeologicalMapOfCyprus_250k_en.jpg?OpenElement](http://www.moa.gov.cy/moa/gsd/gsd.nsf/All/43CA34467BC412EAC2256FB30035287E/$file/GeologicalMapOfCyprus_250k_en.jpg?OpenElement) (accessed 13 September 2018 14:00), Cyprus Geological Survey, Nicosia, Cyprus.
- Cyprus Mail, 2018. 'Zohr-like play' in Block 6, Turkish Navtex will not stop plans (Wrap-up), <https://cyprus-mail.com/2018/02/08/zohr-like-play-block-6-turkish-navtex-will-not-stop-plans-wrap/> (accessed 13 September 2018 17:00), Cyprus Mail Company LTD., Nicosia, Cyprus.
- Dai, A., Trenberth, K.E. (2002). Estimates of freshwater discharge from continents: Latitudinal and seasonal variations. *Journal of Hydrometeorology* 3, 660-687.
- Dean, W.E., Arthur, M.A., (1989). Iron-sulfur-carbon relationships in organic-carbon-rich sequences I: Cretaceous Western Interior Seaway. *American Journal of Science* 289, 708-743.
- Dunham, R.J., (1962). Classification of Carbonate Rocks According to Depositional Texture. in: Ham, W.E. (Ed.), *Classification of Carbonate Rocks*, AAPG, Tulsa, pp. 108-121.
- Durand, B., Nicaise, G., (1980). Procedures for Kerogen Isolation. in: Durand, B. (Ed.), *Kerogen Insoluble Organic Matter from Sedimentary Rocks*, Editions Technip, Paris, pp. 35-53.
- Eastwell, D., Hodgson, N., Rodriguez, K. (2018). Source rock characterization in frontier basins—a global approach. *First Break* 36, 53-60.

Bibliography

- Eaton, S., Robertson, A. (1993). The Miocene Pakhna Formation, southern Cyprus and its relationship to the Neogene tectonic evolution of the Eastern Mediterranean. *Sedimentary Geology* 86, 273-296.
- Einsele, G., Chough, S.K., Shiki, T. (1996). Depositional events and their records—an introduction. *Sedimentary Geology* 104, 1-9.
- El Nady, M.M., (2007). Organic geochemistry of source rocks, condensates, and thermal geochemical modeling of Miocene sequence of some wells, onshore Nile Delta, Egypt. *Petroleum science and technology* 25, 791-818.
- Emeis, K.C., Robertson, A.H.F., Richter, C., et al. (1996). Proc. ODP, Init. Repts., 160: College Station, TX (Ocean Drilling Program).
- Eni (2018) Eni announces a gas discovery Offshore Cyprus, retrieved from: http://www.eni.com/docs/en_IT/enicom/media/press-release/2018/02/PR_Eni-Cyprus_Calypto.pdf
- Esestime, P., Hewitt, A., Hodgson, N. (2016). Zohr - A newborn carbonate play in the Levantine Basin, East-Mediterranean, *First Break* 34, 87-93.
- Espitalié, J., Laporte, J.L., Madec, M., Marquis, F., Leplat, P., Paulet, J., Boutefeu, A. (1977). Méthode rapide de caractérisation des roches mères, de leur potentiel pétrolier et de leur degré d'évolution, *Rev. IFP* 32,1, 23-42.
- Espitalié, J., Senga Makadi, K., Trichet, J. (1984). Role of the mineral matrix during kerogen pyrolysis. *Organic Geochemistry* 6, 365-382.
- ExxonMobil (2019). ExxonMobil makes natural gas discovery offshore Cyprus, https://corporate.exxonmobil.com/news/newsroom/news-releases/2019/0228_exxonmobil-makes-natural-gas-discovery-offshore-cyprus (accessed 3 April 2019 14:00), ExxonMobil Corporation, Texas, USA.
- Eyal, Y. (2011). The Syrian Arc Fold System: age and rate of folding. In *Geophysical Research Abstracts* 13.
- Feinstein, S., Aizenshtat, Z., Miloslavski, I., Gerling, P., Slager, J., McQuilken, J. (2002). Genetic characterization of gas shows in the east Mediterranean offshore of southwestern Israel, *Organic Geochem* 33, 1401-1413.
- Follows, E.J., Robertson, A.H., Scoffin, T.P. (1996). Tectonic controls on Miocene reefs and related carbonate facies in Cyprus.
- Galindo-Zaldivar, J., Nieto, L., Robertson, A., Woodside, J. (2001). Recent tectonics of Eratosthenes Seamount: an example of seamount deformation during incipient continental collision, *Geo-Mar Lett.* 20, 233-242.

-
- Gardosh, M.A., Druckman, Y. (2006). Seismic stratigraphy, structure and tectonic evolution of the Levantine Basin, offshore Israel, *Geol. Society London Special Publications* 260, 201-227.
- Gardosh, M.A., Druckman, Y., Buchbinder, B., Calvo, R., (2008). The Oligo-Miocene deepwater system of the Levant basin. *Geological survey of Israel* 33, 1-73.
- Gardosh, M.A., Druckman, Y., Buchbinder, B. (2009). The Late Tertiary Deep-Water Siliciclastic System of the Levant Margin—An Emerging Play Offshore Israel. *American Association of Petroleum Geologists Search and Discovery Article*, 10211.
- Gardosh, M.A., Garfunkel, Z., Druckman, Y., Buchbinder, B. (2010). Tethyan rifting in the Levant Region and its role in Early Mesozoic crustal evolution. *Geological Society, London, Special Publications* 341, 9-36.
- Garfunkel, Z. (2004). Origin of the Eastern Mediterranean basin: a reevaluation. *Tectonophysics* 391, 11-34.
- Genin, A., Boehlert, G.W. (1985). Dynamics of temperature and chlorophyll structures above a seamount: an oceanic experiment, *Journal of Marine Research* 43, 907-924.
- Ghalayini, R., Daniel, J. M., Homberg, C., Nader, F.H., Comstock, J.E. (2014). Impact of Cenozoic strike-slip tectonics on the evolution of the northern Levant Basin (offshore Lebanon). *Tectonics* 33, 2121-2142.
- Ghalayini, R., Nader, F.H., Bou Daher, S., Hawie, N., Chbat, W.E. (2018). Petroleum systems of Lebanon: An update and review. *Journal of Petroleum Geology* 41, 189-214.
- Granjeon, D., Joseph, P. (1999). Concepts and applications of a 3-D multiple lithology, diffusive model in stratigraphic modeling.
- Granot, R. (2016). Palaeozoic oceanic crust preserved beneath the eastern Mediterranean. *Nature Geoscience* 9, 701.
- Grohmann, S., Fietz, S. W., Littke, R., Daher, S. B., Romero-Sarmiento, M.F., Nader, F.H., Baudin, F. (2018). Source rock characterization of mesozoic to cenozoic organic matter rich marls and shales of the Eratosthenes Seamount, Eastern Mediterranean Sea. *Oil & Gas Science and Technology—Revue d'IFP Energies nouvelles* 73, 49.
- Grohmann, S., Romero-Sarmiento, M.F., Nader, F.H., Baudin, F., Littke, R. (2019). Characterization of Potential Source Rock Intervals of Late Mesozoic to Cenozoic Age in the On-and Offshore Area of Cyprus and Their Impact on Petroleum Systems in the Eastern Mediterranean Sea. In *Advances in Petroleum Engineering and Petroleum Geochemistry* (pp. 135-137). Springer, Cham.
- Hall, J., Calon, T.J., Aksu, A. E., Meade, S.R. (2005). Structural evolution of the Latakia Ridge and Cyprus Basin at the front of the Cyprus Arc, eastern Mediterranean Sea. *Marine Geology* 221, 261-297.

Bibliography

- Haq, B.U., Hardenbol, J., Vail, P.R. (1988). Mesozoic and Cenozoic chronostratigraphy and cycles of sea-level change. SEPM Special Publications 42.
- Hatem, B.A., Abdullah, W.H., Hakimi, M.H., Mustapha, K.A. (2016). Origin of organic matter and paleoenvironment conditions of the Late Jurassic organic-rich shales from shabwah sub-basin (western Yemen): Constraints from petrology and biological markers. *Mar. Petrol. Geol.* 72, 83-97.
- Hawie, N., Deschamps, R., Nader, F.H., Gorini, C., Müller, C., Desmares, D., Hoteit, A., Granjeon, D., Montadert, L., Baudin, F. (2013a). Sedimentological and stratigraphic evolution of northern Lebanon since the Late Cretaceous: implications for the Levant margin and basin. *Arabian Journal of Geosciences* 7, 1323-1349.
- Hawie, N., Gorini, C., Deschamps, R., Nader, F.H., Montadert, L., Granjeon, D., Baudin, F. (2013b). Tectono-stratigraphic evolution of the northern Levant Basin (offshore Lebanon). *Marine and Petroleum Geology* 48, 392-410.
- Hawie, N., Deschamps, R., Granjeon, D., Nader, F.H., Gorini, C., Müller, C., Montadert, L., Baudin, F. (2017). Multi-scale constraints of sediment source to sink systems in frontier basins: a forward stratigraphic modelling case study of the Levant region. *Basin Research* 29, 418-445.
- Henson, F.R.S., Browne, R.V., McGinty, J. (1949). A synopsis of the stratigraphy and geological history of Cyprus. *Quarterly Journal of the Geological Society* 105, 1-41.
- Honjo, S., Manganini, S. J., Krishfield, R.A., Francois, R. (2008). Particulate organic carbon fluxes to the ocean interior and factors controlling the biological pump: A synthesis of global sediment trap programs since 1983. *Progress in Oceanography* 76, 217-285.
- Houghton, S. D., Jenkins, D.G., Xenophontos, C., Gass, I. G. (1987). Microfossil evidence for a latest Pliocene ages for Amathus and Khirokitia channel deposits, southern Cyprus, and thereby the unroofing of the Troodos Massif. In *Ophiolites: Oceanic Crustal Analogues. Proc. Symp.* "Troodos (pp. 231-234).
- Hsü, K. J., Montadert, L., Bernoulli, D., Cita, M.B., Erickson, A., Garrison, R. E., Kidd, R.B., Mélières, F., Müller, C., Wright, R. (1977). History of the Mediterranean salinity crisis. *Nature* 267, 399-403.
- Huang, W.Y., Meinschein, W.G. (1979). Sterols as ecological indicators, *Geochimica et Cosmochimica Acta* 43, 739-745.
- Hunt, J.M. (1967). The Origin of Petroleum in Carbonate Rocks, in: Chillingar G.V., Bissel H.J., Fairbridge R.W. (eds), *Developments in Sedimentology Vol. 9 Carbonate Rocks Physical and Chemical Aspects*, Elsevier, Amsterdam, pp. 225-251.
- Hunt, J.M. (1995). *Petroleum Geochemistry and Geology*. W. H. Freeman and Company, New York, pp. 1-20.

-
- Inati, L., Zeyen, H., Nader, F.H., Adelinet, M., Sursock, A., Rahhal, M.E., Roure, F. (2016). Lithospheric architecture of the Levant Basin (Eastern Mediterranean region): A 2D modeling approach. *Tectonophysics* 693, 143-156.
- Inati, L., Lecomte, J. C., Zeyen, H., Nader, F.H., Adelinet, M., Rahhal, M.E., Sursock, A. (2018). Crustal configuration in the northern Levant basin based on seismic interpretation and numerical modeling. *Marine and Petroleum Geology* 93, 182-204.
- Kähler, G. (1994). Stratigraphy and sedimentology of the Lefkara formation, Cyprus (Palaeogene to Early Neogene). PhD thesis, Department of Geology, University of Southampton.
- Kähler, G., Stow, D.A. (1998). Turbidites and contourites of the Palaeogene Lefkara Formation, southern Cyprus. *Sedimentary Geology* 115, 215-231.
- Katz, B.J. (1983). Limitations of 'Rock-Eval' pyrolysis for typing organic matter, *Organic Geochemistry* 4, 195-199.
- Katz, B. J. (2012). *Petroleum source rocks*. Springer Science & Business Media, Berlin.
- Kinnaird, T.C., Robertson, A.H., Morris, A. (2011). Timing of uplift of the Troodos Massif (Cyprus) constrained by sedimentary and magnetic polarity evidence. *Journal of the Geological Society* 168, 457-470.
- Klein Goldewijk, C.G.M. (2016). A historical land use data set for the Holocene. EGU General Assembly Conference Abstracts. 2016. p. 1574.
- Kouwenhoven, T.J., Van der Zwaan, G.J. (2006). A reconstruction of late Miocene Mediterranean circulation patterns using benthic foraminifera. *Palaeogeography, Palaeoclimatology, Palaeoecology* 238, 373-385.
- Krijgsman, W., Blanc-Valleron, M.M., Flecker, R., Hilgen, F.J., Kouwenhoven, T J., Merle, D., Orszag-Sperber, F., Rouchy, J.M. (2002). The onset of the Messinian salinity crisis in the Eastern Mediterranean (Pissouri Basin, Cyprus). *Earth and Planetary Science Letters* 194, 299-310.
- Lapierre, H. (1975). Les formations sédimentaires et éruptives des nappes de Mamonia et leurs relations avec le Massif du Troodos (Chypre occidentale). *Mémoires de la Société géologique de France* no. 123, pp. 131. ISBN-10: 2704000549.
- Lapierre, H., Bosch, D., Narros, A., Mascle, G.H., Tardy, M., Demant, A. (2007). The Mamonia Complex (SW Cyprus) revisited: remnant of Late Triassic intra-oceanic volcanism along the Tethyan southwestern passive margin. *Geological Magazine* 144, 1-19.
- Le Pichon, X., Kreemer, C., 2010. The Miocene-to-Present Kinematic Evolution of the Eastern Mediterranean and Middle East and Its Implications for Dynamics. *Annu. Rev. Earth and Planetary Science Letters* 38, 323-351.

Bibliography

- Lewan, M.D. (1984). Factors controlling the proportionality of vanadium to nickel in crude oils. *Geochimica et Cosmochimica Acta*, 48, 2231-2238.
- Lie Ø., Skiple C., Lowrey C. (2011). New insights into the Levantine Basin, *GeoExPro8*, 1, 24-27.
- Littke, R. (1993). Deposition, Diagenesis and Weathering of Organic Matter-Rich Sediments, in: Bhattacharji S., Friedmann G.M., Neugebauer H.J., Seilacher A. (eds) *Lecture Notes in Earth Sciences*, Springer, Berlin, pp. 22-27, pp. 169-182.
- Lord, A.R., Panayides, I., Urquhart, E., Xenophontos, C., Malpas, J. (2000). A biochronostratigraphical framework for the Late Cretaceous–Recent circum-Troodos sedimentary sequence, Cyprus, in: *Proceedings of the Third International Conference on the Geology of the Eastern Mediterranean*. Geological Survey Department, Nicosia, Vol. 289, pp. 297, ISBN: 9963175066.
- Makris, J., Stobbe, C. (1984). Physical properties and state of the crust and upper mantle of the Eastern Mediterranean Sea deduced from geophysical data. *Marine Geology* 55, 347-363.
- Mann, U., Zweigel, J. (2008). Modeling source-rock distribution and quality variations: the organic facies modelling approach. *Spec. Publ. Int. Assoc. Sedimentology* 40, 139–274.
- Martin, J.H., Knauer, G.A., Karl, D.M., Broenkow, W.W. (1987). VERTEX: carbon cycling in the northeast Pacific. *Deep-Sea Research* 34, 267–285.
- May, P.R. (1991). The Eastern Mediterranean Mesozoic Basin: Evolution and Oil Habitat (1), *AAPG Bull.*75, 1215-1232.
- Meilijson, A., Steinberg, J., Hilgen, F., Bialik, O. M., Waldmann, N.D., Makovsky, Y. (2018). Deep-basin evidence resolves a 50-year-old debate and demonstrates synchronous onset of Messinian evaporite deposition in a non-desiccated Mediterranean. *Geology* 46, 243-246.
- Milliman, J.D., Syvitski, J.P.M. (1992). Geomorphic/tectonic control of sediment discharge to the ocean: The importance of small mountainous rivers. *Journal of Geology* 100, 525-544:
- Montadert, L., Nicolaides, S., Semb, P.H., Lie, Ø. (2014). Petroleum Systems Offshore Cyprus, in: Marlow L., Kendall C., Yose L. (eds), *AAPG Special Volumes Memoir 160: Petroleum systems of the Tethyan region*, AAPG, Tulsa, OK, pp. 301-334.
- Morris, A.N., Marder, O., Davidzon, A., Ibrahim, F. (1998). Putting Humpty together again: Preliminary observations on refitting studies in the eastern Mediterranean. The organization of lithic technology in late glacial and early postglacial Europe, 700, 149-182.
- Mulder, T., Syvitski, J.P. (1995). Turbidity currents generated at river mouths during exceptional discharges to the world oceans. *The Journal of Geology* 103, 285-299.

-
- Nader, F.H. (2014). Insights into the petroleum prospectivity of Lebanon, in : Marlow L., Kendall C., Yose L. (eds), AAPG Special Volumes Memoir 160: Petroleum systems of the Tethyan region, AAPG, Tulsa, OK, pp. 241–278.
- Nader, F.H., Inati, L., Ghalayini, R., Hawie, N., Bou Daher, S. (2018). Key geological characteristics of the Saida-Tyr Platform along the eastern margin of the Levant Basin, offshore Lebanon: implications for hydrocarbon exploration. *Oil & Gas Science and Technology–Revue d'IFP Energies nouvelles* 73, 50.
- National Oceanic and Atmospheric Administration (2018). Bathymetric Data Viewer, <https://maps.ngdc.noaa.gov/viewers/bathymetry/> (accessed 28 November 2018 11:00), National Centers for Environmental Information, U.S. Department of Commerce, Washington, D.C., USA.
- Naylor, D., Al-Rawi, M., Clayton, G., Fitzpatrick, M.J., Green, P.F. (2013). Hydrocarbon potential in Jordan, *Journal of Petroleum Geology* 36, 205-236.
- Needham, D., Hosler, J., Nowak, S., Christensen, C., French J. (2013). The Tamar Field from Discovery to Production (Abstract), in: AAPG Search and Discovery Article #90161©2013, AAPG European Conference.
- Netzeband, G.L., Gohl, K., Hübscher, C.P., Ben-Avraham, Z., Dehghani, G.A., Gajewski, D., Liersch P. (2006). The Levantine Basin—crustal structure and origin, *Tectonophysics* 418, 167-188.
- Nixon, S.W., Oviatt, C.A., Frithsen, J., Sullivan, B. (1986). Nutrients and the productivity of estuarine and coastal marine ecosystems. *Journal of the Limnological Society of Southern Africa* 12, 43-71.
- Papadimitriou, N. (2017). Geodynamics and synchronous filling of a rift type-basin evolved through compression tectonics (The western margin of the Levant Basin). PhD thesis, Géoscience Ressources naturelles et Environnement, Institut de Sciences de la Terre de Paris, Université Pierre et Marie Curie, Paris.
- Papadimitriou, N., Gorini, C., Nader, F.H., Deschamps, R., Symeou, V., Lecomte, J.C. (2018). Tectono-stratigraphic evolution of the western margin of the Levant Basin (offshore Cyprus), *Marine and Petroleum Geology* 91, 683-705.
- Pearce, J.A., Robinson, P.T. (2010). The Troodos ophiolitic complex probably formed in a subduction initiation, slab edge setting. *Gondwana Research* 18, 60-81.
- Peters, K.E. (1986). Guidelines for evaluating petroleum source rock using programmed pyrolysis, *AAPG bull.* 70, 318-329.
- Peters, K.E., Walters, C.C., Moldowan, J.M. (2005). *The biomarker guide: Volume 1, Biomarkers and isotopes in the environment and human history.* Cambridge University Press, New York, ISBN: 0521781582.

Bibliography

- Peters, K.E., Walters, C.C., Moldowan, J.M. (2007). The biomarker guide: Volume 2, Biomarkers and isotopes in petroleum systems and earth history. Cambridge University Press, New York, ISBN:9780521039987.
- Pillot, D., Deville, E., Prinzhofer, A. (2014). Identification and quantification of carbonate species using Rock-Eval pyrolysis. *Oil and Gas Science Technology – Rev. IFP69*, 341-349.
- Premoli-Silva, I., Spezzaferri, S., D'angelantonio, A. (1998). Cretaceous foraminiferal bio-isotope stratigraphy of Hole 967E and Paleogene planktonic foraminiferal biostratigraphy of Hole 966F, eastern Mediterranean, in: *Proceedings of the Ocean Drilling Program. Scientific results (Vol. 160)*, Ocean Drilling Program, pp. 377-394.
- Racka, M., Marynowski, L., Filipiak, P., Sobstel, M., Piszczowska, A., Bond, D.P. (2010). Anoxic Annulata events in the Late Famennian of the Holy Cross Mountains (Southern Poland): geochemical and palaeontological record. *Palaeogeography, Palaeoclimatology, Palaeoecology* 297, 549-575.
- Rasoul, M. A., Khaled, A. (2019). Integrated Study on Oligocene Sediments and Petroleum Systems of the Offshore Eastern Nile Delta, Egypt. In 81st EAGE Conference and Exhibition 2019.
- Ratner, M. (2016). Natural Gas Discoveries in the Eastern Mediterranean, Congressional Research Service, Washington, D.C., pp. 1-15.
- Regelous, M., Haase, K. M., Freund, S., Keith, M., Weinzierl, C. G., Beier, C., Brandl, P.A., Endres, T., Schmidt, H. (2014). Formation of the Troodos Ophiolite at a triple junction: Evidence from trace elements in volcanic glass. *Chemical Geology* 386, 66-79.
- Reiche, S., Hübscher, C., Ehrhardt, A. (2016). The impact of salt on the late Messinian to recent tectonostratigraphic evolution of the Cyprus subduction zone. *Basin Research* 28, 569-597.
- Rice, D.D, Claypool G.E. (1981). Generation, accumulation, and resource potential of biogenic gas, *AAPG Bull.*65, 5-25.
- Ricken, W. (1993). Sedimentation as a three-component system. Organic carbon, carbonate, noncarbonated. in: Fairchild, I. (Ed.) *Lecture Notes in Earth Sciences, Volume 51*, Springer, Berlin, pp. 358, ISBN: 3540573860.
- Roberts, G., Peace D. (2007). Hydrocarbon plays and prospectivity of the Levantine Basin, offshore Lebanon and Syria from modern seismic data, *GeoArabia* 12, 99-124.
- Robertson, A.H.F., Woodcock, N.H. (1979). Mamonia Complex, southwest Cyprus: Evolution and emplacement of a Mesozoic continental margin. *Geological Society of America Bulletin* 90, 651-665.
- Robertson, A., Xenophontos, C. (1993). Development of concepts concerning the Troodos ophiolite and adjacent units in Cyprus. *Geological Society, London, Special Publications* 76, 85-119.

-
- Robertson, A.H.F. (1998a). Mesozoic-Tertiary Tectonic Evolution of the Easternmost Mediterranean Area: Integration of Marine and Land Evidence, in: Proceedings of the Ocean Drilling Program. Scientific Results (Vol. 160), Ocean Drilling Program, pp. 723-782.
- Robertson, A.H.F. (1998b). Miocene shallow-water carbonates on the Eratosthenes Seamount, easternmost Mediterranean Sea, in: Proceedings of the Ocean Drilling Program. Scientific Results (Vol. 160), Ocean Drilling Program, pp. 419-436.
- Robertson, A.H.F. (1998c). Lithofacies evidence for the Cretaceous-Paleogene sedimentary history of Eratosthenes Seamount, Eastern Mediterranean, in its regional tectonic context (sites 966 and 967), in: Proceedings of the Ocean Drilling Program. Scientific Results (Vol. 160), Ocean Drilling Program, pp. 403-418.
- Robertson, A.H.F., Parlak O., Ustaömer T. (2012). Overview of the Palaeozoic-Neogene evolution of Neotethys in the Eastern Mediterranean region (southern Turkey, Cyprus, Syria), *Petroleum Geosciences* 18, 381-404.
- Robertson, A.H.F., (1998). Mesozoic-Tertiary tectonic evolution of the easternmost Mediterranean area: integration of marine and land evidence. Proceedings of the Ocean Drilling Program, Scientific Results, Vol. 160; Chapter 54, 723-782.
- Robertson, A.H.F., Parlak, O., Ustaömer, T. (2012). Overview of the Palaeozoic–Neogene evolution of neotethys in the Eastern Mediterranean region (Southern Turkey, Cyprus, Syria). *Petroleum Geoscience* 18, 381-404.
- Rohling, E.J., Marino, G., Grant, K.M. (2015). Mediterranean climate and oceanography, and the periodic development of anoxic events (sapropels). *Earth-Science Reviews* 143, 62-97.
- Sachse, V.F., Littke R., Jabour H., Schümann T., Kluth, O. (2012). Late Cretaceous (late Turonian, Coniacian and Santonian) petroleum source rocks as part of an OAE, Tarfaya Basin, Morocco, *Marine and Petroleum Geology* 29, 35-49.
- Scalan, E.S., Smith J.E. (1970). An improved measure of the odd-even predominance in the normal alkanes of sediment extracts and petroleum, *Geochimica et Cosmochimica Acta* 34, 611-620.
- Schauder, R., Kröger, A. (1993). Bacterial sulphur respiration, *Archives of Microbiology* 159, 491-497.
- Schenk, C.J., Kirschbaum, M.A., Charpentier, R.R., Klett, T.R., Brownfield, M.E., Pitman, J.K., Tennyson, M.E. (2010). Assessment of undiscovered oil and gas resources of the Levant Basin Province, Eastern Mediterranean, US Geol. Surv. Fact Sheet 3014, 1-4.
- Schieber, J., Southard, J., Thaisen, K. (2007). Accretion of Mudstone Beds from Migrating Floccule Ripples. *Science* 318, 1760–1763.
- Schneider, F., Dubille, M., Montadert, L. (2016). Modeling of microbial gas generation: application to the eastern Mediterranean “Biogenic Play”. *Geologica Acta* 14, 403-417.

Bibliography

- Segev, A., Rybakov, M. (2010). Effects of Cretaceous plume and convergence, and Early Tertiary tectonomagmatic quiescence on the central and southern Levant continental margin, *Journal of Geological Society* 167, 731-749.
- Sestini, G. (1989). Nile Delta: a review of depositional environments and geological history, *Geological Society London. S.P.41*, 99-127.
- Silva, I.P., Spezzaferri, S., d'Angelantonio, A. (1998). Cretaceous foraminiferal bio-isotope stratigraphy of Hole 967E and Paleogene planktonic foraminiferal biostratigraphy of Hole 966F, eastern Mediterranean. In *Proceedings of the Ocean Drilling Program. Scientific results (Vol. 160, pp. 377-394)*. Ocean Drilling Program.
- Shaaban, F., Lutz, R., Littke, R., Bueker, C., Odisho, K. (2006). Source-rock evaluation and basin modeling in NE Egypt (NE Nile Delta and northern Sinai), *Journal of Petroleum Geology* 29, 103-124.
- Smil, V. (2017). *Energy: a beginner's guide*. Oneworld Publications.
- Staerker S.T. (1998). Data Report: Biostratigraphy of Eocene and Upper Cretaceous chalks from the Eratosthenes Seamount region in the Eastern Mediterranean, in: *Proceedings of the Ocean Drilling Program. Scientific Results (Vol. 160)*, Ocean Drilling Program, pp. 395-402.
- Stock, A.T., Littke, R., Schwarzbauer, J., Horsfield, B., Hartkopf-Fröder, C. (2017). Organic geochemistry and petrology of Posidonia Shale (Lower Toarcian, Western Europe) - The evolution from immature oil-prone to overmature dry gas-producing kerogen. *International Journal of Coal Geology*, 176-177, 36-48.
- Stolper, D.A., Lawson, M., Davis, C.L., Ferreira, A.A., Neto, E.S., Ellis, G.S., Lewan, M.D., Martini, A.M., Tang, Y., Schoell, M., Sessions, A.L., Eiler, J.M. (2014). Formation temperatures of thermogenic and biogenic methane, *Science* 344, , 1500-1503.
- Suess, E., Thiede, J. (1983, eds). *Coastal Upwelling Its Sediment Record: Part A: Responses of the Sedimentary Regime to Present Coastal Upwelling*, Plenum Press, New York.
- Swarbrick, R.E., Robertson, A.H.F. (1980). Revised stratigraphy of the Mesozoic rocks of southern Cyprus. *Geological Magazine* 117, 547-563.
- Symeou, V., Homberg, C., Nader, F.H., Darnault, R., Lecomte, J.C., Papadimitriou, N. (2018). Longitudinal and Temporal Evolution of the Tectonic Style Along the Cyprus Arc System, Assessed Through 2-D Reflection Seismic Interpretation, *Tectonics* 37, 30-47.
- Tassy, A., Crouzy, E., Gorini, C., Rubino, J.L., Bouroullec, J.L., Sapin, F. (2015). Egyptian Tethyan margin in the Mesozoic: Evolution of a mixed carbonate-siliciclastic shelf edge (from Western Desert to Sinai). *Marine and Petroleum Geology* 68, 565-581.

-
- Taylor, G.H., Teichmüller, M., Davis, A., Diessel, C.F.K., Littke, R., Robert, P. (1998). *Organic Petrology*. Gebrüder Bornträger, Berlin, Stuttgart, pp. 704, ISBN: 3443010369.
- Tissot, B.P., Welte, D.H. (1984). *Petroleum Formation and occurrence*. Springer, Berlin.
- Tucker, G.E., Slingerland, R.L. (1994). Erosional dynamics, flexural isostasy, and long-lived escarpments: A numerical modeling study. *Journal of Geophysical Research: Solid Earth*, 99(B6), 12229-12243.
- Tyson, R.V. (1995). Palynological kerogen classification, in: *Sedimentary Organic Matter*, Springer, Dordrecht, pp. 341-365.
- Tyson, R.V. (1995). *Sedimentary Organic Matter: Organic facies and palynofacies*. Chapman and Hall, London, 615 p.
- Van der Zwaan, G.J., Jorissen, F.J. (1991). Biofacial patterns in river-induced shelf anoxia. *Geological Society, London, Special Publications* 58, 65-82.
- Vandré, C., Cramer, B., Gerling, P., Winseman, J. (2007). Natural gas formation in the western Nile delta (Eastern Mediterranean): Thermogenic versus microbial, *Organic Geochemistry* 38, 523-539.
- Wigger, S., Bailey, J., Larsen, M., Wallace, M. (1997). Ha'py field: a Pliocene bright spot example from the Nile delta, Egypt. *The Leading Edge* 16, 1827-1829.
- Wilkin, R.T., Barnes, H.L. (1996). Pyrite formation by reactions of iron monosulfides with dissolved inorganic and organic sulfur species. *Geochimica et Cosmochimica Acta* 60, 4167-4179.
- Wilkin, R.T., Arthur, M.A., Dean, W.E. (1997). History of water-column anoxia in the Black Sea indicated by pyrite framboid size distributions. *Earth and Planetary Science Letters* 148, 517-525.
- Wolfram, C., Shelef, O., Gertler, P. (2012). How will energy demand develop in the developing world?. *Journal of Economic Perspectives* 26, 119-38.
- Wygrala, B. (1989). Integrated study of an oil field in the southern Po basin, northern Italy (No. FZJ-2014-03033). Publikationen vor 2000.
- Zieger, L., Littke, R., Schwarzbauer, J. (2018). Chemical and structural changes in vitrinites and megaspores from Carboniferous coals during maturation. *International Journal of Coal Geology* 185, 91-102.

List of figures

1.1	Evolution of the world population between 1820 and 2016 with respect to the single evolution on each continent (figure from OurWorldinData.org; data from Klein Goldewi, 2016)	1
1.2	Evolution of the global primary energy consumption between 1800 and 2016, separated by different energy sources. (Figure from ourworldindata.org; data from Vaclav Smil, 2017).....	1
1.3	Prediction of the primary energy demand till 2040. While the usage of coal will decrease Renewables but also gas as source of energy will increase. (theenergycollective.com, 2018).....	2
1.4	Location of gas fields in the Eastern Mediterranean Sea (modified after: Crystolenergy.com).....	4
2.1	Plate tectonical setting of the Eastern Mediterranean region (from Dilek and Sandvol, 2009).....	7
2.2	Main geological features of the Eastern Mediterranean Sea (modified after Montadert et al., 2014).....	8
2.3	Simplified geological map of Cyprus showing the main important features. White dots represent sample locations.....	9
2.4	Stratigraphy of Cyprus including the Troodos Ophiolite and its autochthonous Circum Sedimentary Succession. The formation colors refer to the colors of the official geological map of Cyprus.....	10
2.5	A schematic overview of the expected lithostratigraphy of the ESM, the Herodotus and the Levant basin, as well as the well-constrained columns of the northern and southern shelf of the Levant Basin (modified after Bou Daher 2016).....	11
2.6	Stratigraphy of Cyprus including the Troodos Ophiolite and its autochthonous Circum Sedimentary Succession. The formation colors refer to the colors of the official geological map of Cyprus.....	12
2.7	A schematic overview of the expected lithostratigraphy of the Eratosthenes Seamount, the Herodotus and the Levant Basin, as well as the well-constrained columns of the northern and southern shelf of the Levant Basin (modified after Bou Dahert et al., 2016).....	16
3.1	Carbonate classification after Dunham (1962).....	19
3.2	Location 7, Lefkara Formation.....	21
3.3	Location 9, Lefkara Formation.....	21
3.4	Location M, Lefkara Formation.....	22
3.5	Location 5, Pakhna Formation.....	23
3.6	Location 16, Pakhna Formatio.....	23
3.7	Location 10, Pakhna Formation.....	24
3.8	Location 21, Pakhna Formation.....	24
3.9	Location 4, Nicosia Formation.....	25
3.10	Location 26, Vlambouros Formation.....	25
3.11	Location 24, Vlambouros Formation.....	26

3.12	Representative example of large internal folding observed in the Episkopi Formation. The folding is interpreted as syn-depositional slump structures.....	26
3.13	Taken logs of the Vlambouros and the Pakhna Formation showing sample locations. (figure continues on next page.....)	27
3.14	Location 12, Pakhna Formation.....	29
3.15	Location 2, Pakhna Formation.....	30
3.16	Location 18A (A) and 18B (B), Pakhna Formation.....	31
3.17	Location 18A, Pakhna Formation.....	32
3.18	Location 10, Pakhna Formation.....	32
3.19	Location 1, Pakhna Formation.....	33
3.20	Location 33, Vlambouros Formation.....	34
3.21	Conglomeratic channel fills near Loc. 33 and 32.....	34
3.22	Location 32, Vlambouros Formation.....	35
3.23	Locations of the ODP Leg 160 wells along the Eratosthenes Seamount (ESM)....	36
3.24	Representative core photos of dark mudstone intervals in the Upper Cretaceous of well 967 E (A) and in the Eocene of well 966 (B).....	37
4.1	Overview of the study area. Onshore areas colored in grey, subsea bathymetry colored in shades according to scale. Marked gas fields (yellow) represent recent discoveries. The area is mainly controlled by the interplay of the African, Arabian, and Eurasian plates. The Eratosthenes Seamount (ESM) represents a large carbonate platform which is located on the underlying, larger Eratosthenes Continental Block (ECB). The southern Exclusive Economic Zone (EEZ) of Cyprus represents the available blocks for hydrocarbon exploration. The samples of this study were collected from the cores that were drilled along the northern lobe of the ESM during the ODO Leg 160 campaign. Modified after Hawie et al. (2013) and Symeou et al. (2018).....	41
4.2	Schematic overview of the sedimentary successions to be found in the Levant Basin (LB), the Eratosthenes Seamount (ESM) and at the Levant margin (LM) along Lebanon. Modified after Bou Daher et al. (2016).....	43
4.3	Elemental analysis and Rock-Eval results of ODP Leg 160 core samples that originate from the Eratosthenes Seamount (ESM), southern offshore area of Cyprus. Note that scales vary in the different intervals. Big crosses mark intervals where no results were obtained. (figure continues on next page.....)	52
4.4	Photomicrographs: indicate bedding orientation. ● no bedding observable. A: Incident light (left) and ultraviolet light (right). Vitrinite particle with a highly structured surface surrounded by a fine grained matrix and amorphous liptinite. Red arrow marks a lam alginite. B: Incident light (left) and ultraviolet light (right). Vitrinite particle with structured surface (circle) surrounded by fine grained matrix, dolomite rhombs (Dolo), amorphous liptinite and different alginites (red arrows). C: Incident light. The typical occurrence of small framboidal and euhedral pyrite (Py). A large solid bitumen accumulation within a calcareous, organic-poor matrix. Large framboidal pyrite (Py) is observed around its border.....	55
4.5	Representative gas chromatographs for the aliphatic hydrocarbon fraction (A) Sample 15/906 shows a clear predominance of medium-chain n-alkanes (n-C12–n-C20) with almost no longer chain molecules. (B) Sample 15/899 illustrates a predominance of medium-chain n-alkanes over abundant long-chain n-alkanes (n-C21–n-C35). (C) Partial m/z 191 mass fragmentograms showing hopane	

	distributions for sample 15/890. (D) Partial m/z 217 mass fragmentograms showing sterane distributions for sample 15/872. Peak identifications are provided on Table 4.2.....	57
4.6	C27 to C29 $\beta\alpha\alpha$ sterane distribution indicating an open marine environment as source for the OM. Eocene samples (Bartonian to Priabonian and Ypresian to Lutetian) show a slightly higher concentration of C29 $\beta\alpha\alpha$ sterane concentrations. Paleoenvironmental and source interpretation after Hatem et al. (2016) (modified after Huang and Meinschein, 1979).....	59
4.7	(A) The samples in the pseudo van Krevelen diagram scatter from Type II to Type III. (B) In the TOC vs. S2 diagram, most samples plot within the Type II area. (C) All samples in the TOC-TS diagram show a positive correlation but plot below the normal marine line derived from Berner (1984) indicating a lack of iron to precipitate pyrite.....	59
4.8	Comparison of bulk and HCl-treated samples in the pseudo van Krevelen diagram. OI values are decreased while HI values are increased. The effect is more prominent for low TOC samples (see Table 4.4).....	60
4.9	Typical plot of Pr/n-C17 vs. Ph/n-C18 ratios for offshore Cyprus samples indicating marine organic matter deposited under mainly dysoxic conditions (modified from Hunt, 1995).....	61
4.10	Source rock potential and thermal maturity evaluation based on the TOC vs. S2 classification.....	63
5.1	(A) Overview of the Eastern Mediterranean Sea showing the recent tectonic setting. The study area is located at the triple-junction point between the African, the Arabian and the Eurasian plates. White arrows indicate movement orientation of the African and Arabian plates relative to Eurasia (fault location according to Symeou et al., 2018), recent gas field discoveries are delimited in green, ESM=Eratothenes Seamount, (B) Overview of the study area showing a simplified geological map of Cyprus (modified after the official geological map, Cyprus Geological Survey, 1995) and the surrounding basins and the ESM. Yellow dots show the Ocean Drilling Program (ODP) Leg 160 wells (see Grohmann et al. (2018) for respective offshore samples). White (TOC < 0.3 wt%) and black dots (TOC > 0.3 wt.%) show onshore sample locations. (For all locations and GPS coordinates, see Table 5.1.) Bathymetric and topographic maps taken from the National Oceanic and Atmospheric Administration (2018) Bathymetric Data Viewer. Fm=Formation.....	69
5.2	Simplified lithostratigraphy of southern Cyprus as it can be observed within the different sub-basins (modified after Kinnaird et al., 2011) and the main tectonic events. Proposed estimated thicknesses are speculative and must be treated with caution as they can vary throughout each basin. Note that the Mamonia Complex (C.) does not apply to the time scale, as it represents an allochthonous melange that was overthrust onto the Troodos Ophiolite (its rocks span ages from Triassic to Late Cretaceous). Green stars mark sampled intervals.....	71
5.3	Sedimentological and geochemical logs of the Mid Triassic Vlambouras Formation (Fm). at location 31 and 32 (For locations see Fig. 1 and Table 1). Colors of the lithological column indicates observed rock color. Horizontal lines indicate recognizable normal lamination, while inclined lines indicate cross bedding. Although the clay-rich sections partly show elevated total organic carbon (TOC) contents, the source rock quality is poor due to low hydrogen index (HI) values < 50 mg HC/g TOC on average. Total sulfur (TS)/TOC ratios indicate oxic conditions during deposition (Berner, 1984). TS/Fe ratios indicate that most sulfur	

is bound to pyrite. White line and arrow indicates small normal fault observed in the outcrop.....	76
5.4 Sedimentological and geochemical logs of the Late Miocene Upper Pakhna Formation at location 1 and 10 (for locations see Fig. 1 and Table 1). Colors of the lithological column indicates observed rock color. Total organic (TOC) and inorganic carbon (TIC) contents and hydrogen index (HI) values indicate good source rock quality. Total sulfur (TS)/Fe ratios show that all sulfur is bound to pyrite. TS/TOC ratios are mainly lower than those observed under normal marine conditions, suggesting a deposition under anoxic conditions (Berner, 1984).....	77
5.5 Rock-Eval® results for all >0.3 wt% total organic carbon (TOC) samples. (A) Pseudo-van Krevelen diagram (Hydrogen Index (HI) vs. Oxygen Index (OI)) after Espitalie et al. (1986) showing high OI values. (B) Rock-Eval® HI vs. T _{max} plot to avoid misinterpretation in kerogen typing related to probably inaccurate OI values. In both plots, the majority of the Pakhna samples is interpreted as Type II kerogen while the Vlambouros samples are Type III. However, some Pakhna samples (mainly from Location (Loc.) 2, 11, 20, and 21) also plot as Type III kerogen, although their depositional setting is supposed to be marine.....	83
5.6 Fig. 5.6 Reflected light (A, C, E, G, H, I, J) and fluorescence (B, D, F) microphotographs. (A and B) Representative sample for the organic-rich sections of the Pakhna Formation (Fm.) from location (Loc.) 10. The sample is composed of a fine-grained siliciclastic matrix with patchy carbonate (carb). Pyrite (py) is mainly present as framboids. Organic matter (OM) is mainly present as fine, disseminated liptinites (Lipt) as indicated by the yellowish background fluorescence (B). Only small amounts of terrestrial particles such as vitrinites (Vit) can be observed. The OM as well as the pyrite framboids seem to be more abundant in the more siliciclastic parts, while foraminifera (foram) can rather be observed in the more calcareous parts. (C and D) Representative sample for the organic-rich sections of the Pakhna Fm. from Loc. 1. Additionally to liptodetrinite, alginites can be observed parallel to the bedding planes. Many pyrite framboids show diameters >5 µm. OM seems to be related to the more clastic parts. (E and F) Representative sample of the less organic-rich samples of the Pakhna Fm. from the southwestern outcrops (Loc. 11, 12, 20, 21). The samples are characterized by more calcareous deposits and a reduced abundance of amorphous liptinites. Alginites can still be observed but are here also present in the calcareous parts (F). (G and H) Sample 228 is the only sample from the Pakhna Fm. where intense pyrite weathering could be observed. The pyrite is partly present as pore filling within foraminifera. I & J) Large vitrinite (Vit) and inertinites (Inert) particles with recognizable cell structures in the Vlambouros Fm. at Loc. 32 and 24, respectively.....	85
5.7 (A and B) Comparison of Rock-Eval® pyrograms for the bulk rock (BR) and the respective total organic matter (TOM) concentrates of two Pakhna samples. For comparison, the curves are normalized to the sample weight and the respective total organic carbon (TOC) content. (A) It can be seen that a large proportion of the thermovaporized and pyrolyzable hydrocarbon (HC) is retained by the mineral matrix. (B) The effect is even more prominent if the bulk TOC is lower. (C) The absolute difference between bulk and TOM HI and OI in the Pakhna samples seems to decrease with increasing bulk TOC content. (D) The Pakhna TOM concentrates plot closer to the kerogen Type II pathway than the respective bulk rock samples in the pseudo van Krevelen diagram and correlate better with the elemental results (E). Loc.=Location.....	87
5.8 Several thermal maturity parameters. (A) Random vitrinite reflectance (VRr) and Rock-Eval® T _{max} values indicate an immature state of organic matter with only the Vlambouros samples reaching up to early maturity. (B) The configuration of	

- 20S/(20S+20R) and $\alpha\beta\beta/(\alpha\alpha\alpha+\alpha\beta\beta)$ regular steranes indicates an immature to early mature state for all samples..... 88
- 5.9** Distribution of organic molecular compounds in the aliphatic fraction of representative samples of the Pakhna Formation (Fm.) from location (Loc.) 1 and 10 in the northeast (sample 20), and from the southwest (sample 233), and of the Vlambouros Fm. (sample 250). (A) Representative full chromatograms (GC-FID) showing distribution of n-alkanes and pristane (Pr) and phytane (Ph). (B) Mass chromatograms m/z 191 of the aliphatic fraction showing distribution of hopanes. (C) Mass chromatograms m/z 217 showing distribution of steranes..... 89
- 5.10** Transmitted light microphotographs of palynological components. The general palynofacies of the Pakhna samples is represented by A and B: The largest percentage (up to >90%) is made up by amorphous organic matter (AOM) of dark brownish color which forms large, clumpy aggregates. Minor components include different types of pollen (A and C), highly oxidized palynomacerals (PM4) and algae. The Vlambouros samples are almost exclusively characterized by oxidized PM (D). For the statistical overview of the different compounds see Fig. 5.11..... 90
- 5.11** Results of the palynological observations. Values expressed in wt% indicates the total organic carbon (TOC) content of the respective sample. The Pakhna samples are mainly (up to >90%) composed of amorphous organic matter (AOM). Terrestrial particles like palynomacerals (PM) are highly oxidized (mainly PM4 and PM1). Other terrestrial and marine constituents like spores, pollen, algae, and foraminifera are relatively constant to each other. Samples containing low TOC show also a decrease in the percentage of AOM. In the Vlambouros samples the OM is almost exclusively (> 90%) composed of highly oxidized PM..... 91
- 5.12** Results of the pyrite framboid size distribution in Pakhna samples originating from location 10. (A) Histograms showing the distribution of pyrite framboid diameters (bin size=1 μm). n=number of measured framboids, mean=mean framboid diameter, std.=standard deviation to mean value, skew=skewness of distribution. (B) and (C) plot of the mean framboid diameters vs. the standard deviation and skewness of the distribution, respectively, pointing towards euxinic/anoxic conditions (plots after Wilkin and Barnes, 1996)..... 93
- 5.13** Ternary diagram showing the original sediment composition calculated according to Littke (1993) under the assumption that all sulfur now present as pyrite/marcasite is derived from early diagenetic sulfate reduction and organic carbon oxidation. 2 mol carbon are lost in order to create one mole of (reduced) sulfur: $\text{TOC}^* = \text{TOC} \times 2S \times (\text{MC}/\text{MS})$ with TOC^* : TOC (total organic carbon) before bacterial sulfate reduction, S: sulfur content, MC and MS: Molar mass of carbon and sulfur, respectively. $\text{M}^* = \text{TOC}^* \times (\text{COM})$ with OM^* =original organic matter, COM: carbon percentage in the OM (here an average of 70% is assumed for marine organic matter; see Stock et al., 2017). In the Littke plot, the carbon (Carb) content is determined based on the elemental carbon analysis and the silicate (Sil) content is calculated as $\text{Sil} = 100 - \% \text{OM}^* - \% \text{Carb}$. The Pakhna samples (especially samples from the northeastern locations (Loc.) 1 and 10) show a tendency to increasing OM with increasing silicate and decreasing carbonate content, respectively, while the OM in the Vlambouros samples shows no correlation..... 94
- 5.14** Various elemental ratios to interpret paleo-redox conditions. (A) D) Total sulfur (TS) vs. total organic carbon (TOC) contents (Berner, 1984). (B) TS vs. vanadium-nickel fraction ($\text{V}/(\text{Ni}+\text{V})$). The three fields with the roman numbers correspond to the stability regimes of different species as proposed by Lewan (1984). (C) Ternary diagram showing the relative concentration of total organic

carbon (TOC), total sulfur (TS) and iron (Fe). Diagram after Dean and Arthur (1989) and Racka et al. (2010). For samples which have excess iron, it can be assumed that most sulfur is incorporated in pyrite. In total, the Pakhna samples are interpreted as dys- to anoxic conditions, while the samples of the Vlambouros Fm. are related to oxic, sulfate-depleted conditions.....	95
5.15 Various biomarker ratios to determine source of organic matter (OM) and paleo redox-conditions. (A) Pristane (Pr) over n-C17 vs. Phytane (Ph) over n-C18 indicating oxygen depleted conditions for the Pakhna samples. Samples from Location (Loc.) 1 and 10 seem to be slightly more oxygen depleted than samples from the other outcrops. The samples of the Vlambouros Formation (Fm.) indicate more oxic conditions. (B) Pr/n-C17 vs. Pr/Ph indicating a mainly marine/aquatic source of OM for Pakhna samples from Loc. 1 and 10, while the other Pakhna samples as well as the Vlambouros samples indicate also a contribution of terrestrial OM. (C)The ratio of C29 to C27 regular steranes, however, indicates for all samples a mainly marine algal source. (D) According to the ratio of tricyclic hopanes C24/C23 vs.C22/C21 the depositional setting is to interpret as somewhat between a marly-carbonaceous source and a more marine or freshwater dominated environment.Loc.=Location.....	96
5.16 Relative distribution of C27 to C29 regular steranes showing a mainly marine source of organic matter (OM) for the Pakhna samples and partly increased terrestrial influence in the Vlambouros samples. Paleoenvironmentaland source interpretation after Huang and Meinschein, 1979). Loc.=Location.....	97
6.1 A) Overview of the Eastern Mediterranean. Black rectangle showing the model area. Yellow and green dashed polygons show the zones where isopach maps provided by Hawie et al. (2013b) and Gardosh and Druckman(2006) were used to construct the eastern part of the static model. Red dashed polygon shows the area with new isopach maps of the Eratosthenes Seamount, provided by Papadimitriou et al. (2018). Profiles A-A' and B-B' of the respective petroleum system model are shown in Figure 9D and E. The burial history of locations E1 and E2 (pink dots) are illustrated in Figure 13. B) Depth horizons providing the base structure for the static model.	103
6.2 Geological and tectonic evolution of the greater realm of the Eastern Mediterranean since the Middle Jurassic. (modified after Hawie et al., 2017 and Symeou et al., 2018).....	105
6.3 Used paleo-bathymetry maps for the Upper Cretaceous to Eocene (A), Oligocene (B), Lower Miocene (C), and Upper Miocene (D) intervals. The color scale indicates water depth (negative values above sea level) The arrows in B-D represent sediment input sources defined in the Oligocene and Miocene intervals: 1 to 3: Sediment originating from the Arabian Plate in the east, 4 to 7: sediments originating from the Nile, 8: sediment input from the western Anatolian Plate, 9: sediment input from the Latakia region.	107
6.4 Assigned carbonate production law as a function of water depth for carbonate mud and carbonate grains in the present model.....	108
6.5 Global relationship between (A) drainage area and water discharge and (B) drainage area and sediment load. Estimated conditions for the Latakia (L), Arabian Plate (A) and Nile (N) area are indicated for the Miocene. (Figure from Barabsch et al., 2018, modified after Hawie et al., 2015. Datasets based on Dai and Trenberth, 2002 and Milliman and Syvitski, 1992).....	109
6.6 A) Upwelling induced primary bioproductivity (PP) as a function of underlying bathymetry. B) Example of the applied function from A above the basin-margin transition. Red line showing the highest PP at the shelf break.	110

6.7	Stratigraphic forward modeling results of the Upper Cretaceous (89 to 65 Ma). A) Facies distribution, B) sedimentation rate (black cells indicate erosion), C) simulated primary productivity caused by upwelling, D) oxygen concentration at the sediment water interface (0 = anoxic, 1 = oxic), E) simulated initial total organic carbon (TOC) content, F) simulated initial bulk hydrogen index (HI). LevantMargin on the right (eastern) side, ESM in the center-left.....	116
6.8	Stratigraphic forward modeling results of the Oligocene (34 to 24 Ma). A) Facies distribution, B) sedimentation rate, C) primary marine productivity, D) oxygen concentration at sediment water interface (0 = anoxic, 1 = oxic), E to G) simulated initial marine, terrestrial, and total TOC, respectively, H) simulated initial hydrogen index (HI). Levant Margin on the right (eastern) side, ESM in the center-left.....	117
6.9	Comparison of simulated with measured TOC contents at (A) the Chekka region in Lebanon (modified after Bou Daher et al.,2014) and at ODP Leg 160 well 967 (Geochemical data from Grohmann et al., 2018).....	118
6.10	A) Long-(green) and short-term (blue) sea level curves after Haq et al.(1987) and the composite curve (red), which is used for the present model. High stand (HS) and low stand (LS) periods are indicated, which are used to define the relative clastic sediment composition during the oligo-Miocene period. LS periods bring more coarse grained material into the basin (B), while HS periods are defined by more fine grained deposits (C). Fig. D and E show the resulting intercalation of fine and coarse grained intervals in the basin at present day burial. For location of the profiles, see Figure 1.	119
6.11	Distribution of simulated total organic carbon (TOC) contents during the different intervals. The location of the cross section corresponds to the profile A-A' (Fig. 1A).	120
6.12	Absolute and relative thickness errors maps for the Upper Cretaceous to Eocene (A and B), the Oligocene (C and D), the Lower Miocene (E and F) and the Upper Miocene (G and H) intervals. For the relative thickness error "0" means 0% of the actual thickness (from isopach maps) was reproduced by the numerical simulation. This means that the model resulted in no sediment deposition at this location. "1" means perfect match of simulated and actual thickness values. "2" means simulated thickness value is two times larger than the actual thickness value at this location. The figure caption was changed for clarification.....	121
6.13	A) Simulated present day temperature. For calibration, wells and pseudo wells provided by Bou Daher et al. (2016) plus ODP Leg 160 well 967E (Emeis et al., 1996) are used. Note that the grey temperature dots (B) represent most likely inaccurate temperature measurements (see Emeis et al., 1996). B) Temperature calibration, C) vitrinite reflectance calibration. Depth given in meters below sea level. In (B) and (C) depth values represent meters of burial, relative to the sediment surface.	125
6.14	Burial plot showing simulated temperature and Easy R_o evolution through time extracted from location E1 (A and B) and for location E2 (C and D). See Figure 1 for locations E1 and E2.....	126
6.15	Extracted maps from the petroleum system model showing the initial distribution of the total organic carbon (TOC) content at the lower (A) and upper boundary (B) of the Upper Cretaceous source rock interval. C and D showing the simulated present day temperature at the lower and upper boundary. E and F showing the simulated present day vitrinite reflection at the lower and upper boundary. Shaded areas in C to F indicate source rocks with TOC contents > 0.3%. G and H showing the evolution of the kerogen transformation ratio for different locations (see	

	location numbers. Location 1 and 6 correspond to the extracted burial plots E2 and E1 (Fig. 1 and 13) at the lower and upper boundary, respectively. The cumulative thickness of the source rock at the respective six locations is as follows: 1 = 1000 m, 2 = 300 m, 3 = 260 m, 4 = 470 m, 5 = 600 m, 6 = 400 m.	127
6.16	Extracted maps from the petroleum system model showing the initial distribution of the total organic carbon (TOC) content in the Eocene source rocks. B showing the simulated present day temperature. C showing the simulated present day vitrinite reflectance. Shaded areas in B and C indicate source rocks with TOC contents >0.3%. D showing the evolution of the kerogen transformation ratio for different locations (see location numbers, Location corresponds roughly to the burial plot of E1 (Fig. 1 and 13). The cumulative thickness of the source rock at the respective six locations is as follows: 1 = 60 m, 2 = 130 m, 3 = 100 m, 4 = 100 m.	129
6.17	Extracted maps from the petroleum system model showing the initial distribution of the total organic carbon (TOC) content at the lower (A) and upper boundary (B) of the Oligocene source rock interval. C and D showing the simulated present day temperature at the lower and upper boundary. E and F showing the simulated present day vitrinite reflection at the lower and upper boundary. Shaded areas in C to F indicate source rocks with TOC contents > 0.3%. G and H showing the evolution of the kerogen transformation ratio for different locations (see location numbers, location 1 corresponds roughly to the burial plot E2 (Fig. 1 and 13)) at the lower and upper boundary, respectively. The cumulative thickness of the source rock at the respective six locations is as follows: 1 = 1300 m, 2 = 1100 m, 3 = 1100 m, 4 = 100 m.	130
6.18	Extracted maps from the petroleum system model showing the initial distribution of the total organic carbon (TOC) content at the lower (A) and upper boundary (B) of the Miocene source rock interval. C and D showing the simulated present day temperature at the lower and upper boundary. E and F showing the simulated present day vitrinite reflection at the lower and upper boundary. Shaded areas in C to F indicate source rocks with TOC contents > 0.3%. G and H showing the evolution of the kerogen transformation ratio for different locations (see location numbers) at the lower and upper boundary, respectively. The cumulative thickness of the source rock at the respective six locations is as follows: 1 = 3000 m, 2 = 2000 m.	131
7.1	Comparison of several Triassic to Miocene source rocks in the greater area of the Levant Basin. A) Pseudo van Krevelen diagram for kerogen interpretation based on oxygen index (OI) vs. hydrogen index (HI), B) source rock quality based on total organic carbon (TOC) content and hydrocarbon generation potential (S ₂), C) TOC vs. total sulfur (TS) content for aquatic environment interpretation, D) Phytane (Ph) over n-C ₁₈ vs. Pristane (Pr) over n-C ₁₇ ratio for interpretation of paleo redox conditions.	136
7.2	Comparison of Rock-Eval results of bulk rock samples v.s total organic matter (TOM) concentrates obtained from samples of the Miocene pakhna Fm. (onshore Cyprus) from this study with samples of the Posidonia Shale (Stock et al., 2017).	139

List of tables

4.1	Samples obtained from the OPD Leg 160 campaign along the Eratosthenes Seamount (offshore Cyprus) and the respective core interval, ordered by age. (Table continues on next page.....)	41
4.2	Identified hopane and sterane peaks used in this work.....	45
4.3	Results of the elemental analysis and Rock-Eval pyrolysis. TOC = Total Organic Carbon, TIC = Total Inorganic Carbon, TS = Total Sulfur, T _{max} = temperature at the peak of S2, HI = Hydrogen Index (S2/TOC x 100), OI = Oxygen Index (S3/TOC x 100), [---]: not determined. (Table continue on next page.....)	48
4.4	Comparison of bulk rock and HCl-treated samples. TOC = Total Organic Carbon, TIC = Total Inorganic Carbon, HI = Hydrogen Index (S2/TOC x 100), OI = Oxygen Index (S3/TOC x 100).....	49
4.5	Results from microscopic analysis: Qualitative amounts of analyzed feature (OM = total observable organic matter; V = vitrinite; I = inertinite L = liptinite; Foram = foraminifera; Py = pyrite; Dolo = dolomite) decreases from +++ to +; - indicates that the feature occurs only rarely or not at all.....	50
4.6	Results of vitrinite reflectance measurements (VRr), the respective measured points (n) and their standard deviation (Std dev), as well as the calculated maximum burial temperature (T _{peak}).....	52
4.7	Molecular geochemical ratios from GC-FID analysis. Pr = pristane, Ph = phytane, TAR = terrigenous/aquatic ratio, OEP = Odd Even Predominance, CPI = Carbon preference Index.....	53
4.8	Various biomarker ratios from GC-MS analysis. [---]: not determined.....	53
5.1	List of investigated locations and the respective formation, taken samples and GPS coordinates. Locations where organic matter could be proven are marked by *. Locations are shown on the geological map (Fig. 5.1) and in the lithostratigraphic column (Fig. 5.2).....	69
5.2	Total organic (TOC) and inorganic carbon (TIC) and Rock-Eval® results for bulk rock samples > 0.3 wt.% TOC. For locations (Loc.) see Fig. 1 and 2. Fm. = Formation, P = Pakhna; V = Vlambouros, [---] = T _{max} was not determined due to bad resolution of the S2 peak. HI = hydrogen index, OI = oxygen index, T _{max} = temperature at S2 peak.....	76
5.3	Comparison of Rock-Eval® results obtained from bulk rock samples and the respective total organic matter concentrates. TOC = total organic carbon, HI = hydrogen index, OI = oxygen index, T _{max} = temperature at S2 peak.....	78
5.4	Average random vitrinite reflectance (VRr) for each outcrop based on one or several samples (nsamples). Fm. = Formation (P = Pakhna, V = Vlambouros); Loc. = Location; ntotal = total amount of measured vitrinite particles per outcrop; Std dev = standard deviation.....	80
5.5	Various molecular ratios calculated from the saturated hydrocarbon fraction. Loc. = Location, Fm. = Formation (P = Pakhna, V = Vlambouros).....	82
5.6	Hopane and sterane ratios obtained from the saturated fraction. [---] = no results obtained. Loc. = Location, Fm. = Formation (P = Pakhna, V = Vlambouros).....	82
5.7	Elemental concentrations in the bulk rock samples. [---] = not measured. Loc. = Location, Fm. = Formation (P = Pakhna, V = Vlambouros), TS = total sulfur, Fe = iron, Ni = nickel, V = vanadium.....	87

6.1	Definition of the simulated sdiments in the stratigraphic forward.....	101
6.2	Exported facies from the initial stratigraphic forward model and their respective sedimentary composition. Threshold values for sediment composition given in %.....	107
6.3	Facies used in the petroleum system model and their petrophysical properties.....	107
6.4	Layers of the petroleum system model.....	108

Appendix

Table A: Sample obtained from the first field campaign.

Sample	IFP ID	Age	Formation	Location	Lat	Lon
1	173920	Tortonian	Up. Pachna	5	35 00 23.785 N	0333025.448 E
2	173921	Tortonian	Up. Pachna	5	35 00 23.914 N	03 30 25.531 E
3	173922	Tortonian	Up. Pachna	5	35 00 23.915 N	033 30 25.531 E
4	173923	Tortonian	Up. Pachna	5	35 00 23.915 N	033 30 25.531 E
5	173924	Tortonian	Up. Pachna	5	35 00 24.059 N	033 30 25.578 E
6	173967	Paleocene	low. Lefkara	8	35 02 02.353 N	033 35 58.672 E
7	173917	Paleocene	low. Lefkara	7	35 01 47.352 N	033 35 42.054 E
8	173918	Paleocene	low. Lefkara	7	35 01 47.352 N	033 35 42.054 E
9	173919	Paleocene	low. Lefkara	7	35 01 47.352 N	033 35 42.054 E
10	173925	Paleocene	low. Lefkara	6	35 00 50.447 N	033 33 24.354 E
11	173926	Late Miocene	Up. Pachna	10	34 57 29.538 N	033 34 43.133 E
12	173927	Late Miocene	Up. Pachna	10	34 57 29.538 N	033 34 43.133 E
13	173928	Late Miocene	Up. Pachna	10	34 57 29.538 N	033 34 43.133 E
14	173929	Late Miocene	Up. Pachna	10	34 57 29.538 N	033 34 43.133 E
15	173930	Late Miocene	Up. Pachna	10	34 57 29.538 N	033 34 43.133 E
16	173931	Late Miocene	Up. Pachna	10	34 57 29.538 N	033 34 43.133 E
17	173932	Late Miocene	Up. Pachna	10	34 57 29.538 N	033 34 43.133 E
18	173933	Late Miocene	Up. Pachna	10	34 57 29.538 N	033 34 43.133 E
19	173934	Late Miocene	Up. Pachna	10	34 57 29.538 N	033 34 43.133 E
20	173935	Late Miocene	Up. Pachna	10	34 57 29.538 N	033 34 43.133 E
21	173936	Late Miocene	Up. Pachna	10	34 57 29.538 N	033 34 43.133 E
22	173937	Paleocene	low. Lefkara	9	34 59 47.695 N	033 36 51.275 E
23	173938	Paleocene	low. Lefkara	9	34 59 47.234 N	033 36 51.761 E
24	173968	Miocene	Pachna - Up. Pachna	16	34 45 53.179 N	033 18 30.910 E
25	173969	Miocene	Pachna - Up. Pachna	16	34 45 53.179 N	033 18 30.910 E
26	173970	Miocene	Pachna - Up. Pachna	16	34 45 52.704 N	033 18 40.248 E
27	173971	Miocene	Pachna - Up. Pachna	16	34 45 52.704 N	033 18 40.248 E
28	173972	Miocene	Pachna - Up. Pachna	16	34 45 52.175 N	033 18 40.702 E
29	173973	Miocene	Pachna - Up. Pachna	16	34 45 54.832 N	033 18 20.441 E
30	173974	Miocene	Pachna - Up. Pachna	16	34 45 54.162 N	033 18 30.470 E
31	173975	Paleocene	low. Lefkara	22	34 51 22.388 N	032 52 16.770 E
32	173939	Miocene	(Up?) Pachna	21	34 48 55.580 N	032 49 27.016 E
33	173940	Miocene	(Up?) Pachna	21	34 48 55.580 N	032 49 27.016 E
34	173941	Miocene	(Up?) Pachna	21	34 48 55.580 N	032 49 27.016 E
35	173942	Pliocene	Nicosia	4	35 00 55.037 N	033 30 32.123 E
36	173943	Pliocene	Nicosia	4	35 00 54.529 N	033 30 32.569 E
37	173944	Pliocene	Nicosia	4	35 00 54.529 N	033 30 32.569 E
38	173945	Pliocene	Nicosia	4	35 00 52.412 N	033 30 36.958 E
39	173946	Pliocene	Nicosia	4	35 00 52.412 N	033 30 36.958 E
40	173947	Pliocene	Nicosia	4	35 00 52.412 N	033 30 36.958 E
41	173948	Pliocene	Nicosia	4	35 00 52.412 N	033 30 36.958 E
42	173949	Pliocene	Nicosia	4	35 00 52.412 N	033 30 36.958 E
43	173950	Pliocene	Nicosia	4	35 00 52.412 N	033 30 36.958 E
44	173951	Pliocene	Nicosia	4	35 00 52.412 N	033 30 36.958 E
45	173952	Mid. Jurassic	Episkopi	near 28	34 52 32.394 N	032 35 47.317 E
46	173953	Mid. Jurassic	Episkopi	near 28	34 52 32.761 N	032 35 55.788 E
47	173954	Mid. Jurassic	Episkopi	near 28	34 52 32.761 N	032 35 55.788 E
48	173955	Mid. Jurassic	Episkopi	near 28	34 52 32.761 N	032 35 55.788 E
49	173956	Mid. Jurassic	Episkopi	29	34 52 29.366 N	032 35 48.044 E
50	173976	Mid. Jurassic	Episkopi	27	34 52 08.854 N	032 36 25.952 E
51	173957	Mid. Jurassic	Episkopi	28	34 51 58.194 N	032 36 10.411 E
52	173958	Mid. Jurassic	Episkopi	28	34 51 58.194 N	032 36 10.411 E
53	173959	Mid. Jurassic	Episkopi	near 27	34 51 56.858 N	032 36 11.560 E
54	173960	Mid. Jurassic	Episkopi	near 27	34 51 56.858 N	032 36 11.560 E
55	173977	Mid. Jurassic	Episkopi	25	34 48 12.560 N	032 38 43.710 E
56	173961	Mid. Jurassic	Episkopi	24	34 47 39.671 N	032 39 22.075 E
57	173962	Mid. Jurassic	Episkopi	24	34 47 39.671 N	032 39 22.075 E
58	173963	Mid. Jurassic	Episkopi	24	34 47 39.671 N	032 39 22.075 E
59	173983	Rhaetian	Vlambouros	26	34 44 05.046 N	032 35 54.179 E
60	173978	Rhaetian	Vlambouros	26	34 44 05.046 N	032 35 54.179 E
61	173964	Late Miocene	lower Lefkara	M	35 01 18.347 N	033 19 28.866 E
62	173979	Late Miocene	lower Lefkara	M	35 01 06.085 N	033 20 33.677 E
63	173980	Late Miocene	lower Lefkara	M	35 01 06.085 N	033 20 33.677 E
64	173981	Late Miocene	lower Lefkara	M	35 01 06.085 N	033 20 33.677 E
65	173982	Late Miocene	lower Lefkara	M	35 01 06.085 N	033 20 33.677 E
66	173965	Paleocene	lowest Lefkara	3	34 59 53.203 N	033 25 29.392 E
67	173966	Paleocene	lower Lefkara	3	34 59 53.218 N	033 25 28.967 E

Table B: Samples obtained from the second field campaign.

Sample	IFP ID	Age	Formation	Location	Lat	Lon
227	174259	Miocene	Pakhna	12	34°46'38.21"N	33°23'56.29"E
228	174260	Miocene	Pakhna	11	34°48'8.56"N	33°26'8.74"E
229	174261	Miocene	Pakhna	14	34°49'40.04"N	33°23'29.82"E
230	174262	Miocene	Pakhna	15	34°49'4.70"N	33°23'37.92"E
231	174338	Miocene	Pakhna	15	34°49'4.70"N	33°23'37.92"E
232	174263	Miocene	Pakhna	19	34°45'43.12"N	32°50'35.95"E
233	174264	Miocene	Pakhna	20	34°46'25.23"N	32°49'55.88"E
234	174265	Miocene	Pakhna	13	34°50'13.50"N	33°23'58.10"E
235	174266	Jurassic	Episkopi	28	34°52'32.39"N	32°35'47.32"E
236	174267	Jurassic	Episkopi	27	34°51'56.86"N	32°36'11.56"E
237	174268	Jurassic	Episkopi	26	34°52'8.85"N	32°36'25.95"E
238	174269	Miocene	Pakhna	30	34°52'34.04"N	32°35'38.65"E
239	174270	Miocene	Pakhna	30	34°52'34.04"N	32°35'38.65"E
240	174271	Miocene	Pakhna	30	34°52'34.04"N	32°35'38.65"E
241	174272	Miocene	Pakhna	18a	34°45'51.40"N	32°55'52.38"E
242	174273	Miocene	Pakhna	18a	34°45'51.40"N	32°55'52.38"E
243	174274	Miocene	Pakhna	18a	34°45'51.40"N	32°55'52.38"E
244	174275	Miocene	Pakhna	18a	34°45'51.40"N	32°55'52.38"E
245	174276	Miocene	Pakhna	18b	34°45'56.08"N	32°55'59.01"E
246	174277	Miocene	Pakhna	18b	34°45'56.08"N	32°55'59.01"E
247	174278	Miocene	Pakhna	18b	34°45'56.08"N	32°55'59.01"E
248	174279	Triassic	Vlambouros	33	34°58'50.01"N	32°19'0.37"E
249	174280	Triassic	Vlambouros	33	34°58'50.01"N	32°19'0.37"E
250	174281	Triassic	Vlambouros	33	34°58'50.01"N	32°19'0.37"E
251	174282	Triassic	Vlambouros	33	34°58'50.01"N	32°19'0.37"E
252	174283	Triassic	Vlambouros	33	34°58'50.01"N	32°19'0.37"E
253	174284	Triassic	Vlambouros	33	34°58'50.01"N	32°19'0.37"E
254	174285	Triassic	Vlambouros	32	34°58'54.70"N	32°19'9.44"E
255	174286	Triassic	Vlambouros	32	34°58'54.70"N	32°19'9.44"E
256	174287	Triassic	Vlambouros	32	34°58'54.70"N	32°19'9.44"E
257	174288	Triassic	Vlambouros	32	34°58'54.70"N	32°19'9.44"E
258	174289	Triassic	Vlambouros	32	34°58'54.70"N	32°19'9.44"E
259	174290	Triassic	Vlambouros	32	34°58'54.70"N	32°19'9.44"E
260	174291	Triassic	Vlambouros	32	34°58'54.70"N	32°19'9.44"E
261	174292	Triassic	Vlambouros	32	34°58'54.70"N	32°19'9.44"E
262	174293	Triassic	Vlambouros	32	34°58'54.70"N	32°19'9.44"E
263	174294	Triassic	Vlambouros	32	34°58'54.70"N	32°19'9.44"E
264	174295	Triassic	Vlambouros	32	34°58'54.70"N	32°19'9.44"E
265	174296	Miocene	Pakhna	23	34°39'37.84"N	32°39'8.18"E
266	174297	Miocene	Pakhna	23	34°39'37.84"N	32°39'8.18"E
267	174298	Miocene	Pakhna	23	34°39'37.84"N	32°39'8.18"E
268	174299	Miocene	Pakhna	23	34°39'37.84"N	32°39'8.18"E
269	174300	Miocene	Pakhna	23	34°39'37.84"N	32°39'8.18"E
270	174301	Maastrichtian	Moni	17	34°45'14.58"N	33° 6'23.90"E
271	174302	Miocene	Pakhna	12	34°46'38.21"N	33°23'56.29"E
272	174303	Miocene	Pakhna	12	34°46'38.21"N	33°23'56.29"E
273	174304	Miocene	Pakhna	12	34°46'38.21"N	33°23'56.29"E
274	174305	Miocene	Pakhna	10	34°57'29.54"N	33°34'43.13"E
275	174306	Miocene	Pakhna	10	34°57'29.54"N	33°34'43.13"E
276	174307	Miocene	Pakhna	10	34°57'29.54"N	33°34'43.13"E
277	174308	Miocene	Pakhna	10	34°57'29.54"N	33°34'43.13"E
278	174309	Miocene	Pakhna	10	34°57'29.54"N	33°34'43.13"E
279	174310	Miocene	Pakhna	10	34°57'29.54"N	33°34'43.13"E
280	174311	Miocene	Pakhna	10	34°57'29.54"N	33°34'43.13"E
281	174312	Miocene	Pakhna	10	34°57'29.54"N	33°34'43.13"E
282	174313	Miocene	Pakhna	10	34°57'29.54"N	33°34'43.13"E
283	174314	Miocene	Pakhna	10	34°57'29.54"N	33°34'43.13"E
284	174315	Miocene	Pakhna	10	34°57'29.54"N	33°34'43.13"E
285	174316	Miocene	Pakhna	10	34°57'29.54"N	33°34'43.13"E
286	174317	Miocene	Pakhna	2	35° 1'57.25"N	33°20'39.12"E
287	174318	Miocene	Pakhna	2	35° 1'57.25"N	33°20'39.12"E
288	174319	Miocene	Pakhna	2	35° 1'57.25"N	33°20'39.12"E
289	174320	Miocene	Pakhna	2	35° 1'57.25"N	33°20'39.12"E
290	174321	Miocene	Pakhna	2	35° 1'57.25"N	33°20'39.12"E
291	174322	Miocene	Pakhna	2	35° 1'57.25"N	33°20'39.12"E
292	174323	Miocene	Pakhna	2	35° 1'57.25"N	33°20'39.12"E
293	174324	Miocene	Pakhna	2	35° 1'57.25"N	33°20'39.12"E
294	174325	Miocene	Pakhna	2	35° 1'57.25"N	33°20'39.12"E
295	174326	Miocene	Pakhna	2	35° 1'57.25"N	33°20'39.12"E
296	174327	Miocene	Pakhna	2	35° 1'57.25"N	33°20'39.12"E
297	174328	Miocene	Pakhna	1	35° 1'58.27"N	33°20'35.56"E
298	174329	Miocene	Pakhna	1	35° 1'58.27"N	33°20'35.56"E
299	174330	Miocene	Pakhna	1	35° 1'58.27"N	33°20'35.56"E
300	174331	Miocene	Pakhna	1	35° 1'58.27"N	33°20'35.56"E
301	174332	Miocene	Pakhna	1	35° 1'58.27"N	33°20'35.56"E
302	174333	Miocene	Pakhna	1	35° 1'58.27"N	33°20'35.56"E
303	174334	Miocene	Pakhna	1	35° 1'58.27"N	33°20'35.56"E
304	174335	Miocene	Pakhna	1	35° 1'58.27"N	33°20'35.56"E
305	174336	Miocene	Pakhna	1	35° 1'58.27"N	33°20'35.56"E
306	174337	Miocene	Pakhna	1	35° 1'58.27"N	33°20'35.56"E

Table C: Offshore samples from the ODP Leg 160 wells.

Sample	LEK ID	Age	Site	Hole	Core	Section	Top	Bottom	MBSF Top
68	17/1643	Miocene	965	A	14	1	0	4	115.7
69	17/1644	Miocene	965	A	14	1	15	17	115.85
70	17/1645	Miocene	965	A	14	1	86	98	116.56
71	17/1646	Miocene?	965	A	16	1	1	4	135.11
72	17/1647	Miocene?	965	A	16	1	12	15	135.22
73	17/1648	Miocene?	965	A	16	1	28	30	135.38
74	17/1649	Miocene?	965	A	16	1	53	56	135.63
75	17/1650	Miocene?	965	A	16	1	66	68	135.76
76	17/1651	Miocene?	965	A	16	1	81	85	135.91
77	17/1652	Miocene?	965	A	19	1	0	6	163.9
78	17/1653	Miocene?	965	A	21	1	0	3	183.1
79	17/1654	Miocene?	965	A	21	1	6	9	183.16
80	17/1655	Miocene?	965	A	21	1	21	23	183.31
81	17/1656	Miocene?	965	A	21	1	33	35	183.43
82	17/1657	Miocene?	965	A	21	1	40	43	183.5
83	17/1658	Miocene?	965	A	23	1	28	31	202.48
84	17/1659	Miocene?	965	A	26	1	97	100	232.07
85	17/1660	Miocene?	965	A	26	1	124	126	232.34
86	17/1661	Miocene?	965	A	27	1	20	22	241
87	17/1662	Miocene	966	D	20	1	5	7	126.95
88	17/1663	Miocene	966	D	20	1	14	17	127.04
89	17/1664	Miocene	966	D	20	1	26	28	127.16
90	17/1665	Miocene	966	D	20	1	29	30	127.19
91	17/1666	Miocene	966	F	10	1	0	3	144.2
92	17/1667	Miocene	966	F	12	1	80	82	164.3
93	17/1668	Miocene	966	F	12	1	128	130	164.78
94	17/1669	Miocene	966	F	13	1	77	80	173.87
95	17/1670	Miocene	966	F	14	1	10	13	182.8
96	17/1671	Miocene	966	F	15	1	32	35	192.72
97	17/1672	Miocene	966	F	15	1	63	66	193.03
98	17/1673	Miocene	966	F	15	1	90	93	193.3
99	17/1674	Miocene	966	F	16	1	9	13	202.09
100	17/1675	Miocene	966	F	16	3	10	13	205.08
101	17/1676	Miocene	966	F	17	1	96	100	212.56
102	17/1677	Miocene	966	F	18	1	33	35	221.63
103	17/1678	Miocene	966	F	18	1	98	100	222.28
104	17/1679	Eocene	966	F	26	1	18	22	298.48
105	17/1680	Eocene	966	F	26	1	26	29	298.56
106	17/1681	Eocene	966	F	26	1	31	33	298.61
107	17/1682	Eocene	966	F	26	1	42	44	298.72
108	17/1683	Eocene	966	F	26	1	56	59	298.86
109	17/1684	Eocene	966	F	26	1	66	68	298.96
110	17/1685	Eocene	966	F	26	2	5	7	299.11
111	17/1686	Eocene	966	F	26	2	13	14	299.19
112	17/1687	Eocene	966	F	26	2	29	30	299.35
113	17/1688	Eocene	966	F	26	2	40	41	299.46
114	17/1689	Eocene	966	F	26	2	50	51	299.56
115	17/1690	Eocene	966	F	26	2	65	67	299.71
116	17/1691	Eocene	966	F	26	2	76	78	299.82
117	17/1692	Eocene	966	F	26	2	99	100	300.05
118	17/1693	Eocene	966	F	26	3	52	54	301.03
119	17/1694	Eocene	966	F	26	3	67	69	301.18
120	17/1695	Eocene	966	F	27	6	46	49	315.26
121	17/1696	Eocene	966	F	28	1	30	33	317.8
122	17/1697	Eocene	966	F	28	2	6	8	318.18
123	17/1698	Eocene	966	F	28	2	34	36	318.46
124	17/1699	Eocene	966	F	28	2	61	62	318.73
125	17/1700	Eocene	966	F	28	2	108	112	319.2
126	17/1701	Eocene	966	F	28	3	6	7	319.6
127	17/1702	Eocene	966	F	28	3	118	120	320.72
128	17/1703	Eocene	966	F	28	3	138	139	320.92
129	17/1704	Eocene	966	F	28	4	30	34	321.29
130	17/1705	Eocene	966	F	28	4	64	65	321.63
131	17/1706	Eocene	966	F	28	4	114	116	322.13
132	17/1707	Eocene	966	F	28	5	86	91	323.28
133	17/1708	Eocene	966	F	28	6	31	34	324.23
134	17/1709	Eocene	966	F	29	1	39	42	327.49
135	17/1710	Eocene	966	F	29	1	101	102	328.11
136	17/1711	Eocene	966	F	29	2	47	50	329.07
137	17/1712	Eocene	966	F	29	2	67	71	329.27
138	17/1713	Eocene	966	F	29	2	136	139	329.96
139	17/1714	Eocene	966	F	29	3	35	37	330.45
140	17/1715	Eocene	966	F	29	3	50	52	330.6
141	17/1716	Eocene	966	F	30	1	15	17	336.95
142	17/1717	Eocene	966	F	30	1	38	40	337.18
143	17/1718	Eocene	966	F	30	1	71	72	337.51
144	17/1719	Eocene	966	F	30	1	105	110	337.85
145	17/1720	Eocene	966	F	30	1	132	137	338.12

146	17/1721	Eocene	966	F	30	2	10	13	338.4
147	17/1722	Eocene	966	F	30	2	55	57	338.85
148	17/1723	Eocene	966	F	30	2	71	75	339.01
149	17/1724	Eocene	966	F	30	2	125	127	339.55
150	17/1725	Eocene	966	F	30	2	136	138	339.66
151	17/1726	Eocene	966	F	30	3	1	3	339.78
152	17/1727	Eocene	966	F	30	3	12	15	339.89
153	17/1728	Eocene	966	F	30	3	36	38	340.13
154	17/1729	Eocene	966	F	30	3	76	78	340.53
155	17/1730	Eocene	966	F	30	3	95	97	340.72
156	17/1731	Eocene	966	F	30	3	116	118	340.93
157	17/1732	Eocene	966	F	30	3	130	135	341.07
158	17/1733	Eocene	966	F	31	1	3	7	346.43
159	17/1734	Eocene	966	F	31	1	24	28	346.64
160	17/1735	Eocene	966	F	31	1	62	63	347.02
161	17/1736	Eocene	966	F	31	1	136	138	347.76
162	17/1737	Eocene	966	F	31	2	6	9	347.96
163	17/1738	Eocene	966	F	31	2	57	59	348.47
164	17/1739	Eocene	966	F	31	2	71	73	348.61
165	17/1740	Eocene	966	F	31	2	90	93	348.8
166	17/1741	Eocene	966	F	31	2	113	119	349.03
167	17/1742	Eocene	966	F	31	3	31	34	349.53
168	17/1743	Eocene	966	F	31	3	70	73	349.92
169	17/1744	mid Eocene	967	E	7	1	0	4	167.3
170	17/1745	mid Eocene	967	E	7	1	49	57	167.79
171	17/1746	late Cretaceous	967	E	8	1	15	18	177.05
172	17/1747	late Cretaceous	967	E	8	1	42	44	177.32
173	17/1748	late Cretaceous	967	E	8	1	53	55	177.43
174	17/1749	late Cretaceous	967	E	18	1	17	20	273.27
175	17/1750	late Cretaceous	967	E	18	1	36	39	273.46
176	17/1751	late Cretaceous	967	E	18	1	96	99	274.06
177	17/1752	late Cretaceous	967	E	18	1	126	128	274.36
178	17/1753	late Cretaceous	967	E	18	2	27	30	274.65
179	17/1754	late Cretaceous	967	E	18	2	66	70	275.04
180	17/1755	late Cretaceous	967	E	18	2	117	120	275.55
181	17/1756	late Cretaceous	967	E	18	3	51	54	276.31
182	17/1757	late Cretaceous	967	E	25	1	43	45	340.93
183	17/1758	late Cretaceous	967	E	25	1	84	87	341.34
184	17/1759	late Cretaceous	967	E	25	2	22	25	342.18
185	17/1760	late Cretaceous	967	E	25	2	84	87	342.8
186	17/1761	late Cretaceous	967	E	25	2	115	115	343.11
187	17/1762	late Cretaceous	967	E	25	3	97	100	344.4
188	17/1763	late Cretaceous	967	E	29	1	42	45	379.22
189	17/1764	late Cretaceous	967	E	29	1	107	110	379.87
190	17/1765	late Cretaceous	967	E	29	1	118	120	379.98
191	17/1766	late Cretaceous	967	E	29	2	0	4	380.3
192	17/1767	late Cretaceous	967	E	29	2	24	27	380.54
193	17/1768	late Cretaceous	967	E	29	2	64	66	380.94
194	17/1769	late Cretaceous	967	E	30	1	6	10	388.46
195	17/1770	late Cretaceous	967	E	30	1	27	30	388.67
196	17/1771	late Cretaceous	967	E	30	1	30	35	388.7
197	17/1772	late Cretaceous	967	E	30	1	42	44	388.82
198	17/1773	mixed late Miocene-early Pliocene with Late Cretaceous-middle Miocene	968	A	17	2	23	24	153.93
199	17/1774	"	968	A	17	2	74	76	154.44
200	17/1775	"	968	A	17	2	136	138	155.06
201	17/1776	"	968	A	17	3	23	24	155.43
202	17/1777	"	968	A	17	3	74	76	155.94
203	17/1778	"	968	A	17	3	136	138	156.56
204	17/1779	"	968	A	17	4	23	24	156.93
205	17/1780	"	968	A	18	8	31	32	171.52
206	17/1781	"	968	A	24	1	20	21	200.6
207	17/1782	"	968	A	24	1	49	51	200.89
208	17/1783	"	968	A	24	1	87	89	201.27
209	17/1784	"	968	A	24	1	122	124	201.62
210	17/1785	"	968	A	26	4	21	23	224.41
211	17/1786	"	968	A	26	4	45	48	224.65
212	17/1787	"	968	A	26	4	84	86	225.04
213	17/1788	"	968	A	29	1	19	23	248.79
214	17/1789	"	968	A	29	1	52	55	249.12
215	17/1790	"	968	A	29	1	78	80	249.38
216	17/1791	"	968	A	29	1	110	113	249.7
217	17/1792	"	968	A	30	7	12	14	267.32
218	17/1793	"	968	A	32	4	23	25	282.13
219	17/1794	"	968	A	32	4	29	31	282.19
220	17/1795	"	968	A	32	4	75	78	282.65
221	17/1796	"	968	A	33	3	28	30	290.28
222	17/1797	"	968	A	33	3	66	68	290.66
223	17/1798	"	968	A	33	3	126	128	291.26
224	17/1799	"	968	A	34	1	11	14	296.71
225	17/1800	"	968	A	34	1	48	50	297.08
226	17/1801	"	968	A	34	1	89	91	297.49